Collège Doctoral du Languedoc-Roussillon

THÈSE

Pour obtenir le grade de

Docteur

Délivré par l'**Université de Montpellier**

Préparée au sein de l'école doctorale **I2S**
Et de l'unité de recherche **Laboratoire Charles Coulomb**

Spécialité: **Physique**

Présentée par **Ana Carolina LOPES SELVATI**

Confinement d'oligomères π-conjugués dans des nanotubes de carbone mono-feuillets: interactions, dynamique et structure

Soutenue le 16 décembre 2016 devant le jury composé de

Mr A. San Miguel, Professeur, Université Claude Bernard Lyon 1	**Rapporteur**
Mme P. Launois, Directeur de Recherche, Université Paris-Sud	**Rapporteur**
Mr G. Cassabois, Professeur, Université de Montpellier	**Président**
Mr P. Puech, Maître de conférences, CEMES, Toulouse	**Examinateur**
Mme M. Jimenez Ruiz, Chercheur, Institut Laue-Langevin	**Examinateur**
Mr S. Rols, Chercheur, Institut Laue-Langevin	**Examinateur**
Mr J.-L. Bantignies, Professeur, Université de Montpellier	**Directeur**
Mme R. Le Parc, Maître de conférences, Université de Montpellier	**Co-encadrant**

Université de Montpellier

To Ana Maria and Amauri . . .

Useful quantities in Neutron Scattering

Energy relationships

$$
\begin{aligned}
E(\text{meV}) &= \frac{mv^2}{2} = 5.2267 \cdot v^2, \text{ where } [v] = \text{km} \cdot \text{s}^{-1} \\
&= \frac{\hbar^2 k^2}{2m} = 2.072 \cdot k^2, \text{ where } [k] = \text{Å}^{-1} \\
&= \frac{h^2}{2m\lambda^2} = \frac{81.799}{\lambda^2}, \text{ where } [\lambda] = \text{Å}
\end{aligned}
$$

Energy unit conversions									
1meV	=	8.06554cm^{-1}	=	0.24180THz	=	4135.66752fs	=	4.13567ps	

Neutron scattering lengths and cross sections[1]

Isotope	bound coh scatt length	bound coh scatt xs	bound incoh scatt xs
	$b_{\text{atom}}^{\text{coh}}$ **(fm)**	$\sigma_{\text{atom}}^{\text{coh}}$ **(barn)**	$\sigma_{\text{atom}}^{\text{inc}}$ **(barn)**
H	-3.7390	1.7568	80.26
D	6.671	5.592	2.05
C	6.6460	5.551	0.001
N	9.36	11.01	0.5
O	5.803	4.232	0.0008
S	2.847	1.0186	0.007
Fe	9.45	11.22	0.4

Note: Where in SI units, fm $= 1 \times 10^{-15}$m and barn $= 1 \times 10^{-28}$m^2.

[1] https://www.ncnr.nist.gov/resources/n-lengths/

List of Abbreviations

SWCNT	Single-Walled Carbon Nanotube
DWCNT	Double-Walled Carbon Nanotube
MWCNT	Multi-Walled Carbon Nanotube
AP	As-prepared nanotubes
NTϕ	Carbon Nanotube of diameter ϕ Å
CoMoCAT	Cobalt Molybdenum catalyser synthesis
eDIPS	enhanced Direct Injection Pyrolytic Synthesis
oT	oligomers of Thiophene
$4TCH_3$	Dimethyl-Quaterthiophene
FePc	Iron-Phthalocyanine
HRTEM	High-Resolution Transmission Electron Microscopy
XPS	X-ray Photoelectron Spectrometry
NEXAFS	Near-edge Absorption X-ray Fine Structure
PL	Photoluminescence
RS	Raman scattering
INS	Inelastic Neutron Scattering
TOF	Time-of-flight
SANS	Small-Angle Neutron Scattering
SAXS	Small-Angle X-ray Scattering
DFT	Density Functional Theory
eDOS	Electronic Density of States

vDOS	Vibrational Density of States
HPDOS	Hydrogen Partial Density of States
LAGRANGE	Large Area GRaphite ANalyser for Genuine Excitations
BEAR	Bending Magnet for Emission Absorption and Reflectivity
PAXY	Petits Angles, détecteur 2d XY

Contents

Introduction and Motivation

Since their discovery [1], single-walled carbon nanotubes (SWCNTs) have stimulated widespread scientific interest due to their *pseudo-one-dimensional structures*, unique electronic [2] and mechanical [3] properties.

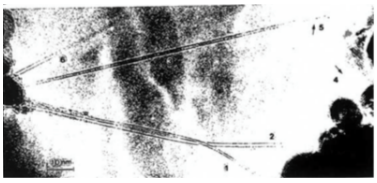

Figure 1 First electron micrograph of individual SWCNTs with diameters ranging from 7.5 to 13.7 Å. Taken from reference [1].

Due to their size and geometry, SWCNTs also provide a unique opportunity for nanoscale engineering of original one-dimensional systems, created by encapsulation of molecules inside the SWCNT's hollow core. This internal channel [4] offers the opportunity to encapsulate various molecules (M) leading to elaboration of hybrid nanotubes (M@SWCNT). After the first synthesis of organic "*peapods*": encapsulated fullerenes (C_{60}) inside carbon nanotubes: C_{60}@SWCNT [5], the hollow space of these carbon cages attracted increasing interest. In the past decade, many materials, including metallofullerenes [6–8], metallocenes [9], organometallic molecules [10, 11], and nanocrystals [12–16], have been successfully confined in the nanosized inner cavity of carbon nanotubes.

There are several advantages to use carbon nanotubes as nano-container. Being built of sp^2-carbon atoms, nanotubes are significantly more thermally stable (*e.g.* up to 700 °C in air and up to 2800 °C in vacuum) and mechanically more robust than any other molecular or supramolecular nano-containers, which is highly advantageous for device fabrication. The inner wall of the nanotubes has very low chemical reactivity, so that some aggressive chemical process can be contained within the nanotube. They also protect the guest molecule from the environment, for example oxidation [17], that would otherwise induce deterioration, which is highly detrimental for applications.

The encapsulation of species inside carbon nanotubes has motivated different types of studies. One type of study is related to fundamental interest for the physics of one-dimensional (1D) systems [18]. Once encapsulated inside the nanotubes, the behaviour of the guest molecule is greatly affected by the confinement of the 1D local environment. For example, fullerene forms molecular arrays inside nanotubes that are dramatically different from the face-centered cubic structure of the bulk fullerene [19–21]. The exact structure of the array is dependent on the nanotube diameter, as simple linear chains of C_{60}, typically observed inside a SWCNT with diameter of [13, 15 Å], are replaced by more complex packing patterns in wider host carbon nanotubes. Inorganic atomic and ionic lattices can be similarly controlled by confinement in nanotubes [12]. Cobalt iodide, for instance, forms a helically twisted structure inside nanotubes that is fundamentally different from bulk CoI_2 crystals [15] while atoms of iodine assemble into single chains or double and triple helices depending on the SWCNT diameter [22]. This list of examples is not exhaustive, as there are other illustrations that the nanotube is not just a passive container. In many cases, it acts as an effective template to control the structures of molecular and atomic arrays. The key parameter of this control is the *diameter* of the nanotubes: the size of the hollow core is close to the size of the trapped species, yielding in an effective interaction between the guest species and the host SWCNTs.

A second type of study is related to the potential opportunity of tuning the properties of the new hybrids by encapsulation but also keeps the peculiar physical properties of SWCNTs. Indeed, since the particular one-dimensional advantages and the nanoscale structures make the fillers possess novel properties which are quite different from those of their bulk counterparts, filling SWCNTs with chosen materials can lead to nano-structures with exciting new applications. As a consequence, significant changes in the electronic energy levels can appear, leading to very different properties. Considerable efforts have been directed towards elucidating properties of hybrid nanotubes composed of organic molecules encapsulated inside carbon nanotubes which present different advantages for potential *nano-optoelectronics* applications. At least two main advantages are identified:

On one hand, *photonic devices* with SWCNTs as active material [23–25] are limited to the near-infrared (NIR) region due to the intrinsically small bandgaps of SWCNTs. Inserting organic molecules inside the SWCNT opens opportunities for them, to become optically active in the visible region. One the other hand, for molecular electronics, it is crucial to obtain both p- and n-type air-stable SWCNTs and control their carrier density. For molecular electronics, it is crucial to obtain both p- and n-type air-stable SWCNTs and control their carrier density. Indeed, SWCNTs field-effect transistors (FETs) under ambient conditions are always p-type due to electron withdrawing by the absorbed O_2. The production of air-stable

n-type SWCNT transistors is thus especially important technologically. Several doping methods, including adsorption of alkali metals [13], annealing in vacuum [26], inert gas [27], or hydrogen [28], and electrochemical method [29], have been developed for producing n-type SWCNTs, but their stability in air was not satisfactory. Polymer functionalization of SWCNTs can yield air-stable n-type SWCNTs with low carrier concentration [30], however, a fine tuning of carrier concentration remains very difficult in this scheme.

An alternative, is to perform air-stable amphoteric doping on SWCNTs by encapsulation of organic molecules inside of it [31]. The characteristic optical absorption intensities of these doped SWCNTs change with the electron affinity (EA) or ionization potential (IP) of the encapsulated organic molecules [31]. This suggests that the carrier concentration of SWCNTs can be controlled by tuning the EA or IP of the encapsulated organic molecules. Furthermore, the process of doping SWCNTs by organic molecules is simple, thus a viable route for the large-scale production of SWCNTs with controllable doping state is offered.

In this context, significant efforts have been performed to elaborate and study the physical properties of hybrid nanotubes after encapsulation of oligothiophenes (oT@SWCNT). α-Oligothiophenes are electron-rich and chemically stable conjugated oligomers, renowned for their optoelectronic properties and wide applications as active components in organic devices [32–35]. Besides that, their size and structure fit the size of the hollow core of the nanotubes. Loi and collaborators have first reported the synthesis of oligothiophenes inside carbon nanotubes [36] for the first time in 2010. A 1D geometrical confinement effect on oligothiophenes structural properties has been both theoretically and experimentally demonstrated. The supramolecular organizations of the confined oligothiophenes is shown to be depend on the nano-container size [36, 37].

Concerning interaction between oT and SWCNTs and especially charge transfer, its existence has been examined both experimentally and theoretically but lead to contradictory conclusions indicating that the question is still open [36–39].

The occurrence of energy transfer from the molecules to SWCNTs can neither be excluded nor unambiguously proven at this stage [39].

As a result, an interesting question is whether a significant interaction occurs after oligothiophene encapsulation inside SWCNTs. In order to elucidate the nature of the *confinement effect*, we address in the part I of this thesis the following issues:

- How does the size of the nano-container influence the interactions between encapsulated oligothiophenes and the nanotube?
- Is there any energy transfer (ET) or charge transfer (CT) between the two subsystems after 1D confinement?

- Does the variation on the confinement affect potential ET or CT?
- What does one learn from encapsulation of conducting oligomers in confined environments?

To address these questions, we have carried out experimental investigations on dimethyl-quaterthiophene molecules ($4TCH_3$) encapsulated inside SWCNTs as a function of the size of the nano-container. Complementary, the study of the encapsulation of Iron-Phthalocyanine (FePc) molecules inside SWCNTs is also presented. The study of $4TCH_3$@SWCNTs systems is presented in chapter 1 to 4. The manuscript is therefore divided as follows:

Part I $4TCH_3$ encapsulated inside SWCNTs

Chapter 1 gives an introduction to the basic physical concepts of carbon nanotubes necessary to understand its electronic, optic and vibrational properties. After, the bibliographic work on encapsulated oligomers of thiophene is presented.

Chapter 2 first describes of the encapsulation protocol of $4TCH_3$ inside single-walled carbon nanotubes, followed by the characterization of the $4TCH_3$@SWCNTs hybrid systems.

Chapter 3 focuses on the vibrational properties of the encapsulated molecule, which is acessed by Inelastic Neutron Scattering, in order to give insights on both encapsulation and confinement effects of hybrid systems of different sizes.

Chapter 4 is devoted to the spectroscopic study of the charge and energy transfer on the hybrid systems in function of the size of the nanotube.

Complementary to the study of the $4TCH_3$@SWCNT system, we also investigate the geometrical confinement of iron phthalocyanine (FePc) molecules inside SWCNT. The motivation for this exploratory work is related to the influence of the macrocycle character of the FePc on the structural properties of the hybrid FePc@SWCNT. This study is presented in the part II, chapter 5:

Part II FePc encapsulated inside SWCNTs

Chapter 5 is devoted to the study of the hybrid system FePc@SWCNTs. The structural properties of the encapsulated molecule which are probed by Elastic Neutron Scattering along with the vibrational properties of the hybrid systems is discussed. Both structural and spectrocopic behaviours of the system are also studied under pressure.

At last, the Appendices will come to complement some information:

Part I

$4TCH_3$ encapsulated inside SWCNTs

Chapter 1

From pristine to hybrid carbon nanotubes

Contents

This chapter is dedicated to a bibliographic study divided into two main parts. The part 1.1 concerns the physical properties of pristine carbon nanotubes. The structure of carbon nanotubes in real and reciprocal space is presented in order to have the background to discuss the nanotube electronic, optical and vibrational properties. As we are interested in the encapsulation of dye molecules inside the hollow space of carbon nanotubes, the part 1.2 is dedicated to a review on the hybrids systems. We shall first give a quick overview of the first studies on dye molecules encapsulated inside carbon nanotubes. As we are specifically going to study the encapsulation of oligothiophene molecules, the subsection 1.2.1 gives an

account on the results reported in the literature. A particular interest will be driven onto the physical properties (*e.g.* electronic, optical and vibrational) appearing as characteristic of these new materials.

1.1 Pristine Carbon Nanotubes

Carbon atoms are located at the IV column of the periodic table, having six electrons. Two of which are strongly bounded and occupy the 1s orbital. The other four are distributed between the 2s and 2p orbitals. Carbon atoms which have sp^2 have three hybridized in-plane sp orbitals (2s with $2p_x$ and $2p_y$), responsible for the strong σ bonds. The remaining $2p_z$ orbital is out-of-plane, called π orbital, is responsible for the weak van der Waals interactions between graphene layers, see figure 1.1. The three in-plane orbitals are separated by 120 °, building up a bi-dimensional structure in real space, having a trigonal lattice, often called honeycomb lattice. That is the graphene structure, the parent material of carbon nanotubes.

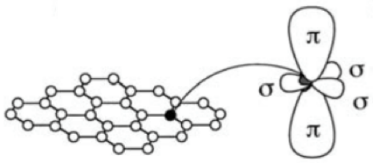

Figure 1.1 Small graphene ribbon with the representation of the π and σ valence orbitals of the carbon atom with the sp^2 hybridization. Taken from reference [40].

A pictorial way to obtain carbon nanotubes from its parent material, is to roll up seamlessly a finite graphene layer. As a consequence, carbon nanotubes differ from the graphene structure through its *curvature*. In one hand, a change in the bond character from the planar parent material (distortion of the C-C bonds) is observed. On the other hand, the reduced dimensionality along its circumferential axis, gives rise to *confinement effects* [41].

The following section is dedicated to describe the structure of nanotubes in the real space. The aim is not to prove all equations, since all the theory can be found in references [42, 43].

1.1.1 Structure of nanotubes in the real space

Carbon nanotubes with a given *diameter* (d_{NT}) can be build up by rolling up a finite graphene layer (see figure 1.2) into a cylindrical shape. The point O is rolled up in order to coincide with the point A and the point B will consequently coincide with the point B'. The unit cell of the nanotube is defined by the losangle OAB'B, in other words, by the chiral vector $\vec{C}_h$ and

translation vector $\vec{T}$. The modulus of the chiral vector $\vec{C}_h$ corresponds to the circumference of the nanotube πd_{NT} and the translational vector $\vec{T}$ corresponding to the period T = $\mid \vec{T} \mid$ along the nanotube axis. The formed nanotubes have a cylindrical structure with a hollow space and axial symmetry.

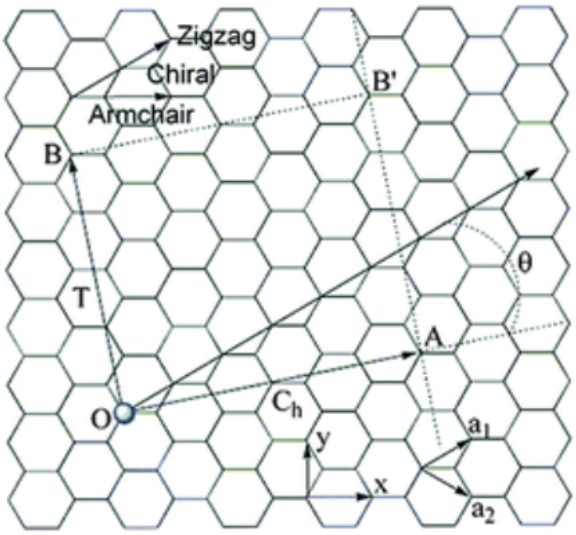

Figure 1.2 Representation of finite graphene layer with unit vectors $\vec{a}_1$ and $\vec{a}_2$ in real space. Those two vectors define the unit cell of a graphene layer which has two carbon atoms. OAB'B defines the unit cell of the nanotube. Chiral and translation vectors are represented by $\vec{C}_h$ (blue vector) and $\vec{T}$ (pink vector), respectively. The chiral angle θ is defined as the angle between the vectors $\vec{a}_1$ and the $\vec{C}_h$.

The chiral vector is denoted by a pair of two integers, (n,m) that can be written in function of the graphene unit vectors in the real space by:

$$\vec{C}_h = n\vec{a}_1 + m\vec{a}_2 \equiv (n,m)\,, \text{ where } -n/2 \leq \mid m \mid \leq n\,. \tag{1.1}$$

Where, a = $\mid \vec{a}_1 \mid$ = $\mid \vec{a}_2 \mid$ = 2.49 Å, with:

$$\vec{a}_1 = \left(\frac{\sqrt{3}a}{2}, \frac{a}{2}\right), \qquad \vec{a}_2 = \left(\frac{\sqrt{3}a}{2}, -\frac{a}{2}\right). \tag{1.2}$$

The hexagons from the honeycomb lattice are arranged in a helical fashion along the nanotube's axis, called *chirality*, see figure 1.3. The orientation of the honeycomb lattice along the nanotube axis depends on the chiral angle θ, which is given by:

$$\cos(\theta) = \frac{\vec{C}_h \cdot \vec{a}_1}{\mid \vec{C}_h \mid \cdot \mid \vec{a}_1 \mid} = \frac{2n+m}{2\sqrt{n^2+m^2+nm}}\,. \tag{1.3}$$

Because of the hexagonal lattice of nanotubes and the possible values that θ can assume, carbon nanotubes can have three different structures, described in Table 1.1:

Table 1.1 Classification of nanotubes by their chirality.

Type	chiral angle	chiral index
zigzag	0 °	(n,0)
armchair	30 °	(n,n)
chiral	0 ° $<\mid \theta \mid <$ 30 °	(n,m)

Note: The chiral angle θ value lies in the range of $0 <\mid \theta \mid < 30$, since the rotational symmetry of graphene is six-fold.

The figure 1.3 shows the representation of those three different structures of nanotubes with the same diameter:

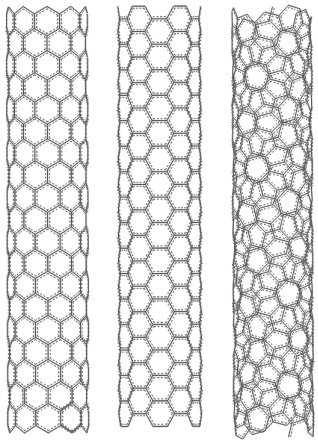

Figure 1.3 Schematic representation of three different chiralities of SWNTs, all with diameter around 8.5 Å. **Left-hand side:** zig-zag (10,0); **Middle:** arm-chair (6,6) and **Right-hand side:** chiral (8,3).

These different structures results from a particular chirality, are also associated to different diameters. Thus diameter d_{NT} can be written as a function of the chiral vector:

$$d_{NT} = \frac{\mid \vec{C}_h \mid}{\pi}, \text{ where } \mid \vec{C}_h \mid = \sqrt{\vec{C}_h \cdot \vec{C}_h} = a\sqrt{n^2 + m^2 + nm}. \tag{1.4}$$

Where a=$\sqrt{3}\,a_{C-C}$ = 2.49 Å is the lattice parameter of the graphene layer and a_{C-C} = 1.44 Å is the nearest C-C distance.

1.1.2 Nanotube's reciprocal space

Electrons and phonons are quasi-particles which are described as waves in the reciprocal space. Since we are interested in the electronic and vibrational properties, it is important to describe and understand the reciprocal lattice of graphene, which will be first described in order to derive the nanotube's reciprocal lattice.

The reciprocal lattice of graphene is constructed from the hexagonal lattice in the real space, where the first Brillouin zone is constructed from the unit cell in the real lattice, with the high-symmetry points Γ, K and M, indicated in figure 1.4.

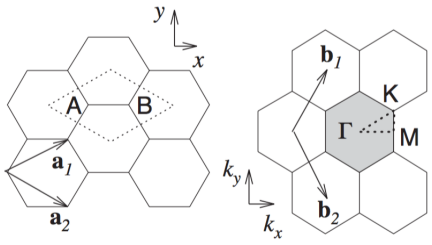

Figure 1.4 Left-hand side: Representation of finite graphene lattice in the real space with unit vectors $\vec{a}_1$ and $\vec{a}_2$ with the two carbon atoms indicated by A and B, belonging to one graphene unit cell. **Right-hand side:** First Brillouin zone of the hexagonal lattice of a graphene layer in gray. The vectors $\vec{b}_1$ and $\vec{b}_2$ are the unit vectors of graphene in the reciprocal space. Taken from reference [44].

Thus the reciprocal lattice vectors of graphene can be obtained from equations 1.2 with the relation $\vec{b_i} \cdot \vec{b_j} = 2\pi\delta_{ij}$, where b = $|\vec{b_1}| = |\vec{b_2}| = {}^{4\pi}/_{\sqrt{3}a}$ in the reciprocal space.

$$\vec{b_1} = \left(\frac{2\pi}{\sqrt{3}a}, \frac{2\pi}{a}\right), \qquad \vec{b_2} = \left(\frac{2\pi}{\sqrt{3}a}, -\frac{2\pi}{a}\right). \tag{1.5}$$

1.1.3 Electronic properties

After having described briefly the real and reciprocal structures of nanotubes, we shall describe first the electronic properties of graphene as a reference material for a further description of the electronic properties of the nanotube. We will show that the finite size of nanotube will induce some modification in the electronic properties as compared to graphene.

Graphene electronic structure It was first described by Wallace using the *tight binding approximation* [45]. The unrolled unit cell of a nanotube has translational symmetry along the nanotube axis, for a finite length nanotube, and periodic boundary conditions along the circumferential axis. Since the nanotube's curvature is neglected, the mixing between the π and σ orbitals is not taken in account and therefore their interaction is neglected. Therefore,

only the electron at the valence orbital p_z is used in the electronic structure description. The Schödinger equation has to be solved:

$$\mathscr{H}\Psi(\vec{k}) = E(\vec{k})\Psi(\vec{k}), \tag{1.6}$$

where $\mathscr{H}$ is the Hamiltonian, $E(\vec{k})$ are the eigenvalues at wavevector $\vec{k}$ and $\Psi(\vec{k})$ are the eigenfunctions. The eigenfunctions can be written as a function of Block functions Φ_n. Within the tight-binding approximation, they are linear combinations of localized atomic wavefunctions of isolated carbon atoms $\varphi(\vec{r})$:

$$\Phi_n = \frac{1}{\sqrt{N}}\exp\left\{(i\vec{k}\cdot\vec{R}_n)\right\}\varphi(\vec{r}-\vec{R}_n). \tag{1.7}$$

Where N is the number of unit cells and $\vec{R}_n$ is the lattice vector. The eigenfunction $\Psi(\vec{k})$ can be written as a linear combination of the Bloch functions for the two electrons from the two carbon atoms A and B from the unit cell of graphene:

$$\Psi = \sum_n C_n\Phi_n = C_A\Phi_A + C_B\Phi_B. \tag{1.8}$$

The detailed calculation of the Schödinger equation 1.6 solved with the eigenfunction 1.8 can be found in references [42, 43]. The energy dispersion of the π electrons for the bi-dimensional structure of graphene is given by:

$$E_{2D}(k_x,k_y) = E_0 \pm \gamma_0\left[4\cos\left(\frac{\sqrt{3}k_x a}{2}\right)\cos\left(\frac{k_y a}{2}\right) + 4\cos^2\left(\frac{k_y a}{2}\right)\right]^{1/2}, \tag{1.9}$$

where γ_0 gives the measure of the interaction of exchange between two neighbouring carbon atoms. For given coordinates (k_{x_1}, k_{y_1}) of the reciprocal vector within the first Brillouin zone, one value of the Energy $E(k_{x_1}, k_{y_1})$ will correspond to an authorized energy within a lower band (negative sign), the other one to another authorized energy in the upper band (positive sign). These two bands separated by the energy gap $(E^+) - (E^-)$ will respectively correspond to π valence band and π^* conduction band. The band structure is plotted in figure 1.5a in 3D for all alowed K values within graphene Brillouin zone, and in figure 1.5b in 2D for the main directions described by KΓ, Γ M and MK.

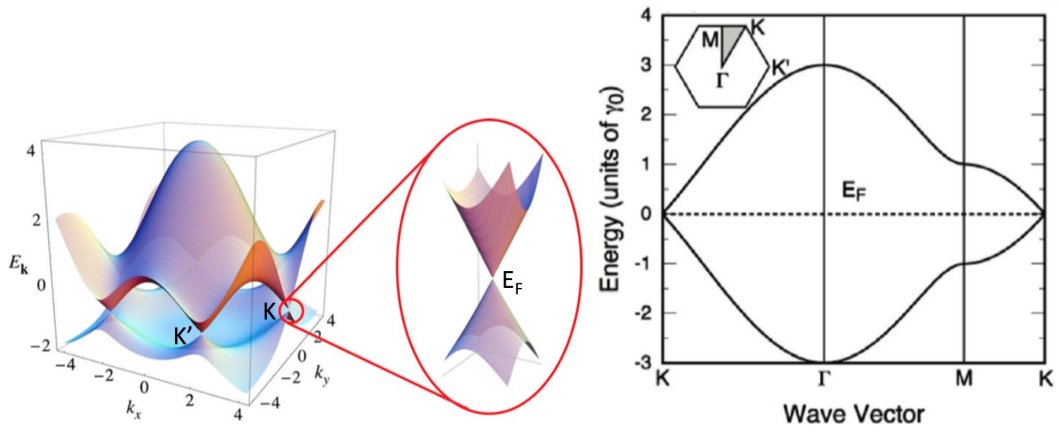

(a) **(b)**

Figure 1.5 (a) Electronic energy dispersion in the first Brillouin zone of graphene. Inset of the Dirac cone at the K point, where the two bands touch each other at the Fermi level E_F. Adapted from reference [44]. **(b)** Energy dispersion of graphene along the highest symmetry points K, Γ and M. Taken from reference [46].

The figure 1.5a, shows the energy dispersion of a graphene layer in the first Brillouin zone, where the valence band touches the conduction band and both are approximately linear near the K point. This is called the Dirac cone. Such a cone is observed for the point K but also for K' point. Lets note that these two points of reciprocal space are different, once they originate from the two non-equivalent carbon atomic positions A and B. Considering there is no mixing of π and σ orbitals due to their different symmetries, the energy bands are obtained for the π band comes only from the p_z orbital.

Nanotube electronic structure From the electronic structure of graphene, the quantum confinement characteristics are taken into account to describe the electronic structure of the nanotubes. That means, the periodic boundary conditions (PBC) have to be applied along the circumference direction (equation 1.10) and we shall consider a nanotube with infinite length.

The unit cell vectors of the reciprocal lattice of a nanotube $\vec{K}_1$ and $\vec{K}_2$ are shown in figure 1.6, along with its first Brillouin zone. Because of the quantization along the circumferential direction, the N alowed wavevectors give rise to N discrete $\vec{k}$ vectors which are also called *cutting lines* [47].

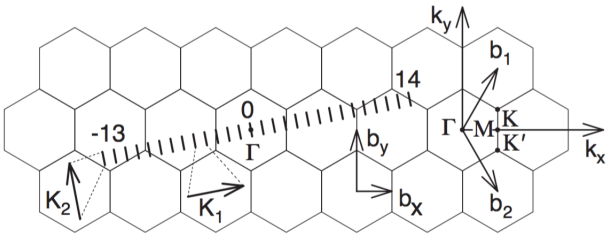

Figure 1.6 Parallel and equidistance cutting lines (labeled as μ), numbered from -13 to 14 for a $(4,2)$ nanotube. μ assumes values from $1-N/2=-13$ to $N/2=14$. Taken from reference [44].

The reciprocal unit cell of nanotubes is therefore defined by the vectors $\vec{K}_1$ and $\vec{K}_2$, which are obtained by the relation $R_i \cdot K_j = 2\pi\delta_{ij}$, where R_i denotes the lattice vectors from real space $\vec{C}_h$ and $\vec{T}$:

$$\vec{C}_h \cdot \vec{K}_1 = 2\pi\,, \qquad \vec{C}_h \cdot \vec{K}_2 = 0\,, \tag{1.10}$$

$$\vec{T} \cdot \vec{K}_2 = 2\pi\,, \qquad \vec{T} \cdot \vec{K}_1 = 0. \tag{1.11}$$

The values of $\vec{K}_1$ and $\vec{K}_2$ can be obtained in function of the reciprocal lattice vectors:

$$\vec{K}_1 = \frac{1}{N}(-t_2\vec{b}_1 + t_1\vec{b}_2)\,, \qquad \vec{K}_2 = \frac{1}{N}(m\vec{b}_1 - n\vec{b}_2)\,, \tag{1.12}$$

where $\vec{b}_1$ and $\vec{b}_2$ are the reciprocal lattice of graphene, t_1 and t_2 are coefficients of the translation vector $\vec{T}$ and n and m are the chiral indices. The N wavevectors $\mu\vec{K}_1(\mu = 1-N/2\cdots,N/2)$ give rise to N discrete cutting lines.

Both vectors $\vec{K}_1$ and $\vec{K}_2$ have been described as reciprocal space vectors of the carbon nanotubes (see subsection 1.1.2). According to the carbon nanotube geometry, it is also possible to define a vector perpendicular $\vec{k_\perp}$ to the nanotube axis and a vector parallel $\vec{k_\parallel}$. Since the nanotube length is infinite in the parallel direction, the reciprocal lattice vector $\vec{k_\parallel}$ is not affected by the dimension effect. However, along the circumference of the nanotube, the $\vec{k_\perp}$ is quantized according to the PBC: $q\lambda = \mid \vec{C}_h \mid = \pi d_{NT}$, so that we obtain:

$$\vec{k_\perp} = \frac{2\pi}{\lambda} = \frac{2\pi}{\mid \vec{C}_h \mid} q\,, \text{ where } q \in [0,\cdots,N-1]\,. \tag{1.13}$$

Where q is an integer for which there are N quantized values of $\vec{k_\perp}$ along the $\vec{K}_1$ direction. The equation 1.13 can be understood in the following way, the wavevectors that do not interfere destructively along the circumferential direction are multiple of 2π. On the other hand, since there is no periodicity along the nanotube's axis, from equation 1.10, we obtain:

$$\vec{k_\perp} \cdot \vec{K_2} = \frac{k}{|\vec{K_2}|}, \text{ where } k \in \left[-\frac{\pi}{T}, \frac{\pi}{T}\right]. \tag{1.14}$$

Where K is an integer of the finite length of the nanotube T. Which means that along the $\vec{K_2}$ direction the length of the vector $\vec{k_\perp}$ is given by $^{2\pi}/_{T}$.

$$\vec{k_\perp} = k\frac{\vec{K_2}}{|\vec{K_2}|} + q\vec{K_1}, \tag{1.15}$$

Where $\vec{k}$ is the 1D wavevector and q is a discrete quantum number.

The one-dimensional energy dispersion relations of a (n,m) nanotube $E_{1D}(k)$ is obtained by superposing the cutting lines from the carbon nanotubes into the 2D electronic energy dispersion of the graphene E_{2D}:

$$E_{1D}(k) = E_{2D}\left(k\frac{\vec{K_2}}{|\vec{K_2}|} + q\vec{K_1}\right). \tag{1.16}$$

Figure 1.7 left-hand side shows the representation of the dispersion equation 3D for graphene within first Brillouin zone. Now, the cutting lines defined for a nanotube (4,2) are superimposed to this dispersion curve, however for this nanotube, only the energy values defined by the equation 1.16 and shown on the cutting lines, are authorized. A 2D dispersion curve is also shown on the right for the wave-vectors from $-k_\perp$ to $+k_\perp$:

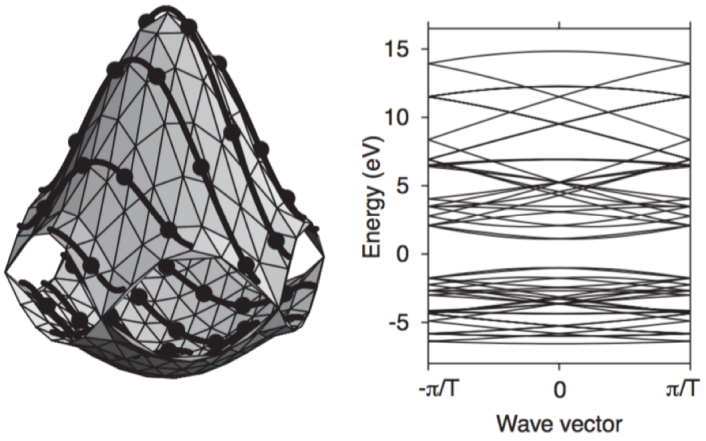

Figure 1.7 Left-hand side: Representation of the theoretical electronic energy dispersion of graphene superposed with the cutting lines for the $(4,2)$ nanotube [47], calculated using the tight-binding model from [42]. **Right-hand side:** Electronic energy band of the same nanotube, obtained by the zone folding method. Taken from reference [44].

The band structure near the Fermi level determines the nature of the nanotube, either *semiconducting* or *metallic*. Figure 1.7, the cutting lines do not pass by the K point, that means, the π and π^* bands of the (4,2) nanotube not intercept each other, opening an energy band gap at the Fermi level. Therefore, the (4,2) nanotube behaves as a semiconductor. On the contrary, whenever an allowed cutting line crosses the K point, it crosses a Dirac cone. The nanotube has a metallic character, since the π and π^* bands intercept each other at the Fermi level in the K point. Therefore, it appears clearly depending on the chirality of a given nanotube the cutting lines will or will not cross K point and depending on that these nanotubes behave as a semiconductor or as a metallic. Hamada [48] and Saito [49] were the first ones to derive the relation of the two chiral integers for a metallic nanotube:

$$\vec{k_\perp} \cdot \vec{C_h} = 2\pi q = \frac{1}{3}(\vec{b_1} - \vec{b_2}) \cdot (n\vec{a_1} + m\vec{a_2}) = \frac{2\pi}{3}(n-m) \tag{1.17}$$

From which, the condition of $n-m$ being a multiple of 3, characterizes the nanotube as metallic, otherwise it is semiconducting. This equation suggests that $1/3$ of the nanotubes are metallic, while the rest are semiconducting:

$$n-m = 3l \rightarrow MOD(n-m;3) = \begin{cases} 0 & \text{metallic nanotube} \\ 1, \text{ or } 2 & \text{semiconducting nanotube} \end{cases}$$

The figure 1.8 shows the band structure of three nanotubes. For the two first ones, (a) and (b), the π and π^* bands crosses, characterizing both as metallic nanotubes. Conversely, the band structure (c) shows a gap opening at the Fermi level, characterizing this nanotube as semiconducting.

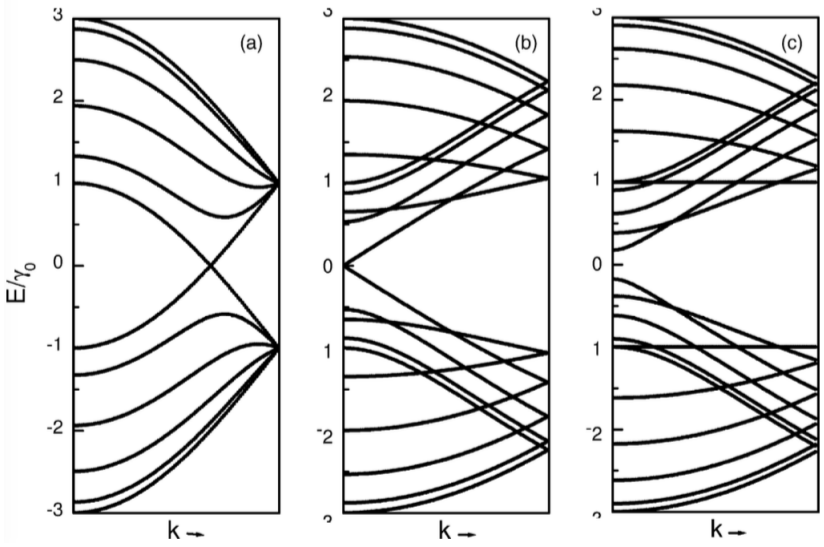

Figure 1.8 Example of three band structures obtained by the zone folding of the graphene finite layer using γ_0=2.9eV for **(a)** (5,5) arm chair; **(b)** (9,0) and **(c)** (10,0) zigzag nanotubes. Extracted from reference [50].

1.1.4 Electronic density of states

The dispersion curve shows the energy levels that are allowed for the electrons for a $\vec{k}$ value allowed by the PBC. The electronic density of states, associated to these authorized levels, characterizes the total number of available states, summed on all k values for a given interval of energy. Mintimire has derived the density of states n(E) of a given number i of 1D electronic bands [51]:

$$n(E) = \frac{2}{q \mid \vec{k_\perp} \mid} \sum_i \int dk_\perp \, \delta(k_\perp - k_i) \left| \frac{\partial E^{\pm}(k_\perp, k_\parallel)}{\partial k_\perp} \right|^{-1}, \tag{1.18}$$

for k_i being the solution of $E\text{-}E^{\pm}(k_\perp, k_\parallel)=0$. For nanotubes with the quantization taken into account, the equation 1.18 can be written as:

$$n(E) = \frac{4\,a_0}{\pi^2\, d_{NT}\, \gamma_0} \sum_{m=-\infty}^{\infty} g(E, E_m), \tag{1.19}$$

with

$$g(E, E_m) = \begin{cases} \frac{|E|}{\sqrt{E^2 - E_q^2}} & |E| > |E_q| \\ 0 & |E| < |E_q| \end{cases}$$

and

$$E_m = \mid 3q - n - m \mid \frac{a_0 \gamma_0}{\sqrt{3} d_{NT}} . \tag{1.20}$$

Where the detailed development can be found in reference [43]. It is worth noticing that whenever $\mid E \mid = \mid E_q \mid$, n(E) in equation 1.19 diverges, it gives rise to a *van Hove singularity* (vHs). The DOS for nanotubes having three different chiralities are shown on figure 1.9. At first glance, the spike-like structure associated to these vHs reflects the 1D character of nanotubes. For the two DOS presented on this figure, 1.9b correspond to metallic nanotubes, where the DOS is different from zero close to the Fermi level. Figure 1.9a shows the electronic DOS of a semiconducting nanotube where the DOS value is zero at the Fermi level.

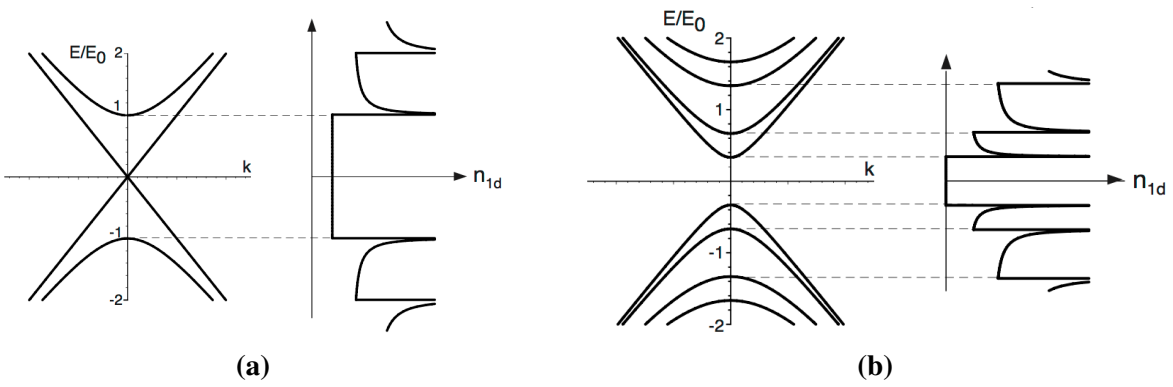

Figure 1.9 Energy bands at the K point (left) and the electronic DOS (right) for **(a)** metallic nanotube; **(b)** semiconducting nanotube.

The DOS determines the optical properties of a nanotube, as the $\pi \rightarrow \pi^*$ optical transitions depend on both valence and conduction bands.

1.1.5 Optical properties

In 1999, Kataura came up with a theoretical plot which relates the nanotube diameter with the optical transition energy between two symmetric vHs, called *Kataura plot* [52]. Figure 1.10 shows this plot along with three different classes of nanotubes: $\mathrm{MOD}(n - m; 3) = 0, 1, 2$. MOD0 stands for metallic and MOD1 and MOD2 stands for semiconducting nanotubes.

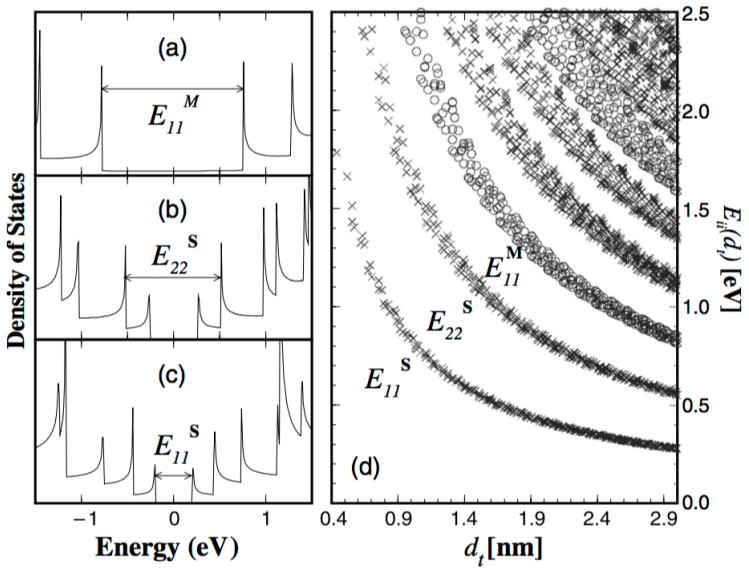

Figure 1.10 Left-hand side: Electronic DOS of **(a)** (10,10) armchair; **(b)** (11,9) chiral and **(c)** (22,0) zigzag nanotubes, obtained from tight binding model from [53]. **Right-hand side:** Transition optical energy of carbon nanotubes with diameter d_{NT}, where each branch belongs to a family of nanotube, either semiconducting or metallic. Taken from reference [54].

Each point of the Kataura plot represents an optical allowed transition energy $E_{ii}(d_{NT})$ corresponds to one single-walled carbon nanotube with a specific diameter d_{NT} and chirality (n,m). The energy of each branch decreases for an increase of nanotube diameter. Also, each branch represents a family of nanotubes for which the nature is either semiconducting E_{ii}^{SC} or metallic E_{ii}^{M}.

The optical properties from NIR to UV are directly related to the nanotube electronic structure. For carbon nanotubes, these optical properties are dependent on its spike-like electronic density of states. The optical transitions are allowed between symmetrical vHs and are denoted as $E_{ii}(d_{NT})(V_i - C_i)$. As an example, for p=1, $E_{11}^{SC}(d_{NT})(V_1 - C_1)$ indicates an optical transition takes place when an electron at the π orbital (valence V) of a nanotube is excited to the π^* orbital (conduction C) of symmetrical pairs of vHs of a semiconducting nanotube of diameter d_{NT}.

As an example, the photoluminescence in a semiconducting nanotube takes place when the excitation energy is higher or equal to E_{ii}^{SC}. That is, then a photon with an energy higher than $E_{11}^{SC}$is absorbed. Then a non-radiative decay will lead the charges to reach C_1 and V_1 level before emission of the photon with energy E_{11}^{SC}. This process is depicted in the figure 1.11.

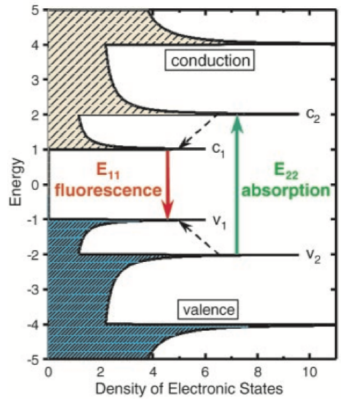

Figure 1.11 Schematic electronic DOS of a semiconducting nanotube. Green arrow depicts the creation of the electron-hole pair, by the absorption of an incoming photon with energy E_{22}eV; red arrow depicts the de-excitation process with radiative emission of a photon, with energy E_{11}eV. Taken from reference [55].

The optical transitions in a nanotube have a specific energy value which depends on the electronic band structure and therefore on the nanotube's structure (d_{NT}) so that only specific energies can yield optical transitions between symmetric vHs. Transmission measurements can be led on carbon nanotubes dispersed in solvents such as bile salt.

This emission lay in the NIR range. In order to avoid any quenching of the luminescence by charge transfer to non emitting metallic nanotubes [56–58], suspensions have to be carefully prepared. When the excitation energy is tuned, it is possible to assign the different transitions observed to the different nanotubes present in the dispersion.

The figure 1.12a shows the absorption spectra for individual small nanotube diameters (ϕ=8Å). The dispersion contains both semiconducting and metallic nanotubes with diameter varying between [8, 12Å]. The different peaks observed can be assigned to transition between symmetrical singularities E_{ii}^{SC} for semi-conducting nanotubes.

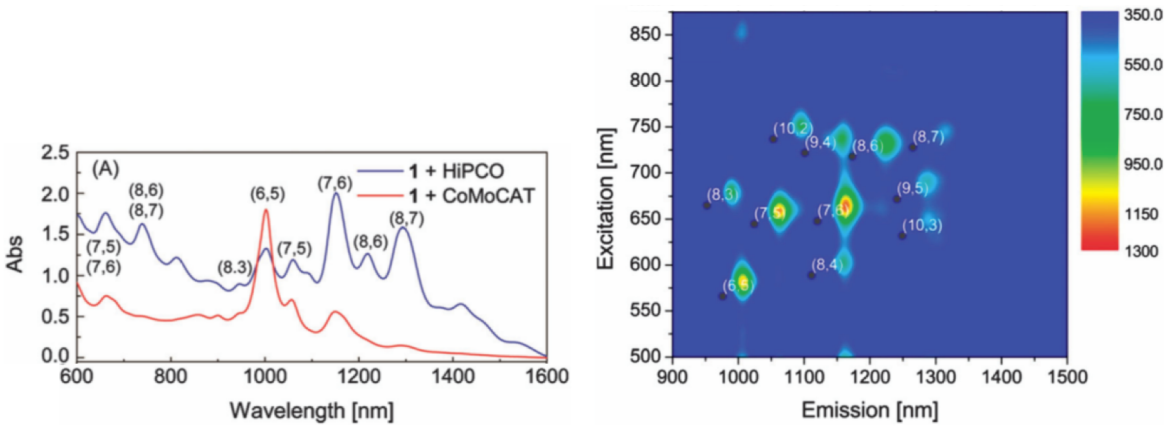

(a) **(b)**

Figure 1.12 (a) UV-vis optical absorption of a solution of HiPCO (blue) and CoMoCAT (red) nanotubes. The chiralities are indicated for all probed semi-conducting nanotubes. **(b)** Photoluminescence map. Adapted from reference [59].

1.1.6 Vibrational properties

Graphene vibrational structure The phonon dispersion of graphene consists of 6 branches originated from the three dimensional displacement in space of the two carbon atoms. As an example, theoretical dispersion curves obtained using force constants[1] is shown in figure 1.13:

[1] Force constants are calculated by finite differences for stripes of graphene which allowed a description of modes propagating along the high-symmetry directions [60].

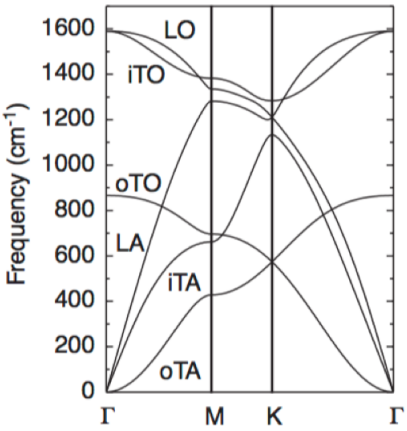

Figure 1.13 Phonon dispersion of a layer of graphite using the force constants from [60]. The phonon branches are labeled: out-of-plane transverse acoustic (oTA); in-plane transverse acoustic (iTA); longitudinal acoustic (LA); out-of-plane transverse optic (oTO); in-plane transverse optic (iTO); longitudinal optic (LO). Taken from reference [44].

The phonon dispersion curves of graphene, at the Γ point is composed of three modes with zero frequency, corresponding to acoustic modes: LA, iTA and oTA, all are in-phase vibrations of carbon atoms in graphene. The three optical modes LO, iTO and oTO, appear at higher frequencies.

Vibrational properties of nanotubes The phonon dispersion of carbon nanotubes has more phonon branches since the unit cell of nanotubes contain 2N carbon atoms. Therefore, the phonon dispersion bands of nanotubes consists in 6N branches. The phonon dispersion curves of nanotubes are obtained from the graphene phonon dispersion with the zone folding procedure. Analogous to the nanotube electronic structure from graphene (described in equation 1.16), the nanotube phonon structure $\omega_{1D}^{mq}(k)$ is obtained from the zone folding from graphene ω_{2D}^{m}:

$$\omega_{1D}^{mq}(k) = \omega_{2D}^{m}\left(k\frac{\vec{K}_2}{|\vec{K}_2|} + q\vec{K}_1\right), \text{ where } m \in [1, 2, \cdots, 6]. \tag{1.21}$$

From the phonon dispersion, we can obtain the phonon density of states, see figure 1.14. It also reflects the 1D character of nanotubes, with van Hove singularities.

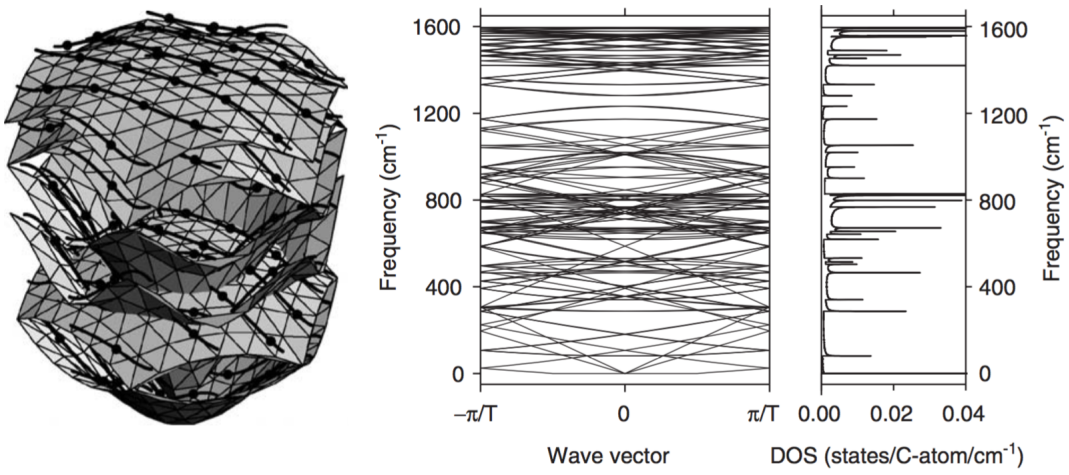

Figure 1.14 Left-hand side: Phonon dispersion curves of the graphene layer calculated with force constants. Superposed cutting lines for the (4,2) nanotube. **Middle:** Phonon dispersion modes of the (4,2) nanotube obtained by zone folding. **Right-hand side:** Phonon density of states, from its dispersion modes. Taken from reference [61].

1.1.7 Raman spectroscopy of carbon nanotubes

Raman spectroscopy is widely used to probe the vibrations of carbon nanotubes, where only vibrations at the Γ point of the Brillouin zone are probed. The theory of Raman scattering is detailed in references [42, 62–64]. However, we will recall here a few elements that are necessary to understand the following part of the study.

In the case of carbon nanotubes, Raman spectroscopy is a resonant process. As a matter of fact, whenever the excitation energy of the laser matches one absorption transition of one type of nanotube from the measured batch, these nanotubes exhibit an signal impressively enhanced. Therefore, it is possible to select the types of nanotubes probed by tuning the excitation wavelength. The Kataura plot can be used as a reference for this selection. An example is given here below, when the wavelength 633 nm (1.87 eV) is chosen to study Carbon Solution nanotubes [65] having a mean diameter around 14±2 Å, from the figure 1.15, we expect to excite the transition E_{11}^{M} from metallic nanotubes.

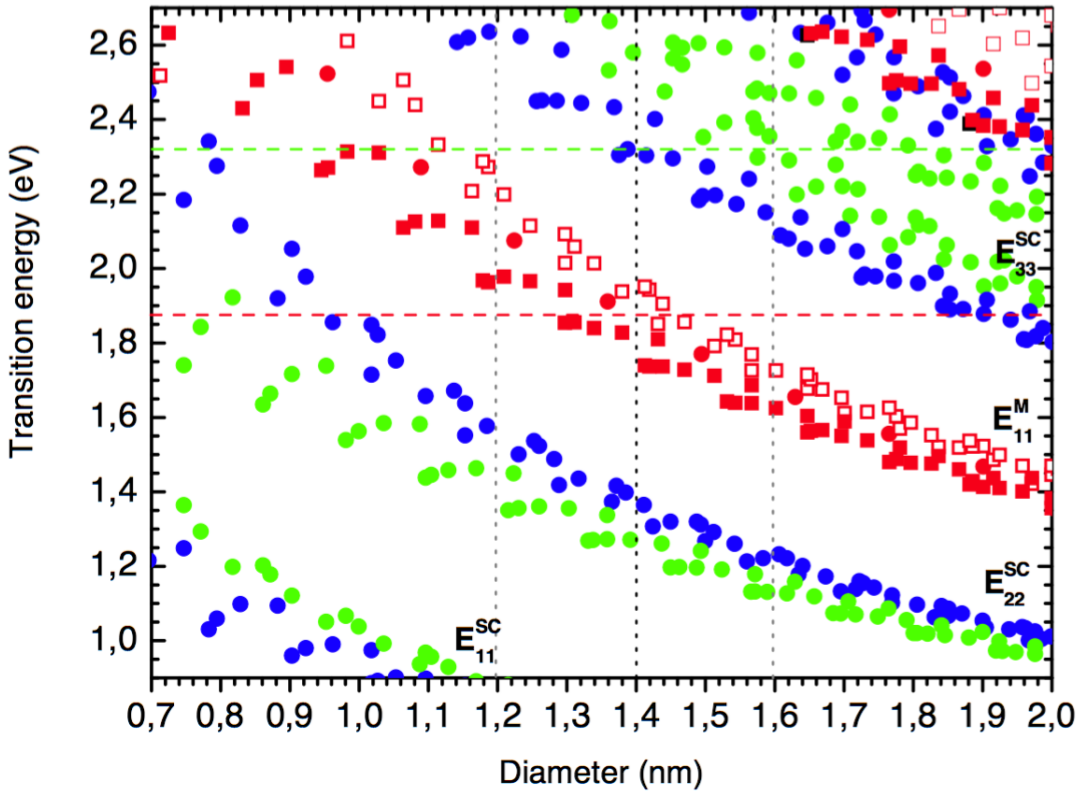

Figure 1.15 Kataura plot with the transition energy as a function of the nanotube diameter d_{NT}. Each dot or square represents a nanotube for a given chirality. Exciting laser wavelengths of 532nm (2.33eV) and 660nm (1.87eV) are represented by horizontal dashed green and red lines, respectively. The mean diameter of 14Å (14nm) with distribution ($\pm$0.2nm) are indicated by grey dotted vertical lines.

According to the Group Theory, seven vibrational modes are expected to be Raman active:

$$\Gamma = 2A_{1g} + 2E_{1g} + 3E_{2g}\,. \tag{1.22}$$

The atomic motions associated to these Raman active modes are shown in figure 1.16 for a (10,10) armchair nanotube [42].

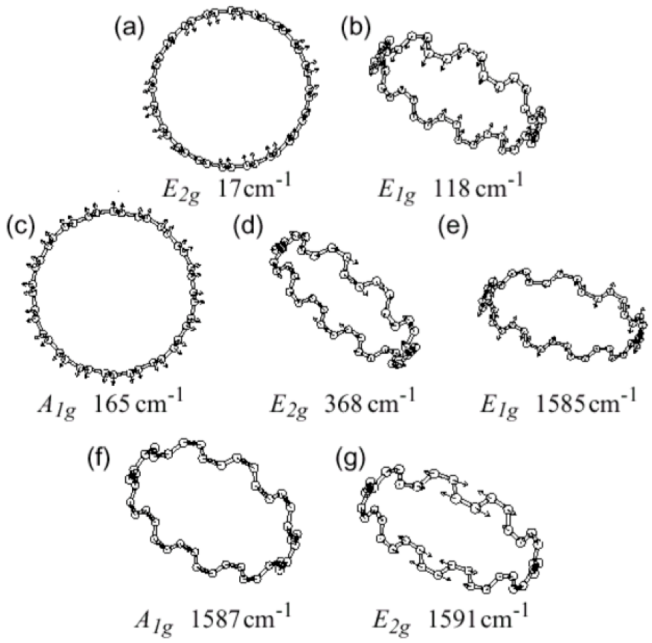

Figure 1.16 Seven strong Raman modes of a (10,10) armchair nanotube predicted by Saito. In the following, we will be referring to: *Radial Breathing mode* (RBM) mode corresponds to the A_{1g} mode with frequency 165cm^{-1}: **(c)**. The *G band* corresponds to the three modes: **(e)**, **(f)** and **(g)**. Taken from reference [66].

Figure 1.17 shows an example of a Raman spectrum of powdered carbon nanotubes, where carbon nanotubes with a mean diameter 14$\pm$ 2 Å are excited by two different exciting wavelength respectively 660 and 532nm. One can notice that the Raman spectra are very different as different nanotubes are probed. Moreover, according to Karaura plot, for the excitation line 532nm, most excited nanotubes are semiconducting whereas for 660nm most excited nanotubes are metallic. One can notice that the two main bands observed respectively in the region between [100, 200 cm^{-1}] and in the region [1500, 1650 cm^{-1}] are very different in the two case.

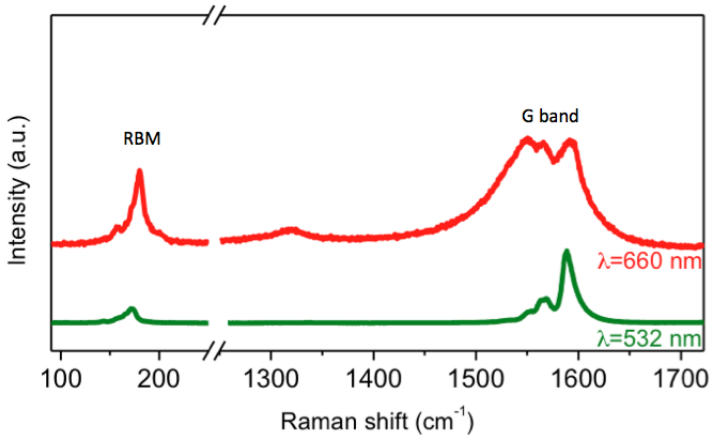

Figure 1.17 Raman spectra of bundles of nanotubes with diameter of 14±0.2 Å probed with two different excitation wavelengths of 660 nm (1.87 eV) and 532 nm (2.33 eV), being resonant therefore to a metallic and a semiconducting nanotubes, respectively.

These two main, bands are referred as the RBM modes at low frequencies and G band at high frequencies, as indicated in the figure 1.17. In this manuscript we will particularly focus on these two modes, for which some detailed explanations are necessary.

RBM mode

Having its origin in the oTA (out-of-plane transversal acoustic) mode of graphite, this mode is characterized by the movements of enlarging and shrinking of nanotubes, from which its acronyms stands for *Radial Breathing Mode*. All the atom carbons vibrate in phase in the radial direction of the nanotube, being therefore a signature of the circumferential character of nanotubes: located in the [120, 350 cm^{-1}], for nanotubes with diameter in the [7, 20 Å] range.

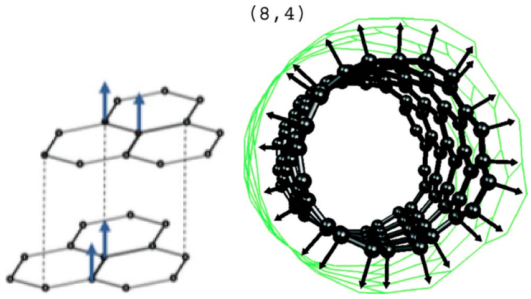

(a) **(b)**

Figure 1.18 (a) oTA modes of graphite, once the graphene layer is folded, it becomes a radial mode of the nanotube. Taken from reference [67]. **(b)** Radial breathing mode of a (8,4) nanotube. The arrows show the phonon eigenvector. Taken from reference [68].

Observing the diameter dependence with the frequency of the RBM modes, in 1993, Jishi proposed a relationship 1.23 linking the diameter of the nanotubes for the Raman scattering to their diameter [69]:

$$\omega_{RBM}(\mathrm{cm}^{-1}) = \frac{\mathrm{A}(\mathrm{cm}^{-1} \times \mathrm{nm})}{\mathrm{d_{NT}(nm)}} + \mathrm{B}(\mathrm{cm}^{-1}), \tag{1.23}$$

where ω_{RBM} is the frequency of the RBM band, $\mathrm{d_{NT}}$ is the diameter of the carbon nanotube, and A and B are parameters depending on the interactions such as bundling of nanotubes, solvents, surfactants or substrates. For instance, for an isolated nanotube on SiO_2 substrate, the relationship is given by $\omega_{RBM} = {}^{248}/_{d_{NT}}$ where $B = 0$ [70]. The parameters $A = 223.5$ and $B = 12.5$ were proposed for isolated SWCNTs on oxidized *Si* substrates by Bachilo and collaborators [55]. However, for bundles of nanotubes, $B \neq 0$, since it comes from the tube-tube interaction [71]. Different values proposed by several groups which have found different experimental values for the A and B parameters [72–75]. All B proposed relations for the RBM frequency in function of the NT diameter agree for the existing range of diameters. In this manuscript we have chosen the parameters proposed by Araujo where $A = 217.8$ and $B = 15.7$ [75].

G band

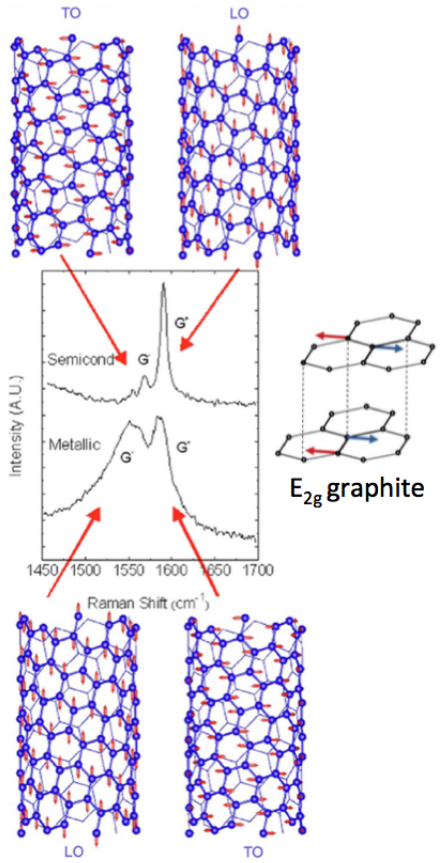

Figure 1.19 G band of a **Left-hand side, top:** semiconducting nanotube with G^- band: TO phonon and G^+ band: LO phonon. **Left-hand side, bottom:** metallic nanotube, with the inverse assignment: G^- band: LO phonon and G^+ band: TO phonon. Taken from reference [41]. **Right-hand side:** E_{2g} mode of graphite. Taken from reference [67].

The strong sp^2 C-C bonds of graphene give rise to a degenerate out-of-phase mode with symmetry E_{2g}, at the Γ point in the Brillouin zone, being called G band [76]. Because of the curvature and confinement effects of carbon nanotubes, specific of its 1D structure, the optical phonons of graphene undergo to a symmetry breaking giving rise to the two features the lower frequency being called G^- and the higher frequency called G^+ bands [77], see figure 1.19. They correspond to in-plane LO and TO modes with symmetry E_{1g}, E_{2g} and A_{1g}.

The differences in frequency for TO and LO phonons are due to the force constants which are different along the axis (higher force constant) and circumferentially (lower force constant). The C-C stretching vibrations along the tube axis are assigned to a longitudinal mode LO whereas the C-C stretching vibrations along the circumferential direction of the nanotube correspond to the TO mode. In figure 1.19, for *semiconducting nanotubes*, the LO mode corresponds to the G^+ band and the TO mode corresponds to the G^- band [78]. The assignment is inverted for the *metallic nanotubes*, the G^- corresponds to the LO phonon and the G^+ corresponds to the TO phonon.

Figure 1.19 shows that the line shape of the G band of nanotubes directly indicates its nature. Semiconducting nanotubes have a lorentzian line-shape for both G^- and G^+ bands whereas only the G^- band of metallic nanotubes shows a large and asymmetric line-shape. It is associated to the Breit-Wigner-Fano (BWF) process [79] which is written as [80]:

$$I_{BWF}(\omega) = I_0 \frac{[1+\omega-\omega_{BWF}/q\Gamma]^2}{1+[\omega-\omega_{BWF}/\Gamma]^2} \tag{1.24}$$

Where I_0 is the intensity, ω_{BWF} and Γ are the renormalized frequency and broadening parameter. $^1/_q$ is the parameter that gives the asymmetry to the peak [79] and is a measure of the interaction between the LO phonon and the continuum electronic states, also called *electron-phonon coupling* [81, 82].

For graphene and metallic nanotubes, the screening is abruptly changed at exactly the Γ and K points of the first Brillouin zone. This phenomenon is called *Kohn anomaly* (KA) [83]. Such effects are stronger for metallic nanotubes rather than graphene, due to the 1D characteristics of the electronic structure of nanotubes [81, 82].

The LO phonons are affected in three different ways, and we shall explain the consequences of the KA in the following.

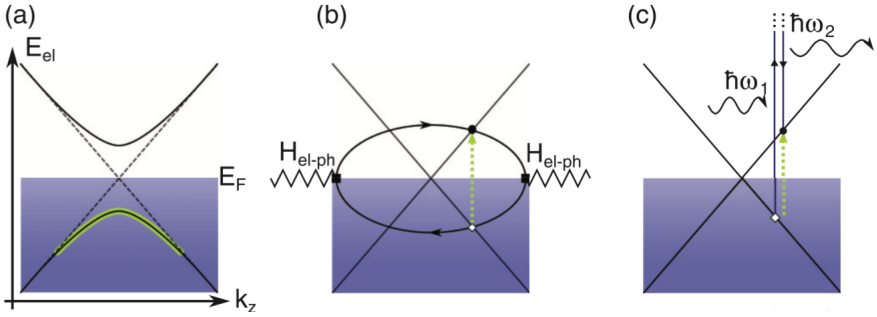

Figure 1.20 Intrinsic Dirac cones for the K point which show the three different processes that affects the LO band in metallic nanotubes regarding the features: **(a)** Softening of LO mode. **(b)** Peak width: The emition of phonon followed by the recombination of the electron-hole pair is shown by the green vertical dashed line. **(c)** Asymmetric line-shape. Taken from reference [84].

LO mode softening takes place since the LO phonons interact strongly with the electrons at $\vec{q} = 0$ at the Γ point. This interaction results in a gap opening [78] (straight dashed lines → thick green line in Figure 1.20 (a)), and as a consequence, the phonon energy is reduced, softening this mode [83, 82].

Width an electron-hole pair is excited since it absorbs the LO phonon (green dashed vertical line in Figure 1.20 (b)). Followed by a recombination of electron-hole pair and an emission of other LO phonon, reducing its life-time [85].

Asymmetric line-shape has its origin in the interaction of the LO phonon with the continuum of electronic states near the Fermi level during the Raman scattering process [79, 86], Figure 1.20 (c).

The specific properties of pristine carbon nanotubes have been presented above. These nanotubes can be combined with some molecules having some specific characteristics in

order to form a hybrid system which combines both properties of the nanotubes and the encapsulated molecules. These molecules can be adsorbed on the surface of carbon nanotubes, chemically grafted or encapsulated within the hollow core of carbon nanotubes. This last type of functionalization has been chosen for this thesis. We shall present now an overview on the work already published about the encapsulation of organic molecules inside carbon nanotubes and the properties measured on these hybrids.

1.2 Hybrid Carbon Nanotubes

Right after the discovery of MWNTs in 1991 [87], theoretical studies suggested that the introduction of guest material into cavities of nanotubes may modify and enhance the properties of the resulting hybrid materials [88–90]. The encapsulation of species, *e.g.* organic molecules, inside the hollow space of nanotubes opens the possibility of creating 1D material withing the nanotube confinement matrix. The new hybrid materials are referred hereafter by M@SWNTs, where M is the encapsulated species, as proposed in 1999 by Burteaux [91].

Metal complexes were the first species to be encapsulated inside MWNTs, *e.g.* lead particles in 1993 [92] and nickel particles in 1994 [4], however the filling rate was very limited. In 1998, C_{60} species were encapsulated inside SWNTs [5], with high filling rate using gas-phase encapsulation process [91]. The new hybrid nanotubes were called *peapods*, making reference that this new material resembles the peapod vegetable, as it can be observed in figure 1.21.

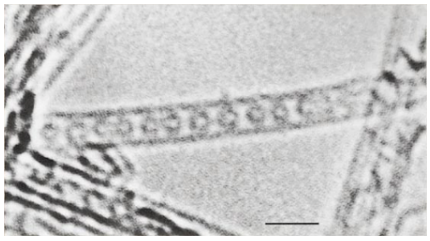

Figure 1.21 HRTEM image of the *peapod* material, a row of fullerene molecules encapsulated inside a SWNT of 14Å of diameter. Taken from reference [5].

The first π-conjugated molecule (or dye molecule) encapsulated inside nanotubes was Zn-diphenylporphyrin (ZnDPP) and was reported by Kataura in 2002 [31]. The encapsulation method used was similar to the one used for encapsulation of C_{60} molecules. This study revealed that properties of the hybrid system could be dominated by ad-molecules stacked on

the surface of the nanotube, and thus some wash process have to be set up to remove these adsorbed molecules. Once adsorbed molecules were removed, a shift could be observed on the optical absorption spectra of the encapsulated molecule and the RBM band was also strongly modified. This was interpreted as a influence of the size of the ZnDPP, compared with the size of either C_{60} or C_{70}, where the ZnDPP may deform the nanotubes and as a consequence, it decreases the intensity of the RBM band and appears shifted to higher frequencies.

In 2003, Takenobu and collaborators [93] have reported a study on the encapsulation of anthracene, TCNQ and TDAE, that are molecules with different electron affinity and ionisation characters inside nanotubes. They have proposed that the choice of the molecule allows the control of the charge transfer, since the character of the encapsulated molecule conditions either a positive or negative charge transfer between the two species. The authors also have reported that the intensity of the RBM band depends on the nature of the encapsulated molecule. It was found that molecules with considerable electron affinity have induced a loss of intensity of the RBM band, same behaviour than for K-doped nanotubes. Also, the loss of the metallic character of G band evidences the charge transfer in the hybrid system.

Moreover, the air stability of the hybrid nanotubes was probed by Raman and optical absorption, its spectra remained unchanged after one week exposed to air, proving therefore that the walls of the nanotube protect the encapsulated molecule to be oxidised by air. Yanagi and collaborators [94] have also reported the protection by encapsulation of a long molecule (29Å) of β-carotene (β-car) inside carbon nanotubes. Therefore, along with new exciting 1D physics, the use of carbon nanotubes as nanocontainers is also motivated by the fact they act as robust confining and shielding environment [95].

They also exhibit unique electron transport, however, their drawback is the small band gap limits them to be only near infrared emitters [23, 24]. That can be overcome with the encapsulation of dye molecules.

After having insight on the possible features of the hybrid nanotubes (dye@NT) and how to probe it, we shall focus on the studies in the literature reporting encapsulation of oligothiophenes oT. As they are known to be electron donor molecules, interesting features can be raised in the hybrid system such as charge or energy transfer in the system. Therefore, in the following, we will restrict ourselves to present the results of oT encapsulated inside SWCNTs, hybrid systems that will be studied in the framework of this thesis.

1.2.1 Oligothiophene encapsulation: A State of the Art Review

In this subsection we will discuss the most important results from literature for which different oligothiophene oT molecules - terthiophene 3T, quatherthiophene 4T, dimethyl-

quatherthiophene $4TCH_3$ and sexithiophene 6T - were encapsulated inside carbon nanotubes: oT@NT. The hybrid systems have the advantage of having combined the electronic properties of oT molecules, already being used in optical devices [96–98], with the protection and pseudo one-dimensional character of nanotubes. That will be helpful in order to comment both the characterization and the physical properties that take place in such hybrid systems in which we are interested in this manuscript.

Theoretical calculations

Some interesting theoretical studies have been led on the encapsulation on oligothiophene inside carbon nanotubes. As an example, Orellana and collaborators have reported a theoretical work on the encapsulation process of 3T inside zigzag nanotubes with diameters [8, 13 Å] [99]. The energy of insertion[2] of 3T inside nanotubes with diameters bigger than 9Å, was found to be exothermic, revealing the energetically favourable insertion of molecules in the hollow space of nanotubes. The calculated electronic DOS of the encapsulated molecule was found to be preserved. However, encapsulation itself influences both entities, in one hand, the small nanotubes were found strongly ovalized after insertion of the molecule and on the other hand, the molecule became planar, with its dihedral angle was found to increase from $157.8\,^{\circ} \rightarrow 180\,^{\circ}$.

Loi and collaborators have calculated the binding energy of encapsulated 6T molecules as a function of the nanotube diameter, see figure 1.22. The number of encapsulated molecules depends on the size of the nanotube diameter: one chain is encapsulated for nanotubes with diameter up to 11 Å whereas two molecules are encapsulated for nanotubes with diameter [11, 14].

[2]The total energy of insertion was described by nanocapillarity forces induced by the interaction between the slightly positive nanotube cavity and the electronic cloud of the molecule.

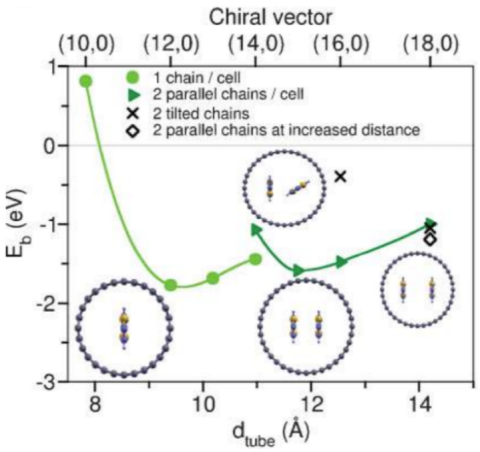

Figure 1.22 Binding energy of the hybrid system as a function of nanotube diameter d_{tube}(Å) for the hybrid systems 6T@(n,0). Taken from reference [36].

The alignment of quaterthiophene molecules inside carbon nanotubes was reported by Milko [100]. The authors report that both subsystems interact with weak van der Waals interaction.

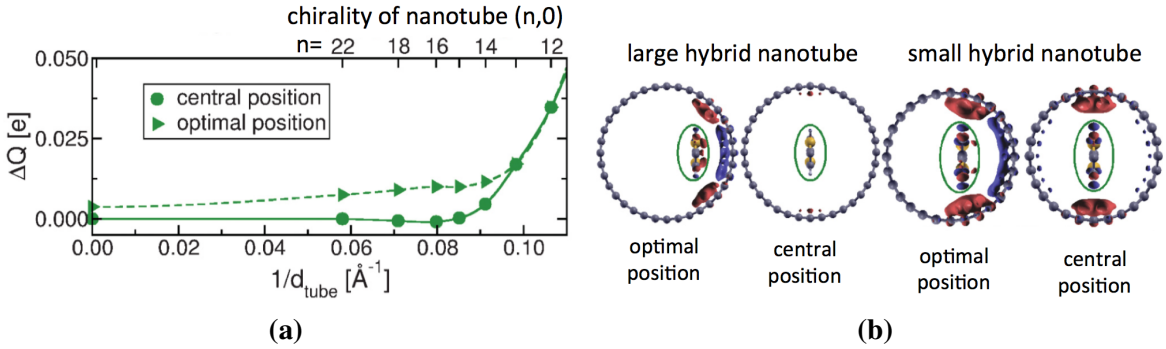

Figure 1.23 (a) Charge exchanged between host nanotube and encapsulated oligomer as a function of the diameter of the nanotube. **(b)** Position of the encapsulated molecule along the nanotube axis. Charge density difference integrated along the tube axis with isovalues of + 0.0001 (red) and ?0.0001 (blue) electrons per a.u. Adapted from reference [100].

In figure 1.23, hybrid systems with nanotube diameter superior to 12.5Å ($< {}^{1}/_{d_{NT}} = 0.08$) are not expected to have a significant charge transfer. However, for nanotubes with diameter inferior to 12.5Å ($> {}^{1}/_{d_{NT}} = 0.08$), the charge transfer is expected to take place in the system, having its maximum value of 0.05 electrons. Figure 1.23b shows the charge density is depicted for hybrid systems with different diameters. When the nanotube diameter is small enough, the encapsulated oligothiophene seems to interact to the inner wall of the nanotube,

so that a charge transfer can take place. Otherwise, the molecule is far from the inner wall of the nanotube in order to interact.

High-Resolution Transmission Electron Microscopy

A common characterization technique of hybrid nanotubes is the high resolution transmission electron microscopy (HRTEM), which allows to obtain of an image of the hybrid systems. That is essential since molecules inside and at the outer surface of the nanotubes can be detected, attesting the quality of the sample. Loi and collaborators have reported HRTEM of 6T@NT with diameter from [12, 15 Å] [36]. The 6T molecules were found to be at a distance between [3.2, 3.5 Å] from the inner walls of the nanotubes, whereas the distance between 2 molecules varies from 4 to 8Å. For the same hybrid system with diameter ranging [13.2, 15 Å], Kalbac and collaborators have reported a slightly bigger distance between the molecule and the nanotube wall of [3.8, 3.9 Å] [101].

Almadori and collaborators focused their attention on 4T@NT hybrid systems for different nanotube diameters. HRTEM images along with contrast profile have shown that for a small nanotube diameter, 4T@NT8.3, one molecule encapsulate in its hollow space, whereas 4T@NT12 has two molecules and 4T@NT17 has three molecules encapsulated. Such results confirmed the theoretical prediction by Loi [36] in which one molecule is encapsulated for nanotubes with diameter up to 11 Å. Two molecules in interaction with each other are encapsulated for nanotube with diameters up to 16 Å. For larger diameters, the two molecules are found far from each other. More than two molecules are shown to be encapsulated for diameters higher than 16 Å.

HRTEM proves to be a powerful local probe of encapsulated hybrid systems. Not only having access to the actual image of them but also giving information such as the distance between the encapsulated oligomers to the inner walls of the carbon nanotubes. In order to have access to the electronic structure of hybrid nanotubes, Raman spectroscopy is well appropriated since it is a resonant process. Besides that, the encapsulated oligomer can also be probed when the excitation laser wavelength is near its optical absorption range.

Raman spectroscopy

In section 1.1.7 of this chapter, we have described the Raman spectra of carbon nanotubes as being composed by RBM bands located at the low frequency domain below 300 cm^{-1}, and the G band with two features at around [1550, 1650 cm^{-1}]. In the medium frequency domain [600, 1550 cm^{-1}] peaks arises from the encapsulated oligothiophenes inside carbon nanotubes. We shall comment each domain separately, for the sake of simplicity.

Let us start by the low frequency domain, where the RBM band shows to be a probe of encapsulation. Loi has reported the RBM band of nanotubes with diameter ranging [12, 15 Å] to be shifted by 5 cm^{-1} upon encapsulation of the 6T, however its intensity is kept upon encapsulation [36]. Conversely, Kalbac has found a loss of intensity of the RBM mode for the 6T@NT, when probed with an exciting laser of energy of 1.83eV [101]. After encapsulation, the RBM band has been also splitted. This behaviour is interpreted as an hybridization between the 6T orbitals and near-free states of the nanotube, and as consequence, the RBM band splits [102]. Likewise, Alvarez has also reported a very considerable loss of intensity of the RBM band for the 4T@NT [37].

The shift of RBM mode is known to be a signature of encapsulation [103], explained formerly by the stiffening of the C-C bonds [104] resulting from the strain imposed by the molecule on the walls of the nanotube. The loss of intensity of the RBM band can have two distinct origins. The first one is a consequence of a loss of resonance conditions according to Kataura plot [52], where the encapsulated molecule absorbs the energy, creating an exciton. The exciton energy is transferred from the molecule to the nanotubes, the exciton energy is dissipated non-radiatively through the metallic nanotubes. The second one has been reported for peapods C_{60}@NTs [102], where the mechanical hindrance along with interaction of near-free electron states of the nanotube yield a lower intensity of the RBM band of nanotube.

In 2014, Almadori has reported a detailed study on the behaviour of the shift of the RBM mode with a nanotube diameter dependence for the encapsulation of 4T, $4TCH_3$ and 6T [105]. After encapsulation, the RBM modes exhibit a systematic upshift for different laser excitation energies. The figure 1.24 shows the relative upshift in terms of $\Delta\omega_{RBM} = \omega_{RBM}$(4T@NT) - ω_{RBM}(NT) in function of the nanotube diameter. The authors highlighted the two different regimes, depending on the range: [6.8, 11 Å] and [14, 16.5 Å] have a monotonic behaviour whereas [11, 14 Å] and above 16 Å show a linear increase. The different regimes are interpreted as the consequence of oligomer-oligomer interactions between two molecules of oligothiophene (linear regime) or oligothiophene and the nanotube's wall interaction (monotonic regime).

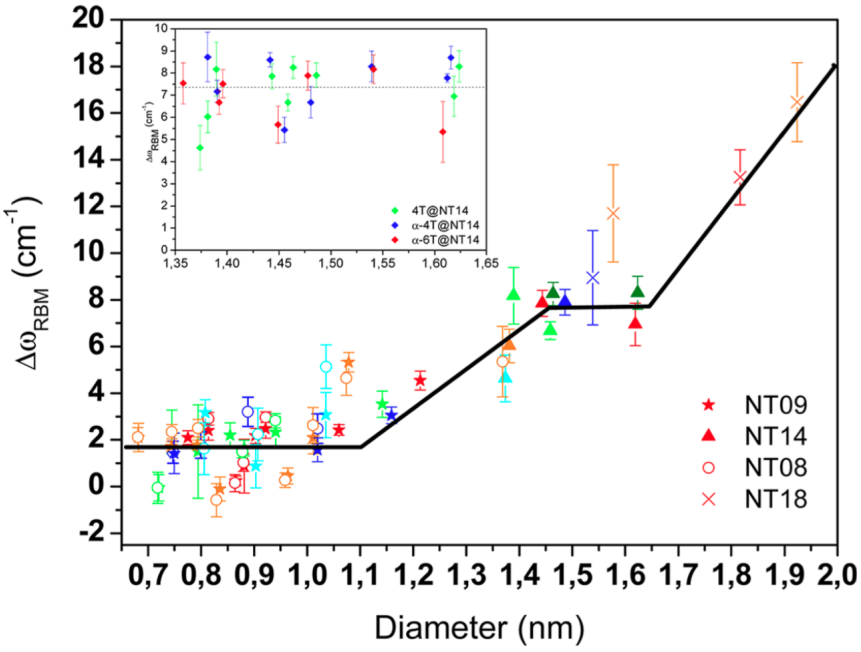

Figure 1.24 Relative upshift of the RBM modes ($\Delta\omega_{\mathrm{RBM}}$) after encapsulation of 4T molecules inside nanotubes with diameters of 8, 9, 14 and 18Å. Different symbol colours are related to the different excitation laser energies of cyan (477.9nm, 2.70 eV), blue (488 nm, 2.54 eV), dark green (532 nm, 2.33 eV), green (514.5 nm, 2.40 eV), red (647.1 nm, 1.91 eV) and orange (568.2 nm, 2.18 eV). Taken from reference [105].

The middle-frequency domain in the Raman spectra has additional peaks from encapsulated oligothiophene molecules. For instance, Loi and collaborators [36] reported their presence for 6T@NT. Kalbac has reported the Raman spectra of the 6T@NT hybrid systems to be a superposition of the spectra of both spectra from 6T and pristine nanotube. Also, the absence of significant charge transfer in the system since the signal of the encapsulated 6T were not significantly altered upon encapsulation. A cation/dication formation upon encapsulation was therefore ruled out by the authors [101].

Alvarez reported a dependence of the intensity of the peak from 4T with the laser wavelength, where the intensity is increased as much as the laser excitation energy is near the optical absorption of the molecule [37].

Throughout the literature, authors have reported the presence of the encapsulated molecules inside nanotubes by Raman spectroscopy. However, the Raman cross section per molecule is about $10^{-28} - 10^{-30}\,\mathrm{cm}^2$, being too low for detection of such objects at high resolution. On this context, Gaufrès has reported a *giant Raman scattering effect* on hybrid 6T@NT in 2014 [106]. That is, the Raman cross-section of the encapsulated 6T $(5 \pm 1) \times 10^{-21}\,\mathrm{cm}^2/\mathrm{sr}$, is high enough to be measured. The hypothesis from the authors is that the confinement of

6T yields the formation of J-aggregates inside the nanotube, which are the responsible for the cooperative effect which ends up in a Giant Raman scattering cross section. Because the influence of nanotube nature or the resonance effect of the scattering of the encapsulated 6T was ruled out, the authors concluded that this effect is only dependent on the optical properties of the molecules.

Lastly, the G band at the high-frequency region, has also some fingerprints of the hybrid system. In 2011, Alvarez reported a downshift of the G band which seemed to indicate a charge transfer for two types of nanotubes [37]. It was explained by an upshift of the Fermi level, caused by the negative charging of the nanotubes by the encapsulated molecules [107]. The author has also reported a dependence of the shift in function of the exciting laser wavelength, where modifications of the G band frequency take place around [2.70, 2.40 eV], whereas slight modifications are seen around [2.18, 1.16 eV]. Kalbac reported that the nature of the nanotube is maintained upon encapsulation [101].

We can therefore see that results concerning in-situ Raman spectro-electrochemical study reveal to be also a powerful probe of hybrid systems. Kalbac and collaborators reported a study of 6T molecules encapsulated inside nanotubes of diameter [13.2, 15 Å] [101]. The study was performed for both positive and negative potentials (see figure 1.25) and two different exciting laser energies of 1.83 eV and 2.54 eV for which the probed nanotubes were metallic and semiconducting according to the Kataura plot [52], respectively.

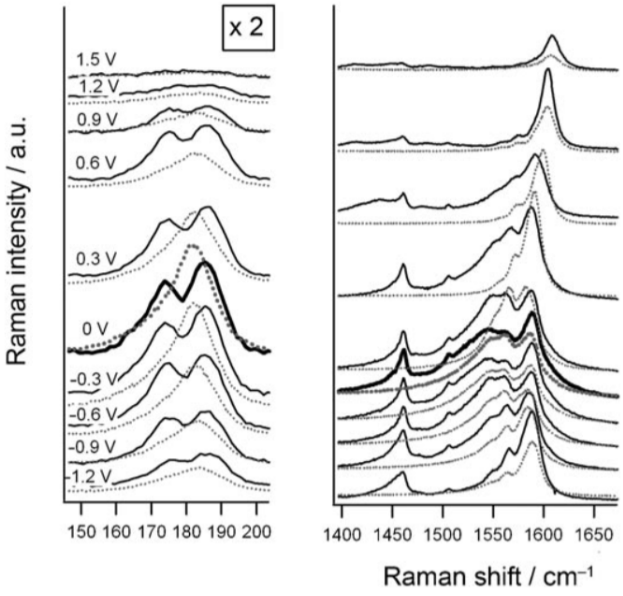

Figure 1.25 Spectroelectrochemical Raman study using laser energy of 1.83eV on the hybrid system 6T@NT (solid line) and pristine nanotube (dotted line). Thick curve corresponds to null charging (V=0eV) of the nanotubes. **Left-hand side:** RBM modes in the Raman shift range of [150, 200 cm^{-1}]. **Right-hand side:** G band mode in the Raman shift range of [1400, 1650 cm^{-1}]. Taken from reference [101].

After encapsulation the two components of the RBM band remain for all different applied potentials eventhough both quench as much as the potential is increased. After the measurements, the features of both molecule and nanotube are recovered for a potential of V = 0eV, showing therefore the stability of the encapsulated 6T. The effect of charging the nanotubes in the G band with either positive or negative potential yields to a loss of the metallic character of the hybrid nanotubes, and at last to complete quenching of the G band. The authors reported that curiously, the loss of the metallic character is faster for positive potentials (anodic doping). Such a behaviour is in accord with the electron donor character of the bulk molecule.

Infrared spectroscopy

In 2011, Alvarez has studied the charge transfer between 4T encapsulated molecules and host nanotubes of mean diameter 14 Å [37]. Photoluminescence results revealed a redshift between the hybrid and pristine nanotubes. Such shifts have already been observed for metallocenes [9] and squarylium dyes [38] encapsulated in nanotubes. Infrared spectroscopy was also used to probe hybrid systems. Alvarez and collaborators reported the intensity of the Infrared bands of encapsulated 4T molecules to be less intense than the crystalline

phase. A comparison with iodene-doped 4T (I@4T) revealed some similarities between both spectra, suggesting that the encapsulated molecule is positively charged as it is when it is iodene-doped [37].

In 2016, Belhboub, coupling Infrared experiments and DFT calculations, has reported for the same system that we are studying here, the interaction between the encapsulated $4TCH_3$ and the host nanotubes. The models used for the theoretical calculations are shown in figure 1.26, we will be using the same models in this manuscript. They are in agreement with the proposed results by Almadori (see figure 1.24) where the number of molecules depends on the nanotube diameter [105]. The $4TCH_3@(11,0)$ hybrid system accommodates one molecule inside its hollow space with a distance of 4.1 Å of distance between the molecule and the nanotube's inner wall. The larger hybrid system, $4TCH_3@(17,0)$, accommodates to molecules which are far from each other and nearer to the inner wall of the nanotube. At last, the π-stacked system has the outer molecule at a distance of 3.3 Å from its outer walls.

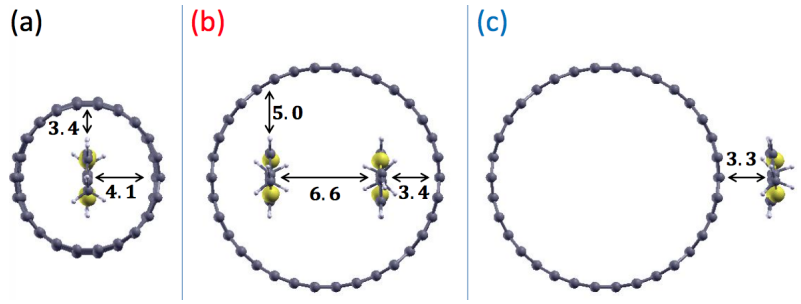

Figure 1.26 Calculated relaxed structures of **(a)** $4TCH_3@(11,0)$, **(b)** $4TCH_3@(17,0)$ and **(c)** $4TCH_3\pi(17,0)$ with distances given in Å. Taken from reference [108].

The interaction between both species yield a symmetry breaking (see figure 1.27) in the $4TCH_3$@NT hybrid system which results in the exaltation of the infrared absorption [108, 109].

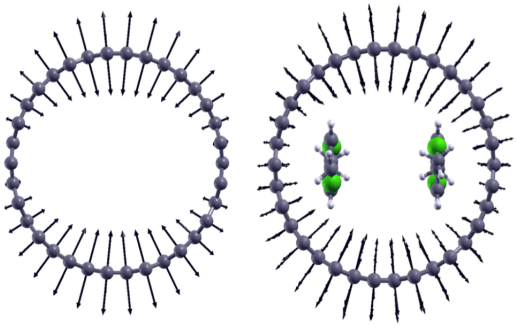

Figure 1.27 Eigen-displacement vectors of **left-hand side:** perfectly symmetric E_{1u} radial mode at 836 cm^{-1} for pristine (17,0) nanotube; **right-hand side:** asymmetric E_{1u} radial mode at 823 cm^{-1} for $4TCH_3@(17,0)$ hybrid system. Taken from reference [108].

The experimental band at 743 cm^{-1} (simulated one at 769 cm^{-1}) was reported by the authors to be a coupling between the mode of nanotubes and molecule, that means, the eigen-displacements have shown that the mode radial motion of nanotube is coupled with the C-H wagging of the encapsulated $4TCH_3$.

In the [580, 900cm^{-1}] infrared range, pristine nanotubes are expected to have one infrared active mode, the symmetric radial mode E_{1u}, see figure 1.27, left-hand side. However, for the hybrid system, the contribution of the nanotube for the infrared spectra reveals to have more than only one expected mode. The additional nanotube bands are originated from symmetry breaking once a molecule/nanotube interaction takes place in the hybrid system, model shown in 1.26 (b). The mode from the hybrid system (823 cm^{-1}) undergoes a shift when compared to the respective mode of the pristine nanotube (836 cm^{-1}) and its intensity is dramatically increased. The downshift has a two-fold explanations: a hybridization between the encapsulated molecules and nanotube, also reported by Joung [102] and a charge transfer reported by [37].

1.2.2 Conclusion

We shall give a summary on the highlights of each study performed on the encapsulated oligomers of thiophene in the literature:

Summary of the encapsulation of oligothiophenes inside carbon nanotubes

2006 Orellana Theoretical work on the encapsulation process of 3T molecules. For nanotubes of diameter larger than 9 Å, encapsulation process is exothermic. Upon encapsulation the molecule becomes planar and the nanotube strongly ovalizes [99].

2010 Loi First experimental work on the encapsulation of 6T inside NT12 to NT15. HRTEM has shown the encapsulation of molecules in the hollow space of nanotubes. It allowed the determination of the distance between 6T and inner walls of the nanotubes [3.2, 3.5 Å] [36].

2010 Kalbac Interaction between 6T and NT: hybridization between the 6T orbitals and near-free states of the nanotube. Such interaction changes the electronic structure of the nanotubes, changing therefore its resonance [101].

2012 Milko A theoretical work on the interaction between 4T and nanotubes reveal the charge transfer is expected to take place when encapsulated molecule is in interaction with inner walls of the nanotubes [100].

2011 Alvarez Infrared measurements evidenced that the encapsulated 4T undergo a positive charge transfer. On the other hand, Raman measurements have seemed to show a weak negative charge transfer towards the nanotubes for two types of nanotubes [37].

2014 Almadori Systematic upshifts of the RBM mode after encapsulation yielded first experimental proof of the dependence of the number of encapsulated molecules and the size of the nanotube. Below 11 Å, one molecule is encapsulated, between 11 and 16 Å, two molecules are encapsulated and above 16 Å, more than two are encapsulated [105].

2014 Gaufrès The authors have proven the nanotube has no influence on the scattering of the encapsulated molecules. Instead, the confinement yields J-aggregates of 6T molecules, which enhances the Raman scattering cross-section. This phenomena opens doors for multispectral Raman labelling and imaging of the encapsulated aggregates which are smaller than the optical resolution of Raman instruments [106].

2016 Belhboub Experimental and theoretical work on the infrared activity of $4TCH_3$@NTs. Due to interaction between encapsulated $4TCH_3$ and host nanotubes, a symmetry breaking enhances a radial-like mode of nanotubes which can be measured by Infrared spectroscopy, as well as other modes from the nanotubes [109, 108].

The bibliographic studies presented before converge on many points. In particular the diameter of the host nanotube is a key element that would determine:

- The number of molecules that can be accommodated in through the diametral section.
- the configuration of these molecules within the diametral section : very close the one from the other or far and more likely to be close to the inner wall of carbon nanotubes.

In order to get some further experimental insight on the influence of the confinement on encapsulated thiophene, we have prepared 4 sets of $4TCH_3$@NTs hybrid systems with four mean diameters ranging from 0.9 to 19 Å. The details about the sample preparation and characterization will be given in Chapter 2. In a second time an original study of the dynamic of the encapsulated molecules through inelastic neutron scattering, for two confining nanotube expected to accommodate respectively one and two $4TCH_3$ molecules will be presented in Chapter 3. Then, we will focus on the open questions addressed in the introduction about the possible interactions between thiophene and nanotubes and their nature. Two electronic processes may take place: either charge transfer or energy transfer. They depend on the HOMO/LUMO energy levels of both sub-systems, depicted in the figure 1.28:

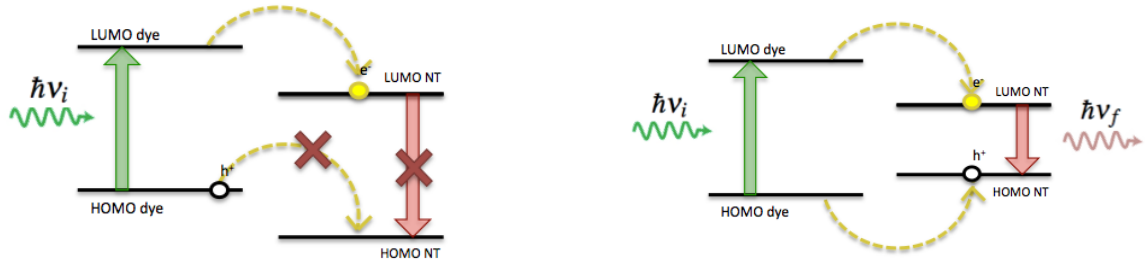

(a) Charge transfer **(b)** Energy transfer

Figure 1.28 Possible processes that take place in the hybrid system composed of carbon nanotubes and dye molecules.

In the case of a charge transfer (CT), the electron-hole pair is excited in the dye molecule by an incoming photon with energy $\hbar\nu_i$. Due to the energy levels of the dye molecule and the carbon nanotube, only the electron can be transferred to the nanotube, the hole remains in the HOMO of the dye. Therefore the recombination does not take place in the nanotube.

In the case of an energy transfer (ET), the excitation process of the electron-hole pair is the same as explained above. The electron is transferred to the nanotube as well as the

hole. A recombination of both takes place in the carbon nanotube emitting a photon with energy $\hbar\nu_f$.

We propose in chapter 4 to treat this question through Raman scattering, as some bibliographic work reported that G band from the nanotube is very sensitive to electrical interaction with its environment, with some support of photoluminescence. In particular, this question will be treated in strong correlation with the influence of the diameter on the confinement of 4TCH3 hosts, as different effects could be expected according to the molecule conformation within the host nanotube.

We will then conclude on these open questions and show the preliminary results on a different hybrid system, hosting phthalocyanine molecules, that also dye molecules, raising strong interest for their numerous properties. Their large size and square shape are raising new questions about their confinement within carbon nanotubes. In particular, we will focus in the last chapter 5 on potential 1D structure formed within the nanotube, the conformation of the molecules and the influence on their properties.

Chapter 2

Elaboration and characterization of hybrid systems

Contents

This chapter is dedicated to the description of elaboration and characterization of the hybrid systems. It is divided into two parts. In the first part, the section 2.1.1, gives a brief description of the synthesis methods of hybrid nanotube samples. The aim is to describe the main characteristics of the synthesis method that yield to a specific nanotube mean diameter. The next section 2.1.2 describes the protocol used in order to prepare hybrid systems. At last, a summary of the different samples and their characteristics will be given at the end of the section 2.1.3.

In the second part of this chapter, the section 2.2 shows the characterization protocol used to check that the encapsulation process has been successful. The last section 2.3 summarizes the characterization of prepared hybrid systems.

2.1 Elaboration of hybrid systems

The different steps of the elaboration of the hybrid systems are presented below, after an introduction to the selected pristine nanotubes.

2.1.1 Presentation of pristine nanotubes

As the purpose of this PhD thesis is to study the influence on the confining matrix (*i.e.* a carbon nanotube) on the physical properties of the encapsulated dyes in its hollow core, the diameter of the carbon nanotube is a key parameter. Therefore, in order to have carbon nanotubes with a variety of diameter suitable for this study -from 9 to 21 Å-, nanotubes obtained from three different synthesis technics have to be considered: CoMoCaT for the smallest, Electric Arc for medium sized and eDIPS for the largest diameter.

CoMoCAT method

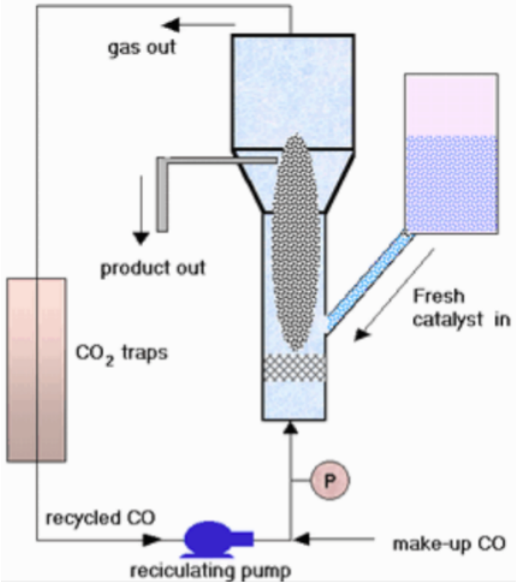

Figure 2.1 Setup of the apparatus corresponding to the CoMoCAT synthesis method. Taken from reference [110].

The pristine nanotubes of small diameter used in this work were synthesised by the CoMoCAT method [111]. This catalytic method is based in the decomposition of carbon monoxide in the presence of bimetallic cobalt-molybdenum catalyst. The metallic catalysts in the presence of flow of pure carbon monoxide gas are carburized, producing molybdenum carbide and small metallic Co clusters. A temperatures about 700-950 °C and pressure in the range of 1-10 atm, the carbon monoxide gas decomposes into carbon and carbon dioxide. The small Co clusters act as a catalyst to the carbon inside the reactor in order to form the small diameter nanotubes which are rich for both (6,5) and (7,6) chiralities. Bundles with few nanotubes are obtained by CoMoCAT method.

Electric Arc method

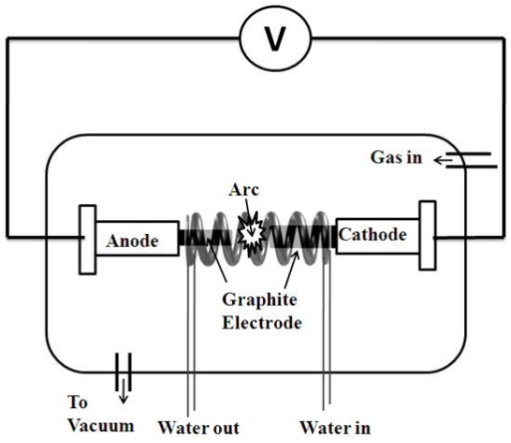

Figure 2.2 Set up of the apparatus correspondent to the Electric arc synthesis method. Taken from reference [112].

The medium diameter pristine nanotube is synthesised by the Electric Arc method [113]. Inside a reactor with an inert gas (helium or argon), an electric current flows between two graphite electrodes. The anode is a bar of graphite which contains metallic nanoparticles and is mobile. It is approached to the cathode which is fixed in the opposite side inside the reactor. When the distance of both cathode and anode is approached to $\sim$ 3mm, an electric arc is produced. The gas inside of the reactor is therefore ionised and a plasma is created. Consequently, the graphite is evaporated by the plasma and it is condensed at a lower temperature region inside the reactor, where the carbon nanotubes are formed. This synthesis yields to carbon nanotubes and by-products such as amorphous carbon, graphite as well as the residues from the catalysers. The single-walled carbon nanotubes samples

produced by this synthesis method aggregates forming large bundles with nanotubes with 14Å of mean diameter.

eDIPS method

The large nanotube diameter are synthesised by the eDIPS method [114–116]. The acronym stands for enhanced Direct Injection Pyrolytic Synthesis. The reactor (see Figure 2.3) contains a vertical tube of 50mm of inner diameter and 600mm of length, where the catalysts are deposited and the different gases flow from top to bottom. Inside the reactor a flow of two kinds of hydrocarbons with different decomposition properties are used as carbon sources. Ferrocene catalysers are decomposed into iron atoms at the top of the reactor which is at 600 °C. The particles aggregate and are catalytically activated with the hydrogen gas flow. The flow is such that it makes small aggregates of nanoparticles to be at the upstream and bigger aggregates of nanoparticles to be at the downstream. The pressure and flow rates of the carbon sources determine where the nanotubes will grow, and according to the size of the aggregate of nanoparticles, the nanotube diameter is determined.

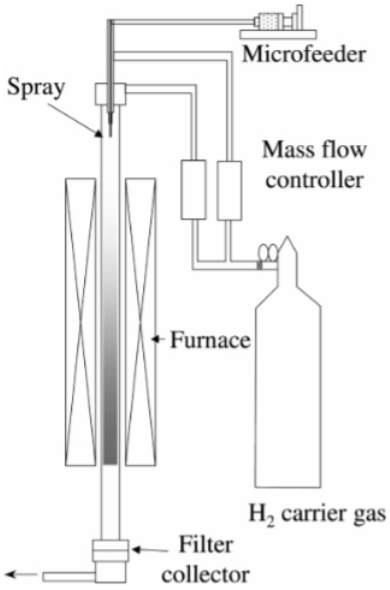

Figure 2.3 Setup of the direct injection pyrolytic synthesis (eDIPS) method. Taken from reference [114].

Summary of pristine carbon nanotubes used in this work

Depending on the synthesis method, the single-walled carbon nanotubes have a dispersion in diameter, containing different type of impurities, such as metal catalysts and amorphous

carbon, and small or large bundles of nanotubes. All these elements will impact the final hybrid systems that we are elaborating. Table 2.1 summarises the characteristics of the pristine nanotubes used in this work.

Table 2.1 List of pristine nanotubes with respective synthesis method and corresponding characteristics.

Synthesis method	**CoMoCAT** [111]	**Arc Discharge** [113]	**eDIPS** [117]
Company	Carbon solutions [65]	Sigma-Aldrich [118]	Takeshi Saito [119]
Mean diameter	9 ± 2Å	14 ± 2Å	18 ± 2Å 21 ± 2Å
Chirality distribution	>50% (7,6)	-	-
Metal catalyst	Co/Mo	Ni/Y	Fe
Carbonaceous content	>90% [120]	-	
SWCNT content	$\geq$77% [121]	-	-
Metal content (wt%)	-	4-8	-
State	opened-end	opened-end	closed-end

Note: The nanotubes will be referred in this work hereafter as: NT09 for CoMoCAT, NT14 for Arc Discharge and NT18 for eDIPS. The symbol "-" indicates the information is not given by the company.

2.1.2 Preparation of hybrid nanotubes: encapsulation protocol

The extremities of closed-end nanotubes is constituted of hexagons and pentagons inducing a curvature of these bowl shape caps. Apart from defects sites, the nanotube body is mainly composed of sp^2 carbon and the caps contain both sp^2 an sp^3 carbon. Therefore, the caps are more reactive to oxidation processes which are relevant in order to open the nanotubes. Different oxidation processes can be considered such as oxidative thermal treatments or chemical oxidation. Exposing the nanotubes to nitric acid [4] is an efficient technic to open nanotubes, moreover, it is well known for removal of amorphous carbon and metal catalyst resulting from the synthesis. Therefore, the chemical treatment used to purify carbon nanotubes from by-products such as graphite, amorphous carbon and metal catalysts directly gives opened carbon nanotubes.

As this chemical treatment results in generation of defects on the nanotube's walls [122, 123], the nanotubes need to be healed from the created defects. They undergo by an annealing treatment under vacuum with a temperature high enough to dissociate the functions at the walls of the nanotubes.

In the framework of this thesis, CoMoCAT and Electric Arc nanotubes were purchased readily opened, purified and healed from defects. For the NT18, obtained by eDIPS synthesis from the collaborator Takeshi Saito [119], oxidation treatment was performed by other collaborator, Stéphane Campidelli.

Preparation of the dye molecules

The class of the dye molecule chosen to be encapsulated inside carbon nanotubes in the frame of this work is the oligothiophene (oT). Prior to the encapsulation process, a preparation step is necessary in order to purify the compound and identify the sublimation temperature range.

The chosen oligomer is the dimethyl-quatherthiophene ($4TCH_3$). The addition of methyl ends in both extremities of the quaterthiophene molecule has a two-fold interest, it prevents polymerisation of adjacent molecules once they are encapsulated and it makes the molecule more soluble for the wash step during the preparation of the sample [124]. The methylated compound is not readily available for purchasing and was prepared by our collaborator Bruno Jousselme. The crystalline compound forms yellow platelets and has a high degree of purity, see figure 2.4. The sublimation temperature has been identified formerly [124] at around 250 °C.

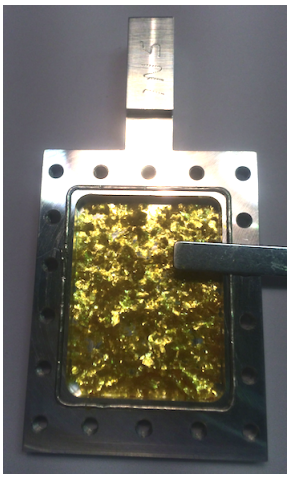

Figure 2.4 Bright yellow flakes of $4TCH_3$ molecule inside the sample holder for inelastic neutron experiments.

The Table 2.2 summarizes the relevant information such as its purity, sublimation temperature and respective solvent in order to perform the washing of the hybrid systems:

Table 2.2 Description of relevant parameters of the $4TCH_3$ used in this work for the encapsulation.

organic molecule	**Dimethyl-quaterthiophene**
Company	Sigma-Aldrich [125]
Functionalization	IRAMIS laboratory
Empirical Formula	$C_{18}H_{14}S_4$
Molecular Weight (g/mol)	358.56
Dye content	100% (purified)
Sublimation temperature for encapsulation (°C)	250
Solvent of the molecule	Dichloromethane (DCM)

Note: The dimethyl-quaterthiophene molecules were bought in Sigma-Aldrich and functionalized by the collaborators Bruno Jousselme and Stéphane Campidelli, from the IRAMIS laboratory.

Degassing of nanotubes

It has been shown that opened-end nanotubes can adsorb H_2O and O_2 inside its hollow core and also in the interstitial sites of the bundle [126]. Therefore, before the functionalization of the nanotubes, it is important to evacuate adsorbed species it in order to have clean nanotubes samples for encapsulation.

In order to proceed, the powdered sample (nanotubes) are placed inside a glass tube which is connected to a vacuum pump, according to the setup shown in Figure 2.5. The nanotubes are degassed for about 48 hours under dynamic vacuum (about 10^{-6} mbar) in order to avoid oxidation of the nanotubes. Once the process is finished, the glass tube is sealed under vacuum.

Figure 2.5 Powdered sample of nanotubes placed inside a glass tube made of quartz. After being connected to the vacuum pump it is placed inside a cylindrical oven.

Encapsulation by sublimation of PAM molecules

The encapsulation of species inside carbon nanotubes can be performed by different methods which are capillarity, pressure and solvent carrier [127]. The method used in this work for

encapsulation is the gas-phase method, because of the intrinsic attractive potential [128] inside carbon nanotubes and consequently their ability to drawn up species.

In order promote the filling of the nanotubes, the ratio of molecules and nanotubes is chosen to be 2:1. The encapsulation starts with a physical mixture between the molecules and the nanotubes inside the set up shown in Figure 2.6a. The nanotubes are kept under vacuum after the degassing step. The molecules are placed inside the tube and afterwards and the glass apparatus is connected to to the pumping system. The air is removed from the glass tubes in which the molecules are under dynamic vacuum (5×10^{-6} mBar). The tube is immersed in liquid nitrogen in order to maintain the molecules in the bottom of the glass tube during evacuation of air.

A magnet which was previously added inside the apparatus is used to break the fragile wall so that the nanotubes can be lead to the bottom of the glass tube and mix with the molecules, see figure 2.6b:

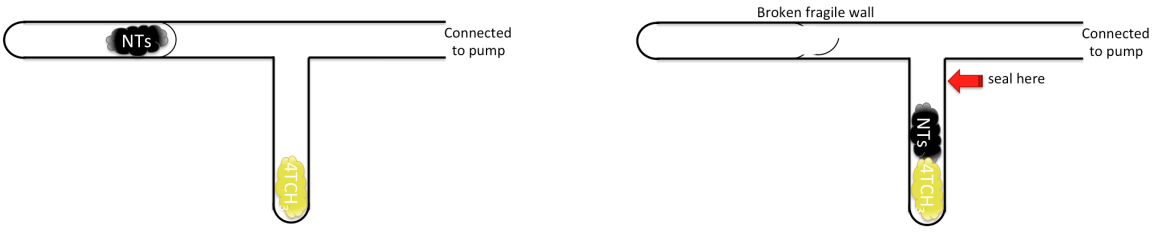

(a) Degassing of $4TCH_3$ under dynamic vacuum.

(b) Physical mixture of $4TCH_3$ and nanotubes.

Figure 2.6 Setup connected to vacuum pump for encapsulation.

The glass tube is sealed in order to keep a pressure about 5×10^{-6} mBar inside the glass with the mixture: nanotubes + dye molecules. The sealed glass tubes are placed inside the muffle furnace for 72 h at a temperature of 250 °C has been slightly higher than the sublimation temperature of the molecule, of 20 °C [124]. After this thermal treatment, it is possible to observe the yellowish mixture nanotube + $4TCH_3$ is appearing as a black powder, after the thermal treatment, see figure 2.7.

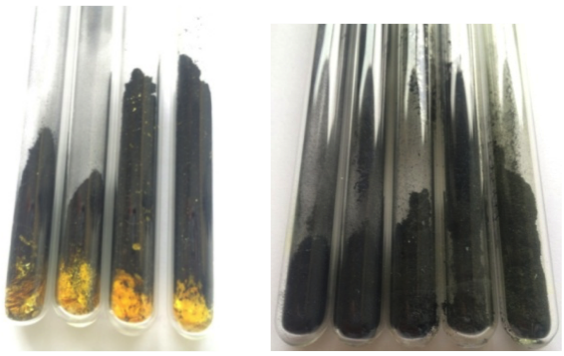

(a) **(b)**

Figure 2.7 (a) Physical mixture of flakes of $4TCH_3$ (bright yellow) and powdered nanotubes (black) inside sealed glass tube under static vacuum before annealing treatment. **(b)** After annealing treatment, complete disappearance of the yellow colour of the $4TCH_3$ molecules.

Degassing step

As the encapsulation has been performed with an excess of molecules, the sublimation step is performed in order to extract this excess of molecules from the outer part of the hybrid nanotubes.

The procedure is the following: the powdered sample lays at the bottom of a glass tube which is fitted inside an cylindrical oven, see figure 2.8. The resistance of the oven releases heat by Joule effect heating therefore the hybrid sample covered by molecules in excess. The temperature is chosen to be 10 to 20 °C lower than the encapsulation temperature of the molecule. This temperature is supposed to be sufficient to extract the agglomerates of molecules from the outer surface of the bundles.

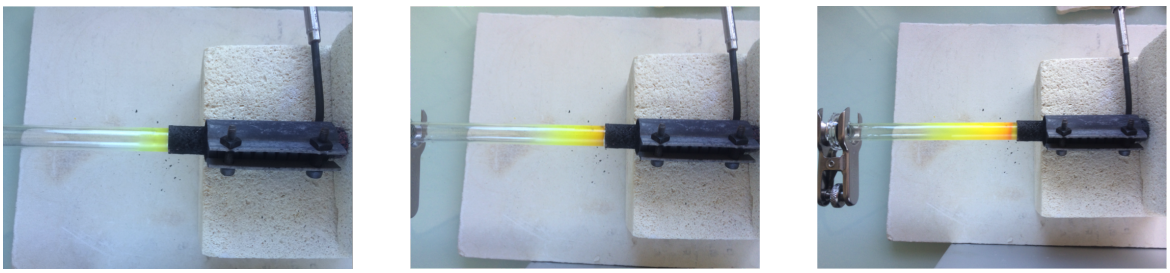

Figure 2.8 Degassing of the $4TCH_3$@NT sample at three different times during heating, form left to right. The yellow colour is the condensed $4TCH_3$ molecules which have not been encapsulated.

The other extremity of the glass tube is connected to the pump with a dynamic vacuum of 5×10^{-6} mBar. The aim is to sublimate the non encapsulated molecules and condensate

them on the cooler part of the glass tube which is not inside the small cylinder furnace. Thus, the excess of molecule can be separated from the hybrid nanotubes.

Rinsing step

The last step of the preparation of the hybrid samples consist in rinsing the hybrid system in a solvent in order to extract the remaining molecules which are in interaction with the outer walls of the nanotubes.

This step consists in preparing a solution of hybrid samples with the respective solvent inside an erlenmeyer flask with a magnet in order to agitate the solution in a magnetic stirrer. After 30 min of agitation, the powdered hybrid nanotubes will sediment at the bottom of the erlenmeyer flask whether the excess of organic molecules are dissolved into the solvent. With a needle, the supernatant is removed from the solution. This process is repeated about 14 times until the absorption intensity of the supernatant is about 70-80% of transmittance, see Figure 2.10.

Figure 2.9 Supernatant of the first four washes for the $4TCH_3$@NT09 hybrid sample.

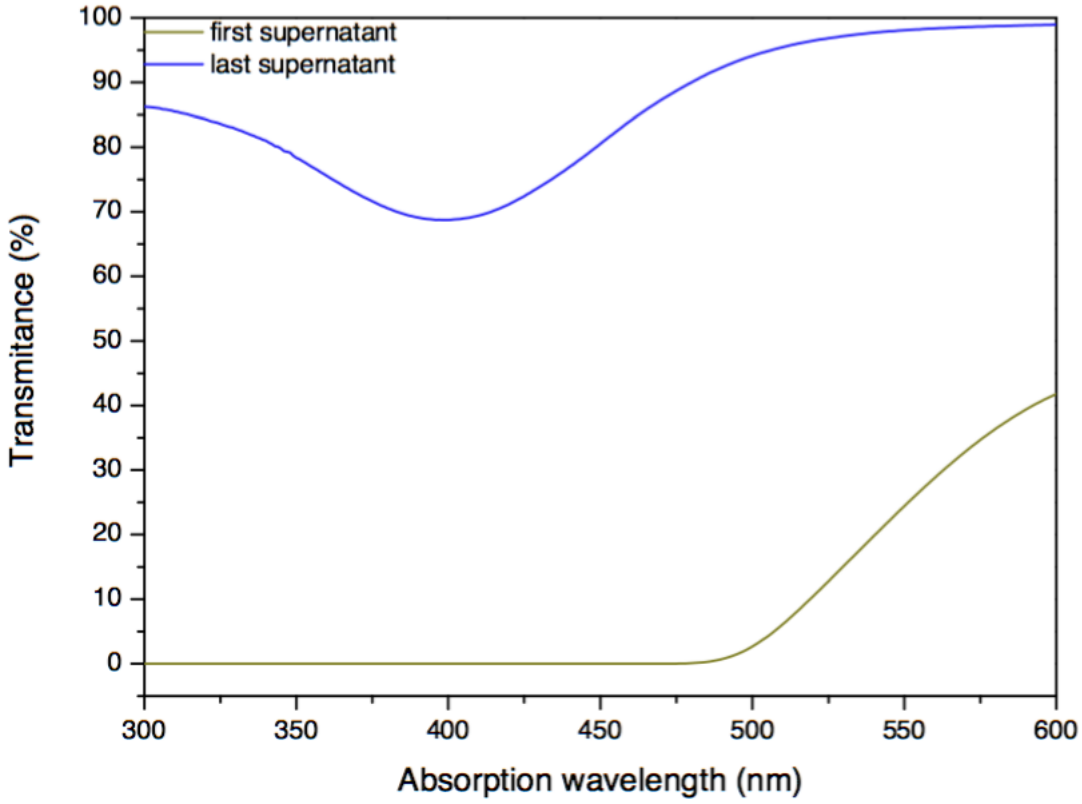

Figure 2.10 UV-vis absorption spectra of the first and last supernatants of the rinsing step of $4TCH_3$@NT09 hybrid sample.

The optical absorption of a solution of $4TCH_3$ corresponds to an optical transition between the highest occupied molecular orbital HOMO to the lowest unoccupied molecular orbital LUMO. As the first supernatant is very concentrated (see figure the solution on the left of figure 2.9), its optical absorption is very high, meaning that its transmittance is 0%. Likewise, the optical absorption of the last supernatant (14^{th} washing) transmits 70% of the incident light.

Reference samples with exohedral functionnalization

Despite exohedral functionalization is not the subject of this study, some references samples named oTπNT have also been synthesized, following the exact functionalization process described in section 2.1.2 with closed-end nanotubes. These samples are used as a reference to differentiate the signatures of endohedral functionalization from exohedral functionalization.

2.1.3 Summary of prepared hybrid nanotubes samples

The list of prepared samples for the following studies is summarized in table 2.3.

Table 2.3 List of pristine and hybrid nanotubes prepared in the framework of this thesis with description.

Samples		Comments
pristine nanotube	**hybrid nanotube**	
NT09	$4TCH_3$@NT09	opened-end CoMoCAT nanotube
NT14	$4TCH_3$@NT14	opened-end arc discharge nanotube
NT18	$4TCH_3$@NT18	opened-end eDIPS nanotube
AP	$4TCH_3\pi$AP	closed-end arc discharge nanotube

2.2 Characterization of hybrid systems

In this second part of the chapter, several technics will be used in order to probe the successful encapsulation of the dye molecules within the carbon nanotubes of different diameters. We will first show the results from optical characterizations, which are simple and rapid technics requiring a small amount of sample.

2.2.1 Absorption in NIR and visible

We have first characterized the pristine nanotubes by measuring the optical absorption of individual nanotubes. The suspension of carbon nanotubes was prepared dispersing the nanotubes in a solution of bile salt surfactant and ultra pure water (UPW). The powdered nanotubes are mixed with 35ml of solution was prepared with a solution of 0.01wt% bile salt in ultra pure water (UPW), with a ratio SWCNT:solution equal to 1:1 for NT09 and 2:1 for NT14. In a second step, the bundles are exfoliated by the sonication performed in an VWR sonic bath (model USC500D) at room temperature. Different sonication times were tested from 20 to 80 min. It was shown that, in order to obtain a suspension giving the best absorption signal at least 60 min sonication are required for NT09 and 80 min for NT14. The third step consists in centrifugation in order to separate the individual nanotubes from the large aggregates inside the suspension since the supernatant contains mostly individual SWCNTs and the precipitate consists of non-dispersed SWCNTs (bundled SWCNTs), dispersant residues, metal oxides and other impurities. The supernatant is extracted with a syringe and is studied through Optical absorption.

The same procedure was followed for the preparation of the solution of the hybrid nanotubes: $4TCH_3$@NT09 and $4TCH_3$@NT14, see figures 2.11a and 2.11b. The different transitions between Von Hove singularities are identified for pristine nanotubes and are shown respectively on figure 2.11a and 2.11b for $4TCH_3$@NT09 and $4TCH_3$@NT14.

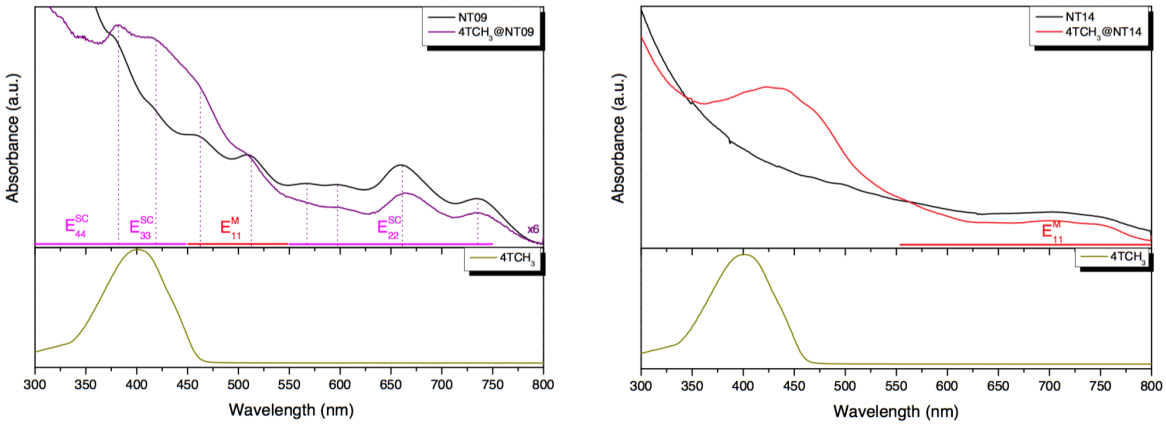

(a) $4TCH_3$@NT09 (violet) and NT09 (black).

(b) $4TCH_3$@NT14 (red) and NT14 (black).

Figure 2.11 Comparison of the absorption spectra of pristine and hybrid nanotubes.

For both hybrids, a broad massif appears around 425nm as the signature of encapsulated $4TCH_3$, one can note that the signature of $4TCH_3$ in DCM solvent appears at 400 nm, therefore the signal observed in not a simple superimposition of the absorption of pristine and that of $4TCH_3$. This blue shift of the signature of the encapsulated molecule could be the signature of some degree of oxidation. As a matter of fact it was shown that the radical di-cation exhibit a maximum absorption around 440nm.

Moreover, the signal from the nanotube also exhibits some shifts as already reported by Almadori [124]. Some blues shifts (see figure 2.12a and 2.12b) associated to the transition E_{11}^{SC} would be associated to a reduction of the band gap energy and would thus have an impact on the nanotube electronic properties. These results will be discussed together with the results of Chapter 4.

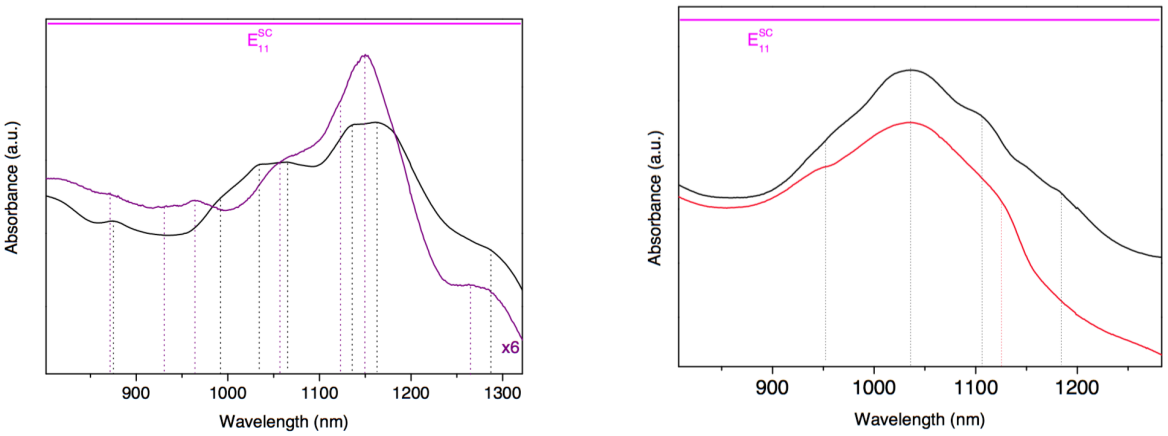

(a) $4TCH_3$@NT09 (violet) and NT09 (black).

(b) $4TCH_3$@NT14 (red) and NT14 (black).

Figure 2.12 Comparison of the absorption spectra of pristine and hybrid nanotubes.

2.2.2 Raman Spectroscopy

In this subsection, the Raman spectra of the pristine nanotube will be compared with the hybrid system and bulk molecule for both hybrid systems $4TCH_3$@NTϕ.

Raman Spectroscopy characterization of $4TCH_3$**@NT**ϕ

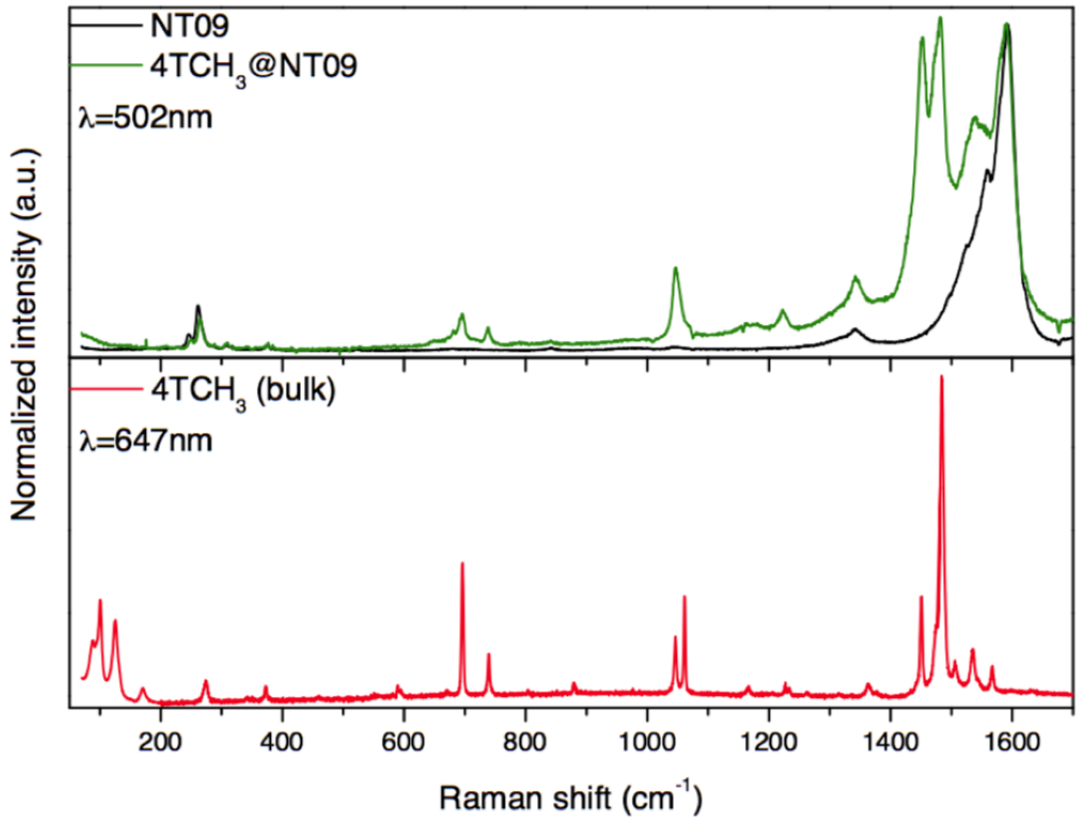

Figure 2.13 Raman spectra of powdered sample of NT09 (black) and $4TCH_3$@NT09 (green). All the spectra are normalised to the intensity of the G band. The exciting laser wavelength used was 502 nm. The bulk molecule is shown on the bottom graph, probed with exciting laser wavelength of 633 nm, once it has fluorescence when probed at 502 nm due to its optical properties.

The Figure 2.13 shows the spectra of pristine (black), hybrid (green) nanotubes and $4TCH_3$ crystal (red). The features observed at 1598 cm^{-1}, 1350 cm^{-1} and 260 cm^{-1}, respectively known as G, D band band and Radial Breathing Mode (RBM) are well known characteristic features of carbon nanotubes and will be explained in details in the Chapter 4. Comparing now the profiles of the hybrid and pristine nanotubes, additional bands that do not have their origin in the nanotubes appear for the hybrid system and can be suspected to be signatures from the photoactive molecules. Looking at the bottom graph in Figure 2.13, the spectra for $4TCH_3$ crystal is given for comparison. Most of the bands observed on the hybrids suspected to originated from the molecule have counterpart vibrational feature in the crystal. Yet some differences in relative intensity ratio and bandwidth are observed. These differences are a good indicator that the $4TCH_3$ in the hybrid sample does not adopt the crystalline phase of

the bulk sample. Moreover, the larger bandwith account for a more disordered form of the encapsulated molecules in the hybrid system.

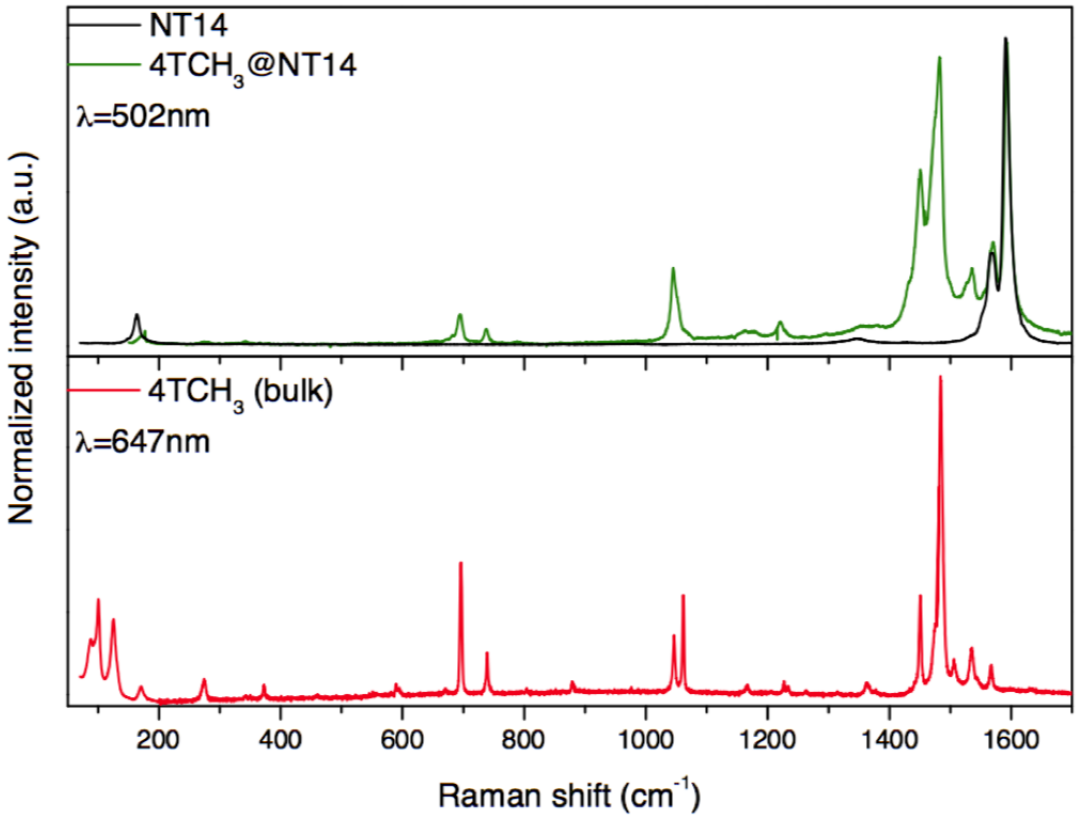

Figure 2.14 Raman spectra of powdered sample of NT14 (black) and $4TCH_3$@NT14 (green). All the spectra are normalised to the intensity of the G band. The exciting laser wavelength used was 502 nm. The bulk molecule is shown on the bottom graph, probed with exciting laser wavelength of 633 nm, once it has fluorescence at 502 nm.

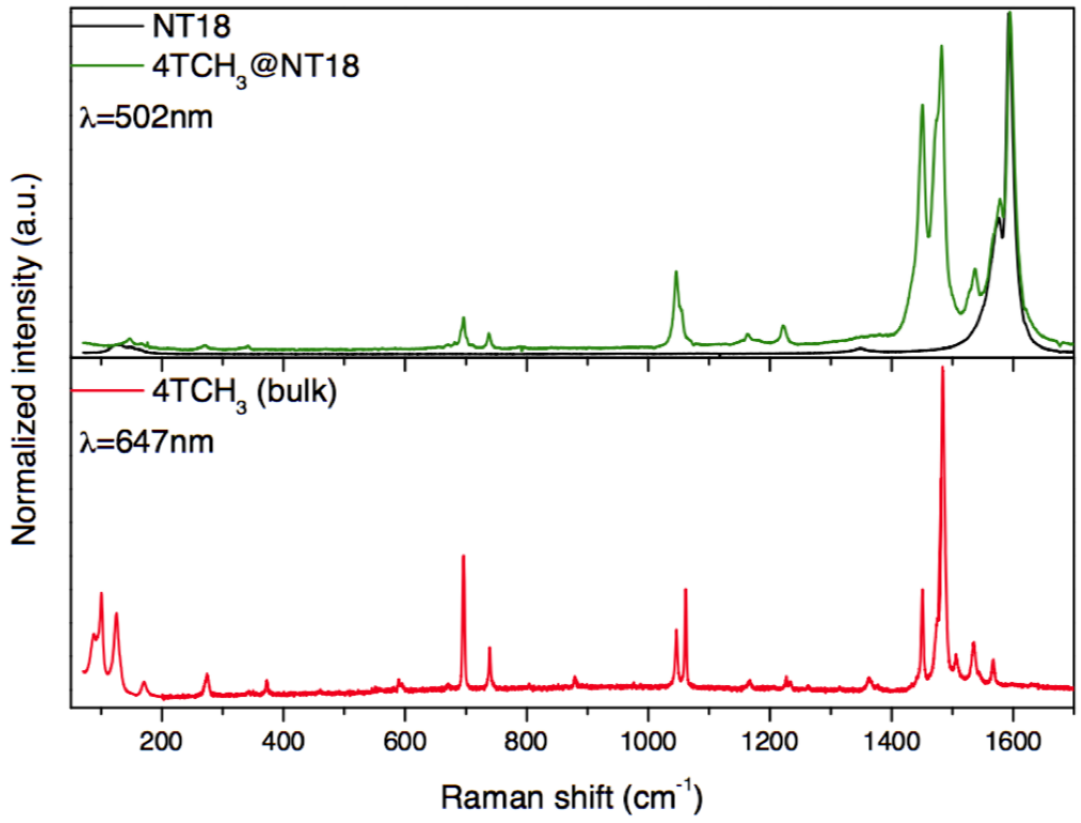

Figure 2.15 Raman spectra of powdered sample of NT18 (black) and $4TCH_3$@NT18 (green). All the spectra are normalised to the intensity of the G band. The exciting laser wavelength used was 502 nm. The bulk molecule is shown on the bottom graph, probed with exciting laser wavelength of 633 nm, once it has fluorescence at 502 nm.

Both hybrid systems and respective pristine nanotubes shown are for $4TCH_3$@NT18 and $4TCH_3$@NT14 in Figure 2.14 and 2.15. As for $4TCH_3$@NT09, some new features appear superimposed to the hybrid nanotubes NT14 and NT18. These features can easily be correlated to $4TCH_3$ molecules but with signatures slightly different from the ones from the crystalline $4TCH_3$. According to Kataura plot [52], the G-bands of the pristine nanotubes have a semi-conducting character. And, as for the $4TCH_3$@NT09 hybrid system, the photoluminescence of the molecule is quenched and a superposition of the Raman spectra of pristine nanotubes is superposed to the bulk $4TCH_3$, giving rise to the Raman spectra of the hybrid system. We will assign the most intense vibrational peaks of the bulk $4TCH_3$. which are found in the encapsulated on in Table 2.4, based on the references [129, 130].

Table 2.4 Assignment of vibrational peaks of the bulk molecule which are found in the encapsulated one inside NT09.

Frequency (cm^{-1})	**Assignment**[129, 130]
694	deformation of the C-S-C
737	stretching of the C-S
1047	stretching of C-H from the rings
1060	stretching of C-H from the methyl ends
1222	stretching of C-C between the rings
1451	stretching of C-C belonging to the rings
1481	stretching of C=C belonging to the rings

In summary, from Raman spectroscopy results, the hybrid nanotubes with mean diameters 9, 14 and 18 Å, the presence of the $4TCH_3$ molecule is detected in a form that differs from the crystalline $4TCH_3$.

2.2.3 X-ray diffraction and High-Resolution Transmission Electron Microscopy

X-ray diffraction has been performed for all the hybrid samples synthesised within the framework of this PhD thesis. The direct observation of an isolated hybrid nanotube can be achieved by means of Transmission Electron Microscopy (HRTEM). For some samples, HRTEM was also performed by the collaborators from ONERA and AIST [131]. The powdered sample is diluted in ethanol and ultrasonicated. After that, the solution is deposited on holey carbon copper grids.

For a sample such as NT14, the diffractogram (Figure 2.17a) exhibits peaks that are characteristics of the bundles. As a matter of fact, nanotubes have the tendency to aggregate one to the other due to the attractive van der Waals force, forming bundles. This structure which comprises from few to hundreds of nanotubes [113] has an hexagonal lattice is with lattice parameter is equal to $\phi_{NT} + d_{VdW}$, where ϕ_{NT} corresponds to the diameter of the nanotubes and d_{vdW} to the Van der Waals distance of 3.2 Å between tubes (see Figure 2.16a) [132].

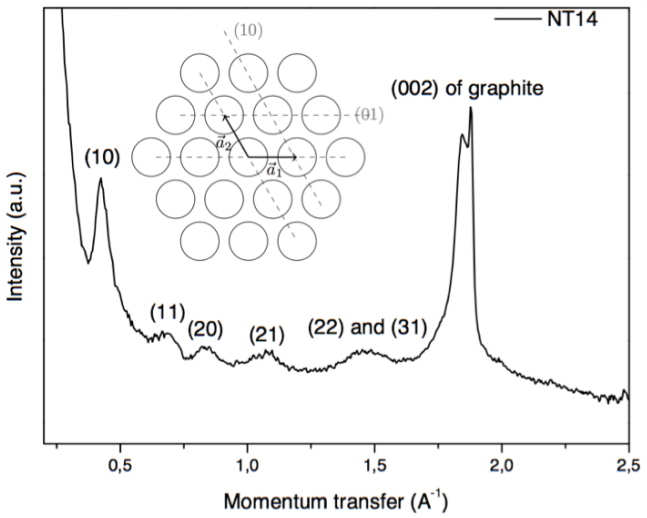

(a) Diffractogram of the pristine NT14. Inset: Diagram of the (10) and (01) planes in a bundle of nanotube with lattice parameter equal to $\phi_{NT} + d_{VdW}$.

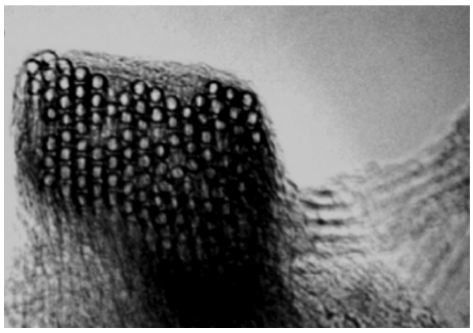

(b) A high-resolution TEM image of a nanotube bundle made of about 100 SWCNTs. Taken from reference [132].

Figure 2.16 Bundle of carbon nanotubes of **(a)** uniform diameter with **(b)** its diagram representation.

Such an hexagonal lattice can be pictorially represented by Figure 2.16a. The two indicated gray dotted lines represent the two planes (10) and (01) which are characteristic of the hexagonal lattice of a bundle of nanotubes: they give the inter-tube distance.

It has been shown formerly that these diffraction peaks signing the bundle structure can be modified when molecules are encapsulated within carbon nanotubes. As a matter of fact, J. Cambedouzou et al [133, 134] have studied the aspects of the (10) peak when it comes to encapsulation of C_{60}. It has been experimentally shown that once C_{60} is encapsulated, the (10) peak quenches. The explanation is the contribution of the atomic form factor of encapsulated species is in anti-phase with the bundles structure factor

Therefore, the peak (10) could be a sensible probe of the encapsulation of species inside the hollow space of nanotubes. Using this technique and the characteristics of the bundle-like structure and being interested in probing the encapsulation, lets first discuss the X-ray characterization of encapsulation of $4TCH_3$.

Characterization of $4TCH_3$@NTϕ

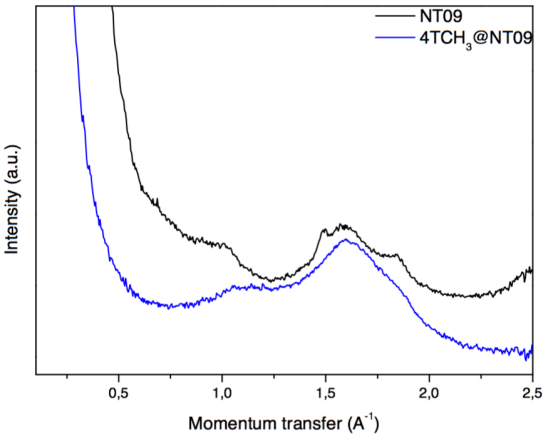

(a) X-ray diffractogram of a powder of empty NT09 and a powder of hybrid $4TCH_3$@NT09.

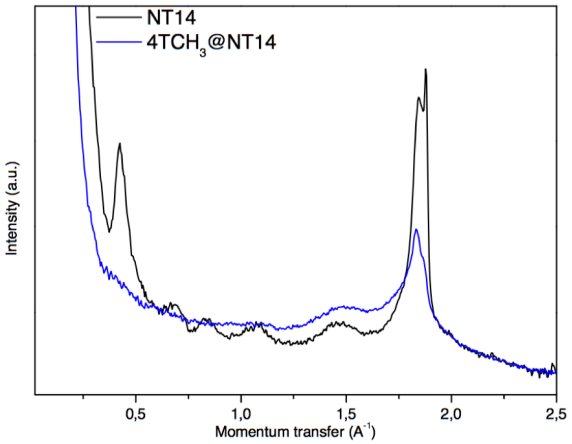

(b) X-ray diffractogram of a powder of empty NT14 and a powder of hybrid $4TCH_3$@NT14

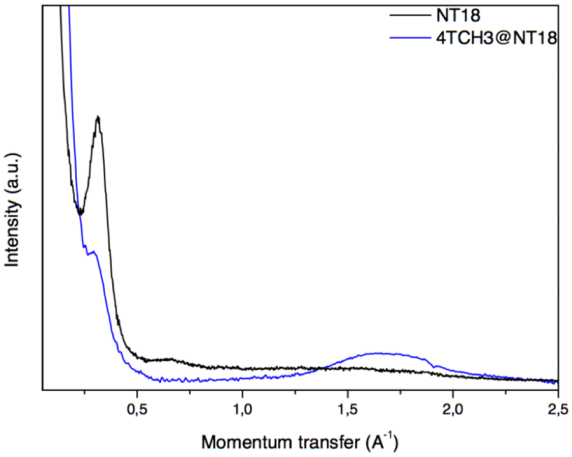

(c) X-ray diffractogram of a powder of empty NT18 and a powder of hybrid $4TCH_3$@NT18.

Figure 2.17 X-ray diffractogram of empty and hybrid nanotubes for both samples **(a)** $4TCH_3$@NT09; **(b)** $4TCH_3$@NT14 and **(c)** $4TCH_3$@NT18.

The Figure 2.17b shows the X-ray diffraction of $4TCH_3$@NT14 hybrid sample in the range of 0.1 to 1.75 $Å^{-1}$. The black curve corresponds to the diffraction of a powdered sample of pristine nanotubes with mean diameter of 14 Å and gaussian distribution of diameter from 1.2 to 1.6 Å. The first intense peak at 0.4 $Å^{-1}$ is the (10) peak, followed by four peaks (assigned in Figure 2.16a) and the last intense peak is the (002) peak of graphite at 2 $Å^{-1}$. Therefore the pristine NT14 sample is composed by large bundles with a large number of nanotubes. For the corresponding hybrid sample (blue curve) the (10) peak is quenched,

giving an indication on encapsulation of the $4TCH_3$ molecules inside of it. The Figure 2.17c shows the diffraction for both pristine and hybrid system with mean diameter 18 Å. The (10) feature, observed at lower angle ($0.30/Å^{-1}$) consistently with the larger tube diameter is also very well defined in pristine sample and is strongly quenched for hybrid sample.

In the Figure 2.17a, the pristine nanotube with mean diameter of NT09 and gaussian distribution of diameter from 0.7 to 1.1 Å do not have all peaks from a bundle of nanotubes. It is an evidence that nanotubes aggregate into bundles which contain few nanotubes, not achieving the optimal conditions in order to obtain a (10) peak. For this specific sample, on the basis of the (10) peak, it is not possible to say whether the nanotube is filled in or not, on the basis of the XRD only.

For $4TCH_3$@NT08, and $4TCH_3$@NT14, HRTEM has been performed on the samples synthesised during Yann Amadori's PhD thesis [124], following the same encapsulation protocol of the one described in section 2.1.2. The HRTEM results (Figure 2.18a and 2.18c), are well detailed in [105]. These results have shown, thanks to contrast profiles (Figures 2.18b, 2.18d and 2.18f), that in the section of $4TCH_3$@NT08 one single molecule was found whether $4TCH_3$@NT14, $4TCH_3$@NT18 nanotubes can accommodate two and three molecules, respectively, within a section.

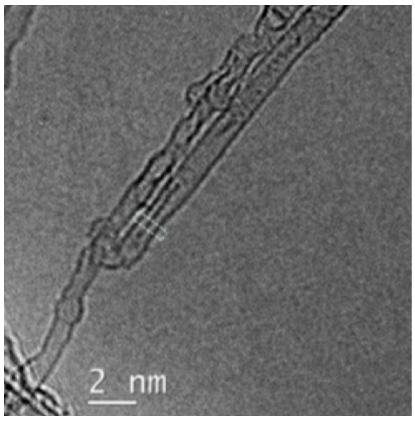

(a) HRTEM image of $4TCH_3$@NT08.

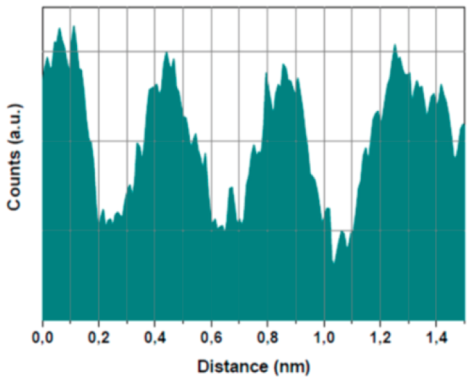

(b) Constrast profile of $4TCH_3$@NT08.

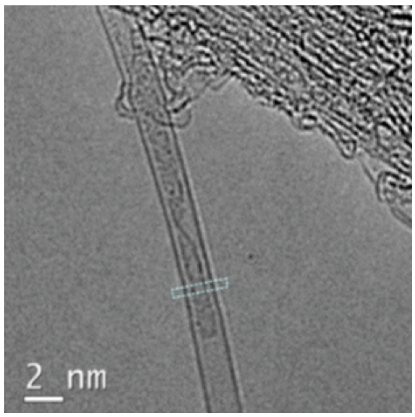

(c) HRTEM image of $4TCH_3$@NT14.

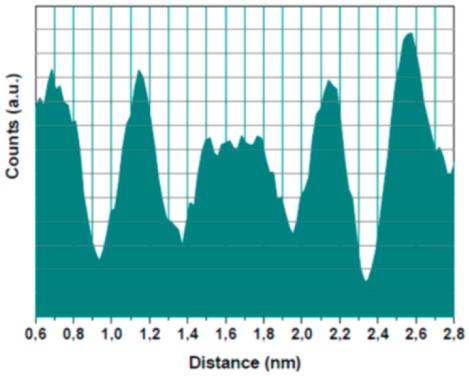

(d) Constrast profile of $4TCH_3$@NT14.

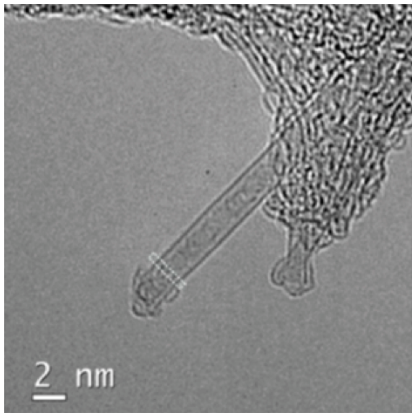

(e) HRTEM image of $4TCH_3$@NT18.

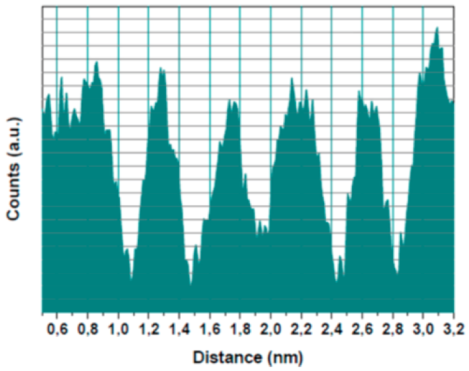

(f) Constrast profile of $4TCH_3$@NT18.

Figure 2.18 HRTEM micrograph of hybrid carbon nanotubes on the left and contrast profiles (along the white rectangle of TEM images) on the right. Taken from reference [105].

2.2.4 Defects on hybrid carbon nanotubes

All nanotubes used in this study for encapsulation have been opened by some oxidation process. Besides breaking sp^3 link founds in the end cap, these processes can also attack the graphene-like cylinder, and creates sp^3 bonds between carbon atoms. Therefore some oxidative defects can be created on the nanotube walls by these treatments. A healing treatment, under vacuum and at high temperature, is often applied after oxidation. It is important to verify the efficiency of this treatment.

As a matter of fact in Chapter 4, the dynamics of encapsulated $4TCH_3$ within NT14 is studied through neutron scattering thanks to the large hydrogen incoherent neutron cross section. Therefore, it is important to double check that the hydrogen related vDOS measured is not mixed with any signal related to oxygenated defects such as COOH created at the surface of NT14.

In the same manner, tshe aim of the Chapter 3, is to study the fine interaction between host nanotube and encapsulated molecule, it is important to characterize the hybrid nanotubes once the remaining defects may influence the electronic properties of the nanotubes. For these reasons, NEXAFS (Near Edge X-Ray Absorption Fine Structure) experiments were performed on nanotubes NT14 used as host matrix for encapsulation. These nanotubes have been healed by thermal treatments, they are compared to AP pristine closed nanotube (before oxidation) and to nanotubes opened by oxidation NT14o before thermal healing, see table 2.5.

Table 2.5 List of hybrid nanotubes prepared in the framework of this thesis for the structural defects study.

pristine nanotube		**corresponding**
named as	**description**	**hybrid nanotube**
AP [135]	as received from synthesis, closed-end nanotube	$4TCH_3\pi$AP
NT14o [136]	after oxidative treatment, opened-end nanotube	$4TCH_3$@NT14o
NT14 [65]	healed after oxidative treatment, opened-end nanotube	$4TCH_3$@NT14

Note: AP, NT14o and NT14 are SWCNTs synthesized by the arc electric process, described in section 2.1.1 of the present chapter. All three nanotubes samples were purchased from Carbon Solutions company.

These NEXAFS (Near-edge Absorption X-ray Fine Structure) experiments were performed at the Bear beam-line [137] of Elettra synchrotron radiation facility (Trieste, Italy). The spectral resolving power ($E/\Delta E$) of incident photons at 400 eV was respectively 800 and 4000 at normal and high resolution, respectively. The X-ray spot area was 0.01 mm^2. Spectra were recorded in the total electron yield mode in an ultrahigh vacuum chamber. The solid powder of nanotubes was pressed on a copper plate thanks to copper tape. Samples were outgassed for a few hours at around before the recordings.

The principle of NEXAFS is briefly described in figure 2.19, this technic is particularly relevant to probe electronic structure of carbon nanotubes [138], in particular it was shown that oxygenated defects could be evidenced [139].

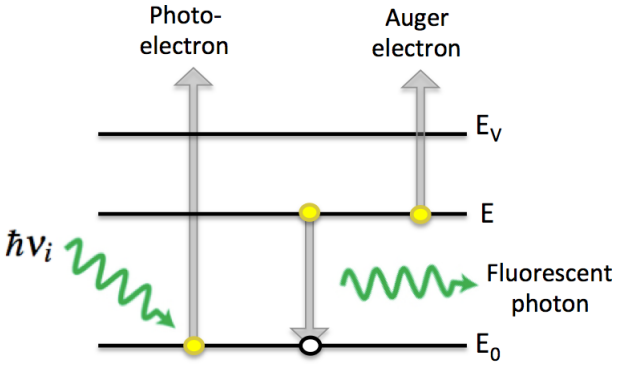

Figure 2.19 The target atom absorbs the incoming photon with energy $\hbar\nu_i$ and emits a core electron from the core level E_0 (either K (1s) or L (2p) orbitals), which is emitted to an unoccupied discrete level, creating a hole. An electron from the level E may either be released as an Auger electron or by emission of fluorescence photons. The NEXAFS spectra are therefore obtained either by measuring the electron yield or the fluorescence yield as a function of incident photon energy. Adapted from reference [138].

We first study the pristine nanotubes AP, NT14 and NT14o. The figure 2.20 shows NEXAFS signal at carbon K-edge. Three main regions can be studied. The first region is dominated by the sharp C-C $1s \rightarrow \pi^*$ transition at $\sim$284 eV, which is related to sp^2 carbon [140, 139]. This feature is intense for as received AP tube, decreases in intensity after oxidation treatment (NT14o) showing that the number of sp^2 Carbon decreases strongly after this chemical treatment. The second region in between [285, 289 eV] is associated with sp^3 carbon [141]. Two features observed at 288.5 eV and 290 eV are shown to increase in intensity on NT14o as compared to AP.

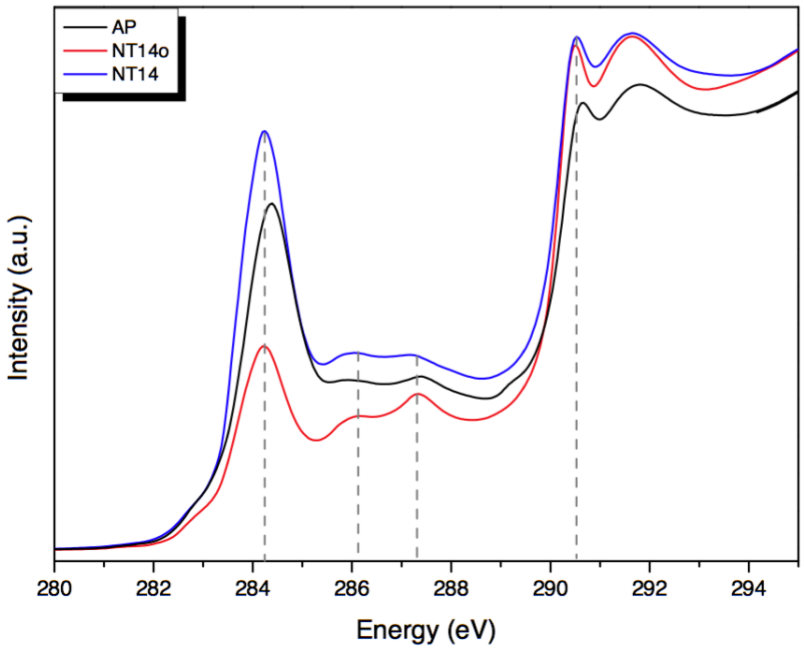

Figure 2.20 Carbon K edge NEXAFS spectra for the three pristine nanotubes AP, NT14o, NT14.

The feature at 288.5 eV has been assigned to NT-(OH-C*=O) or NT*-(OH-C=O) by Vigolo and collaborators [139] and to C-O 1s$\rightarrow \pi^*$ transition by Wang [141]. This latest group assigned the second feature to C-O 1s$\rightarrow \sigma^*$ transition. Therefore the increase of these two features clearly indicates the appearance sp^3 related to of oxygenated defects.

The excitations beyond 290 eV associated with 1s$\rightarrow \sigma^*$ transitions [140] are less affected by the oxidative treatment.

If we now focus on the nanotubes that have been thermally healed after oxidation treatment, so called NT14, one can notice that after healing, the features related to sp^2 and sp^3 species have recovered the level measured on pristine sample. Therefore as reported by Abbas and Kuznetsova, after a suitable thermal treatment, sp^2 carbon can be restored and concomitantly sp^3 carbon are less numerous [140, 142].

In a second step, hybrids systems have been studied at sulphur $L_{2,3}$ edge and compared to crystalline $4TCH_3$ in order check if defects would have any influence of the electronic state of the encapsulated molecule. As a matter of fact, $L_{2,3}$ edge is sensitive to reduced forms of thiophene. The NEXAFS spectra at sulphur $L_{2,3}$ edge for hybrid nanotubes and the crystalline molecule is shown in figure 2.21a. The three peaks (at 166.5 eV, 167.5 eV and 169 eV and the shoulder at 170 eV) observed are assigned from literature as arising from the overlapping of the four transitions of the sulphur spin-orbit split from $L_{2,3}$ levels which split by $\sim$1.2 eV [143, 144].

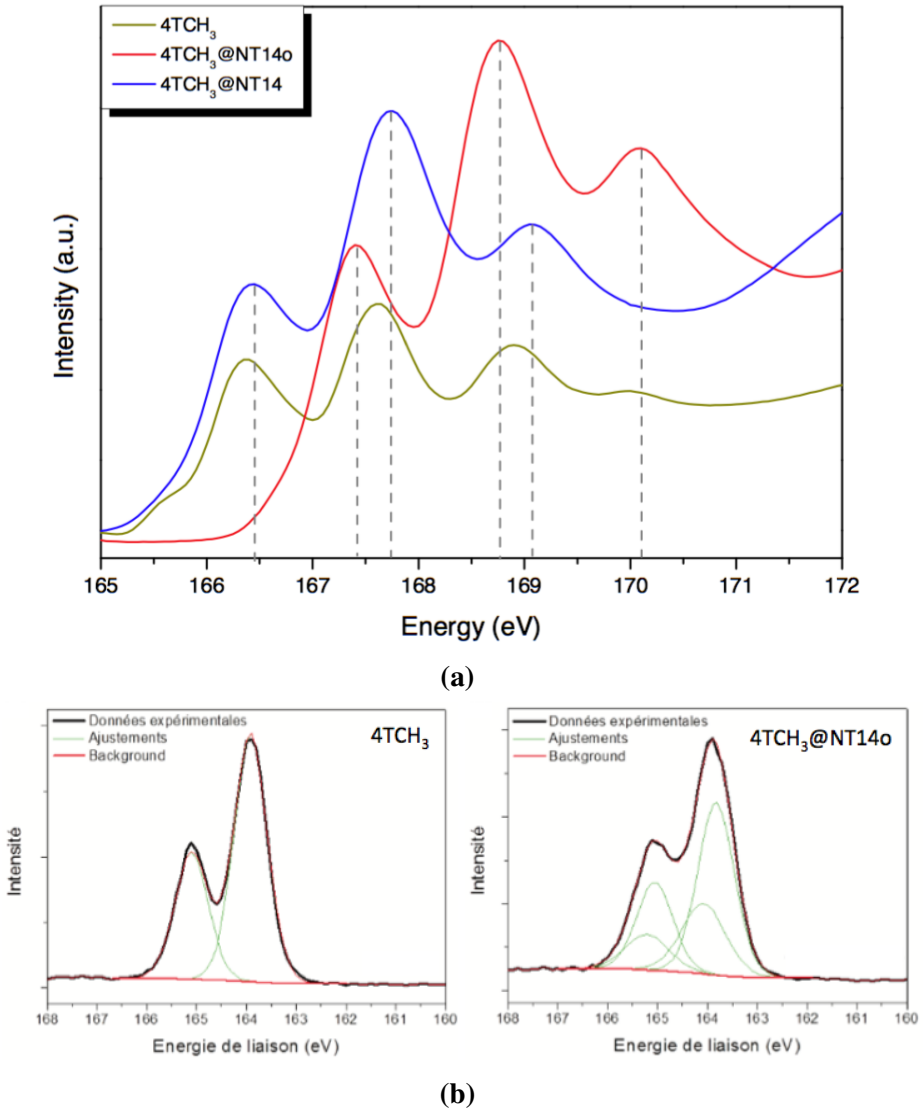

Figure 2.21 **(a)** Sulphur $L_{2,3}$ edge NEXAFS spectra for the hybrid systems: $4TCH_3$@NT14o, $4TCH_3$@NT14 and crystalline $4TCH_3$. **(b)** XPS spectra near the bonding energy of the sulphur atoms S 2p of the samples. **Left-hand side:** $4TCH_3$. **Right-hand side:** $4TCH_3$@NT14o. Taken from reference [124].

Figure 2.21a One can notice that for $4TCH_3$ and $4TCH_3$@NT14, are at the same position. However, the signal of the $4TCH_3$@NT14o has a considerable rigid shift of 1eV. Therefore, when the host nanotubes are defective, contrary to hosting healed nanotubes, the electronic state of $4TCH_3$ encapsulated molecules is different from the electronic state of the molecule within the crystal. These results are confirmed by XPS performed on both $4TCH_3$ and $4TCH_3$@NT14o (2p state), see figure 2.21b. The XPS signal of the crystalline $4TCH_3$ molecule has two different contributions, one at 163.8 eV and the other at 165.1 eV. This

doublet is associated with the C-S bonds of the $4TCH_3$ [145]. Almadori has reported that a part of the sulphur atoms in the $4TCH_3$@NT14o hybrid system has a different electronic state, due to the presence of a second doublet, see figure 2.21b. This new contribution can be interpreted, as the reference [146] suggests, that it is originated from the O-S bonding between the sulphur atoms and the surface defects present in the NT14o [124].

Therefore results from XPS and NEXAFS converge and suggest a specific interaction of some sulphur with the defective nanotube surface functions, that be studied in the framework of chapter 4.

To summarize, we have shown that:

- Healing treatment is efficient for NT14 nanotubes, used as confinement matrix for the following studies.
- For hybrids $4TCH_3$@NT14o synthetized with defective nanotubes, a specific interaction is shown between $4TCH_3$ and the defective nanotube related to surface functions giving rise to a modification of the molecule electronic state as compared to $4TCH_3$ crystal.
- Such effect is not observed when the host matrix has been healed.

2.3 Summary

In this chapter, the protocol used for the synthesis of hybrids systems consisting in the encapsulation of either $4TCH_3$ molecules, inside nanotubes with diameters ranging from 8 to 21Å is explained in details.

The characterization of the hybrid systems has been performed by Raman Spectroscopy, X-ray diffraction and Transmission Electron Microscopy. Eventhough HRTEM and Raman spectroscopy are techniques which probes the hybrid systems locally, X-ray diffraction in the other hand probes globally the hybrid samples. Therefore, the various approaches give results which all converge to prove that $4TCH_3$ molecules are encapsulated within the selected carbon nanotubes. and that the encapsulated species are the dominant species.

The study of the structural defects has revealed a considerable difference of the NEXAFS signal of pristine nanotubes expected have less surface functions, when compared to defective nanotubes. It has also revealed that the $4TCH_3$ molecules interact with surface functions when the nanotube has a considerable amount of structural defects. Therefore, a pristine nanotube which has less structural defects is more likely to have encapsulated molecules which do not interact with the surface functions.

Chapter 3

Study of the dynamics of $4TCH_3$ confined inside carbon nanotubes by Inelastic Neutron Scattering

Contents

3.1 Introduction and Motivations

The study of the state of matter confined at the nanoscale is a very active domain. At a fundamental level, it is motivated by the fact that the physical properties of such systems differ significantly from those of the bulk. By limiting the range of the interactions, important

changes in the structure, dynamics and thermodynamics of the systems are observed: original structures, *i.e.* not existing in the phase diagram of the bulk material, are often observed together with glass states which might be difficult to obtain from the melts. Some phase transitions (melting, glass transition, order-disorder transition, structural changes, etc...) see their critical temperature varying by a substantial amount, when they are not simply suppressed. In the peculiar case of carbon nanotubes, an additional ingredient is the asymmetry of the confining matrix, which holds a strong 1D character. This dimensionality aspect was shown to be preponderant in the physics of the so-called carbon nanopeapods, the inner C_{60} chain showing all aspect of a 1D harmonic crystal in a large temperature range before it "melts" at a temperature of $\sim$ 600 K [147]. In the case of water confined inside single-walled carbon nanotubes, Kolesnikov and co-authors [148] have reported the specific dynamics of a single water chain confined at the center of the tube. The very strong frustration of the hydrogen bond scheme provides the inner water chain with a specific soft dynamics. The latter shares strong similarities with water at the surface of proteins, of special importance in biophysics.

This chapter is dedicated to the study of the vibrational properties of the encapsulated $4TCH_3$ molecules. The aim is to understand the specific modifications of the dynamics when the molecules are encapsulated inside a nanotube, which in turn give details on the local structure of the molecule. The low frequency domain of the vibrational spectrum is also precisely studied as a function of temperature between 2 K and 300 K, in order to follow any change of the physical state of the inner molecules with temperature.

Studying specifically the encapsulated molecules using Infrared and Raman spectroscopies is a difficult task. On one hand, carbon nanotubes are strongly absorbent material, rendering the infrared signal from the molecules confined within their core extremely small. On the other hand, the Raman resonant signal from carbon nanotubes dominates the spectra so much that the signal from the encapsulated molecules is not visible unless the molecules are themselves found in resonance. In that case, a signal from the molecules is actually measurable. However, the comparison of different molecules in different confinement matrices is possible only if the electronic structure of the molecules are close to keep similar resonance scheme, which renders the experimental approach difficult.

For such systems, neutron spectroscopy (or inelastic neutron scattering - INS in the following) appears as a particularly well suited technique, the peculiarity of the neutron beam making it extremely sensitive to hydrogen atom. This is characterized by the so called "scattering cross-section" which, for hydrogen, is the largest of all the elements. It amounts $\sigma_{\mathrm{H}}^{\mathrm{inc}}$ = 80.26 barn for hydrogen which has to be compared to $\sigma_{\mathrm{C}}^{\mathrm{coh}}$ = 5.551 barn for carbon atoms and only $\sigma_{\mathrm{S}}^{\mathrm{coh}}$ = 1.026 barn for sulphur. If one considers that one $4TCH_3$ molecule can be encapsulated in a section of a (11,0) armchair nanotube (see below) with

a length of $\sim$ 30 Å, the total cross section from this section of tube is $\sim$ 3000 barn, with about a third of the scattered signal originating from the $4TCH_3$ itself. As we will show later in this chapter, the scattered intensity is also inversely proportional to the mass of the elements, further enhancing the scattering from hydrogen, which makes the signal from $4TCH_3$ dominant in a spectrum of $4TCH_3$@NT hybrids sample. In addition, by contrast to optical spectroscopy, other specificity of neutron scattering is the absence of any selection rule for neutron spectroscopy, so that all vibrations are visible in the spectra[1]. The INS spectrum is therefore a "neutron weighted" version of the vibrational density of states, that we will refer to as *GDOS* standing for Generalized Density Of States.

In this chapter, we report on INS investigations of a series of three samples:

- a bulk $4TCH_3$ sample, containing a powder of pure $4TCH_3$ in crystalline phase.
- a sample composed of a powder of $4TCH_3$ molecules confined inside nanotubes having an averaged diameter equal to 9 Å. We will refer to this sample as to the *hybrid* $4TCH_3$@NT09 sample.
- idem but for nanotube having an averaged diameter of 14 Å. This sample will be called *hybrid* $4TCH_3$@NT14 sample.

The investigations were done in the energy range [0, 500 meV], using the IN4C and LAGRANGE spectrometers, so as to cover the entire domain of the structural excitations present in these molecular systems. Powders of nanotubes, taken from the same batches prior to the encapsulation step, were also measured in the same conditions. The neutron intensity obtained on the latter samples, even if found to be very weak, was systematically subtracted from their hybrid counterpart. They are not shown nor discussed in details in this chapter, their global features being closed to those described in previous theses and papers (see for example reference [150]).

The experimental features observed in the INS data are discussed based on the results of DFT calculations performed by our collaborators Anouar Belhboub and Patrick Hermet. The numerical versions of the hybrids $4TCH_3$@NT09 and $4TCH_3$@NT14 samples are atomic models constructed by encapsulating one or two $4TCH_3$ molecules inside a (11,0) or (17,0) zigzag nanotubes respectively. A section of $\sim$ 29 Å of these tubes was modelized, and periodic boundary conditions were used along the nanotube axis. A model composed of an isolated $4TCH_3$, *i.e* in the gas phase, is also studied. The Hessian matrix was derived

[1] Recent neutron studies performed on molecular hydrogen confined inside fullerene molecules showed that under very specific conditions, selection rules actually exist for the quantum transition of the H_2 molecule [149]

from the calculation of the Helmann-Feynman forces using the direct method. The vibration frequencies and polarization vectors were thereafter extracted by diagonalization of the matrix. The partial vibration density of state could then be derived and the GDOS simulated. This is this last quantity that is discussed in direct comparison with the data.

In a first section, we present some results from the literature on neutron scattering applied to the study of carbon peapods and $4TCH_3$ and water confined inside nanotubes. The second part will present, after a short introduction, the results of the INS investigations in the form of an article. And at last, the conclusion of this chapter.

3.2 Some INS results obtained on carbon nanotubes, carbon peapods, water confined inside carbon nanotubes and quaterthiophene

The first INS studies of carbon nanotubes published in 2000 [151] report that the GDOS of single-walled carbon nanotubes and graphite are very similar in the range of energy transfer above 60 meV. However, they strongly differ in the low frequency domain where the modes are sensitive to the global shape of the material. Specific nanotube modes, *e.g.* radial deformation of the nanotubes or intertube "bundle" vibrations, are observed in the [0, 20 meV] range [151, 152].

The first "all carbon" hybrid system was discovered by Smith et al. in 1998 [5] in the form of carbon peapods consisting of C_{60}@NT. In 2005, the results on inelastic neutron scattering of peapods was reported by Cambedouzou [150]. On figure 3.1, it is possible to see that the signal of encapsulated C_{60} (bottom) could be obtained by a subtraction of the pristine nanotube signal (middle) from the peapod signal (top).

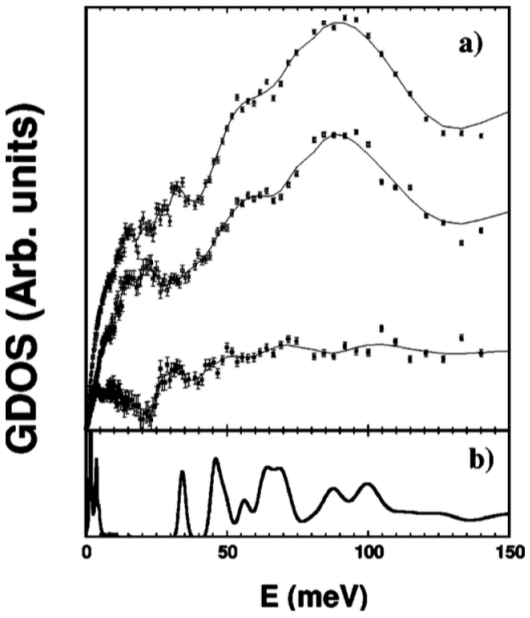

Figure 3.1 (a) Signal of peapod (top), pristine nanotube (middle) and subtraction of peapod by nanotube signal (below). **(b)** Calculated GDOS of isolated chain of C_{60}. Taken from reference [150].

The study of the temperature dependence of the rotational and translational dynamics of the confined system, using INS revealed some specific signatures of the confinement. On one side, the C_{60} orientations were found to evolve from a dynamical to a static disorder at a temperature of $\sim$ 150 K. This revealed that the order-disorder transition, at 255 K in bulk C_{60}, is suppressed under such confinement [153]. The neutron data obtained in the energy and wave-vector transfer range of the longitudinal acoustic phonons of the inner chain, revealed a progressive change from a 1D crystal behavior to a liquid-like character at a temperature of 650 K [147, 154]. For a review on the use of INS to study carbon based nanostructures, see reference [155].

The GDOS of confined water inside carbon nanotubes was reported by Kolesnikov [148]. The comparison of the GDOS of the confined water with that of ice-Ih revealed important changes in the dynamics induced by confinement. On one hand, the librational band of water softens under confinement, whereas the bending and stretching modes hardens. Along with Molecular Dynamics simulations, the authors concluded that the structure for the encapsulated water molecules is composed of an inner chain at the center of the nanotube axis and a "tubular" structure of water near the inner wall of the nanotube. They also concluded that the inner chain is particularly mobile down to low temperature with a very large longitudinal mean square displacement. They proposed that this low frequency soft dynamics is induced by the frustration of the hydrogen bonding scheme induced by confinement.

The vibrational dynamics of the crystalline α-quaterthiophene α-4T, has been extensively studied through INS by Hermet and collaborators, the experimental investigations being coupled to DFT calculations [156]. In particular, the transition from a high temperature 4T/HT phase to a low temperature 4T/LT phase was shown thanks to the intra-molecular out-of-plane bending mode around 700 cm^{-1} which depends strongly on the polymorph phase, see figure 3.2. In this thesis, we will often refer to this work for the assignment of the vibrational features observed for our crystalline $4TCH_3$ reference.

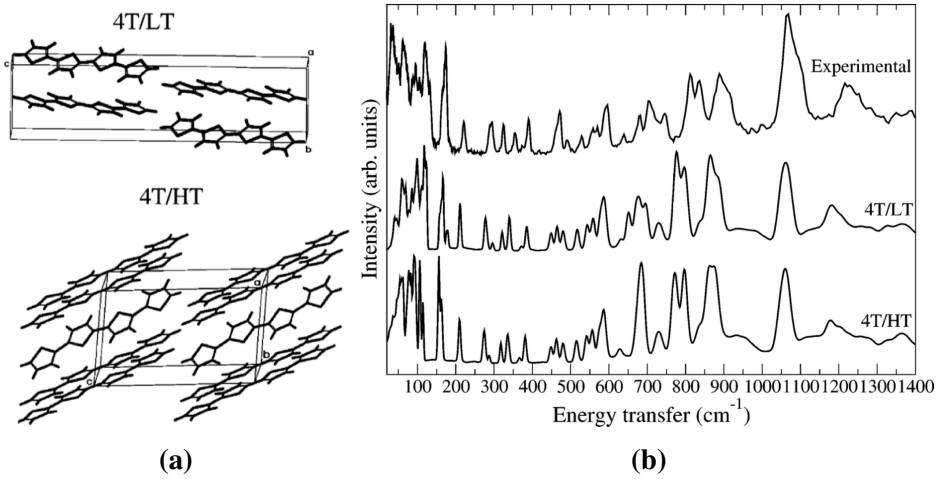

Figure 3.2 (a) Two polymorphs of α-4T: **top:** low temperature 4T/LT; **bottom:** high temperature 4T/HT. **(b)** INS spectra of **top:** experimental spectra from crystalline 4T; **middle:** calculated spectra of 4T/LT polymorph; **bottom:** calculated spectra of 4T/HT polymorph. Taken from reference [156].

3.3 Article: A combined experimental inelastic neutron scattering and ab initio dynamics study of oligothiophene encapsulated in carbon nanotubes

Abstract: Dimethyl-quarterthiophene ($4TCH_3$) encapsulated inside single-walled carbon nanotubes was studied by inelastic neutron scattering. The results reveal specific dynamics of the $4TCH_3$ modes characterized in particular by a large sensitivity in the low frequency domain of the methyl libration to the confinement. DFT based calculations consistently describe the observed phenomena and give insights on the structure of the hybrid nanotubes at low temperature where molecules preferentially interact with the nanotube wall.

3.3.1 Introduction

Molecules confined in nanoscale one-dimensional channels are of great interest to materials science [18]. An excellent model for such a system consists of different molecular species encapsulated inside single-walled carbon nanotubes (SWNT) leading to "hybrid" nanotubes compounds. Following the first synthesis of organic all-carbon "peapods", resulting from the encapsulation of fullerenes (C_{60}) inside single wall carbon nanotubes in 1998 [5], many hybrid materials have been successfully synthesized. Guests species are very diverse, ranging from *e.g.* metallofullerenes, metallocenes, organic and organometallic molecules or nanocrystals, and allow one to tune the physico-chemical properties of the hybrid compound in a large extent [6–14, 16, 31, 157, 158].

Recently, considerable efforts have been put to elaborate hybrid nanotubes from the encapsulation of organic photoactive molecules. The peculiar 1D nature of the SWCNTs internal channel was recently exploited to induce a specific molecular order of the confined molecules leading to an enhancement of the nonlinear response [159] of the compound, further creating a giant Raman scattering effect [106]. They also have potential advantages for Nano-optoelectronics applications. Of particular interest is their ability to emit light in the visible range of the spectrum, opening new opportunities for the design of carbon nanotube based nano-devices, pure carbon nanotubes being Infrared emitters while being passive in the visible range [39, 100]. Encapsulation of specific molecules allows modulating the charge carrier density of the SWCNT, performing air-stable amphoteric doping of SWCNTs [31, 157], leading to p- and n-type air-stable hybrid nanotubes that are required for the production of air-stable n-type SWNT-based field-effect transistors [31, 39, 93, 157].

In this Framework, a large number of studies concerned the physical properties of hybrid nanotubes (oT@SWCNTs) obtained after encapsulation of oligothiophene (oT). α-Oligothiophenes are electron-rich and chemically stable conjugated oligomers, renowned for their optoelectronic properties [32–35]. Likewise, their size and linear conformation make them good candidates as guest molecules for hybrid nanotubes.

The 1D geometrical confinement of oligothiphenes led to specific structural properties that were both theoretically and experimentally studied. The supramolecular organization of the confined oligothiophenes is shown to depend on the nano-container size [36, 105] and leads to Giant Raman scattering due to "J-aggregation" [106]. Photoluminescence (PL) emission in the visible spectral range of oT@SWCNTs has been reported [36, 160]. DFT calculations spotted van der Waals interactions as the major bonding mechanism between the tube host and the molecule guest. No specific dependence of the results with the length of the oT was shown [39]. Nevertheless, other studies on different dyes, including oT, inside SWCNTs reported efficient fluorescence quenching by the SWCNTs, this effect being seen

in weakly bonded chromophore-SWCNT complexes [106]. For small tubes (below 1 nm diameter), experimental results show also an evidence of a significant positive charge transfer (CT) on the inserted oligothiophene, in agreement with Raman behaviour of the G band of oT@SWCNTs [37]. DFT calculations predict the appearance of a very small CT when the diameter of the tube is reduced below 1 nm [100]. The disagreement concerning the nature of the interactions reported in the literature could originate from the dependence of the supramolecular organization of the confined oligothiophenes with the tube diameter. Below a 1.1 nm critical tube diameter, only one molecule is encapsulated in its hollow core. Between 1.1 and 1.6 nm tube diameter, two oligothiophenes are confined, while above 1.6 nm tube diameter, three molecules can be inserted [105]. Therefore, an increased C-$H_{thienylene}$-π_{NT} interaction is expected for small nanotubes with large inner wall curvature, whereas the stacking interaction between $\pi_{thienylene}$-π_{NT} drives their relative arrangement for small inner wall curvature nanotubes (*i.e.* tube diameters between 1.40 and 1.6 nm).

In these previous studies no dependency of the interactions between the tube and the encapsulated molecules as the function of the size of the nano-container was performed. An interesting question is whether a significant interaction occurs after oligothiophene encapsulation in SWCNT depending of the tube diameter. To elucidate the nature of the confinement effect, we address in this article the following issues:

- How does the size of the nano-container influences the interactions between inserted oligothiophenes and the nanotube.
- Does the variation on the confinement effect influences the vibration dynamic of the confined molecules ?

To address this question, we present here a joint Inelastic neutron-scattering (INS) and DFT study of the confinement of dimethyl-quaterthiophene ($4TCH_3$) in single wall carbon nanotubes (4T@NT) where the encapsulated molecules are used as probe of the confinement.

Sample preparations Two sources of nanotubes have been used in this study: commercial electric arc single-walled carbon nanotubes (1.2nm < d < 1.6nm), provided by Carbon Solution [65] and called NT14 in the following and CoMoCAT carbon nanotubes enriched in (7,6) nanotubes (0.6nm < d < 1nm) [118], called NT09 in the following. Carbon Solution, and CoMoCAT nanotubes were purifed by air oxidation and subsequently treated to remove the catalysts. The high purity and the narrow variation of the nanotube diameter were quantified by transmission electron microscopy and Raman measurements.

Encapsulation of $4TCH_3$ into carbon nanotubes was performed using the vapour reaction method previously described [37]. Before the encapsulation treatment, carbon nanotubes

were outgassed at 300 °C for 48 h. Then, nanotubes were mixed with $4TCH_3$ in the weight ratio $^{w_{NTs}}/_{w_{4TCH_3}}$ = 0.5 in the glove box and out gassed under 2×10^{-6} mbar at ambient temperature for 1 h. Then, nanotubes with $4TCH_3$ were sealed in glass tube at 2×10^{-6} mbar and heated to 250 °C for 72 h. The sublimation step was then performed. The sample was then washed with organic solvent and stored in the oven at 120 °C for 24 h. The hybrid material is named $4TCH_3$@NT in the following.

In this paper, we report on INS investigations of a series of three samples: i) a bulk $4TCH_3$ sample, containing a powder of pure $4TCH_3$ in crystalline phase, ii) a sample composed of a powder of $4TCH_3$ molecules confined inside nanotubes having an averaged diameter equal to 9 Å. We will refer to this sample as to the *hybrid* $4TCH_3$@NT09 sample and iii) idem but for nanotubes having an averaged diameter of 14 Å. This sample will be called *hybrid* $4TCH_3$@NT14 in the following.

3.3.2 Experimental section

The INS investigations were done in the energy range [0, 500 meV], using the IN4C and IN1-LAGRANGE spectrometers at the Institut Laue Langevin (ILL) in Grenoble (France), so as to cover the entire domain of the structural excitations present in these molecular systems. IN1-LAGRANGE is a graphite analyser, inverse geometry, neutron spectrometer installed on the hot neutron source at the ILL. It permits to measure excitations in the [40, 1000] meV range with a 2-4% resolution. IN4C is a time-of-flight spectrometer installed on the thermal source at the ILL. It allows at investigating excitations in the [1, 100] meV range with 4-6% resolution. For more details on the spectrometers, see references [161] and [162].

For both experiments ∼100 mg of $4TCH_3$@SWNT were wrapped inside an aluminium foil and placed inside an orange cryostat. The measurements were performed at 2 K on IN1-LAGRANGE and at the temperatures of 2 K, 25 K, 50 K, 75 K, 100 K, 125 K, 150 K, 200 K and 250 K on IN4C. Empty SWNT (NT14 and NT09) and bulk $4TCH_3$ samples were also measured to allow for a direct comparison with the hybrid samples.

The INS neutron data will be presented in the form of the generalized phonon density of states, as derived from the classical data treatment scheme published in *e.g.* reference [163]. Usual corrections are applied. They concern correction of the raw data from scattering of the sample cell and corrections from the intrinsic and energy dependent efficiency of the detectors. Powders of pure nanotubes, taken from the same batches prior to the encapsulation step, were also measured in the same conditions. The neutron intensity obtained on the latter samples, even if found to be very weak, was systematically subtracted from their hybrid counterparts. They are not shown nor discussed in details in this paper, their global features being closed to those described in previous papers (see for example reference [155]).

3.3.3 Simulation model

Among the previous ab initio simulations of hybrid $4TCH_3$@NT [36, 99, 100, 164], Loi performed energy minimization of $4TCH_3$ encapsulated inside nanotubes and proposed different inner structures for the confined molecules, the latter being significantly dependent on the nanotube diameter. According to this study we developed the models presented in figure 3.3: the numerical versions of the hybrids $4TCH_3$@NT09 and $4TCH_3$@NT14 samples are atomic models constructed by encapsulating one or two $4TCH_3$ molecules inside a (11,0) or (17,0) zigzag nanotubes respectively. A section of ~ 29 Å of these tubes was modelled, and periodic boundary conditions were used along the nanotube axis. A model composed of an isolated $4TCH_3$, *i.e* in the gas phase, is also studied.

Vibrational density-of-states are calculated within the formalism of the density functional theory (DFT). We use the SIESTA package [165] and the generalized gradient approximation to the exchange correlation functional as proposed by Perdew, Burke and Ernzerhof [166]. Core electrons are replaced by nonlocal norm-conserving pseudopotentials. The valence electrons are described by a double-z singly polarized basis set. The localization of the basis is controlled by an energy shift of 50 meV. Real space integration is performed on a regular grid corresponding to a plane-wave cutoff of 300 Ry. Van der Waals corrections (DFT-D) between the nanotube and the molecule are considered using the semi-empirical dispersion potentiel parametrized by Grimme [167]. Atomic displacements of each of the atom in the models by 0.03 Å were performed along the $\pm x$, $\pm y$ and $\pm z$ direction axis. The electronic calculations were performed at point Γ only. We considered four model systems : $4TCH_3$@(11,0) and $4TCH_3$@(17,0). In the first system, only one dimethyl-quaterthiophene ($4TCH_3$) molecule is placed inside the nanotube whereas in the last system, two molecules are placed inside the nanotube. The vibration frequencies and polarization vectors were thereafter extracted by diagonalization of the dynamical matrix. The partial vibration density of state could then be derived and the GDOS simulated. It is this quantity that is discussed in direct comparison with the data.

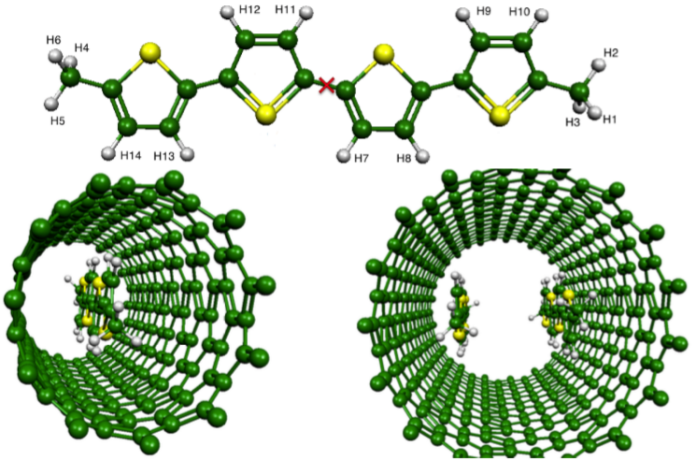

Figure 3.3 The used models for the HPDOS calculations. The length of the $4TCH_3$ molecule being 18Å.

The relation between the partial density of states and the GDOS G(E) is given by:

$$G(E) = \sum_i \frac{\sigma_i}{M_i} g_i(E) \tag{3.1}$$

with i=H,C,S the different atomic species in the sample, σ_i the neutron scattering cross section of atom i, $g_i(E)$ the partial density of state of atom i (iPDOS), and M_i its mass. The combination of the very large cross section of hydrogen (σ_H^{inc} = 82.02 barn, σ_C^{coh} = 5.55 barn, σ_S^{coh} = 1.03 barn) and low atomic mass provides H with the dominant contribution to the scattering. As a consequence, the GDOS will be largely dominating by the H partial density of states.

3.3.4 Results and discussion

Low Temperature measurements

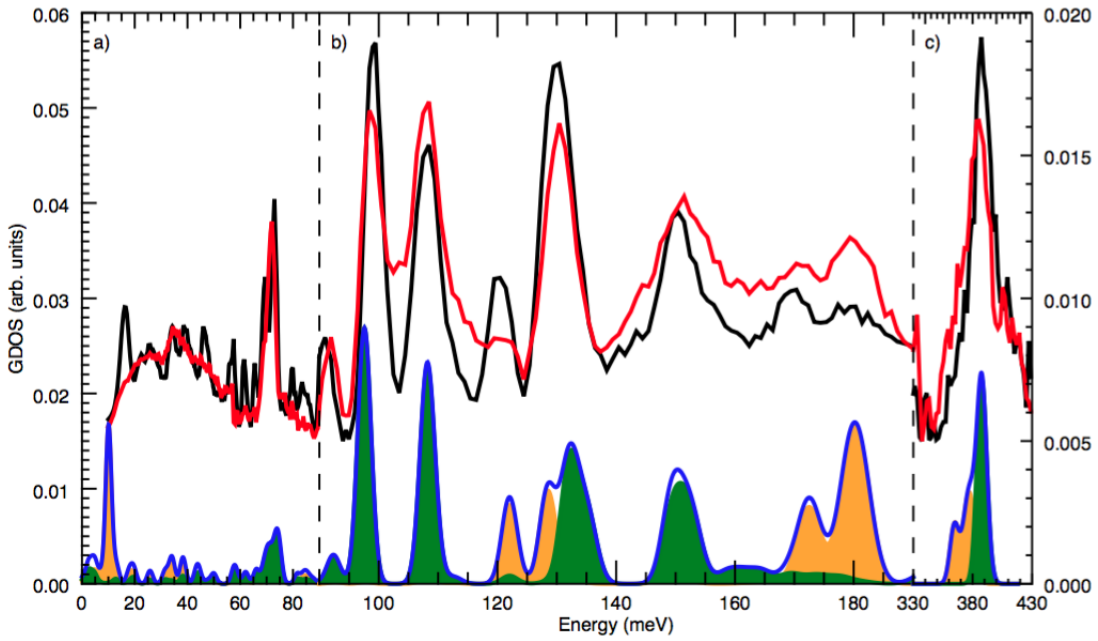

Figure 3.4 Comparison between the GDOS of the $4TCH_3$ bulk (black line), the GDOS of the $4TCH_3$@NT14 hybrid (red line) and the calculation of a $4TCH_3$ molecule in the gas phase (blue line). Orange and green surfaces represent the calculated partial mhGDOS and thGDOS, respectively. Experimental data measured at 2K.

The $4TCH_3$@NT14 GDOS is shown on figure 3.4 and is compared to that measured in the same conditions on a sample of bulk $4TCH_3$ in its crystalline phase. The total GDOS calculated from the DFT simulations of the isolated $4TCH_3$ molecule is shown at the bottom part of the figure, together with the partial contributions of the H atoms belonging either to the methyl groups (mH, mHPDOS, H(1) to H(6) on figure 3.3 top) or to the thienylene groups (tH, tHPDOS, H(7) to H(14) on 3.3 top).

The large neutron intensity difference between the carbon GDOS and the hydrogen GPDOS is reflected in the very weak intensity measured for a NT14 sample (not shown). As a consequence, pure nanotube modes, *i.e.* those not hybridized with the encapsulated molecule, do not contribute significantly to the $4TCH_3$@NT14 spectrum. However their main contributions to the GDOS, located in the 100 meV and 180 meV region, can bring some extra intensity to the neutron spectra.

The calculations show that the typical GDOS of a $4TCH_3$ molecule is dominated by sharp peaks that can be attributed either to tH or to mH modes. They mostly contribute to the GDOS in different domains. In particular, the mHGDOS dominates the spectrum in the low frequency range, with a strong peak at $\sim$ 10 meV characteristics of methyl librations. The first significant contribution of the tH to the GDOS is calculated at $\sim$ 65 meV. In addition to the above mentioned features, the low frequency range (E $\leq$ 50 meV) of the calculated $4TCH_3$ spectrum shows a series of peaks which are known to result from low-frequency fluctuations of the planar molecule backbone [156]. Those modes, e.g. librations of the thienylene rings, out-of-plane bending of the whole molecule, bring the termination H (either tH or mH) far from their rest positions. These "adiabatic" movements of the H atoms provide these modes with a large neutron weight, therefore giving a large contribution to the GDOS. Certain modes have a larger contribution from the mH than from the tH. In general the latter contain a certain degree of rotation or bending with regards to the center of the quaterthiophene chain. As the mH are located the farthest from the axis of rotation, their displacements are maximum. This explains the larger contribution to the mHGDOS of these modes.

Most of these characteristic features are observed in the experimental data. In particular, the peaks observed in the energy range $\geq$ 60 meV in the $4TCH_3$ spectrum can be assigned almost one by one from their corresponding feature in the calculations. The assignments of the vibrational modes of the isolated molecule can be found in Appendix A. The low frequency range (E $\leq$ 50 meV) of the experimental spectrum is less well reproduced by the calculations: the data show a rather large component centred around 25 meV above which well defined features superimpose, the latter being convincingly reproduced by the simulations (see discussion above). We believe that this broad component originates from the phonon density of states, *i.e.* lattice modes (acoustic phonons and rotations) involving whole -rigid- molecule movements, which are not accounted for in our calculations, the latter being performed in the gas phase. In particular, Brillouin edge contributions to the GDOS are not calculated.

The C-H stretching mode region (E $\sim$ 380 meV) of the calculated $4TCH_3$ spectrum features a complex peak composed of symmetric and anti-symmetric C-H modes. Accordingly, the mH contributions in this range are composed of three peaks, while the tHGDOS presents two closely positioned peaks at the high frequency side of this band. After convolution with the experimental resolution, the total spectrum shows a complex feature with a low energy shoulder and an intense high energy component (see figure 3.4 c)) in good correspondence with the line-shape of the peaks observed in the $4TCH_3$ spectrum.

If the global shape of the hybrid spectrum $4TCH_3$@NT14 shares strong similarities with that of the bulk $4TCH_3$, significant differences are also observed:

- the high-energy stretch band (see figure 3.4 c)) of the $4TCH_3$@NT14 is strongly affected by encapsulation. A significant part of the intensity of the high energy edge of this band is transferred to the low energy shoulder. This indicates a modification of the force constant associated to the tH bond stretch. There is no sign of strong modification of the component associated to the mH stretch.

- the intermediate energy range (60 meV < E < 200 meV, see figure 3.4 b)) is the region of the spectra showing the less pronounced differences between the $4TCH_3$@NT14 and the $4TCH_3$ GDOS. Encapsulation mostly affects the feature at $\sim$117 meV originating from a mH mode, the latter being broaden in the $4TCH_3$@NT14 spectrum. Some extra intensity is observed in between the principal peaks in the NT14 spectrum, e.g. around 100 meV and 180 meV where the contribution of the nanotubes modes is known to be maximum. Finally the first tH double peak feature at 75 meV in the bulk data is replaced by a symmetric peak.

- as expected from the very different supramolecular organisations of the $4TCH_3$ molecules between the bulk and in the hybrid samples, the spectra strongly differ at low frequencies (see figure 3.4 a)). In particular, the sharp and well defined low frequency features, observed below 60 meV in the bulk spectrum, are replaced by a large, featureless, bump centred around $\sim$25 meV with a kink at $\sim$37 meV. In particular, the first and most intense feature observed in the bulk spectrum at $\sim$15 meV is totally absent in the $4TCH_3$@NT14 spectrum. This feature is associated to the methyl group libration and constitutes a powerful local probe of the direct environment of the $4TCH_3$ molecules as its frequency depends strongly on the symmetry of the local environment. The absence of a well defined libration mode in the $4TCH_3$@NT14 spectrum indicates the absence of well defined minima for the methyl group orientations, further reflecting the low symmetry of the local environment of the mH. The large variety of local potential from one molecule to another might increase the disorder effect and therefore helps to dilute the intensity of this mode over a large energy region. In addition, this observation proves the very good quality of the sample, in particular the absence of any residual unreacted crystallite of $4TCH_3$ in the samples studied.

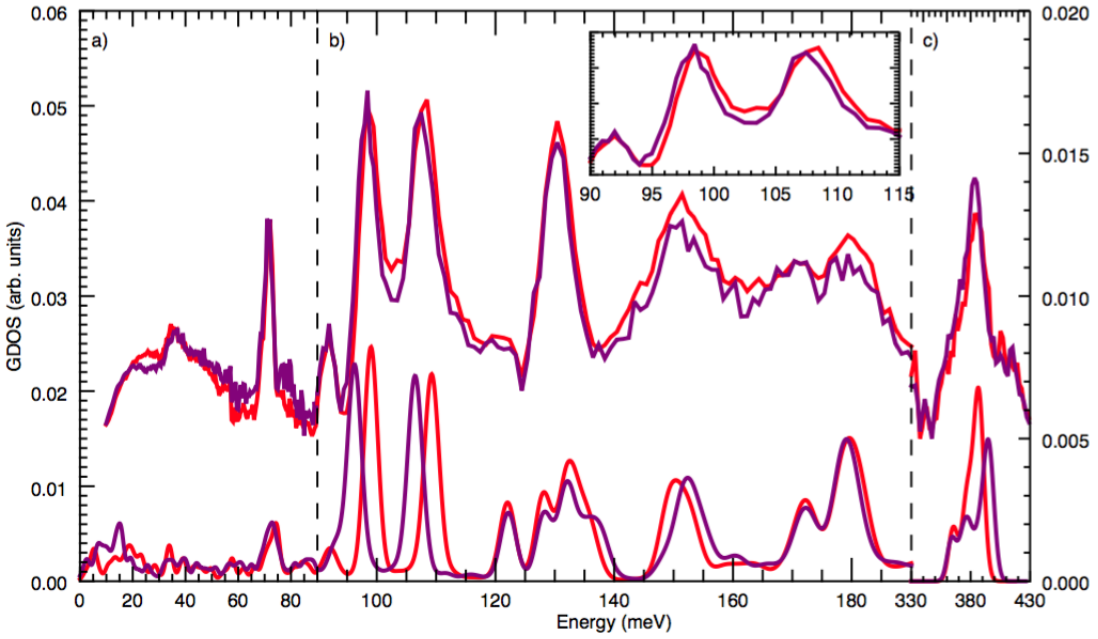

Figure 3.5 Comparison between the $4TCH_3$@NT14 (red line) and $4TCH_3$@NT09 (purple line) GDOS. calculations are shown at the bottom, with the same colour code. Experimental data measured at 2K.

In order to probe the effect of increasing confinement on the dynamics of the $4TCH_3$ molecule, we compare on figure 3.5 the GDOS obtained on $4TCH_3$@NT14 and $4TCH_3$@NT09. We also compare the data to the GDOS derived from the calculations performed on the hybrid models presented in section 3.3.3.

The calculations predict weak differences between the $4TCH_3$@NT14 and $4TCH_3$@NT09 GDOS. The latter mostly concern the stretching bands, the two most intense tH features at $\sim$100 and $\sim$110 meV, and the low frequency mH libration range below 20 meV: The stretching band of the $4TCH_3$@NT09 is calculated to be slightly deformed with regards to that of $4TCH_3$@NT14, with the component from the tH atoms being shifted to larger energies, indicating a stronger C-H bond for the thienylene H. By contrast, no difference in this spectral range are observe in the data. The tH modes in the 95 meV - 105 meV region involve out-of-plane bending of the thienylene C-H bonds. The calculations predict a significant shift of these modes (by $\sim$1.5 meV) from the $4TCH_3$@NT09, to bulk $4TCH_3$ and to $4TCH_3$@NT14, the modes being softer for the $4TCH_3$@NT09 model. In our model, the location of the molecules with regards to the nanotube edge (or center) for the hybrid systems varies significantly: the pressure exerted on the inner molecule, (perpendicular to its surface) by its surrounding environment is therefore significantly different and contribute to shift the bending modes frequencies apart from those calculated for individual $4TCH_3$. In particular,

the additional $4TCH_3$ molecule in the case of the $4TCH_3$@NT14 model modulates the local potential energy surface resulting in pushing its neighbour closer to the nanotube surface 3.4Å. This extra "positive" pressure hardens the tH bending modes with regards to that in the gas phase. By contrast, keeping the molecule at the center of the nanotube in the case of the $4TCH_3$@NT09 model has the consequence to soften these modes. This can be understood as a "negative" pressure effect, *i.e.* the tH being attracted by the nanotube wall at this position.

In the data, a slight shift is actually observed for these modes, in the same trend as that observed in the simulations, with a much weaker amplitude (see figure 3.5 inset). The much smaller shift observed ($\sim$1 meV) might indicate that the actual situation, especially for the $4TCH_3$@NT09 is slightly different in term of the structure, with inner molecules probably located off-centre and therefore closer to the nanotube inner surface, therefore reducing the pressure effect. This certainly also explains the lack of difference observed in the stretch mode region between the hybrid samples.

In the low frequency range (E < 30 meV), the models show also significant differences: the center of gravity of the GDOS is observed at $\sim$10 meV for the $4TCH_3$@NT09 model, while it is observed at larger frequency ($\sim$20 meV) for the $4TCH_3$@NT14 model. One could be tempted to claim that the same observation holds for the neutron data, as a crossover between the GDOS measured on the hybrid samples is observed at $\sim$ 15 meV. Above 30 meV, the simulations are identical, and this observation holds for the experimental data in this energy range. The C-H_{methyl}-π_{NT} interaction has been reported as one of the possible key factors in determining the configuration of $4TCH_3$ inside a nanotube [164]. In our results, the temperature behaviour of methyl libration presented below gives insights about this interaction.

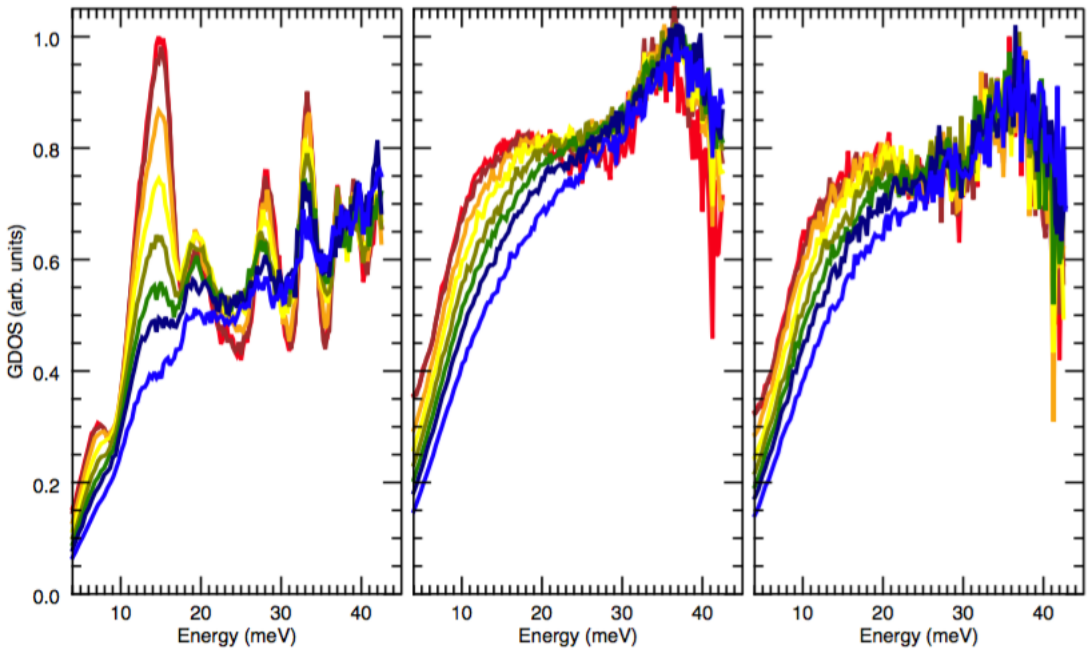

Figure 3.6 Temperature dependence of the low frequency region of the GDOS. **Left-hand side:** for the bulk $4TCH_3$, **Middle:** for the $4TCH_3$@NT14 sample and **Right-hand side:** for the $4TCH_3$@NT09 sample. Red, brown, orange, yellow, olive, green, navy and blue colours correspond respectively to 2 K, 25 K, 50 K, 75 K, 100 K, 125 K, 150 K and 250 K.

Temperature Dependence of the GDOS

Figure 3.6 shows the temperature dependence of the low frequency part of the GDOS for the three samples. They all show a very strong dependence with temperature and a progressive loss of intensity with increasing T. In particular, the methyl libration peak is progressively lost in the $4TCH_3$ data and the intensity of the peaks at higher energy are significantly damped. However, no peak shift nor broadening are clearly observed, ruling out large anharmonicity effects in this system. This observation suggests that the methyl rotation dynamics has progressively changed its character from a periodic time dependence to a relaxation, increasing the mobility of the mH atoms and therefore their intrinsic orientational disorder.

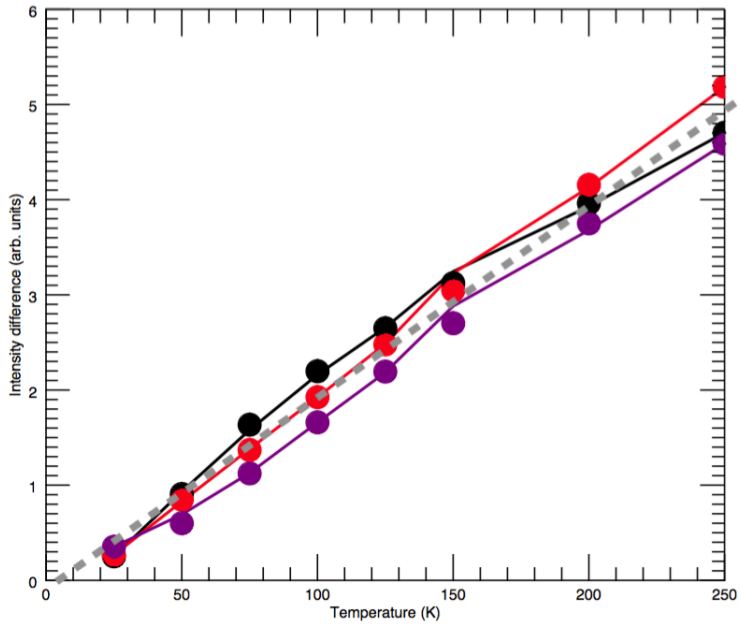

Figure 3.7 Integrated intensity of the difference spectra obtained by subtracting the data at T > 2 K from that at 2 K. black, red and purple lines correspond, respectively to $4TCH_3$, $4TCH_3$@NT14 and $4TCH_3$@NT09.

The first low frequency feature at ∼17 meV in the $4TCH_3$@NT14 and $4TCH_3$@NT09 data is also strongly T dependent and progressively looses its intensity with increasing temperature while the hump at 37 meV in both samples stays surprisingly unaffected. Figure 3.7 shows the integrated intensity of the difference spectra obtained by subtracting the data at T > 2 K from that at 2 K, the integration being performed between 4 and 25 meV, *i.e.* in the strongly T dependent zone of the data. A linear increase of the difference GDOS with T is observed for all samples, and with equivalent slope. This suggests that 1) the dynamics in this region is of very similar origin for all the systems studied in this paper and that 2) the energy barrier to overcome is equivalent in all samples. This barrier height is therefore established by the internal 4T backbone molecular field, while the precise local curvature of the potential, giving rise to the frequency scheme of the libration bands, is dictated by the external field. The librations GDOS therefore appears in the same frequency range but with a significantly different spectra distribution in this range, the temperature for orientational "melting" being the same.

3.3.5 Conclusion

The neutron scattering data presents a series of features sensitive at probing both the encapsulation and confinement effects on the dynamics of the inserted $4TCH_3$ molecules: The mH librations features indicate a large degree of orientational disorder in this system, associated to a low symmetry of their local environment. The not strong evolution in temperature could suggest a long-range ordering of the dye molecule that gradually takes place inside the nanotubes. By contrast, a progressive "melting" of the methyl rotations is observed with increasing temperature, in a similar way to that appearing in the bulk $4TCH_3$ phase. No significant evolution of the mH bending and stretching modes is observed on encapsulation, nor when the confinement is increased. This is coherent with our models for which the methyl end termination are oriented along the tube axis, *i.e.* with minimal interaction with the nanotube wall, whatever its diameter. By contrast, the tH out-of-plane bending modes frequencies show a significant variation with both encapsulation and confinement, hardening with increasing tube diameter. Based on our simulations, we interpreted this observation as the effect of molecule-tube interaction, suggesting that the molecules's cycles align parallel to the inner nanotube surface, *i.e.* minimising the C-H_{methyl}-π_{NT} interactions and maximizing $\pi_{thienylene}$-π_{NT} interactions.

In addition our data univocally prove the high degree of purity of the samples, the latter being free from crystalline unreacted $4TCH_3$.

Acknowledgements The authors acknowledge O. Meulien for technical support during the INS experiments, the Computing for Science group for numerical support and the ILL User Program for beam time allocation. ACLS acknowledges the ILL for financial support through the ILL PhD program.

Chapter 4

Study of the charge transfer between $4TCH_3$ and NTs

Contents

The structure of the $4TCH_3$@NT hybrid system as a function of the diameter of the nanotubes [105] has been discussed in the PhD thesis of Yann Almadori [124] et Anouar Belhboub [108]. The chapter 3 of this manuscript, has discussed the confinement effects which influence significantly the dynamics of the encapsulated oligothiophenes, which remains an open question. The present chapter is devoted to the study of the interactions between both sub-systems. We assess the following question: *"Is there any charge transfer or energy transfer?"*. Our approach to this problem is to couple DFT calculations and experimental spectroscopic investigations, combining photoluminescence and resonant Raman spectroscopy measurements. The photoluminescence measurements were performed in collaboration with the team of professor Guillaume Cassabois from University of Montpellier and with partnership with the team of professor Sébastien Lauret from University of Orsay. These results are correlated with calculated electronic density of states eDOS in collaboration with Patrick Hermet, from Charles Gerhardt Institute from the University of Montpellier.

I present this part of my work in the format of article. My contribution to it, besides the preparation of the samples was to study the interaction between both sub-systems by Raman spectroscopy. Before presenting the paper, I introduce the necessary information on Raman spectroscopy as a probe of charge transfer.

4.1 Resonant Raman spectroscopy as a probe of charge transfer

The *resonant character* of the Raman scattering process is related to the electronic structure of the carbon nanotubes. Therefore any change in the electronic structure of nanotubes may affect the resonance conditions. That is due to the sensitivity of LO and TO phonons to the electronic structure of SWCNTs near the Fermi level which affects the vibrational properties of nanotubes [78, 168, 169]. When carbon nanotubes are in interaction with an electron donor (n-doping) or acceptor molecules (p-doping), its Fermi level is upshifted for the former and downshifted for the later [170], see figure 4.1.

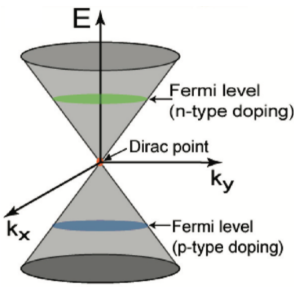

Figure 4.1 Dirac cone at the K point with the Fermi level shifted from the Dirac point, indicating the nature of doping: Fermi level upshift: n-type doping or Fermi level downshift: p-doping. Taken from reference [46].

That is therefore probed in the high frequency mode, the G band, where its intensity I, linewidth Γ and frequency shift ($\Delta\omega_G$) are affected upon charge transfer. That allows one to probe the electronic structure of the nanotubes by means of the modification undergone by the G band, once we can have access to the electronic structure of the nanotubes at the K point [107]. This total phonon shift can be separated into to contributions.

First contribution The first contribution $\Delta\omega_{EP}$ is due to the inter-band electron-phonon coupling [41]. A hardening of the phonons is exhibited due to non-adiabaticity, assigned to

movement of the Fermi level near the Dirac point. We will designate it as a energy phonon renormalization.

To illustrate this point, figure 4.2a shows pictorially the Dirac cone of a (non-doped) metallic nanotube for which the G mode (with energy $\hbar\omega_G$) excites an electron-hole pair. The decay of the phonon into the electron-hole pair gives rise to the broadening of the linewidth of the G mode, once the linewidth of the G band is related to the life-time of the LO phonon [171].

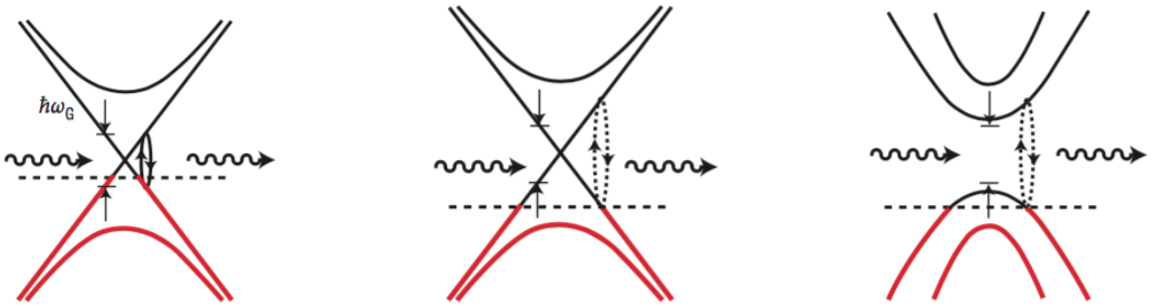

(a) Metallic nanotube where a real electron-hole pair can be excited by the phonon.

(b) Doped metallic nanotube where a virtual electron-hole pair can be excited by the phonon.

(c) Semiconducting nanotube where no electron-hole pair can be excited by the phonon.

Figure 4.2 Scattering mechanism for metallic, doped metallic and semiconducting nanotubes for which the G mode phonon can excite an electron-hole pair. Taken from reference [171].

Other example is a p-doped metallic nanotube, see its Dirac cone in figure 4.2b. The G mode excites a virtual electron-hole pair, which yields in the energy renormalization without any broadening of the linewidth. In this virtual process, the phonon renormalize the electron energies and the electrons renormalizes the phonon energy: the LO phonon of the carbon nanotubes couples with the continuum states and the electrons which are near the Fermi level. Upon doping or charging of intrinsic nanotubes, the energy renormalization becomes reduced as it has its maximum in intrinsic nanotubes [171]. At last, figure 4.2c shows the valence band and conduction bands of a semiconducting nanotube. The phonon energy is smaller than the energy gap of this nanotube, so that no real electron-hole pairs can be created and the energy is renormalized and the linewidth remains unchanged [171].

The electron-phonon coupling gives rise, therefore, to the controllable modification of the G band frequency $\Delta\omega_G$ as a function of the electron-phonon coupling [171].

$$\hbar\omega_\lambda = \hbar\omega_\lambda^{(0)} + \hbar\omega_\lambda^{(2)}, \text{ where } \lambda = LO, iTO \tag{4.1}$$

$\omega_\lambda^{(0)}$ is the frequency without any EPC interaction and $\hbar\omega_\lambda^{(2)}$ is obtained by the term given by the second-order perturbation theory:

$$\hbar\omega_\lambda^{(2)} = 2\sum_k \frac{|\langle eh(\vec{k}) \mid \mathscr{H}_{int} \mid \omega_\lambda \rangle|}{\hbar\omega_\lambda^{(0)} - (E_e(\vec{k}) - E_h(\vec{k})) + i\Gamma_\lambda} [f(E_h(\vec{k} - E_F) - f(E_e(\vec{k} - E_F))], \tag{4.2}$$

where 2 comes from the spin degeneracy, the term $\langle eh(\vec{k}) \mid \mathscr{H}_{int} \mid \omega_\lambda \rangle$ is the matrix element corresponding to the creation of an electron-hole pair at momentum $\vec{k}$ by the EPC with q=0 phonon, $E_e(\tilde{k})$ and $E_h(\tilde{k})$ are the electron and hole energy, respectively, and E_F is the Fermi energy.

Second contribution One can notice that this energy phonon renormalization occurs when the energies of the phonon and the optical gap are comparable, *e.g.* for a large diameter semiconducting nanotube (bandgap varies as $1/d$) [171] and metallic nanotubes. This renormalization of the phonon energy of the G band corresponds always to an upshift of the G band [107].

The frequency shift $\Delta\omega_G$ of the G band of SWCNTs also depends on the force constant of the C-C bond [172]. Electron doping leads to the filling of antibonding states which results in the weakening of the C-C bonds, leading to a specific shift ($\Delta\omega_G$), specific of the lattice effect. As a consequence, softening the G mode frequency. Conversely, the p-doping of nanotubes strengthens the C-C bonds thus upshifting the G mode.

Concerning the Raman intensity of the G band, is controlled by the electron-phonon coupling [171] and it is attenuated by a weakening of the resonance effect [107]. Therefore, the total phonon shift can be separated into the contribution of the lattice (force constants) and a contribution due to non-adiabatic effects. $\Delta\omega_G = \Delta\omega_e + \Delta\omega_{EP}$, where $\Delta\omega_{EP}$ is always positive and in our case, $\Delta\omega_e$ can be negative (n-doping).

As an illustration of the phenomenon described above, we present briefly the results of Kalbac and collaborators who have reported a study of the G^+ band of individual semiconducting nanotubes probed with electrochemical charging [107]. The figure 4.3 shows the Raman shift for the G band of small to large nanotube diameters for both negative and positive potentials.

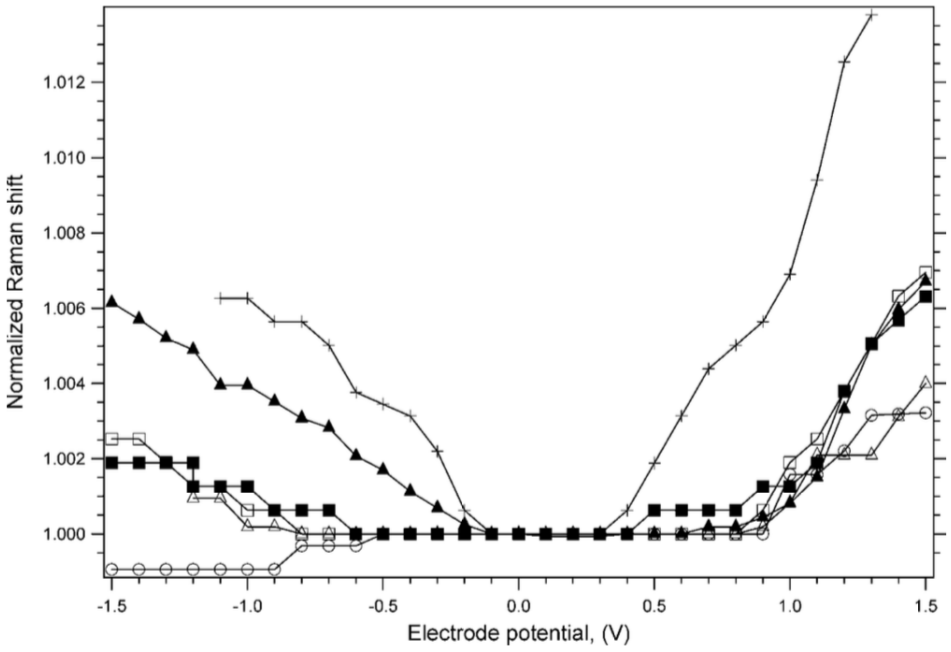

Figure 4.3 Relative G band frequency as a function of the electrode potential (-1.5 to +1.5 V) for five different RBM positions: empty circles (175 cm^{-1}, 13.7 Å); empty triangles (145 cm^{-1}, Å); empty squares 135 cm^{-1}, filled squares 135 cm^{-1}; filled triangles 125 cm^{-1} and crosses 120 cm^{-1}. The spectra were excited by different laser energy excitations: 2.03 eV, 2.33 eV, 1.70 eV, 1.68 eV, 1.62 eV and 1.72 eV, respectively. Take from reference [107].

For negative electrochemical potentials, electrons are injected in the nanotubes, upshifting the Fermi level. As a consequence, the G band of small diameter nanotube is downshifted whereas it upshifts for large diameter nanotubes. For positive potentials, electrons are drawn from nanotubes, downshifting the Fermi level so that the G band of both nanotubes upshifted. The behaviour of the small nanotube diameter is understood by means of the strength of the C-C bond, as discussed previously in this manuscript. However, for large nanotube diameters, the G band upshifts no matter the type of doping. Due to the phonon renormalization energy, the G band of large nanotubes diameter always upshifts. In agreement with that, Tsang [171] has reported that the renormalization is strong for large nanotubes and weak for small nanotube diameter. Therefore, for negative charging, eventhough the G band is supposed to downshift due to the softening of the C-C force constants, the renormalization is stronger than the doping effect as the diameter is larger.

Summary of the behavior of the G band of nanotubes upon the two effects: doping and renormalization of the phonon energy

n-doping Causes the filling of π^* anti-bonding orbitals, which results in the weakening of the force constant of the C-C bond. As a consequence, the G band is downshifted [172].

p-doping Causes the emptying of π bonding orbitals, which results in the strengthening of the force constant of the C-C bond. As a consequence, the G band is upshifted [172].

Renormalization of the phonon energy the larger the nanotube diameter, the stronger is the renormalization of the phonon energy [171].

Metallic nanotube The G band upshifts and narrows its linewidth [171].

Semiconducting nanotube The G band may up/downshift however its linewidth do not change [171].

Small nanotube diameter The doping effect is stronger rather than the renormalization effect, therefore, depending on the doping, the G band may have a upshift (p-doping) or a downshift (n-doping) [107].

Large nanotube diameter The renormalization effect is stronger than either n- or p-doping on the nanotubes, therefore the G band is expected to have an upshift of its frequency [107].

4.2 Article: Modulating single-walled carbon nanotube opto-electronic properties by chromophore confinement

Abstract: Opto-electronic properties of single-walled carbon nanotubes can be significantly modified by chromophore confinement into their hollow core. This study deals with quaterthiophene derivatives encapsulated inside carbon nanotubes displaying different diameter distributions. We report a significant electron transfer from the confined molecules to the nanotubes in our hybrid systems, evidenced by photoluminescence and Raman investigations. This charge transfer leads to an important enhancement of the photoluminescence intensity

by a factor of nearly five depending on the tube diameter. Energy shifts observed on emission on the hybrid system also depend on the nanotube diameters and are interpreted in terms of local structure of the confined molecules. The Raman G band of hybrid systems exhibits a drop in intensity and significant shifts which magnitude and direction strongly depend on the nanotube diameter. These behaviours are consistent with an electron transfer from the molecule to the tube, in good agreement with the PL analysis. In addition, close to the molecule resonance, the magnitude of the G band shifts is modified and the intensity loss is amplified, strongly suggesting a photo-induced electron transfer. Finally, the Breit-Wigner-Fano line-shape (characteristic of electron-phonon coupling) of the Raman G band is strongly reduced for defective metallic nanotubes. After dye encapsulation, this peculiar profile is recovered, suggesting a strengthening of the electron-phonon coupling. Thus, confinement species into nanotubes allow moving the Fermi level and consequently to monitor their opto-electronic properties.

4.2.1 Introduction

Single-walled carbon nanotubes (SWCNTs) have a wide range of potential applications including molecular electronics, photonics and beyond, owing to their unique structural and electronic properties. However, various outstanding issues still need to be resolved before SWCNT-based devices can be made. In particular, large-scale, air-stable and controlled doping is highly desirable and optical properties in the visible domain are needed. The possibility of encapsulation of various molecules opens wide route enabling precise and controlled modification of additional SWCNT/guest complex properties for applications, and for the generation of highly constrained 1D materials in pores of sub-Angstrom controllable diameter.

Such hybrid nanotubes after encapsulation of organic molecules present different potential advantages for nano-optoelectronics applications. One particular feature of the organic molecules is their ability to emit light in the visible range of the spectrum. This provides new opportunities for nano-devices because pure carbon nanotubes are Infrared emitters, while being passive in the visible range [39, 100]. They also allow modulating the carrier density of the SWCNT, performing air-stable amphoteric doping on SWCNTs by encapsulation of organic molecules inside SWCNTs [31, 157] which is a key point for the production of air-stable n-type SWCNT is required for field-effect transistors [31, 39, 93, 157].

In this Framework, significant efforts have been performed to elaborate and study the physical properties of hybrid nanotubes obtained after encapsulation of oligothiophene (oT) named in the following oT@SWCNTs. α-Oligothiophenes are electron-rich and chemically stable conjugated oligomers, renowned for their optoelectronic properties [32–

35]. Likewise, their tunable size and linear conformation make them good candidates as guest molecules for hybrid nanotubes. A 1D geometrical confinement effect on oligothiophene structural properties has been both theoretically and experimentally demonstrated. The supramolecular organization of the confined oligothiophenes is shown to depend on the nano-container size [36, 105] and lead to Giant Raman scattering due to J-aggregation [106]. Photoluminescence (PL) emission in the visible spectral range of oT@SWCNTs have been also shown [36, 160]. Concerning the interactions between oT and nanotubes, previous DFT calculations report van der Waals interaction as the bonding mechanism between the nanotube and the encapsulated molecule [39]. No specific dependences of the results with the length of the oT was shown [39]. Nevertheless, other studies on different dyes, including oT, inside SWCNTs reported efficient fluorescence quenching by the SWCNTs, this effect being seen in weakly bonded chromophore-SWCNT complexes [106]. For small tubes (below 10 Å of diameter), experimental results show also evidence of a significant positive charge transfer (CT) on the inserted oligothiophene in agreement with Raman behaviour of the G band of oT@SWCNTs [37].

One can notice that DFT calculations predict the appearance of a tiny CT when the diameter of the tube is reduced below 10 Å [100]. The debate concerning the different interactions reported in the literature could be related to the dependence of the supramolecular organization of the confined oligothiophenes with the tube diameter. Below 11 Å, critical nanotube diameter Φ_C, only one molecule is encapsulated in its hollow core. Between 11 and 16 Å nanotube diameter, two oligothiophene molecules are confined. Above 16 Å tube diameter, three molecules are inserted [36, 105]. For small nanotube, preferential interaction between the edge of the molecule and the nanotube inner wall is expected whereas nanotube wall - plane of the molecule preferentially are expected to interact preferentially for bigger tubes (tube diameter between 14 and 16 Å). DFT calculations also indicate that indicate that $4TCH_3$-oligomers inside a nanotube are attracted through both C-$H_{thienylene}$-π_{NT} and $\pi_{thienylene}$-π_{NT} and C-H_{methyl}-π_{NT} interactions. The $4TCH_3$-oligomer structure being deformed to match the inner wall of the nanotube to maximize these attractive host-guest interactions [164]. Internal thiophene prefer to be located near the walls of the tubes rather than at their center when possible. In the case of small nanotubes below Φ_C, preferential interactions C-$H_{thienylene}$-π_{NT} and C-H_{methyl} and $S_{thienylene}$-π_{NT} interactions are expected (oT being localized preferentially near the center of the internal cavity) whereas all interactions are possible for tubes above Φ_C.

In the previous experimental studies no dependency of the interactions between the tubes and the encapsulated oT as the function of the size of the nano-container was carried out.

As a result, an interesting question is whether a significant interaction occurs after oligothiophene encapsulation in SWCNT depending on the tube diameter. To elucidate the nature of the confinement effect, we address in this article the following issues:

- How does the size of the nano-container influences the interactions between inserted oligothiophenes and the nanotube?
- Does the variation on the confinement effect influence energy transfer between oT and the nanotube?
- Is there any charge transfer between the oT guest and the nanotube dependent of the nanotube diameter?
- Is there any photo-induced behaviour?
- Is there any structural environments specific of the interactions between the two subsystems after 1D confinement?

To address this question, we present here a combined photoluminescence and Raman studies of the confinement dimethyl-quaterthiophene ($4TCH_3$) in single-walled carbon nanotubes ($4TCH_3$@NT).

4.2.2 Experimental

Sample Preparation

Four sources of nanotubes have been used in this study: commercial electric arc single-walled carbon nanotubes (12 Å < d < 16 Å), provided by Carbon Solution [65] and called NT14 in the following; carbon nanotubes synthesized by the eDIPS method [116] (16 Å < d < 20 Å) (NT17 in the following); and CoMoCAT carbon nanotubes enriched in (7,6) nanotubes (6 Å < d < 10 Å) [121], called NT09 in the following. Carbon Solution, and CoMoCAT nanotubes were purified by air oxidation and subsequently treated to remove the catalysts.

The eDIPS nanotubes were purified according to the following protocol: 20 mg of raw SWCNT material was sonicated in nitric acid (35 vol%, 150 mL) with a sonic bath (160W max) (100% for 5 min and then 40% for 15 min) and then heated at 100 °C for 5h. The suspension was then cooled and vacuum-filtered through a PTFE membrane (Sartorius, 0.2μm). While pursuing vacuum filtration, the thick SWCNT layer formed on the filtration membrane (buckypaper) was washed by 200 mL of deionized water; the pH was monitored during the washing and was about 7 at the end of the process. The nanotubes were redispersed in NaOH (1M, 100 mL) using the sonic bath (100% for 10 min) and then filtered through

a PTFE membrane and washed with 1M of NaOH, deionized water, and then 1M of HCl followed by deionized water until the filtrate was neutral. Finally, the bucky paper was redispersed in hydrogen peroxide (30%, 150mL) using the sonic bath (100% for 5 min and then 40% for 10 min). The suspension was heated at 100 °C for 1 h, cooled down at room temperature, and then vacuum-filtered through a PTFE membrane. The nanotubes were washed by 200 mL of deionized water and then dried at 50 °C under high vacuum. The overall yield of the purification process was 60% (12 mg).

Encapsulation of $4TCH_3$ into carbon nanotubes was performed using the vapor reaction method previously described [37]. Before the encapsulation treatment, carbon nanotubes were outgassed at 300 °*C* for 48 h. Then, nanotubes were mixed with $4TCH_3$ in the weight ratio ${}^{wNTs}/_{w4TCH_3} = 0.5$ in the glovebox and outgassed under 2×10^{-6} mbar at ambient temperature for 1 h. Then, nanotubes with $4TCH_3$ were sealed in glass tube at 2×10^{-6} mbar and heated to 250 °*C* for 72 h. The sublimation step was then performed. The sample was then washed with organic solvent and stored in the oven at 120 °C for 24h. The hybrid material is named $4TCH_3$@NT in the following.

Raman Spectroscopy

Micro Raman experiments have been performed on a triple monochromator spectrometer (Jobin Yvon T64000), equipped with a charge-coupled detector, in a backscattering geometry, using the fixed 457.9, 488.0, 514.5, 532, 568.2, and 647.1 nm excitation wavelengths and a Ti-Sapphire tunable source in the near-infrared region. The spot size is around a few micrometers in diameter, probing an ensemble of nanotubes.

Raman spectra in the UV range (364 nm) were acquired with a Dilor spectrometer (UV). In order to prevent the heating of the tubes and oligomers, the laser power was adjusted at 100μW with a spot diameter of about 3μm using a 50$\times$ objective (40$\times$ in the UV range). The resolution is about 2 cm^{-1}. At least four spatially separated area of each sample were probe to ensure homogeneity.

In order to prevent the heating of the tubes and oligomers, the laser power was adjusted at 100 μW with a spot diameter of about 3M using a 50$\times$ objective. The resolution is about 2 cm^{-1}. At least four spatially separated area of each sample were probe to ensure homogeneity.

HR-TEM and SR-EELS

$4TCH_3$@NT samples were dispersed in n-hexane by ultrasonication, and dropped onto molybdenum microgrids coated with holey amorphous carbon films for analyses by High-

resolution transmission electron microscopy (HR-TEM) and scanning TEM (STEM). A JEOL JEM-2100F electron microscope equipped with double JEOL Delta spherical aberration correctors was operated at an electron accelerating voltage of 60 kV for (S)TEM observation. Spatial-resolved Electron energy-loss spectroscopy (SR-EELS) and energy dispersive X-ray spectroscopy (EDS) measurements were carried out using a Gatan Quantum electron spectrometer and double JEOL Centurio detectors, respectively, attached to the microscope. Elemental distributions of carbon and sulphur in individual SWCNTs were determined based on the intensities of their K and L edges, respectively, at each measured point in the scanned areas by STEM-EELS chemical mapping.

Photoluminescence spectroscopy

Photoluminescence Excitation (PLE) spectroscopy was performed using an home-made μ-PL setup. The output of a Xe lamp was monochromated an focalised on the sample with microscope objective (50×, N.A.=0.5). The emitted PL was collected by the same objective, and the direct excitation light rejected by a dichroic beam splitter and a longpass filter. PL is recorded with a 320mm spectrometer and 150 lines/mm grating, and detection is performed by a nitrogen-cooled 512 pixel linear InGaAs array. Pristine and encapsulated NT were suspended in aqueous solvent using deoxycholate (DOC) surfactant. In this configuration, spot size is $\sim$10 μm, probing an ensemble of nanotubes.

Computational details

Electronic density-of-states are calculated within the formalism of the density functional theory (DFT). We use the SIESTA package [165] and the generalized gradient approximation to the exchange correlation functional as proposed by Perdew, Burke and Ernzerhof [166]. Core electrons are replaced by nonlocal norm-conserving pseudopotentials. The valence electrons are described by a double-z singly polarized basis set. The localization of the basis is controlled by an energy shift of 50 meV. Real space integration is performed on a regular grid corresponding to a plane-wave cutoff of 300 Ry. Van der Waals corrections (DFT-D) between the nanotube and the molecule are considered using the semi-empirical dispersion potentiel parametrized by Grimme [167]. We considered four model systems : $4TCH_3$@(11,0), $4TCH_3$@(13,0), $4TCH_3$@(17,0) and $4TCH_3$@(19,0). In the first two systems, only one dimethyl-quaterthiophene ($4TCH_3$) molecule is placed inside the nanotube whereas in the last two systems two molecules are placed inside the nanotube. The initial position of the $4TCH_3$ molecule(s) is chosen according to the energy minimization performed by Loi et al. [36]. We fix the nanotube length to 29.82 Å (seven unit cells) to accommodate the

length of the dimethyl-quaterthiophene. A vacuum size of 11 Å is used to avoid interactions between adjacent tubes. Atomic positions were relaxed using a conjugate gradient until the maximum residual atomic force was smaller than 0.02 eV/Å. The electronic density-of-states (eDOS) are obtained considering 33 K-points along the nanotube axis.

4.2.3 Results and discussion:

HR-TEM and HR-EELS results

STEM-EELS studies were performed on all the hybrid nanotubes under investigation. We present the results for NT09 nanotubes, similar results are obtained for hybrid NT14 and NT17 nanotubes. Figure 4.4a, 4.4b, 4.4c corresponds to HR-TEM micrographs of $4TCH_3$@NT09. They clearly display SWCNTs filled with presumably $4TCH_3$. In order to go further in the analysis of these materials and to know where the $4TCH_3$ molecules are localized, SR-EELS experiments were carried out. This technique is a very powerful tool to investigate such nano-materials at the (sub)nanometer scale [173].

Figures 4.4c show two EEL spectra recorded in the areas marked in figure 4.4c. The energy loss near-edge feature (ELNES) of the C-K edge consists of a π^* peak at ∼285eV and a well-defined σ^* band starting at ∼292eV [173–177]. The S-$L_{2,3}$ edge consist of a rather large peak around 165-220 eV. Carbon K edge at ∼284 eV is present in both of these two EEL spectra. The $L_{2,3}$ edge of sulphur is clearly visible in Figure 4.4 (e). The marked area in HR-TEM micrographs in Figure 4.4a, 4.4b, 4.4c correspond to domains where chemical imaging is performed. Chemical maps of carbon and sulphur have been extracted from intensities of Carbon K edge and $L_{2,3}$ edge of sulphur. It appears that sulphur (from $4TCH_3$) is not surrounding the nanotubes but mainly localized within the hollow core of the tubes giving thus insights on the quality of the encapsulation procedure.

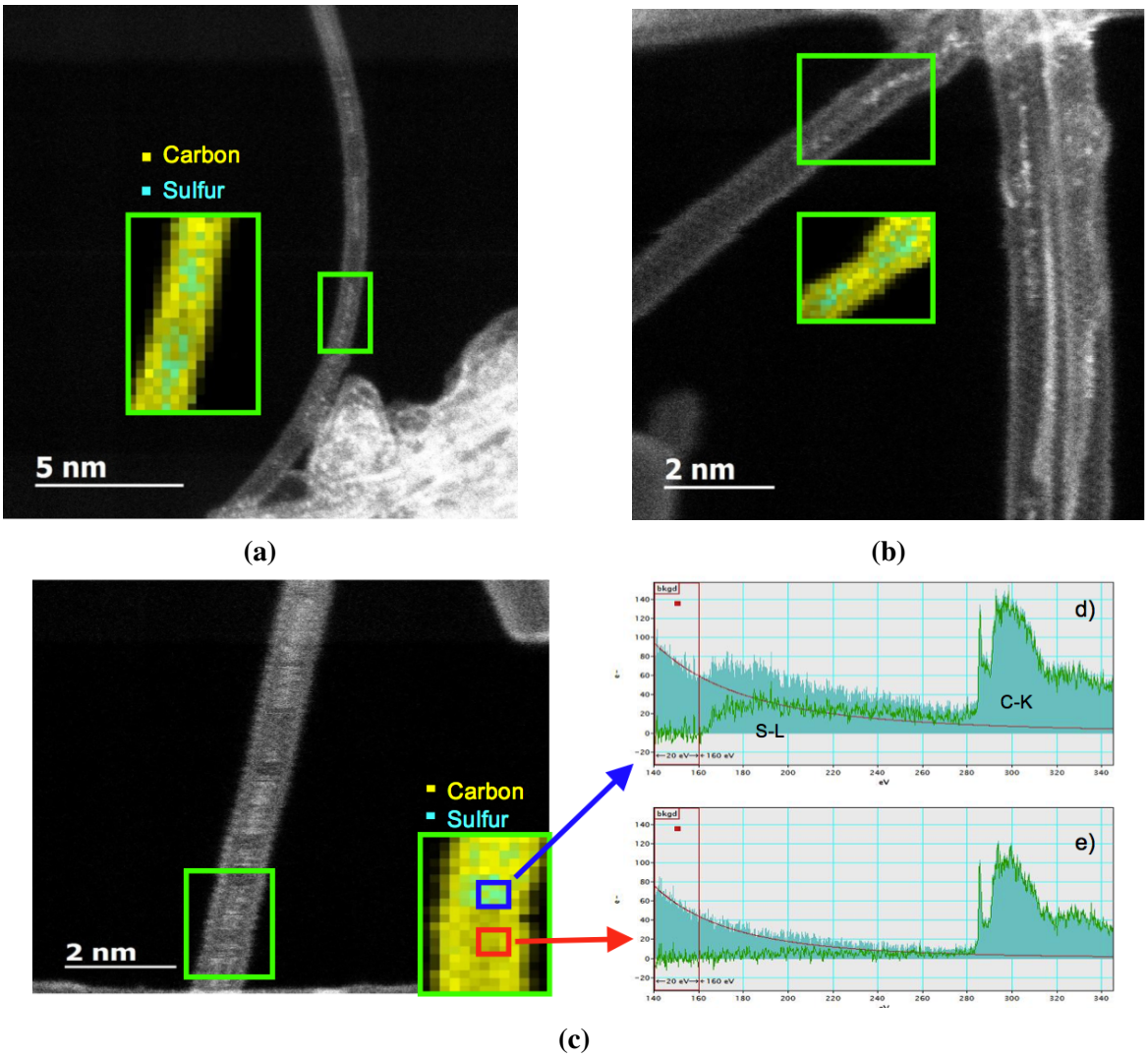

Figure 4.4 HRTEM micrograph of a $4TCH_3$@SWCNT nanotubes and superimposed carbon (yellow) and sulphur (green) elemental maps. Two EEL spectra extracted from the marked areas showing K edge of carbon (∼284eV) and $L_{2,3}$ edge of sulphur (∼165-220eV) only in **(e)**.

Photoluminescence measurements

Figure 4.5 exhibits the photoluminescence (PL) excitation maps of both pristine NT09 (figure 4.5a) and hybrid $4TCH_3$@NT09 (figure 4.5b). Red and black symbols on figure 4.5b represent the peak positions of the pristine nanotube. After $4TCH_3$ encapsulation, both the absorption (E_{22} NT electronic transition) and emission (E_{11} electronic NT transition) energies are shifted. In addition, significant increase of the photoluminescence intensity is

observed. The shifts generally arise from two different origins which are mechanical strain and electronic effects.

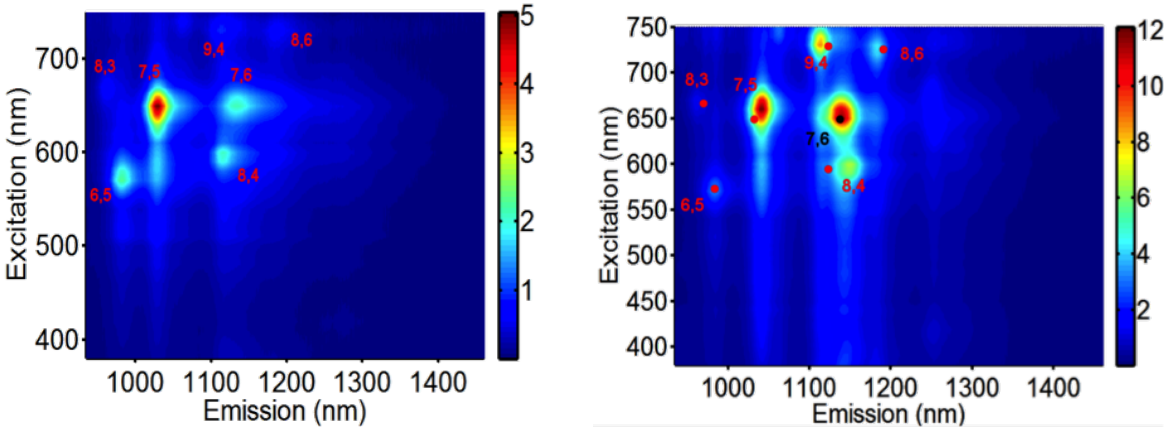

Figure 4.5 PL excitation maps of **(a)** NT09; **(b)** $4TCH_3$@NT09.

It turns out that mechanical strain leads to energy shifts in opposite directions for the E_{11} and E_{22} transitions so that by calculating the difference and the sum of the shifts we can separate the two contributions [178]. Figure 4.6 exhibits the results obtained for our small diameter tubes. We can clearly identify two distinct behaviours, considering that the (6,5) nanotube is probably empty because of its narrow diameter preventing molecule encapsulation.

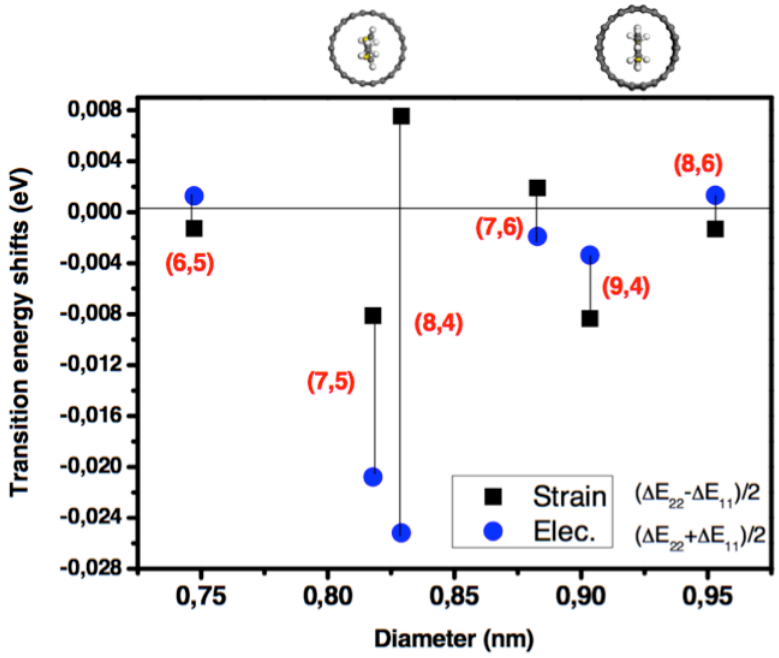

Figure 4.6 Mechanical and electronic contributions of the PL energy shifts for $4TCH_3$@NT09 with respect to NT09.

The (7,5) and (8,4) nanotubes undergo both mechanical strain and electronic effects whereas larger diameter tubes (from (7,6) to (8,6)) display rather small shifts indicating no important changes with respect to the empty nanotubes. These behaviours are very reasonably assigned to the local structures predicted from DFT calculations and illustrated by two schemes above figure 4.6. For small diameter tubes (below 8.6 Å corresponding to minimum diameter matching $4TCH_3$ molecule size + twice the carbon van der Waals radius), the 4T molecule is incorporated but induces important constrains on the nanotube and lead to strong mechanical strains. In contrast, on large diameter tubes, the molecules is located at the center of the tube with only weak mechanical constrains [36].

Figure 4.7 displays the PL intensity ratio between the hybrid and pristine nano-systems versus the nanotube diameters. This plot evidences a kind monotonic dependence of the intensity with the nanotube diameter up to an optimized diameter and then a drop. A similar diameter dependence of the PL intensity was already observed when nanotubes undergo a strong electric field [179]. Large diameter tubes with small bandgap would be more altered as their exciton binding energy is reduced. In our case, the increase of the intensity can be explained by a weak electron transfer from the confined $4TCH_3$ molecule to the nanotube as observed for ferrocene encapsulation [180], compensating the natural p-type doping of pristine nanotubes due to curvature [181], defects, oxygen adsorption. Thus, the charge

transfer moves back the Fermi level, increasing the PL efficiency when the size of the nano-container increases. The maximum PL intensity is reached an optimised tube diameter, here (9,4). The following drop can be interpreted with two hypothesis (1) a progressive negative charge transfer from 4T after natural p doping compensation; (2) a change of chromophore environment, oT preferring to be closer to a tube wall than the center of the cavity when it is possible.

The drop thus, PL spectroscopy can allow to probe the hybrid nano-systems local structure. Molecule confinement increases the PL efficiency by a significant electron transfer onto the nanotube.

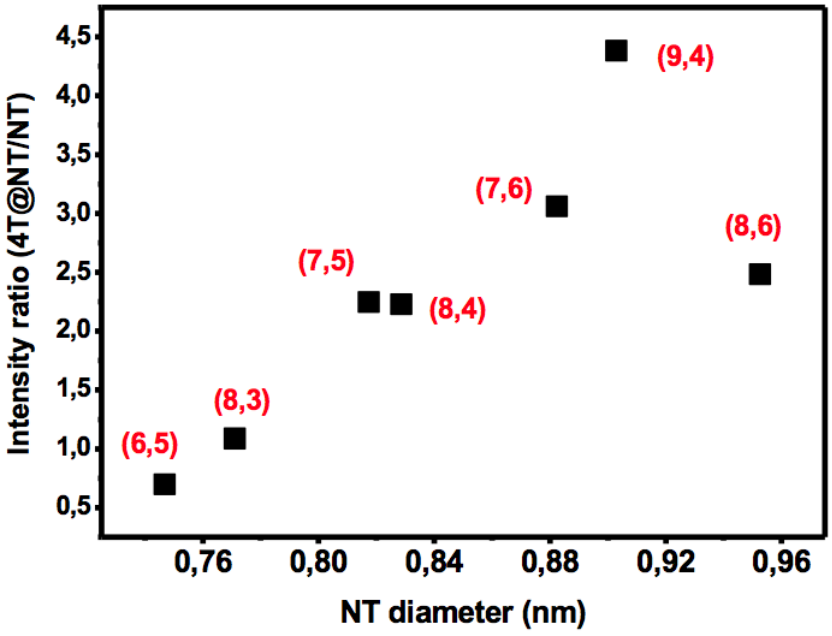

Figure 4.7 PL intensity ratio between $4TCH_3$@NT09 and NT09 nano-systems as a function of NT diameters

Raman measurements

The Raman G band is also a very sensitive probe to detect weak charge transfer on nanotubes. Indeed, a n or p-type doping leads to a change in the force constants in the carbon lattice, leading respectively to a downshift or an upshift. Furthermore, for nanotubes exhibiting no or small bandgap (large diameter), an electron-phonon coupling, involving the tangential modes and described as the creation of an electron-hole pair by a phonon, takes place in metallic (Kohn Anomaly) and large semiconducting tubes (renormalization effect), causing a decrease in the vibration frequency [82, 171]. This energy change is calculated in time-dependent

perturbation theory. Considering the Heisenberg uncertainty principle, the annihilation of the phonon reduces its life time and therefore increases the energy uncertainty, leading to broadening of the peaks. The effect on our hybrid nanotubes remains weak but here macroscopic samples are studied. Under charge transfer, the Fermi level shifts, preventing an electron-hole pair creation as the conduction band is already occupied or the valence band is depopulated [82, 171]. The electron-phonon coupling becomes much lower, inducing a significant upshift of the G band. Furthermore, as the phonon lifetime increases, the width of the Raman peak is reduced. Therefore, the measurement of the position and width of a Raman G mode provide reliable information on the charge transfer.

Figure 4.8 displays the Raman high energy modes of the pristine nanotube (black curves) and hybrid $4TCH_3$@NT nano-systems (blue curves) for two different diameters (NT14 and NT17) measured at different excitation wavelengths. The spectra display the G band of the nanotubes and the C-C stretching vibrations of the confined $4TCH_3$. The spectra are not normalized and the G band clearly shows a loss in intensity after encapsulation. The magnitude of the loss looks more important at small wavelengths, when the laser energy roughly matches the absorption energy of the confined molecules.

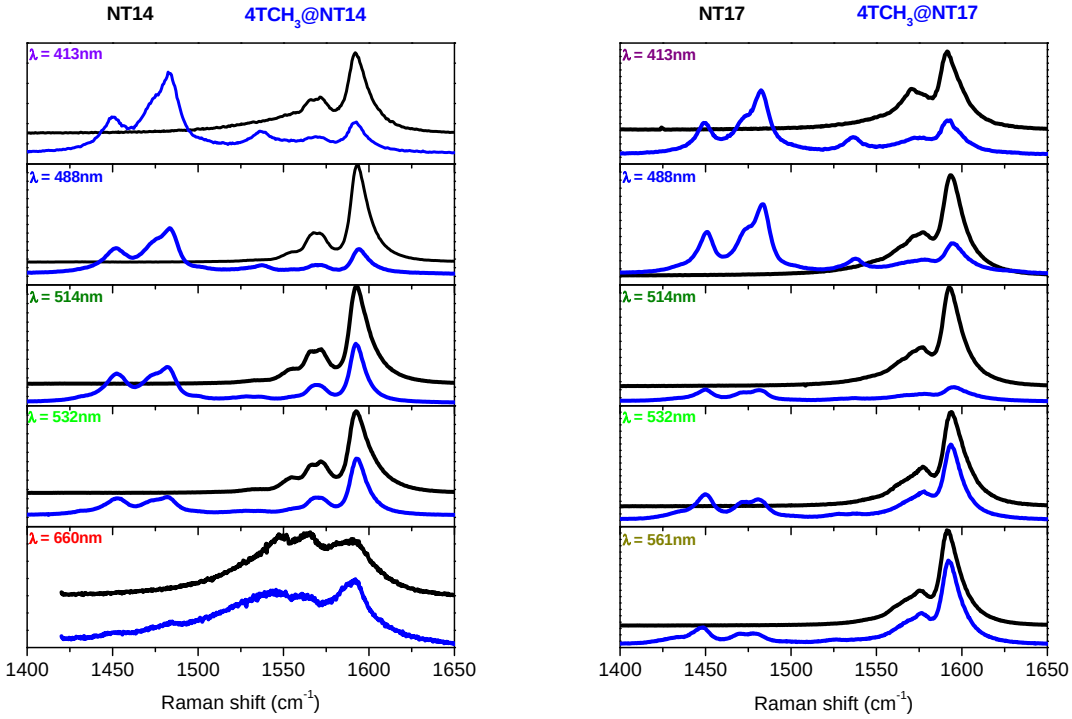

Figure 4.8 Raman high energy modes of the pristine (black) and hybrid (blue) **(a)** NT14 and **(b)** NT17.

Figure 4.9 exhibits four examples of enlarged Raman spectra around 1600 cm^{-1} in order to analyse the G^+ band behaviour which is very sensitive to doping. All spectra clearly show a G^+ band shift which magnitude and direction depend on the nano-system under investigation.

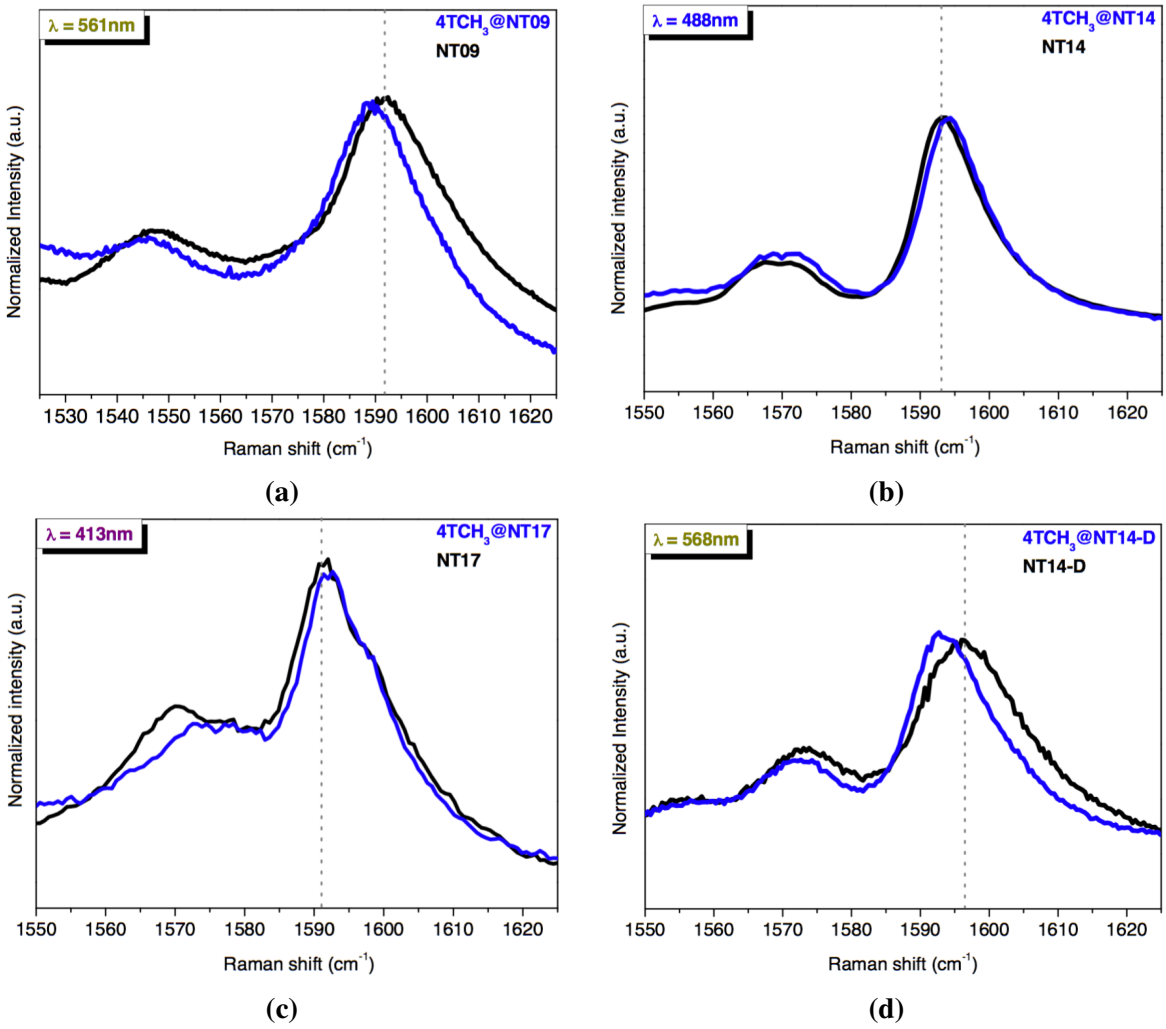

Figure 4.9 Raman spectra of pristine and hybrid nanotubes **(a)** NT09 and $4TCH_3$@NT09 (λ = 561 nm); **(b)** NT14 and $4TCH_3$@NT14 (λ=488 nm); **(c)** NT17 and $4TCH_3$@NT17 (λ = 413 nm); **(d)** NT14-D and $4TCH_3$@NT14 – D (λ = 568 nm).

According to these examples, the Raman G^+ shift depends on the nanotube diameter and on the excitation wavelength. The magnitudes of the shifts for all the nano-systems under investigations and for all the laser excitation available are summarized on figure 4.10.

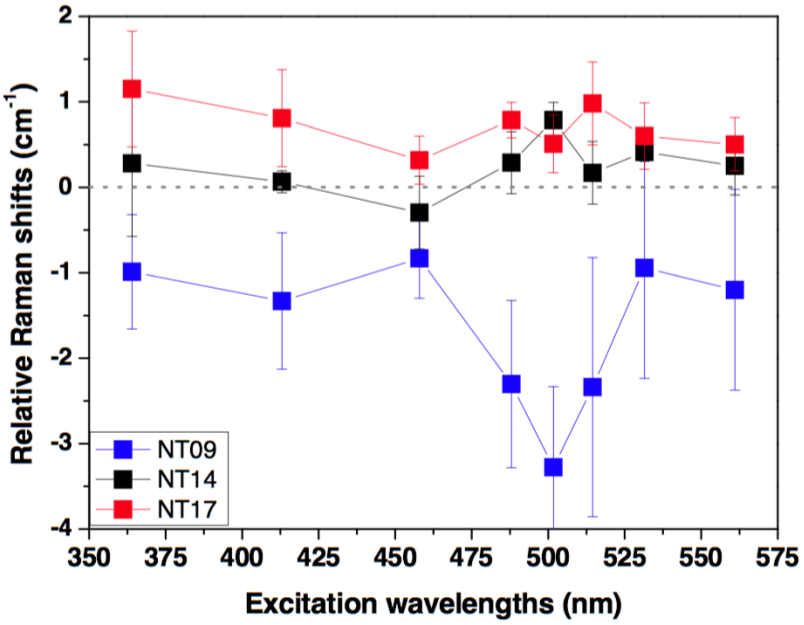

(a)

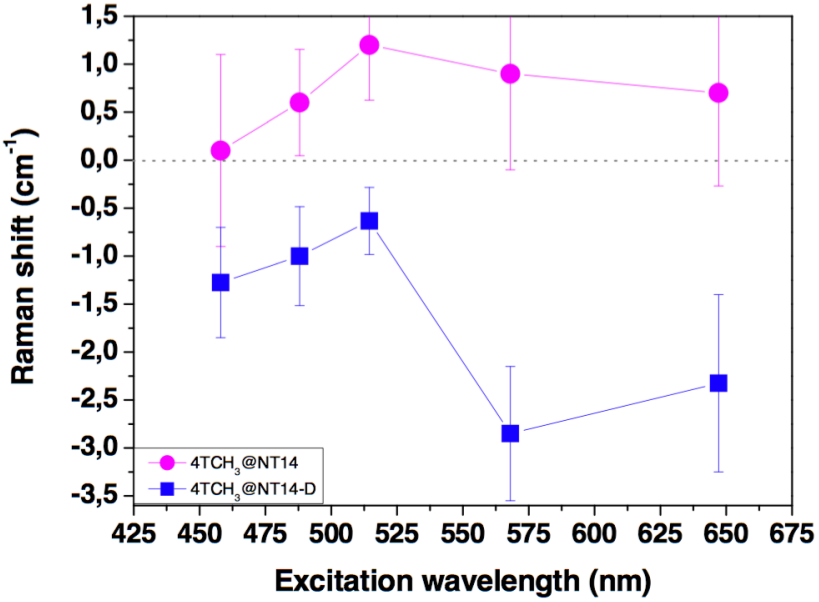

(b)

Figure 4.10 Raman G band shifts as a function of the excitation wavelength for **(a)** three different nanotube diameter NT17 (red), NT14 (black) and NT09 (blue); **(b)** $4TCH_3$@NT14 (magenta) and defected $4TCH_3$@NT14-D (blue) nanotubes.

We can observe two obvious different behaviours depending on the nanotube diameters. For large diameter tubes (>13 Å), a positive shift after encapsulation is observed, roughly

constant around 1 cm^{-1}. In contrast, for narrower diameter tubes (<10 Å), a non-monotonous downshift is observed. Both behaviours, can be explained by a charge transfer between the confined molecules and the nanotube walls in the framework of the phonon energy renormalization (upshift) and weakening of the lattice force constants due to electron doping (downshift). The renormalization occurs when the energies of the phonon and the optical gap are comparable, *i.e.* for large diameter semiconducting tubes (as a bandgap varies as $1/d$) and metallic ones. This coupling is an annihilation of phonon which energy is transferred to an electron, giving rise to an electron-hole pair.

After charge transfer, the Fermi level shifts, strongly reducing this coupling for large diameter tubes and leading to an increase of the phonon energy competing with lattice force constant effect. In contrast, for small diameter tubes (with large bandgap), this coupling no longer exists. Therefore, a charge transfer leads only to a softening of the vibrations, leading to downshift of the Raman modes.

Another striking point is the amplification of the downshift for small diameter nanotubes excited with blue or green excitation wavelengths. As the optical absorption of the confined molecules lies in this electromagnetic range (see figure 4.8 spectra around the molecule absorption (488 nm), we can reasonably assume a photo-induced charge transfer. Thus, an electron-hole pair is created on the encapsulated molecule and the electron is then transferred onto the nanotube. This behaviour strongly suggests a different interaction between the molecules and the nanotubes depending on the diameter as the phenomenon is not observed for large diameter tubes. This result could be the consequence of a the preference to the $4TCH_3$ to be located near the walls of the tubes rather than at their center for big tubes whereas oligomers are localized around the center of the cavity for small nanotubes below π_C, π_{oT}-π_{NT} being less favourable in this latter case. Hence, the Raman G band behaviour after encapsulation is consistent with a permanent charge transfer for all the nanotubes under investigations and a superimposed optically activated charge transfer for small diameter tubes.

Finally, on figure 4.11 we compare the Raman G bands for defective nanotube NT14-D, NT14-D annealed at high temperature and hybrid $4TCH_3$@NT14-D. The Breit-Wigner-Fano (BWF) lineshape (characteristic of electron-phonon coupling) of the Raman G band is strongly reduced for defective metallic nanotubes due to significant positive charge transfer frm the encapsulated dye onto the host nanotube. As expected, after temperature treatment, eliminating the defects the BWF profile is recovered, suggesting a strengthening of the electron-phonon coupling). After dye encapsulation, this peculiar profile is also recovered, suggesting a back donation of electrons to the nanotube (figure 4.10b and 4.11).

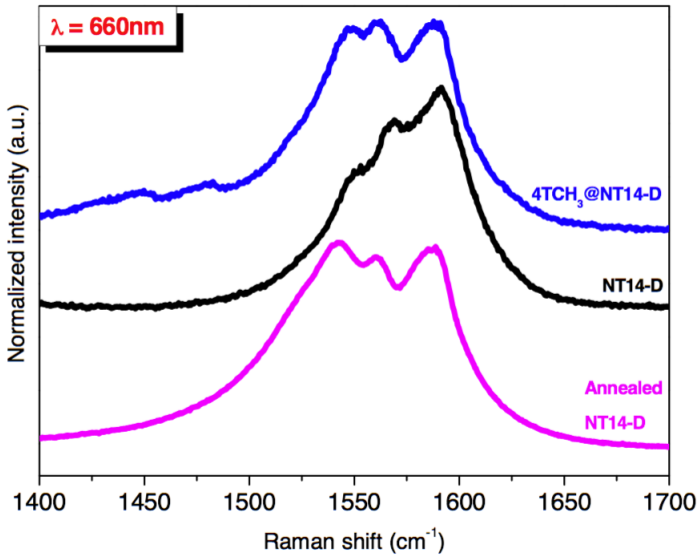

Figure 4.11 Comparison of Raman spectra of annealed-NT14 (magenta), defective nanotube NT14-D (black) and $4TCH_3$@NT14-D (blue), all measured with an excitation wavelength of 660 nm.

Electronic density of states

Calculated electronic density of states (eDOS) for $4TCH_3@SWCNTs$ close to the experimental diameters under investigation and $4TCH_3$ free molecules are shown in figure 4.12. Concerning the carbon nanotubes, we find that (11,0), (13,0), (17,0) and (19,0) nanotubes have decreasing band gaps of 1.0 eV, 0.7 eV, 0.6 eV, and 0.4 eV respectively in close agreement with previous results [99]. We found that the highest occupied and lowest unoccupied molecular orbitals HOMO and LUMO of the free $4TCH_3$ molecules appear as sharp sub bands when these molecules fill the tube, showing additional singularities in the density of states of the hybrid systems.

The estimated values of energy shifts (ΔE_f) between hybrid and pristine nanotubes are +0.15 eV, +0.28 eV, -0.06 eV and -0.03 eV for (11,0), (13,0), (17,0) and (19,0) nanotubes respectively. The ΔE_f values strongly depend on the structure of the hybrid nanotube. For small nanotubes, the Fermi level is shifted upwards in the band structure whereas it is very slightly downshifted for bigger tubes (diameter above 13 Å). The (11,0) and (13,0) hybrid nanotubes (8.6 Å and 10.3 Å in diameter respectively) encapsulate only one oligomer The (17,0) and (19,0) hybrid nanotubes (13.3 Å and 14.88 Å in diameter respectively) encapsulate two oligomers. As a consequence, the electronic band structure is affected close to the Fermi energy when the confinement is maximum for small tubes (diameter below 10 Å) and the shift of the Fermi level towards the conduction band indicates a n doping in agreement with

the Raman results. For bigger tube, the electronic band structure remains the same close to the Fermi level. The presence of encapsulated $4TCH_3$ creates localized electronic states which are far from the Fermi level. In this case the position of the Fermi level is very slightly modified suggesting no charge transfer or a very small positive one. One can notice that even in this latter case, the renormalization effect for the Raman G band is consistent as electron-phonon coupling leads to upshift of the G band for either n- or p-doping. This result suggests that the nature of the charge transfer between the nanotubes and the $4TCH_3$ molecules in these hybrid nanotubes could be modulated by confinement effect by changing the diameter of the nanotube. This point has to be studied in more details in further investigations.

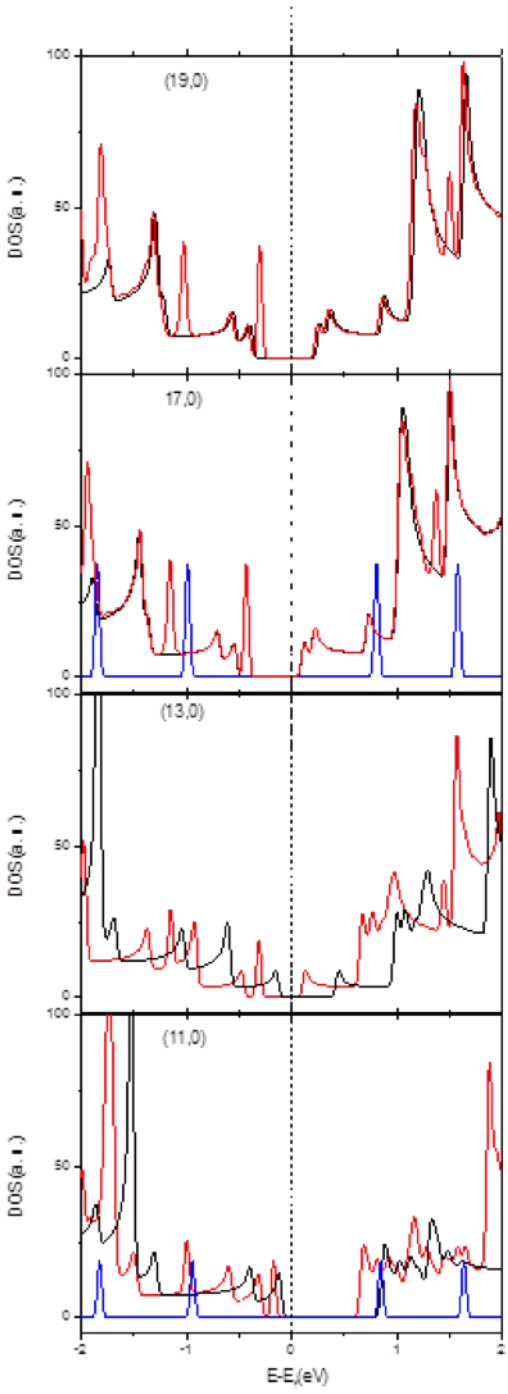

Figure 4.12 Electronic DOS of pristine (black) and hybrid (red) nanotubes with the chiralities: (11,0); (13,0); (17,0); and (19,0), from bottom to the top. Electronic DOS for one and two encapsulated dyes: $4TCH_3$@(11,0) and two $4TCH_3$@(17,0) (blue), respectively.

4.2.4 Conclusion

In summary, diameter dependence of the opto-electronic properties of SWCNTs after chromophore endohedral functionalization is shown. Electron transfer from the confined dies to the nanotubes is shown below a critical tube diameter of 10 Å. This charge transfer leads to an important enhancement of the photoluminescence intensity by a factor of nearly five depending on the tube diameter. Moreover, charge transfer between both subsystems is deeply affected by the increasing the diameter. Our results suggest that it is significant for tube below a critical diameter around 1 nanometer where only one $4TCH_3$ is encapsulated inside the hollow core of the tube. In addition, close to the molecule resonance, a concomitant intensity loss and amplification of the magnitude of the Raman G-band shifts, is strongly exhibited, suggesting a photo-induced electron transfer for these small tubes. Finally, our result indicate that defective metallic nanotubes after endohedral functionalization recover electron phonon coupling suggesting that confinement species into defective nanotubes allow moving the Fermi level and consequently to monitor their opto-electronic properties.

Part II

FePc encapsulated inside SWCNTs

Chapter 5

Vibrational and structural properties of FePc inside NTs

Contents

The last chapter of this thesis is dedicated to the study of iron-phthalocyanine (FePc) dyes encapsulated inside carbon nanotubes. FePc is a photo-active molecule which has attracted significant interests in the field of opto-electronics [182–185]. This is again a molecular

arrangement of a photoactive molecule inside a carbon cavity, forming a new family of hybrid material. However, the physical aspects raised upon encapsulation of FePc are expected to differ significantly from those discussed in the previous parts of this thesis, the properties of the guest FePc molecule being significantly different from those of $4TCH_3$ oligomers.

What makes this molecule unique is its square-planar shape of lateral dimension $\sim$12 Å, together with the metallic nature of its central atom which holds specific magnetic interactions. As we will discuss further in this chapter, encapsulation of FePc requires larger nanotube diameters compared to linear $4TCH_3$, a characteristic which is a direct consequence of its size and geometry. Therefore, the internal packing of the guest molecules, and their dynamics, are supposed to be strongly correlated to the nanotube diameter and external conditions like temperature and pressure. The question of the influence of the confinement on their magnetic properties is also of high fundamental and practical interest.

In this thesis we have initiated a global, multi-technical, experimental investigation of the one-dimensional organization of FePc within carbon nanotubes. We couple X-ray and neutron diffraction experiments to Raman and neutron spectroscopy to characterize this system in terms of its structure and dynamics in a large temperature and pressure range. At the time of writing, the data are still under interpretation (some pillar experiments are scheduled but not performed yet). A large amount of work is still to be done to allow for fine understanding of the neutron data. This will provide the natural continuation of this PhD.

This chapter is structured into four parts. The first one is a bibliographic introduction, aiming at reviewing some characteristic physico-chemical properties of the phtalocyanines molecules. Important results found in the literature on the encapsulation of these molecules are also reported. The second part reports on the procedure followed to synthesize the FePc@NTϕ hybrid samples. Their characterization, using TEM, Raman spectroscopy. Diffraction (X-Ray and neutron) is also detailed in the same part. The third section follows which reports on neutron diffraction investigations performed on samples characterized by different mean tube diameters. These experiments are realized in a large temperature range. The last section concerns a high pressure investigation of these systems. We concentrated our study on FePc molecules encapsulated inside single-walled carbon nanotubes showing a characteristic diameter of $\sim$ 21 Å. Finally, we conclude and give the perspectives of these studies.

5.1 Bibliographic introduction

5.1.1 Introduction to Phthalocyanines

Phthalocyanines (Pcs) are aromatic macrocyclic compounds of chemical formula $C_{32}H_{16}N_8^{2-}$ [186]. They have eighteen π-electrons, a square-planar geometry with a central cavity. A schematic representation of the unsubstituted phthalocyanine molecule is shown in figure 5.1. The latter is referred to as "free-base phthalocyanine" and is abbreviated by H_2Pc.

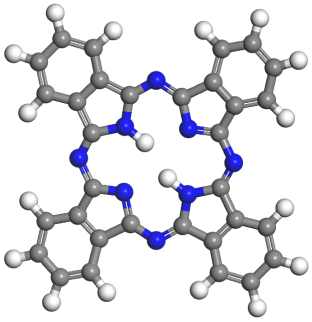

Figure 5.1 Structure of the H_2Pc molecule, with the following colour code: carbon (gray), nitrogen (blue), hydrogen (white). The planar surface of H_2Pc amounts (12.46×12.45) Å^2.

Phtalocyanines are very versatile molecules. Their central cavity can accommodate a large range of metal ions M, *e.g.* Fe, Ni, Co, etc... . Such molecular modification being called *metallation*, results in a fine tuning of their physical properties. Free-base phthalocyanine has a D_{2h} point group symmetry. The latter is changed to the higher symmetry point group D_{4h} by metallation, always maintaining the molecule's planarity [187]. However, some distortions can also appear, *e.g.* insertion of *Pb* ends up with a molecule with a dome-shape geometry [188, 189]. In this manuscript, we restrict our interest to iron-phthalocyanines FePc, the central cavity being populated by the bivalent ion Fe(II).

Metal-phtalocyanines (MPc) have been widely studied for their interesting properties (*e.g.* optical, magnetic) and wide range of applicability [190]. In order to better understand the hybrid system studied in this chapter, we give a brief account of the optical and structural properties of the crystalline FePc.

Structural properties of FePc molecules

The solid state forms of the square-planar MPc molecules depend on the π-π electronic interaction between two adjacent molecules along the stacking direction, yielding different polymorphs of their crystalline structure [191].

Crystalline FePc has two different polymorph phases: a metastable α-phase and a stable β-phase, the latter being obtained by sublimation of the α-polymorph at 350°C [192]. The difference between the two phases is found in the different angle between the normal to the plane of the molecule and the crystallographic b-axis for each polymorph : 25-30° for the α-polymorph and 45-49° for the β-polymorph [191]. The distance between two *herringbones columnar stacks* is therefore found to be smaller in the β-form (14.6 Å) than in the α-form (25.5 Å).

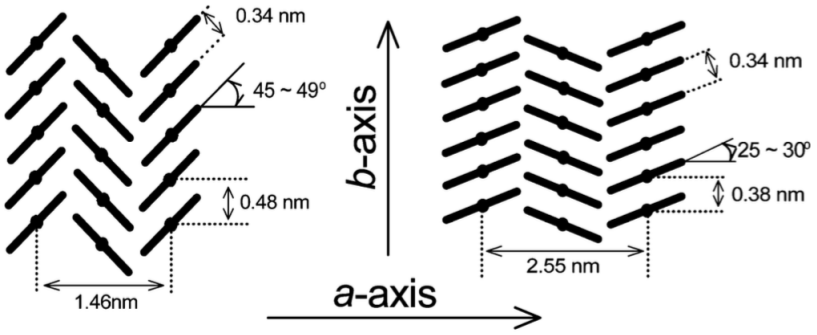

Figure 5.2 Crystalline structures of bulk FePc. **Left-hand side:** β-polymorph. **Right-hand side:** metastable α-polymorph. Taken from reference [191].

Electronic and optical properties of MPcs

MPcs are semi-conducting molecules which have been used as dye. These compounds have strong optical absorption in the [620, 700 nm] range [193], due to their Q band, and in the range of [250, 450 nm] due to their Soret band, or B band.

Figure 5.3 shows the absorption between the ultraviolet and visible regions of a free-base phthalocyanine (black line), with its two intense B and Q bands, both being $\pi \rightarrow \pi^*$ transitions from different ground states to excited states symmetries. The B band has two components B_1 and B_2, corresponding to the optical transition $a_{2u} \rightarrow e_g$ and $b_{2u} \rightarrow e_g$, respectively. The Q band corresponds to the optical transition $a_{1u} \rightarrow e_g$.

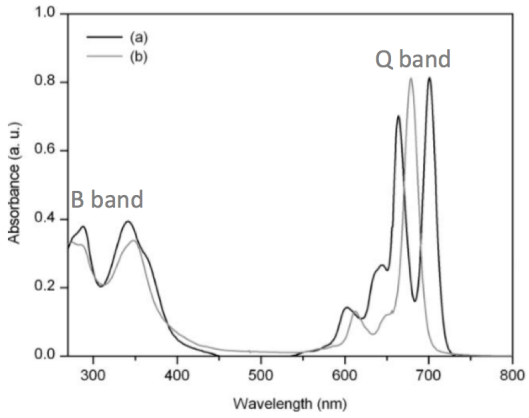

Figure 5.3 UV-vis absorption of free-base (black curve) and metallo-phthalocyanine (gray curve). The band in the range [250, 450 nm] is named Soret or "B band" while that in the range [550, 750 nm] is named "Q band". Taken from reference [193].

Figure 5.3 shows that a *metallation* results in a blue-shift of the Q band [190]. Moreover, additional components for the Q band are observed. It can be understood by considering that the HOMO and LUMO orbitals of the MPc lie in the metal d orbitals of the inserted central metal. Charge transfer can therefore occur between metal and ligand atoms, further giving rise to new absorption components at larger (metal to ligand *MLCT* transfer) or at lower (ligand to metal *LMCT* transfer) energy compared to those observed in the H_2Pc spectrum, see figure 5.4.

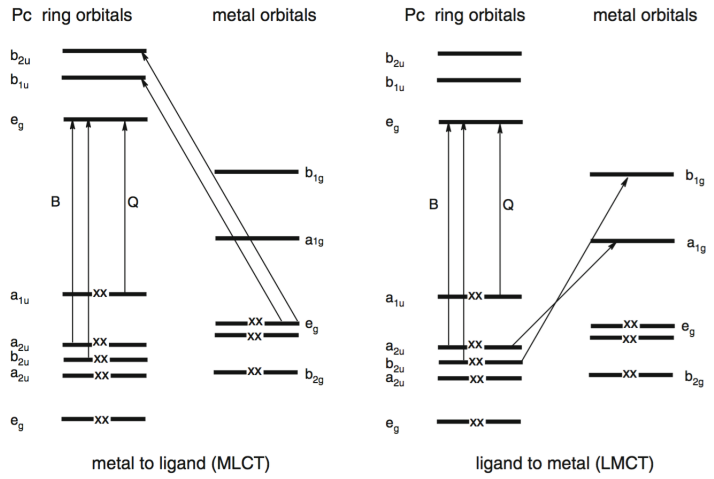

Figure 5.4 Gouterman's four-orbital linear combination of atomic orbital model. **Left-hand side:** Metal to phthalocyanine transition. **Right-hand side:** Phthalocyanine to metal transition. Taken from reference [190].

Figure 5.5 shows the Q band of the absorption spectra of the FePc in solution. Indeed, two intense components are reproduced at ∼630 nm and ∼670 nm.

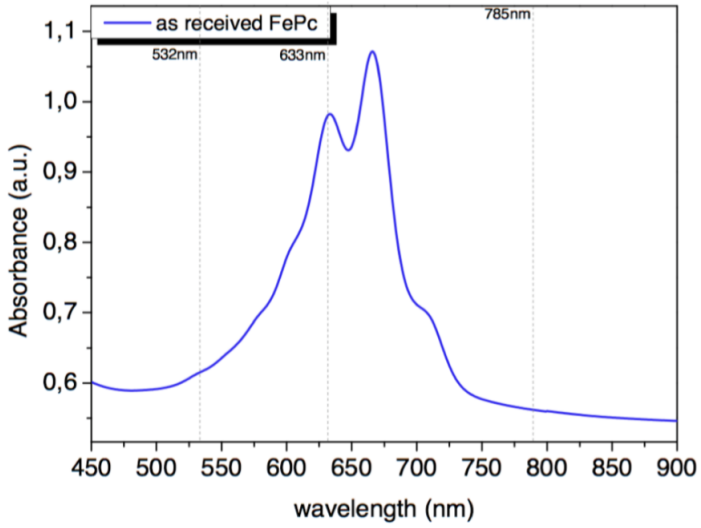

Figure 5.5 Optical absorption of the as received FePc in solution, in the domain of Q band.

5.1.2 Phtalocyanine encapsulation: A State of the Art Review

The first report on the encapsulation of CoPc molecules inside double-walled carbon nanotubes (DWNTs) is dated from 2007 by Schulte and collaborators [194, 195], see Figure 5.6a. The TEM images proved the success of the encapsulation, see Figure 5.6a. However the ordering of the encapsulated molecules could not be probed with confidence due to radiation damage. Such damage under the electron beam is often reported, *e.g.* by Kataura [31] for encapsulation of ZnDPP inside single-walled nanotubes. However the molecule's integrity after encapsulation was confirmed by Photon Emission Spectroscopy (PES) and Near Edge X-ray absorption Fine structure (NEXAFS) investigations [195].

In addition, this study revealed a non-random stacking between the encapsulated molecules, the latter would form a one dimensional chain of aligned CoPc oriented so that an angle equal to $\gamma = 36^\circ \pm 5^\circ$ is formed between the normal vector of the CoPc and the nanotube axis.

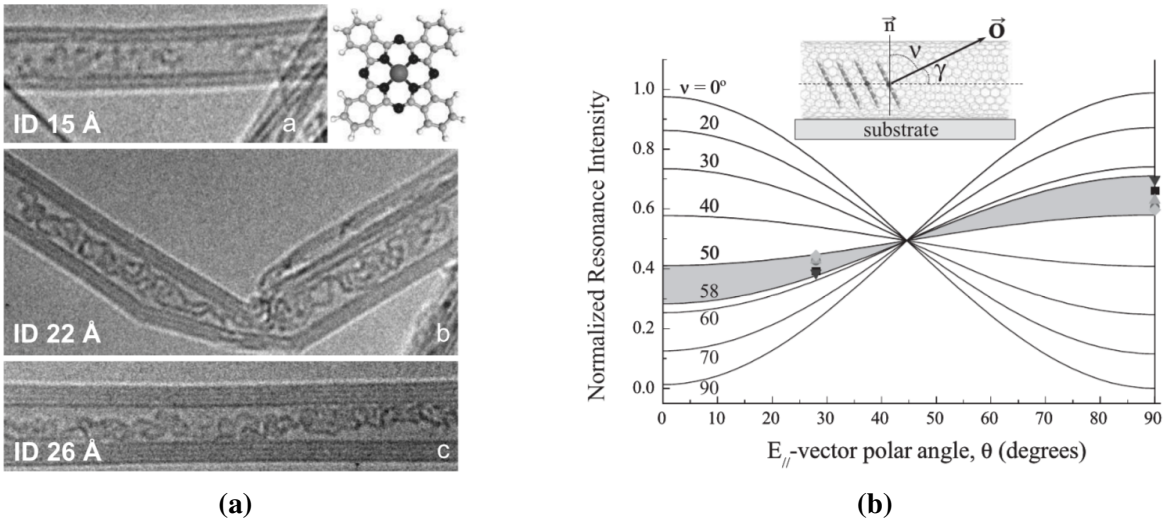

Figure 5.6 (a) TEM images of CoPc@MWNTs hybrid systems of different inner diameters: **Top:** 15 Å of inner diameter of DWNT. **Middle:** CoPc@MWNT with inner diameter of 22 Å. **Bottom:** CoPc@MWNT with 26 Å. **(b)** Normalized NEXAFS intensity for measured angles (at $\theta = 28°$ and $\theta = 90°$) and theoretical curves (lines with indication of ν angle). The normalization at the N K-edge has been performed at 405.2eV. Sketch of the side-on view of the CoPc@NT, where ν is the measured angle and γ is the stacking angle. Taken from reference [194].

In 2010, Swarbrick and collaborators have reported that the CoPc molecules, inside MWCNTs are no longer planar. The central atoms not being anymore in the molecular plane, yields a change of the molecular symmetry from D_{4h} to D_{4v} [196].

In 2015, Alvarez and collaborators have reported a detailed study of different MPcs with M equal to Zn and Fe, and a free-base Pc [197]. For single wall carbon nanotubes with diameter in the range of [14-18 Å] an efficient filling of the FePc@NT hybrid nanotubes was revealed by HRTEM, the nature of the atoms inside the nanotubes being accessed by SREELS. These measurements unambiguously revealed that nitrogen atoms were systematically localised inside the nanotubes, therefore proving the efficiency of the FePc filling process.

In this study, a one-dimensional lattice model is used for the structure of the encapsulated MPc molecules inside the host nanotube (see figure 5.7b for nano-containers with diameter of 17 Å). This model allows to reproduce the main features of the X-Ray diffraction diagram. It was suggested that therefore, the molecules confined inside the nanotubes arrange on a 1D lattice with a nanotube-diameter-dependent tilt angle with regards to the nanotube axis, similar to that adopted by *e.g.* coronene molecules confined inside single walled carbon nanotubes [198, 199]. Through DFT calculations of the binding energy, they have shown

that the more energetically favourable tilt angle between the encapsulated molecule and the axis of the nanotube is equal to 32° for the hybrid system H_2Pc@NT17, see figure 5.7b.

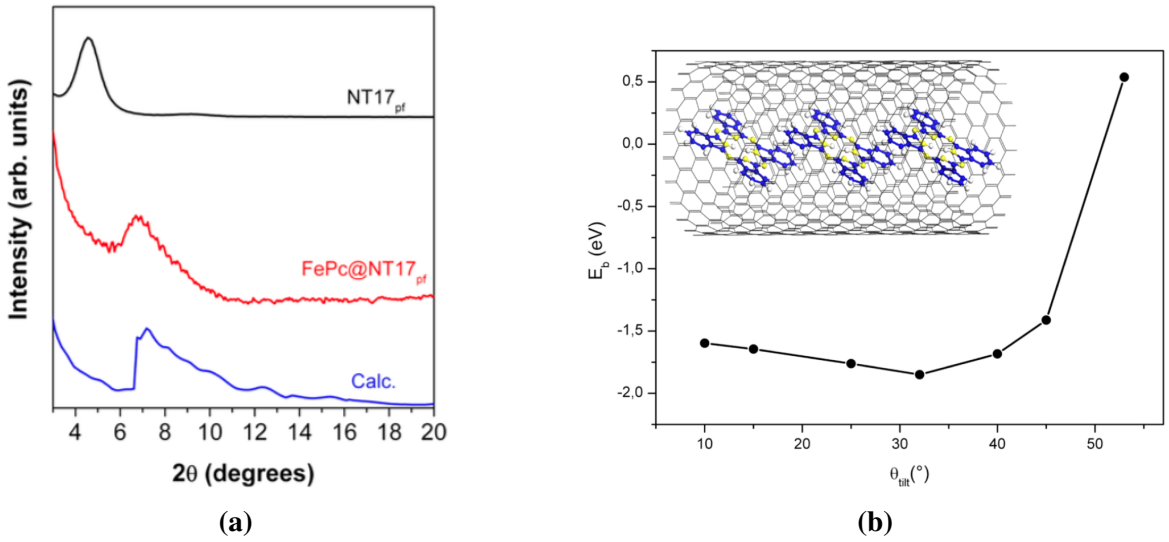

Figure 5.7 (a) Small angle X-ray scattering of: NT17 (black); FePc@NT17 (red) and FePc@NT17 from numerical simulations (blue). After encapsulation, the quenching of the (10) peak and the appearance of a new contribution around 7° are observed. The numerical simulations for the diffractograms of the hybrid system reproduces the quenching of the (10) peak and the new feature is associated to the ordering of the encapsulated FePc inside the nanotubes with typical distance of 12.8 Å. **(b)** DFT calculation of the binding energy in function of the tilt angle θ_{tilt} along the nanotube axis. Taken from reference [197].

Alvarez and collaborators show that the Raman signatures of the encapsulated molecules are found to depend on the central atom, with characteristic peaks lying in the range [1500-1550 cm^{-1}], see figure 5.8a. The spectroscopic feature of the encapsulated molecules are indeed similar to those observed in the spectra of their different crystalline forms. By contrast, closed-end nanotubes with π-stacked molecules on the outer walls reveal a much different spectral shape with a particularly intense peak at $\sim$1540 cm^{-1}. With the support of DFT calculation, this new peak has been assigned to the signature of a distortion of the structure of the molecule when stacked toward the outer shell of the nanotube, with the central atom shifted towards the nanotube, out of the molecule's plane 5.8b.

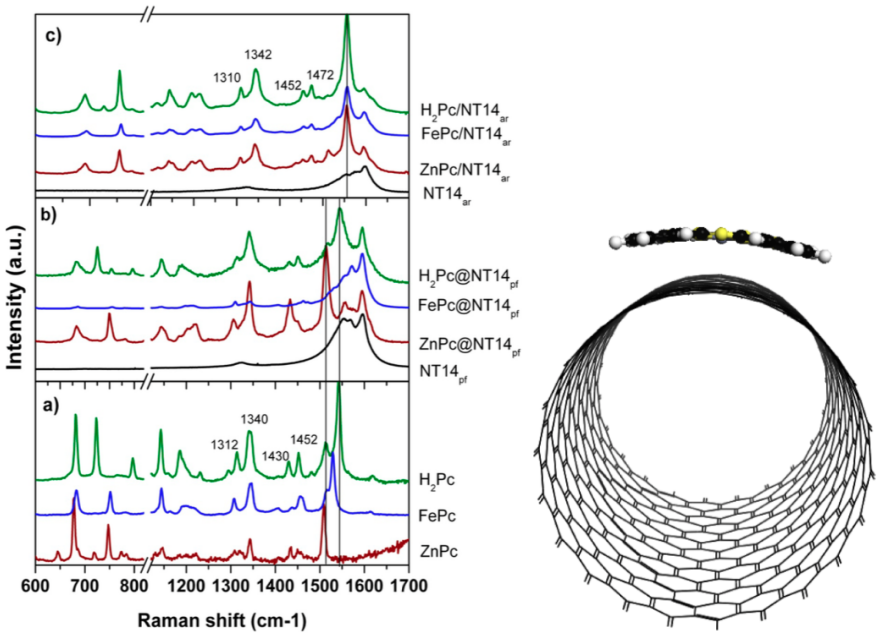

Figure 5.8 **(a)** Raman spectra of **c)** π-stacked hybrid systems with a closed-end NT14 host nanotube, *ar* stands for as-received NT14 nanotube. **b)** Encapsulated hybrid systems and pristine NT14, where *pf* stands for purified NT14 nanotube. **a)** Bulk molecules. **(b)** Structure of the ZnPc π-stacked at the outer surface of a (17,0) nanotube used for the DFT calculations. Taken from reference [197].

Summary of the encapsulation of Phthalocyanies inside carbon nanotubes

2008 Schulte Reported for the first time the encapsulation of CoPc inside carbon nanotubes. From a NEXAFS with linearly polarized light experiments, the stacking of the planar molecules along the nanotube axis was found to be oriented with angle $36° \pm 5°$ along the nanotube axis. The encapsulated phase was found to be α-CoPc [195].

2010 Swarbrick Upon encapsulation CoPc molecules were found to be no longer planar inside nanotubes, DFT calculations revealed a change in symmetry from D_{4h} to C_{4v}, where Co atoms moved out of the plane of the molecule. Shifts in the pre-edge peak to high energy probed by RIXS indicating a charge transfer from the CoPc to the inner walls of the nanotube, as it has been reported by Kataura [31] and Schulte [195]. The authors report that the encapsulation of the CoPc is possible thanks to a change in molecular geometry in order to fit in the hollow space of nanotubes [196].

2015 Alvarez A combined XRD with DFT calculations revealed the stacking angle of the MPcs along the nanotube axis to be 32°. Raman spectra of hybrid nanotubes indicates weak interaction between the encapsulated MPcs and the nanotubes. However, once the molecules are π-stacked at the outer surface, there are strong interactions between both species. The authors report that the central atom move away from the plan of the π-stacked molecule [197].

From the studies reported in the literature on various MPcs encapsulated inside SWCNT, DWCNT and MWCNTs, it seems that the confinement of the square-planar molecules favours the formation of a one-dimensional structure presenting some degree of order. In the following parts of this chapter, we try to better understand the details of the guest lattice structure, and try to correlate it to the nanotube diameter.

To this aim, we report on the investigations of the FePc chain structure when encapsulated into two SWCNT hosts of different sizes, originating from different sources. One is nanotubes produced by the arc discharge technique, referred to as NT14 in coherence with the previous chapters, and the other one are eDIPS nanotubes with a typical mean diameter of 21Å, called NT21. The latter tubes, characterised by a large diameter, were never used as a confinement matrix up to now. The synthesis of these hybrids systems is presented in the following section.

5.2 Synthesis of samples and characterization

The protocol for encapsulation of FePc inside nanotubes is rather similar to the one used for the encapsulation of $4TCH_3$, described in section 2.1.2 of Chapter 2.

The commercial compound of iron-phthalocyanine was purchased from Sigma-Aldrich [118]. It is a crystalline dark-purple powder corresponding to the α-phase [191], with a degree of purity reaching 90 %. This compound was purified by sublimation at 500 °C during 5 h under dynamic vacuum of about 5×10^{-5} mbar, the molecule being placed inside a glass tube fitted inside a tubular furnace, similar to the apparatus shown in figure 2.8. After sublimation, the molecules are condensed on a cold wall of the glass tube, into a thin layer exhibiting a colour different from the as received product. XRD reveals that the purified compound is formed of the β-phase.

For 50 mg of nanotubes, 100 mg of FePc have to be purified, the ratio molecule/nanotube for encapsulation being 2:1. This requires successive purifying steps of the FePc molecule, as 50 mg of product cannot be sublimated in one batch. The purified powdered of FePc is physically mixed under vacuum, with nanotubes previously outgassed from any adsorbed species. The glass tube is sealed under vacuum and the sample is heat treated during 72 h at 500°C.

After this heat treatment, the powdered sample is washed with a solvent of the molecule in order to remove the FePc in excess.

Carbon nanotubes with mean diameter of 14 Å can be purchased in two forms: closed-end and opened-end. The opened-end sample is referred to as NT14, whereas the closed-end is AP, the acronym standing for "As Prepared" nanotubes. From these two powders we prepared two hybrid samples following the same encapsulation process. The hybrid sample prepared from the AP nanotubes is formed of exohedral π-stacked FePc molecules at the outer surface of the tubes. This sample is named FePcπAP.

After the synthesis, HRTEM and Raman scattering and X-ray diffraction characterizations of the samples were carried out in order to test the FePc encapsulation within the opened-end nanotubes.

5.2.1 TEM characterization of FePc@NTϕ

The FePc@NT14 hybrid system prepared following the same preparation process as described above have been studied in reference [197]. HRTEM images are shown in figure 5.9. As already mentioned, SREELS performed on these samples confirmed the presence of nitrogen –and thus indirectly of FePc– within the core of NT14 nanotubes.

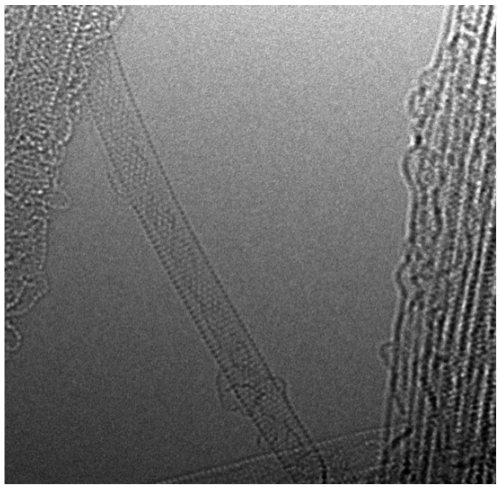

Figure 5.9 HRTEM of the individual hybrid system FePc@NT14, performed by the collaborator Yuta Sato from the Electron Microscopy Group [131].

Figure 5.10 shows the HRTEM image an individual FePc@NT21 nanotubes. The bright spots on the picture corresponds to the iron center of the FePc molecules. This image gives a good indication that the filling of this nanotube with FePc molecule is well achieved. As FePc molecules are unstable under the electron beam, it is not possible to resolve the stable molecular organization of the guests using this technique.

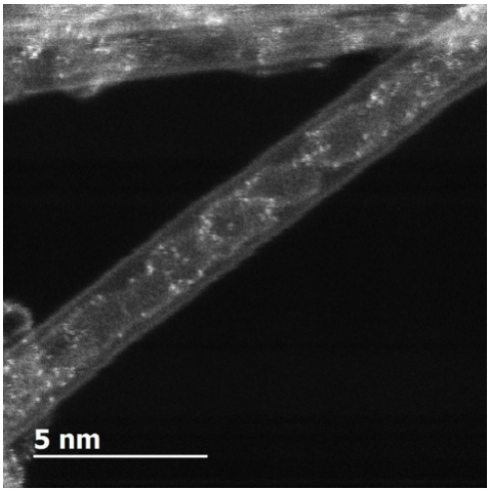

Figure 5.10 HRTEM of the individual hybrids FePc@NT21, performed by the collaborator Yuta Sato from the Electron microscopy group [131].

5.2.2 Raman Spectroscopy characterization of FePc@NTϕ

In a first step, the reference powder of both as-received and purified FePc were measured by Raman spectroscopy with the three exciting wavelengths 532, 633 and 785 nm, see figure 5.11.

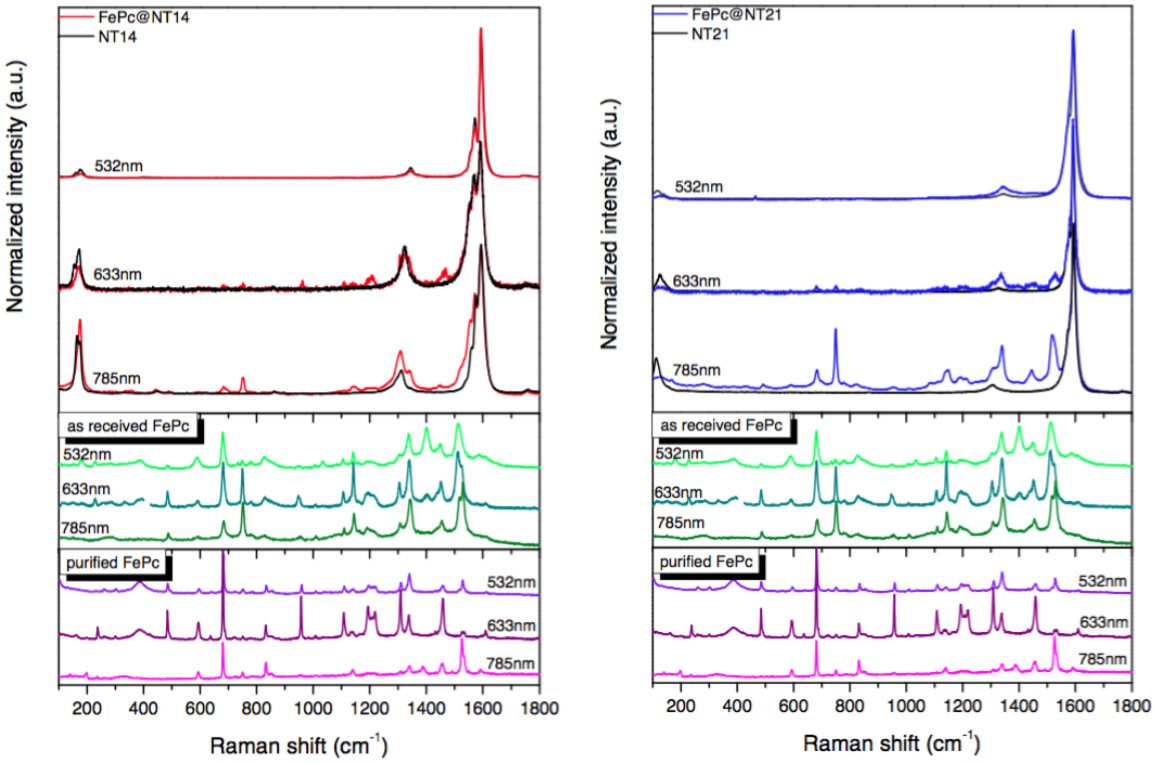

(a) FePc@NT14 **(b)** FePc@NT21

Figure 5.11 Raman scattering spectra of hybrid and pristine nanotubes (top), as received FePc (middle) and purified FePc (bottom). All hybrid and pristine spectra are normalized to unity for the G band.

The spectra of both crystallographic forms, α-FePc (as received) and β-FePc (purified), evolves with the excitation wavelength. That behaviour is due to the resonant Raman effect which exalts specific bands depending on the excitation wavelength. Indeed, the FePc molecule absorbs in the range [550, 750 nm], see figure 5.5.

The Raman spectroscopic characterization of the hybrid systems measured with these exciting wavelengths are shown on 5.11a for FePc@NT14 and 5.11b for FePc@NT21, both hybrid and pristine nanotubes spectra are superimposed for each excitation wavelength. For both NT14 and NT21, the Raman spectra of the hybrids and their respective pristine nanotubes probed at 532nm are similar. Conversely, for the excitation wavelength of 633 nm, few peaks appear between the RBM and G bands. These new features reveal similarities when

compared to the Raman spectra of the as received FePc. When the hybrid systems are probed with the exciting laser wavelength of 785 nm these vibrational features assigned to FePc have higher intensity. The appearance of FePc features for red and near Infrared excitation wavelengths are in agreement with resonant effect induced for FePc within the hybrids systems and confirm the presence of FePc in the hybrids after the complete encapsulation process.

In order to check if the detected FePc does correspond to encapsulated species in FePc@NT14 sample, Raman spectra of both FePc@NT14 and FePcπAP (for which π-stacked FePc molecules are expected at the outer surface of the nanotubes) are compared.

For the 785 nm laser excitation, an additional peak at around 1550 cm^{-1} appears only for the sample FePcπAP superimposed with the G band, see figure 5.12.

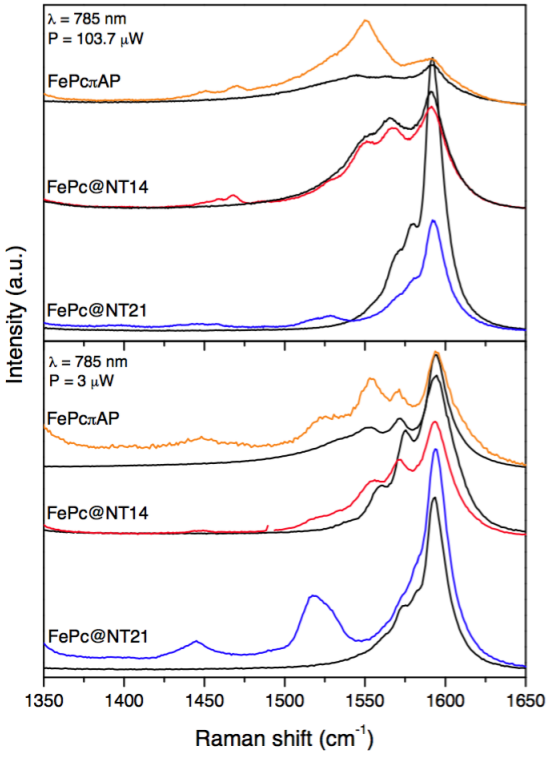

Figure 5.12 Raman spectra of hybrid and pristine nanotubes probed at λ = 785 nm for different laser powers: 103.7 μW (top) and 3 μW (bottom).

In fact, this new feature has already been reported by Alvarez and collaborators [197] as a specific signature of the exohedral interaction and related to the displacement of the central atom toward the nanotube in this pi-staked configuration (see section 5.1.2). The fact that

this signature does not appears for FePc@NT14 and FePc@NT21 therefore indicates that the resonant Raman features observed for the two encapsulated hybrids are dominated by encapsulated species.

Numerous studies have shown that the RBM of the host nanotube is particularly sensitive to any filling of the nanotube. Figure 5.13 shows an enlargement of the RBM from figure 5.11, for the hybrid systems and their respective pristine nanotube.

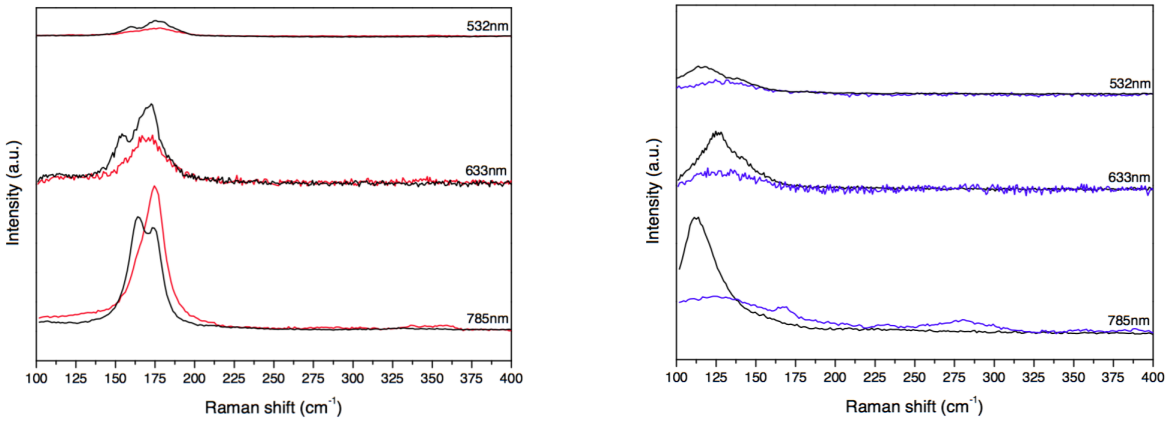

(a) FePc@NT14 **(b)** FePc@NT21

Figure 5.13 Raman scattering spectra of hybrid systems in the RBM region for pristine nanotubes (black) and hybrid system in red and blue. Intensity of the curves are all normalized to the G band intensity to unity.

Table 5.1 summarizes the diameters of the resonant nanotubes probed at 532, 633 785 nm for NT14 and NT21 batches, according to the relationship $d_{NT} = {}^{217.8}/_{\omega_{RBM}} - 15.7$, from reference [75], linking the RBM frequency to the diameter of the resonant nanotubes.

Table 5.1 Probed nanotube nature and diameters

excitation	**FePc@NT14**			**FePc@NT21**		
wavelength (nm)	**nature**	**RBM** (cm^{-1})	**diameter (Å)**	**nature**	*RBM* (cm^{-1})	**diameter (Å)**
532	M	159.93	15.1	SC	116.80	21.5
532	M	177.11	13.4	SC	138.80	17.6
633	M	154.79	15.6	M	126.77	19.6
633	M	172.47	13.8			
785	SC	164.07	14.6	M	112.78	22.4
785	SC	174.29	15.1			

After encapsulation the dominant effect on the RBM is a loss of intensity. This loss of intensity is particularly important for the peaks associated to diameters around [15, 15.6 Å] when the intensity of the RBM corresponding to smaller diameters [13.4, 13.8 Å] is much less reduced. This could be an indication of a preferred filling of the nanotube with diameter larger than 13.8 Å in agreement with the molecular size $\sim$ 12.4 Å. For FePc@NT21, nanotubes excited range [17.6, 22.4 Å] according to the RBM frequency spectrum, and the whole band strongly decreases in intensity after encapsulation. This decrease in intensity has formerly been explained by a loss of resonance for the NT after encapsulation [31, 93]. For the exciting wavelength of 785 nm, an upshift of the RBM of FePc@NT14 is observed, along with a strong modification of the profile of the RBM mode.

Therefore, from TEM and Raman characterization, it was shown that FePc molecules are detected in FePc@NT hybrids. HREELS gives a good indication that most of the molecules are inside NT14 nanotubes. With Raman spectroscopy, the modification of the RBM seems to indicate a preferential interaction between the molecule and the nanotube having diameters higher than 13.8 Å. When excited with red and near IR light, the signal from the molecules in interaction with the nanotubes can be measured, moreover for FePc@NT this signal is clearly dominated by the encapsulation species giving a direct access to the effect of the confinement on FePc molecules.

5.2.3 Diffraction of FePc@NTϕ

Figure 5.14 shows the X-ray diffraction results measured at the L2C by Philippe Dieudonné. Powdered samples inside quartz capillaries are measured in SAXS configuration.

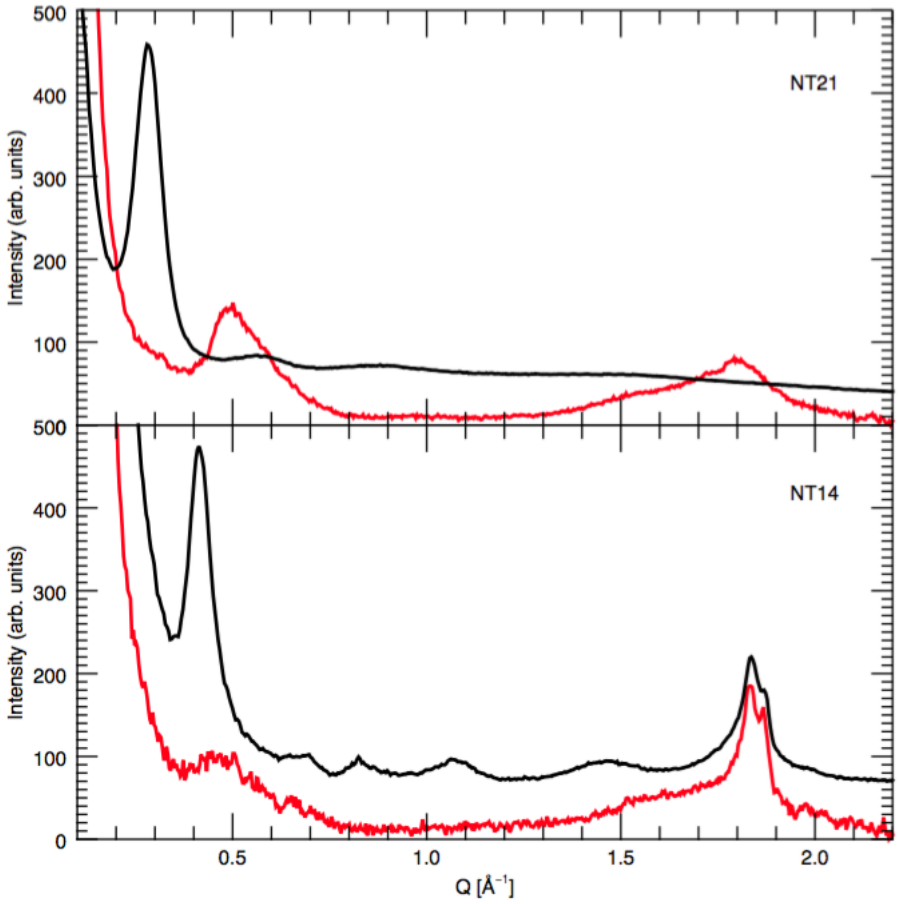

Figure 5.14 XRD of FePc@NT21 (top red), NT21 (top black), FePc@NT14 (bottom red) and NT14 (bottom black)

For the pristine NT14 sample, the sharp peak observed at 0.4 Å^{-1} is assigned to the well known (10) peak from the 2D trigonal lattice formed by the bundles. The relation between the scattering vector of the (10) peak (hereafter noted $Q_{(10)}$) and the trigonal lattice spacing a_b is given by $Q_{(10)}a_b = 7.2552$. The lattice spacing of the bundle is directly related to the tube diameter ϕ_t: $a_b = \phi_t + a_{vdW}$, a_{vdW} being the *van der Waals* distance between adjacent tubes equal to $\sim$ 3.2-3.4 Å. A value of $Q_{(10)}$ of 0.42 Å^{-1} therefore characterizes 14 Å nanotubes [200, 152], the latter characteristic diameter being classically obtained by the electric arc method, see reference [113].

The diffraction diagram is drastically modified by encapsulation: as observed on the FePc@NT14 diagram, the (10) peak is quenched while an additional asymmetric peak appears having a maximum intensity at 0.45 Å^{-1}. It is well know that the disappearance of the (10) Bragg peak is an indication of the filling of the inner core of the nanotubes [133]. The same observations hold for the FePc@NT21 diagram when compared to pristine

opened-end NT21, see figure 5.14. The strong (10) peak appears at ~ 0.3 Å^{-1} for these bundles, which is coherent with tube diameters of ~ 21Å. Again, the (10) peak is quenched for the FePc@NT21 hybrids, and a new component also appears around 0.50 Å^{-1}. In the higher Q range, some excess of intensity is observed between 1.5 and 2 Å^{-1} in the two hybrid diagram. The origin of these features is not clear. It comprises several components of variable width with characteristic length in the range of $\sim$3.5 Å.

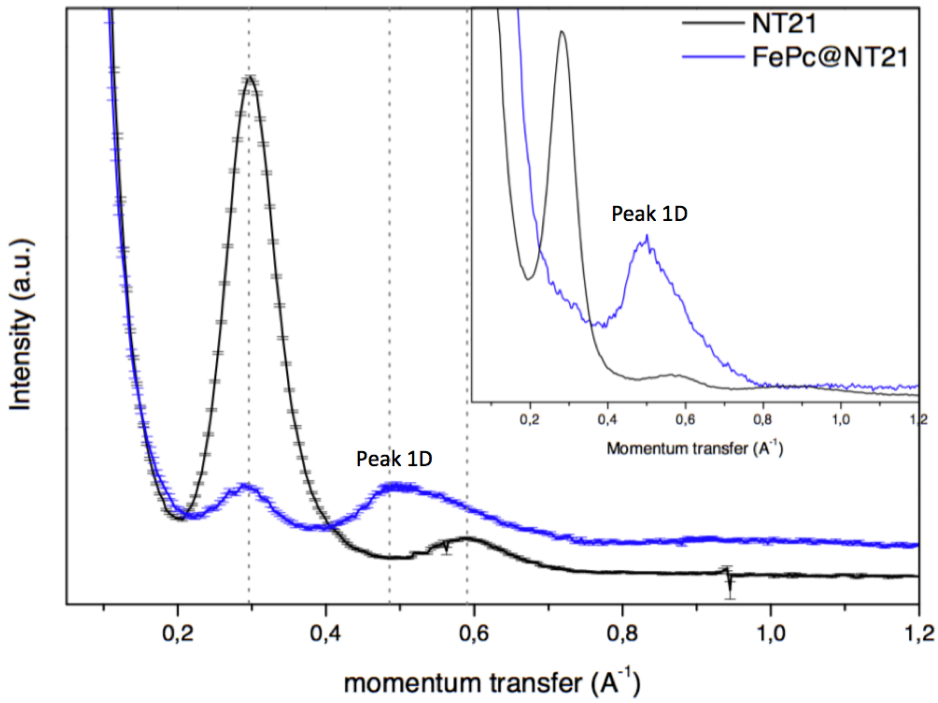

Figure 5.15 SANS signal of NT21 (black) and FePc@NT21 (blue) and on the inset, SAXS measurements.

Figure 5.15 compares the X-ray and neutron diffraction diagrams of the FePc@NT21 samples. The main difference that can be observed between both techniques is the incomplete disappearance of the (10) peak in the neutron diagram. The origin of this discrepancy can be found either in the technique-dependent contrast between the inserted molecules and the carbon nanotube, or in the volume of the sample probed by the techniques. In the case of neutron diffraction, the total volume of the batch is probed, while only a small part was probed using XRD. If some empty tubes are present in the sample, in a non homogeneous way, they will increase the (10) peak in the neutron data. For homogeneous samples, a significantly different contrast results in a similar effect.

As a partial conclusion, we see the quenching of the (10) peak (complete for X-ray and partial for neutrons) for both the FePc@NT14 and FePc@NT21 samples. Moreover, for both hybrids a new component called peak 1D, in figure 5.15 is observed at a momentum transfer close to 0.45-0.50 $Å^{-1}$. This result is consistent with the previous study involving nanotubes having 17 Å diameter, see reference [197] and was interpreted as the signature of the confined 1D lattice of FePc molecules. The 1D lattice parameter thus evolves from $\sim$ 14 Å for FePc@NT14 to 12.5 Å for FePc@NT21. These values are significantly larger than the intermolecular distance of adjacent FePc in the bulk phase (3.4 Å). This observation was interpreted as a result of the confinement by the nanotube matrix, the latter preventing the molecules to orient in a way such as to find the minimum energy configuration.

5.3 Temperature and pressure dependence of the hybrid structure by Neutron Diffraction

As described in the previous section, diffraction allows at probing the structure of the confined chain. The packing of the molecules inside the nanotubes is however not completely clear. Even though it is admitted that the molecules on the chain form a certain angle with regards to the nanotube axis, which in turn is responsible to the large 1D lattice parameter, no information on the fluctuations of this angle (either static or dynamic) is found in the literature. The 1D nature of the confined chain, together with the short range extension of the intermolecular interactions, confer the FePc molecules with a large entropy. This feeds the hybrid system with a certain degree of temperature dependent position and orientation disorder. Significant reduction of this disorder should be observable with decreasing temperature, and the strong rotation-translation correlations of the confined molecules in this system should lead to some change in the position and shape of the 1D features observed in the diffraction diagram, in a way similar to what was observed for the carbon peapods [154, 155]. Any increase of the intermolecular correlations with cooling or application of pressure is expected to shorten the lattice parameter of the confined chain. Eventually, any phase change in this system will be detected by the T dependence of the different observables (position, width and shape of the 1D peak).
Therefore we have used the D16 (ILL) and PAXY (LLB) neutron small angle diffractometers to follow the temperature dependence of both the FePc@NT14 and FePc@NT21 diffractograms, with special attention on the small angle (small Q) range [0.1, 1 $Å^{-1}$]. The [0,300 K] temperature range was probed using a cryostat. Additional experiments as a function of

pressure were performed on D16. The latters are briefly described at the end of this part.

Figure 5.16 shows the neutron diffraction diagrams measured on PAXY at the temperatures of 280 K and 10 K. One clearly observes that neither the (10) peak residue in the FePc@NT21 diffractogram nor the 1D peaks around ~ 0.5 Å^{-1} in both diagrams evolve with temperature.

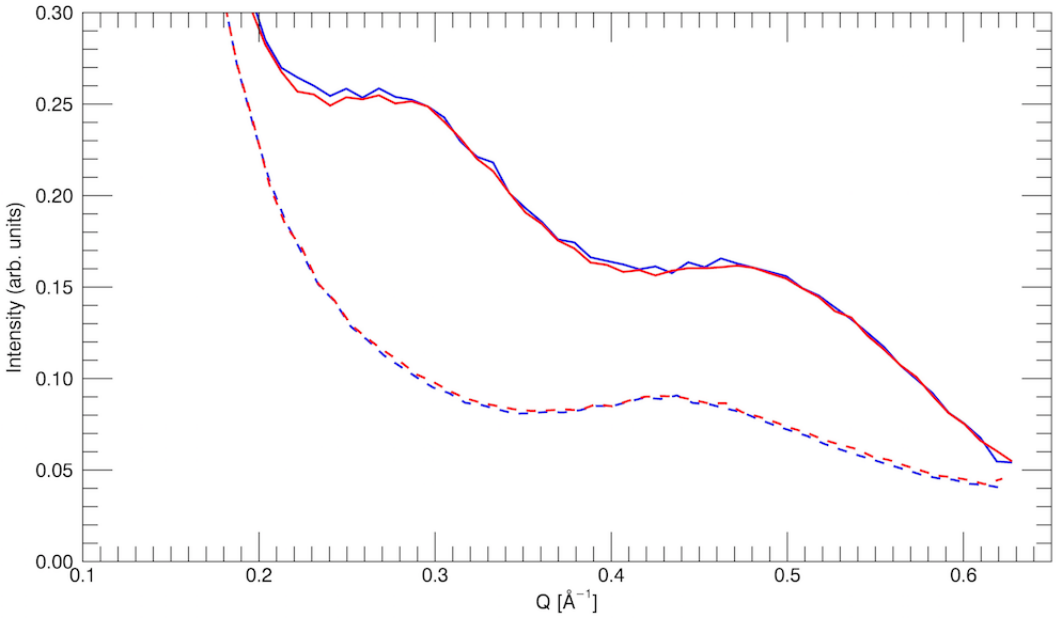

Figure 5.16 Neutron diffraction diagram of the FePc@NT21 at 280 K (Red line) and at 10 K (Blue line) compared to that obtained on the FePc@NT14 at 280 K (Red dashed line) and at 5 K (Bleu dashed line)

Extending these investigations in a wider angular range (up to ~ 1.2 Å^{-1}) and down to 1.5 K using D16 leads to the same conclusions. The diffraction diagrams and their derivatives are shown as a function of temperature in the figures 5.17 and 5.18, respectively for FePc@NT14 and FePc@NT21.

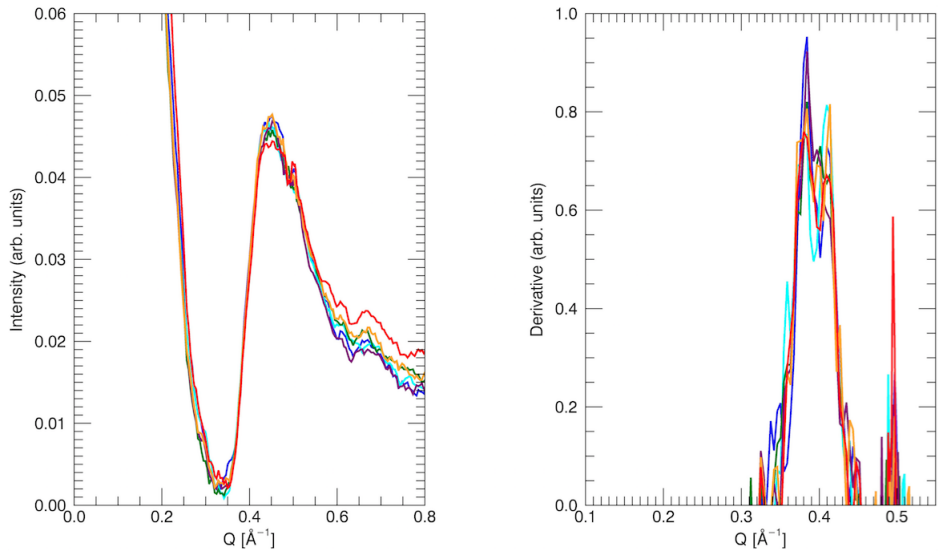

Figure 5.17 Left-hand side: Temperature-dependent diffraction of the FePc@NT14 sample. 100 K (Red), 50 K (Orange), 30 K (Purple), 10 K (Green), 5 K (Cyan) and 1.5 K (Blue); **Right-hand side:** Derivative of the diffraction - same colour code

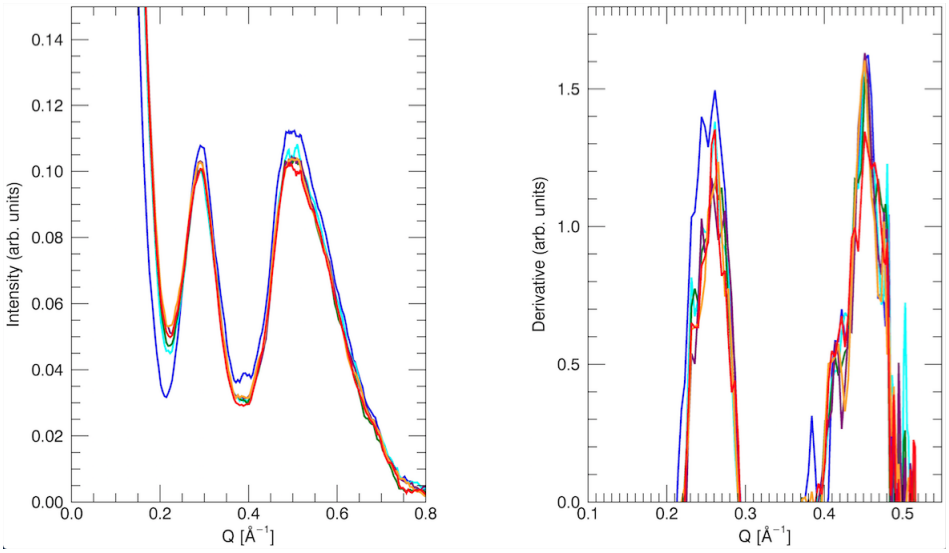

Figure 5.18 Left-hand side: Temperature-dependent diffraction of the FePc@NT21 sample. 100 K (Red), 50 K (Orange), 30 K (Purple), 10 K (Green), 5 K (Cyan) and 1.5 K (Blue); **Right-hand side:** Derivative of the diffraction - same colour code

The 1D peak feature is remarkably temperature independent in the complete temperature range probed. This translates in a constant position and width of the peak in the derivative spectrum characteristic of the 1D feature. The latter is shifted from 0.45 Å^{-1} for the

FePc@NT21 sample to 0.4 $Å^{-1}$ for the FePc@NT14 sample, which suggests that the lattice parameter of the chain is expanded from 14 to 15.7 Å respectively.
The only noticeable change with temperature is observed as an increase of the amplitude of the feature when the temperature is lowered below 5 K. This observation is made for the FePc@NT21 sample only, and is restricted to the lowest Q range, particularly affecting the residual (10) peak. This suggests that the form factor of the nanotubes changes slightly in this temperature range for the largest diameters. One possible explanation can be found by considering that large nanotubes have a strong tendency to ovalization. This results from the competition between van der Waals attraction between adjacent tube, *i.e.* leading to flattening of the tubes surface, and elastic deformation. The vibrational squash mode is the first optical mode of the nanotubes. This mode corresponds to a periodic elliptic deformation of the cross section of the nanotube (see *e.g.* reference [201]). Its frequency scales with the inverse of the tube diameter, and is lying in the range 3 - 5 meV for a 14 Å single walled nanotube, depending on its packing. The frequency of this mode is certainly shifted in the sub-meV frequency range for nanotubes with a diameter larger than 20 Å. This poses the question of the stability of the circular cross section for these tubes at high temperature, and a change from a stable circular to elliptical shape can be expected at the lowest temperatures. Such an hypothesis should be verified by simulations.

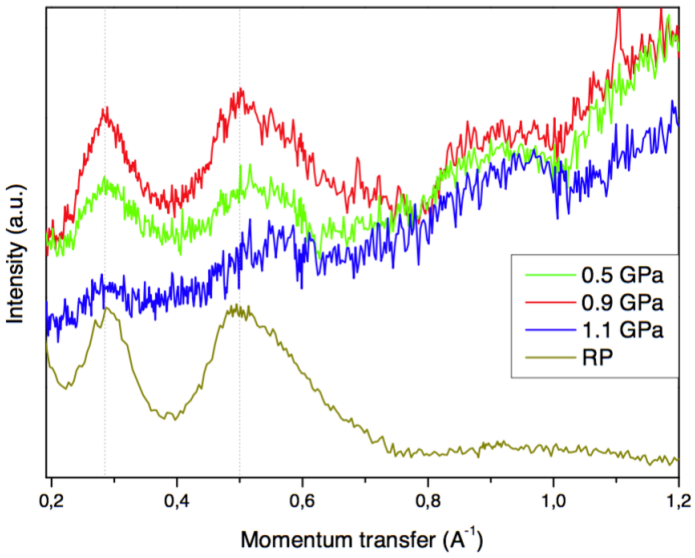

Figure 5.19 Pressure-dependence neutron diffraction of FePc@NT21 at room temperature for the pressures 0.5 GPa (green), 0.9 GPa (red) and 1.1 GPa (blue). The diagram measured at room pressure (yellow), outside of the pressure cell, is also shown for comparison.

Figure 5.19 shows the evolution of the diffractograms of the FePc@NT21 sample under pressure. Again, no clear shift of the position of the 1D peak is observed in the pressure range up to 1.1 GPa.

Our conclusions on the temperature and high pressure studies are rather surprising as, contrary to our expectations, the feature at 0.5 Å^{-1} associated to the structure factor of the confined chain stays remarkably unaffected by:

- varying the temperatures down to 1.5 K for both hybrid systems.
- varying the pressure up to 1.1 GPa for the FePc@NT21 sample.

5.3.1 Partial Conclusion: Re-interpretation of the diffraction data

The lack of any clear evolution of the diffraction features with temperature and pressure, neither in position nor in shape, is rather intriguing. This suggests that the molecules inside the nanotubes have a very stable orientation and that their intermolecular interaction has a strong harmonic character. For soft van der Waals interactions this is quite unusual. In particular, it was shown for C_{60} peapods that the 1D diffraction peak was strongly temperature dependent, revealing increasing orientational correlations between adjacent fullerenes when lowering the temperature [154].

The diffraction diagram of filled nanotubes organized into bundles is not rich, showing only few broad features. Being at the nanometer scale, the bundle organization features are localized in a Q range intermediate between the diffusion regime and diffraction. Their interpretation using conventional methods can lead to errors [202] and one requires numerical models to have a clear idea of the different terms at play in the diffraction response of the structure. The model we have used in this thesis is a modification of the models initially developed by Almairac et al. for the case of nanotubes [200], and further extended to the different cases where molecules are adsorbed either inside the tubes (for example for DWCNTs [134], peapods [133, 203], or Li-THF at the external surface of the bundles [204] etc...). It is no the goal of this chapter to develop the diffraction formalism that we used (details on the model are given in Appendix D). It can be found in the reference [133] dedicated to the calculation of the diffraction diagram of carbon peapods.

The assumption that we have put in our model was to simulate the encapsulated FePc molecules either as a homogeneous rod of radius R filling up the entire nanotube length, or as uniform disks of radius R stacked perpendicular to the nanotube axis with a separation distance of ~ 3.4 Å. Therefore the only modification in the mathematics was to exchange the

form factor of a sphere by that of a rod which writes:

$$F(\vec{Q}) = \frac{2J_1(QRsin(\theta))}{QRsin(\theta)} \frac{sin(QLcos(\theta)/2)}{QLcos(\theta)/2} \tag{5.1}$$

with J_1 the cylindrical Bessel function of first order, $\vec{Q}$ the scattering vector, R the radius of the disk, L its length and θ the angle between $\vec{Q}$ and the disk plane. The form factor for a disk is obtained by taking the limit $L \to 0$ of the expression 5.1.

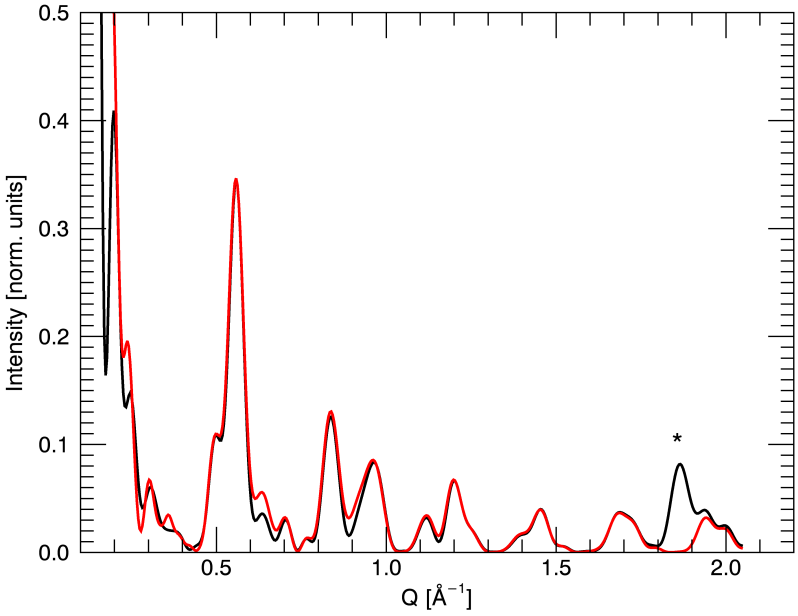

Figure 5.20 X ray diffraction diagram of the following models: *Red:* uniform rod of radius 6 Å with a volume density equal to 1. FePc molecule per 256.354 Å^3, *Black:* uniform disks of radius 6 Å separated by 3.4 Å. The scattering volume density is kept equal to the previous one by artificially scaling the scattering density of the disks by a factor 1.5. The 1D peak is observed at $\sim$ 1.85 Å^{-1} and is indicated by a star.

Figure 5.20 compares the diffraction diagram obtained for a model of rods (red curve) and for a model of 1D lattice of disks (black curve). In a first step, the lattice parameters of the bundle was adjusted to reproduce the experiment diagram of the NT21 sample. We found a good agreement for bundle of $\sim$ 20 tubes with diameter equal to 23 Å. Then the radius of the rod, together with the scattering volume density was adjusted so as to extinguished completely the (10) peak, as observed in the FePc@NT21 X-Ray data. For this model, the calculated diagram is already found in remarkable agreement with the data, with a quenched (10) peak

and a dominant feature at 0.5 $Å^{-1}$. Note that in this model, **no 1D peak is expected as the distribution along the nanotube axis is uniform**. This indicates that the feature calculated in this range originates entirely from the (11) peak of the bundle and from the cross term describing the interferences of the rod and the tube. If we calculate the diffraction response of a 1D lattice of disks with a lattice parameter of 3.4 Å (the characteristic intermolecular distance in the FePc bulk phase), keeping the volume density equal to that used in the rod model, we obtain the black curve on Fig. 5.20. The low Q features match perfectly those calculated for the rod model, while the 1D lattice features an asymmetric additional peak at ~ 1.85 $Å^{-1}$.

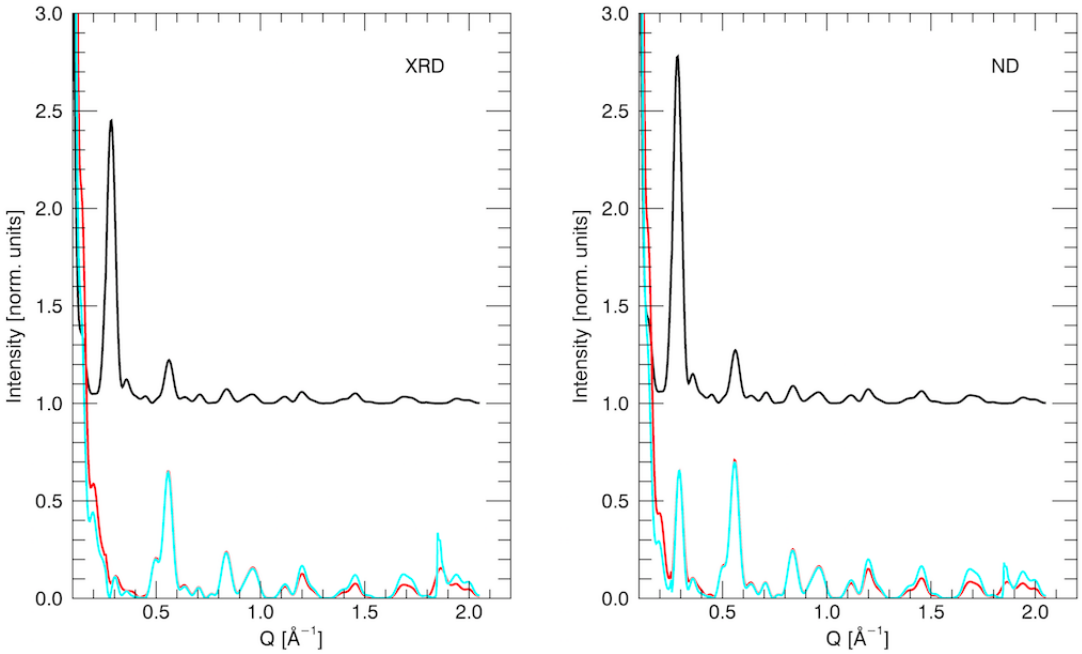

Figure 5.21 Diffraction diagram of the model discussed in the text for the FePc@NT21 sample. **Left-hand side:** for the X-Ray diffraction case, **Right-hand side:** for the neutron diffraction case. Red is the Hybrid sample, black the nanotube. Cyan is the same model as that shown in red but with a number of encapsulated 1D cells ten times larger.

Figure 5.21 shows the diffraction diagram calculated for a bundle consisting of nineteen tubes of diameter 23 Å, filled with disks of radius 6 Å packed into 30 (red) or 300 (cyan) 1D cells along the nanotube axis, with lattice parameter 3.4 Å. The diffraction diagram of the empty nanotubes are shown in black. The calculations were performed for X-Ray (left) and for neutron scattering. The molecular volume density is kept constant for neutron and X-Ray, the only change being the variation of contrast. One reproduces the same differences as those observed in the experimental diagrams when using neutron or X-Ray, see Fig. 5.15,

i.e. the (10) peak completely disappears for X rays while it is very strongly attenuated but still observed for neutron scattering. In addition, additional features, characteristic of the 1D structure, are observed around 1.85 $Å^{-1}$.

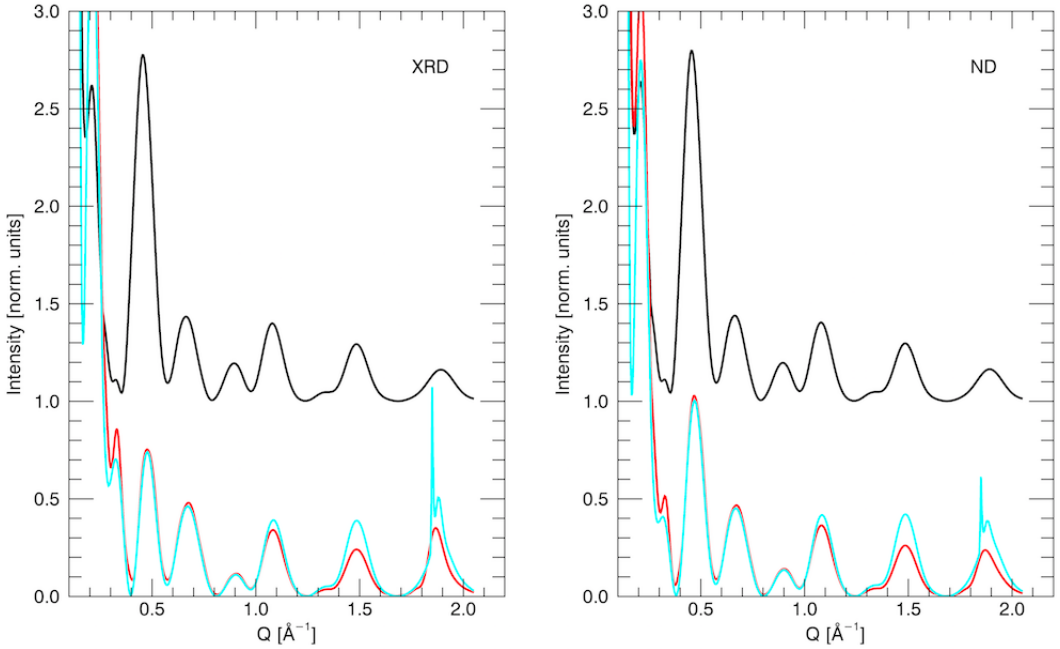

Figure 5.22 Diffraction diagram of the model discussed in the text for the FePc@NT14 sample. **Left-hand side:** for the X-Ray diffraction case, **Right-hand side:** for the neutron diffraction case. Red is the Hybrid sample, black the nanotube. Cyan is the same model as that shown in red but with a number of encapsulated 1D cells ten times larger.

Figure 5.22 shows the same representation for the diagrams calculated for a bundle consisting of seven tubes of diameter 14 Å, filled with disks of radius 6 Å packed into 30 (red) or 300 (cyan) 1D cells along the nanotube axis, with lattice parameter 3.4 Å. The diffraction diagram of the empty nanotubes are again shown in black. A relatively good agreement between the calculations and the X-ray and neutron data is obtained (see Figure 5.14) considering a molecular density equal to a third of that used for the FePc@NT21 simulations. For such density, the neutron and X-ray data show similar features, with a partial disappearance of the (10) peak in addition to a slight upshift (from 0.45 $Å^{-1}$ for the empty nanotubes, to 0.48 $Å^{-1}$ for the FePc@NT14 hybrid). Again, the low Q signal is independent of the chain length, the response of which is also concentrated around 1.85 $Å^{-1}$.

As a conclusion, we have re-interpreted the diffraction data using a numerical model. Our calculations tend to prove that the initial assignment of the feature observed in the neutron and X-ray data around 0.5 $Å^{-1}$ to the 1D lattice parameter of the confined FePc chain is wrong. Our models suggest that these features entirely occurs following a complex interference scheme from the atomic density inside the nanotube and the nanotube surface. Instead we propose that the excess of intensity observed in the diagrams in the 1.8 $Å^{-1}$ range originates from inter-FePc correlations. This Q range should be studied again using diffraction, and in particular its dependence with temperature and/or pressure.

5.4 High-pressure study of the structure of FePc@NT21 by Raman spectroscopy

In order to further investigate the confinement effect on the 1D FePc structure formed within the carbon nanotube, FePc@NT21 hybrids have been studied under pressure, though Raman scattering.

As the behaviour under pressure of encapsulated molecules is strongly correlated to its confinement matrix our interest will also include the pressure behaviour of nano-container. Several studies are reported in Literature about nanotube under pressure and also about peapods-like systems. We will firstly recall in the following section the main results concerning high pressure studies of these materials, a more detailed bibliography is found in Appendix C.

5.4.1 Carbon nanotubes and peapods at high-pressure: A State of the Art Review

Carbon nanotubes and peapods have been widely studied under pressure through Raman [205–210] and neutron scattering [211]. Today most studies converge towards the idea that nanotubes experience several modifications of their radial shape while increasing pressure with a first transition to an hexagonal and/or elliptical section and a second transition from elliptical to peanut or racetrack shape associated to the *collapse transition* for the nanotube [205, 211, 212]. The pressure associated to this transition decreases with increasing diameter of the nanotube [213]. Many factors seems to influence the pressure at which this transition is expected to appear such as bundling, nanotube opening, transmitting media [208, 209, 214–219].

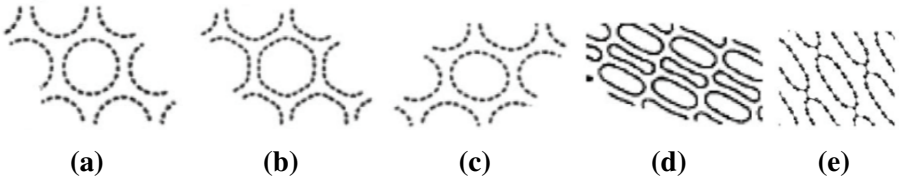

Figure 5.23 **(a)** Trigonal lattice of bundle of nanotubes at room pressure; **(b)** hexagonal poligonization; **(c)** Ovalized; **(d)** Racetrack-type and peanut-like; **(e)** 1D poligonization of ovalized nanotubes. Taken from reference [207]

In particular, when carbon nanotubes are filled, the collapsing pressure is expected to be delayed to higher pressures [220–223]. The molecules within the nanotube modify the dynamic of the nanotube and the collapsing process. Such effect was firstly demonstrated on peapods. Moreover, some coupled effects between the guest fullerene and the nanotube are observed after the first transition (1 GPa above) and for the second transition (downshift of G band and concomitant disappearance of the signal from C_{70}) [220]. Some interactions tube/guest are also reported for C_{60} [224].

To resume, from bibliographic results we could expect an early deformation in the case of NT21, as regard of their size, 1 GPa from reference [225]. Therefore effects on encapsulated FePc are expected at rather small pressure.

5.4.2 Pressure-dependence Raman scattering measurements

Raman experiments have been performed on the FePc@NT21 inside a diamond anvil cell using *ruby chips* as a pressure gauge and a mixture of 4:1 methanol/ethanol [226, 227] as a transmitting media. Experiments have been performed with an exciting laser wavelength of 633nm on a inVia Renishaw spectrometer.

We will first focus on the signal from the nanotubes, as we expect to see how they respond to the applied pressure. Secondly, we will study the signal from the encapsulated FePc, which is expected to respond to the modification undergone by the nanotube.

Figure 5.24 shows the Raman spectra in the region of the RBM modes for pressure ranging from [0.36, 10.31 GPa]. In the bottom graphic, both pristine and hybrid nanotubes at room pressure are recalled as a reference. The RBM mode is shown starting from 100 cm^{-1} because of the *notch filter* cutoff. Yet, it is possible to observe a strong decrease of the intensity of the RBM mode from 0.31 GPa followed by quenching between 3.6 GPa. and 4.4 GPa. Such effects have already been reported in literature and could be related to the loss of resonance due to the distortions undergone by the nanotube when its shape is modified

under applied pressure [228, 205, 229]. A simultaneous blue-shift of the RBM mode is also evidenced on figure 5.25.

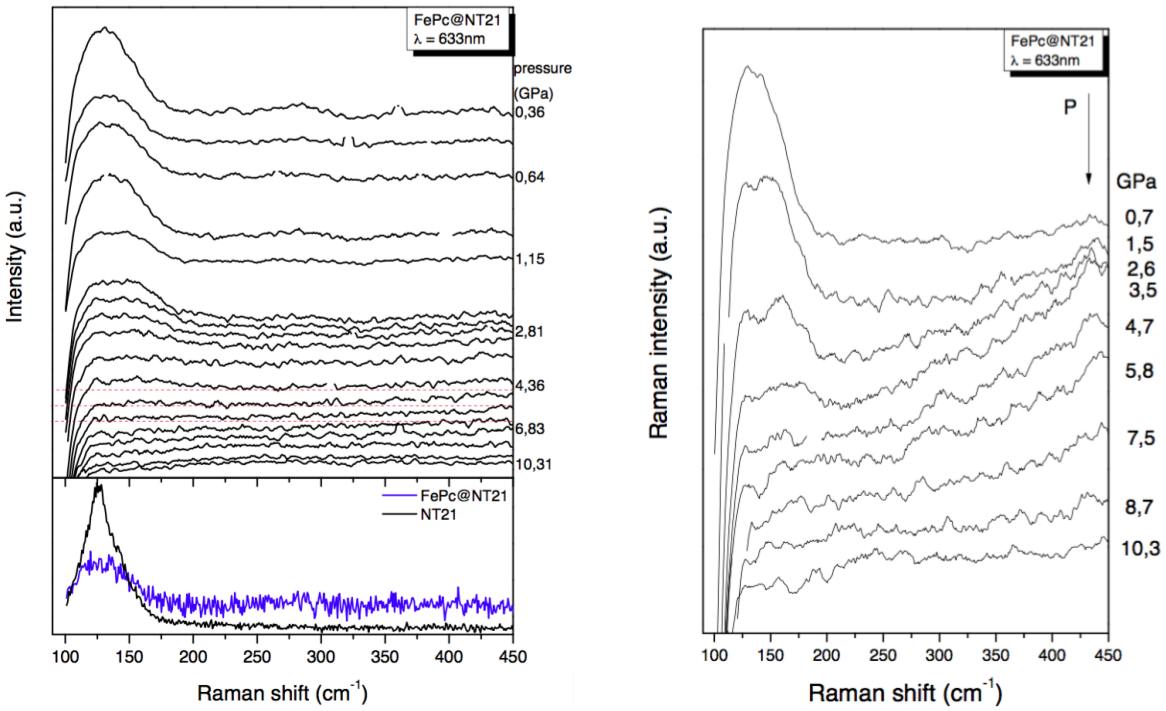

Figure 5.24 Left-hand side: RBM modes of FePc@NT21 for applied pressure. The quench of the RBM band is indicated by three red dotted horizontal lines which correspond to a pressure in the range [3.6,3.8 GPa]. Spectra of hybrid and pristine nanotubes are room pressure are recalled below. **Right-hand side:** RBM modes measure during decompression.

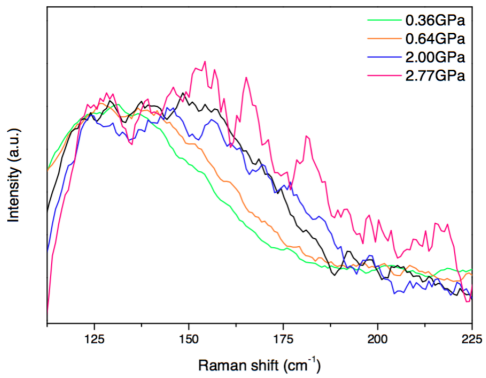

Figure 5.25 RBM modes shift for FePc@NT21 while pressure increases.

The G band, showing a semiconducting profile, is also monitored under applied pressure, see figure 5.26. As for the RBM modes, a strong decrease in intensity, associated to the loss of resonance, is observed. The ratio of RBM on G band is also plotted as an inset in the same figure, showing that RBM intensity is not absolutely following the same trend that G band.

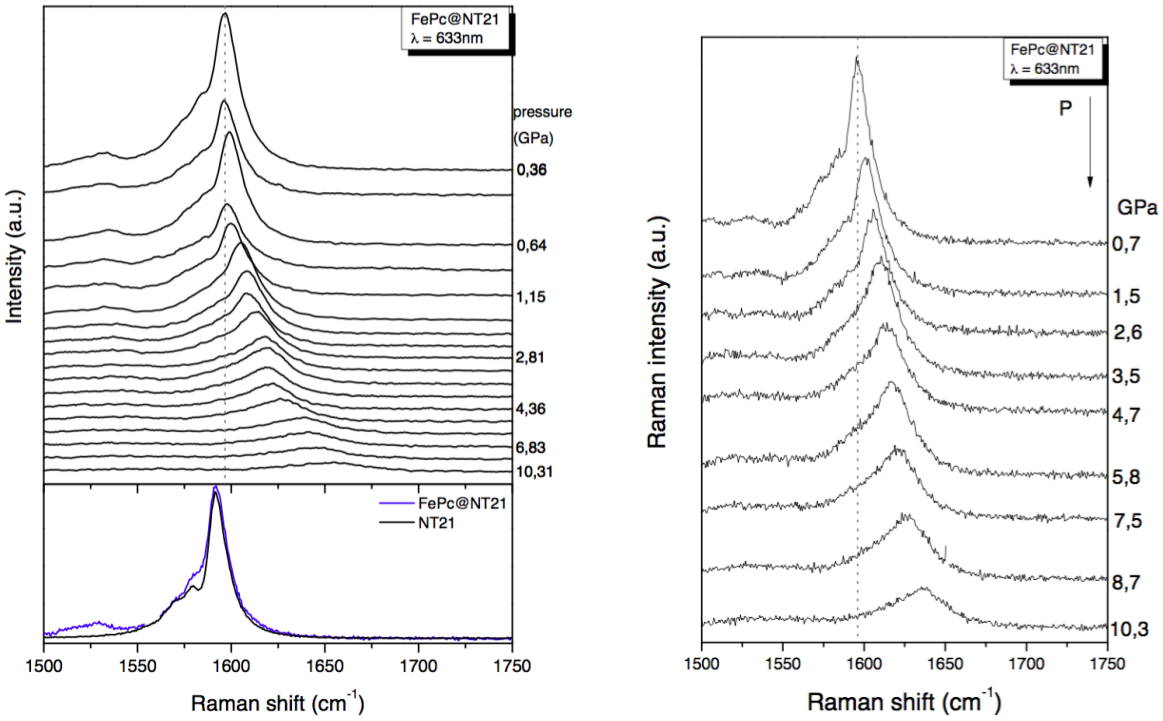

Figure 5.26 Left-hand side: Raman shift of the G band modes in the range of [1500, 1750 cm^{-1}] for compression measurements. Spectra of hybrid and pristine nanotubes are room pressure are recalled below. **Right-hand side:** Evolution of the G band frequency for decompression measurements.

The pressure dependence on figure 5.26 shows a strong redshift of the G band, consistent with a C-C bond hardening under pressure as reported in the literature [205, 228, 229].

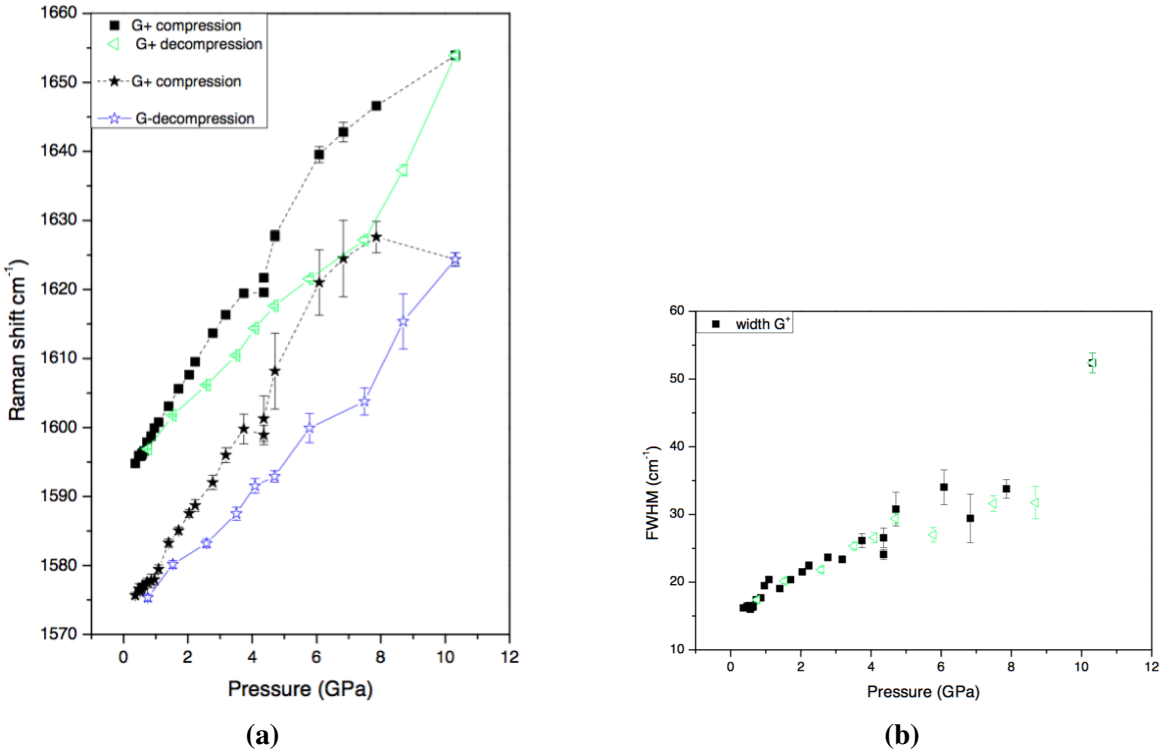

Figure 5.27 Left-hand side: Evolution of the TM modes with the applied pressure. Open green triangles correspond to G band shift while decreasing pressure. **Right-hand side:** FWHM of the G mode during compression (black symbols) and decompression (green symbols).

A strong slope is shown for the range [0, 6 GPa], with a small kink around 4 GPa. From 6 GPa the dependence appears with a weaker slope. In literature, a change in slope for G band is sometimes reported at collapse of the nanotube into a peanut-like structure, losing its 1D character [230, 207].

From these results, it appears that carbon nanotubes filled with FePc molecules are strongly modified under pressure. The RBM shape is modified around 1.5 GPa and quenches completely around 4 GPa. The G band exhibits a strong broadening in that pressure range as well. Therefore, below 1.1 GPa no significative modification could be detected for the nanotube (neutron diffraction, Raman). Above 1.5 GPa the first indications on the modification of the diametral shape of NT21 are shown.

It has been shown in the section 5.2.2, that when hybrid systems are excited at 633 nm, it is possible to get insight on the spectra of phthalocyanine molecules through its resonant signal. In order to understand the behaviour of the different Raman modes under pressure, we first focus on the assignment of the FePc main vibrational modes.

Assignment of Raman modes for isolated FePc molecule The Raman active vibrational modes for the isolated molecule of FePc are calculated with the module DMOL^3 [231, 232] present in the Materials Studio software [233]. The eigenvectors associated to the Raman active frequencies were assigned, according to the atomic designation shown in figure 5.28a.

Table 5.2 Calculated Raman active frequencies in the range [624.9, 1333.2 cm^{-1}] of an isolated planar molecule of FePc with their respective symmetry, activity and description of vibration.

Calculated frequency planar FePc	Symmetry	Approximative assignment
624.9	E_g	ρ_w(C$_\delta$-H) and ρ_t(C$_\gamma$-H)
634.4	E_g	ρ_t(C$_\gamma$-H)
646.4	B_{1g}	δ_{ip}(insoindole ring)
706.5	E_g	ρ_t(C$_\delta$-H) and ρ_t(C$_\gamma$-H)
721.8	B_{2g}	ν(Fe-N$_\alpha$) and ν(C$_\alpha$-N$_\beta$)
744.5	E_g	ρ_t(C$_\delta$-H) and ρ_w(C$_\gamma$-H)
754.8	B_{2g}	δ_{ip}(insoindole ring) and ν(Fe-N$_\alpha$)
790.8	A_{1g}	ν(Fe-N$_\beta$) and ν(Fe-N$_\alpha$)
792.4	E_g	ρ_t(C$_\delta$-H)
880.0	B_{1g}	ν(C$_\alpha$-N$_\beta$-C$_\alpha$)
956.4	B_{2g}	ρ_s(C$_\gamma$-H)
984.6	B_{1g}	ν(C$_\alpha$-N$_\alpha$-C$_\alpha$), ρ_r(C$_\gamma$-H) and ρ_r(C$_\delta$-H)
1042.0	B_{1g}	ρ_r(C$_\delta$-H) and ρ_r(C$_\gamma$-H)
1064.9	A_{1g}	ρ_s(C$_\delta$-H) and ρ_r(C$_\gamma$-H)
1078.6	B_{2g}	ρ_s(C$_\delta$-H) and ρ_r(C$_\delta$-H)
1119.9	B_{2g}	ρ_s(C$_\delta$-H)
1140.7	B_{1g}	ρ_s(C$_\gamma$-H)
1235.6	B_{1g}	ρ_r(C$_\delta$-H) and ρ_t(C$_\gamma$-H)
1260.6	B_{2g}	ρ_s(C$_\delta$-H) ρ_r(C$_\gamma$-H)
1268.3	A_{1g}	ν(Fe-N$_\alpha$) and ν(Fe-N$_\beta$)
1333.2	A_{1g}	ρ_r(C$_\gamma$-H) and ρ_s(C$_\delta$-H)
1523.3	B_{1g}	C$_\alpha$=N$_\beta$ and C$_\alpha$-N$_\beta$,macrocycle

Note: ρ_w: wagging; ρ_r: rocking; ρ_s: scissoring; ν: stretching; δ: deformation; ρ_t: twisting; *ip*: in-plane; *op*: out-of-plane; *iso*: isoindole group; *pyro*: pyrole group. Vibrational modes calculated for an isolated molecule of FePc.

Mostly, the vibrational modes observed in the range [600, 800 cm^{-1}] are characterized as C-H out-of-plane bending modes (wagging and twisting) whereas the range [900, 1300 cm^{-1}] is mainly characterized by C-H in-plane bending modes (rocking and scissoring) of atoms from the isoindole group at the periphery of the molecule. The stretching modes involving the central atom and the N atoms are expected at 721, 790 and 1268 cm^{-1}. The mode observed at 1524cm^{-1} involving C_α=N_β and C_α-N_β bonds from the macrocycle is reported in the literature as a good probe of interaction with different central atoms [234–236], see figure 5.28.

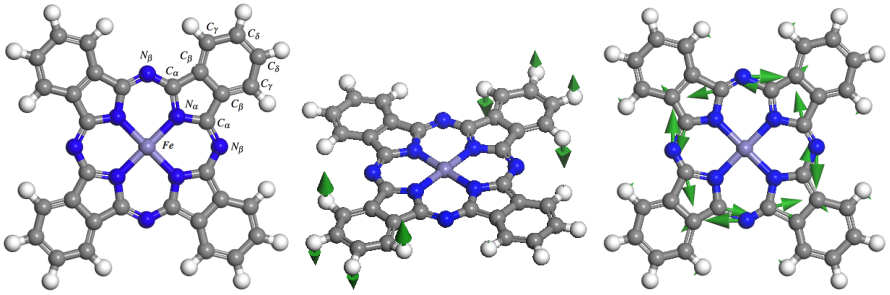

Figure 5.28 **(a)** Structure and atom designation for the isolated molecule of FePc. Vibrations corresponding to measured vibrational modes of the molecule inside the hybrid system: **(b)** Vibrational mode related to C-H wagging and twisting at 744.5 cm^{-1}. **(c)** Vibrational mode related to macrocycle at 1528 cm^{-1}.

Pressure-dependence of the encapsulated molecule Spectra showing the signatures of encapsulated FePc are shown on figure 5.29. Note that in the range of [1350, 1500 cm^{-1}], the spectra are mixed with from ruby luminescence and signal from diamond, therefore this region is not shown.

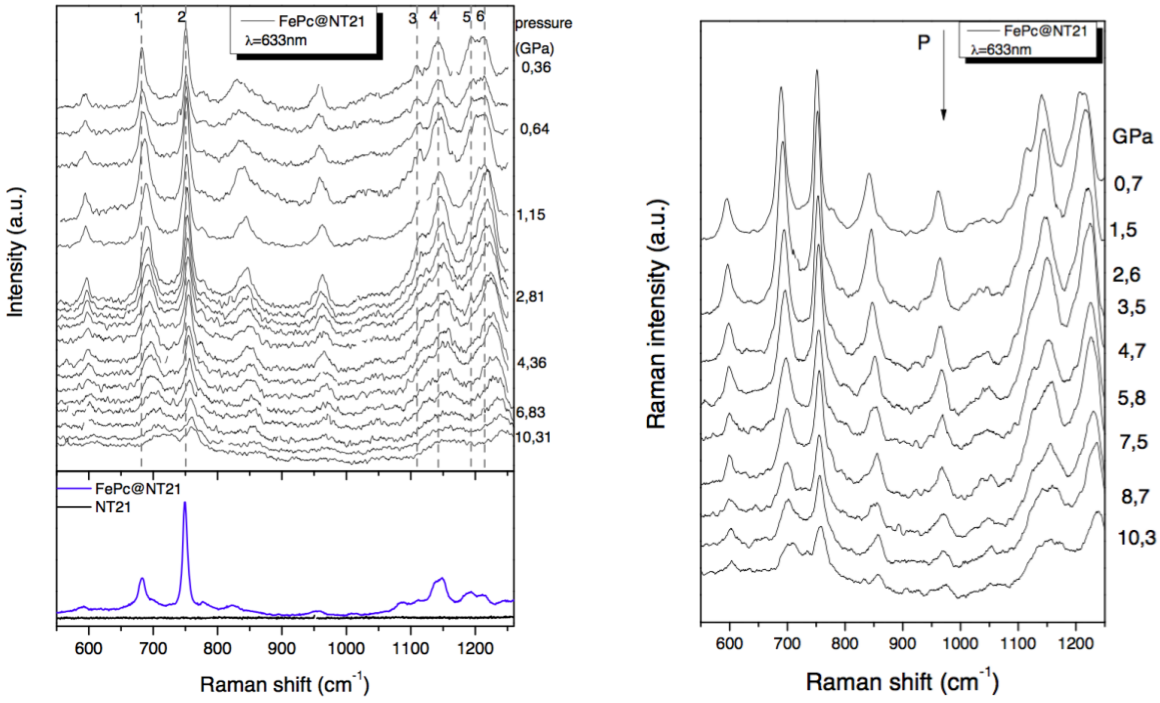

Figure 5.29 Left-hand side: Pressure-dependent Raman spectra of FePc@NT21 hybrid system with pressures indicated on the right side of the graphic. Spectra of hybrid and pristine nanotubes are room pressure are recalled below. **Right-hand side:** Pressure-dependent Raman spectra of FePc@NT21 hybrid system measure for decompression.

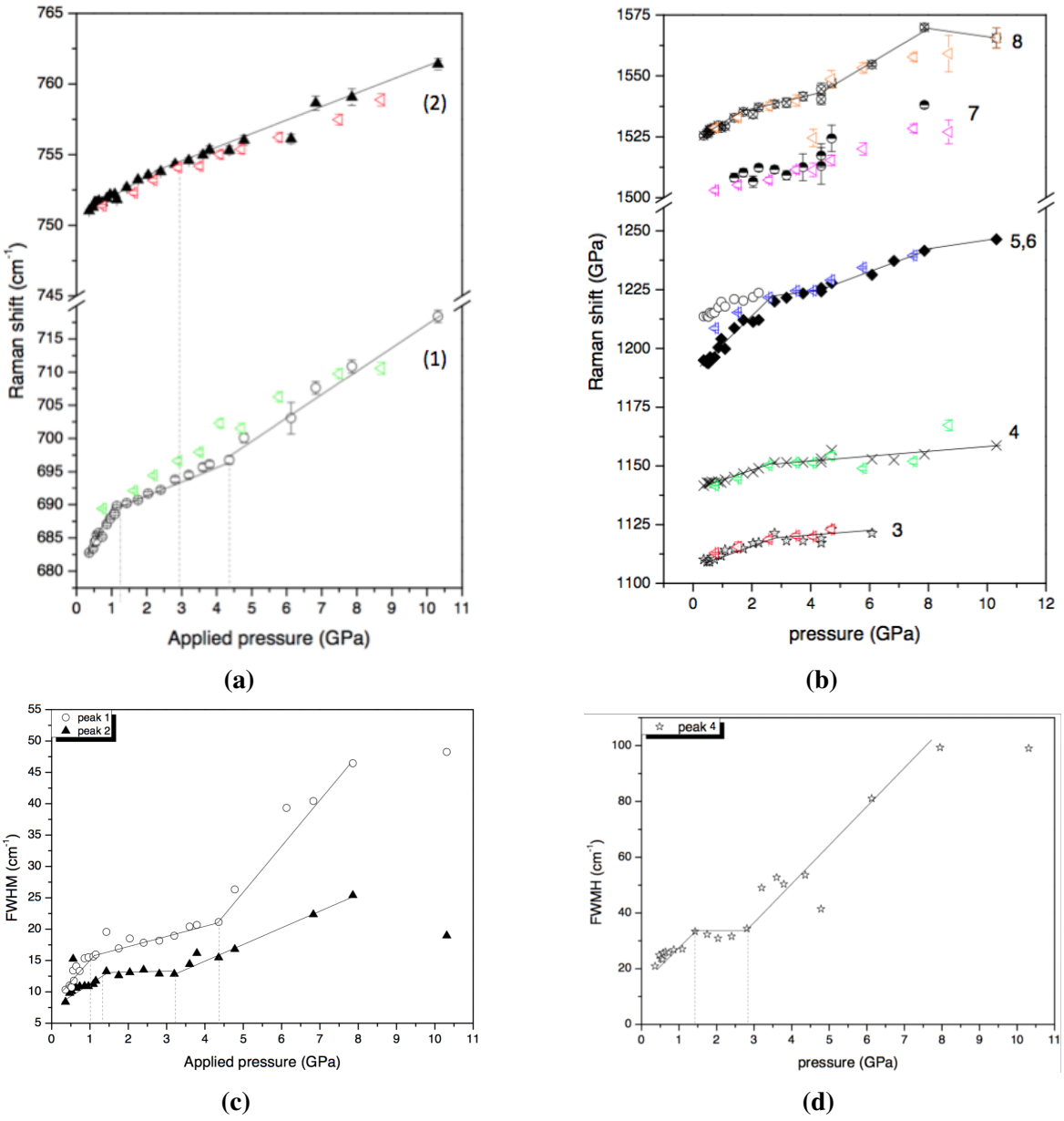

Figure 5.30 Raman shift upon applied pressure for: **(a)** peak one and two; **(b)** three to six. Obtained full-width at half maximum for **(c)** peaks one and two **(d)** peak three. The colored symbols correspond to the pressure release.

Most peaks are upshifted towards high wavenumbers with increasing pressure and at higher pressure a broadening is observed. Pressure dependences for the most intense vibrational bands from the encapsulated molecules are shown on figure 5.30. One can notice that different regimes are observed in the pressure dependence of peaks (1), (3), (4), (5) and (6).

For the doublet observed around 670 cm^{-1} the two peaks show distinct pressure dependences, see figure 5.30a. According to DFT simulations, the peak (1) is assigned to C-H twisting and wagging vibrations (calculated at 744 cm^{-1}). Up to 1.2 GPa a strong hardening of this vibrational mode is observed followed a weaker hardening regime is observed. A second change of slope takes place at 4.5 GPa. These three regimes are also found in the FWHM of the peak, figure 5.30c, showing that when the vibrational mode hardens, the peak broadens, which can be a sign for a distortion of the bonds or a higher dispersion.

The peak labeled (2) is assigned to the in-plane deformation of the isoindole groups and stretching of the Fe-N_α bond, calculated at 754 cm^{-1}. It shows monotonous pressure dependence. In addition, its FWMH also shows three different regimes (change of slope at 1.4 GPa and 3.2 GPa).

Peaks (3) and (4) are found in the region assigned C-H in-plane bending modes of atoms from the isoindole group at the periphery of the molecule (see calculated vibration at 1042 cm^{-1} and 1078 cm^{-1}, respectively). These components show a two regime behaviour with strong and moderate pressure dependences below and above [2.5, 3 GPa], respectively, see figure 5.30b.

The vibrational modes (5) and (6) correspond to scissoring of C-H bonds, calculated at 1119 cm^{-1} and 1140 cm^{-1}, respectively. The vibrational mode (5) exhibits an impressive slope up to 2.5 GPa, at this pressure it merges with the component (6) that has firstly been strongly shifted up to 1.2 GPa.

The vibrational mode (7) observed at 1524 cm^{-1} involving C_α=N_β and C_α-N_β bonds the macrocycle and is reported as strongly correlated to the position and nature of the central atom. When pressure increases this mode is upshifted.Around 1,2 Gpa a¨ new component (7) appears around 1508 cm^{-1}. Interestingly this new component has not disappeared after pressure release down to 0,75 GPa, as shown in figure 5.31.

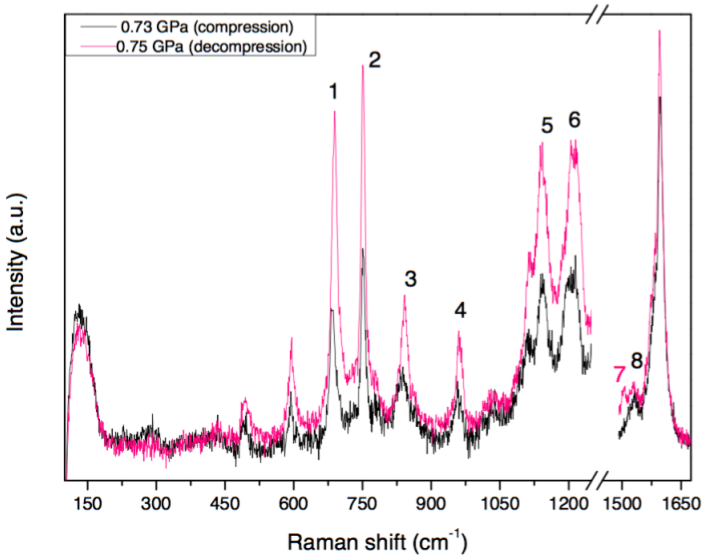

Figure 5.31 Raman spectra for FePc@NT21 hybrid compared around 0,75 GPa during compression and decompression. The additional feature (7) is still shown after pressure release.

To resume, one can notice that multiple regime pressure dependences are observed for C-H bending modes. For out-of-plane twisting and wagging, the first change occurs at 1.2 GPa while C-H scissoring vibrations is changes more likely to be observed at ∼2.5 GPa. Above 3 GPa, most of the components are strongly broadened.

Compression mechanisms from Raman spectroscopy Considering the results from both host nanotube and encapsulated FePc some hypothesis on the compression mechanism can be drawn.

- The nanotube signal exhibits some strong changes from 1.5 to 4 GPa, signing for a change of shape of the host nano-container. Therefore, we can suspect that over 1.5 GPa, the pressure constraint experienced by the host nanotubes is transmitted from nanotubes to the encapsulated molecules (radial compression exerted by the host nanotubes) see figure 5.32b.

- Below 1.5 GPa, nanotube diameter does not seems to be strongly modified by pressure consistently with diffraction results. Yet, for FePc molecules the pressure effects are observed as soon as pressure is applied, with strong hardening and simultaneous broadening of some modes. These early changes observed in FePc signal are likely to support the hypothesis that, as filled nanotubes are opened, transmitting media can

enter within nanotubes so that the pressure would be directly applied on molecules by the transmitting media, in the direction of CNT axis, see figure 5.32a.

- Above 3.5 GPa, the RBM signal is not detected anymore and the G band pressure dependence is modified. This behaviour could be interpreted by the collapse of the nanotube, as described in literature. Concomitantly, the out-of-plane vibrational mode (1) exhibits a stronger compression and higher dispersion from 4.2 GPa.

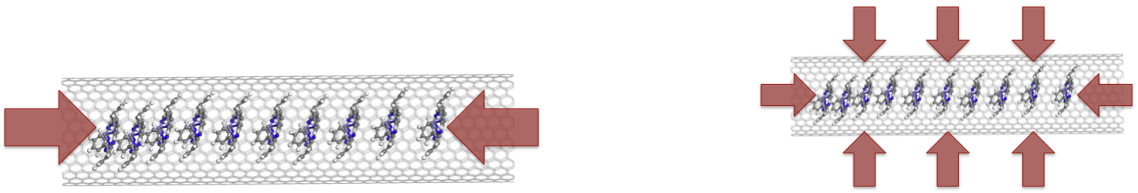

(a) Pressure below 1.5GPa.

(b) Pressure above 1.5GPa.

Figure 5.32 Schematic representation of the modifications undergone by the hybrid system upon pressure. **(a)** Compression of the encapsulated chain of FePc. **(b)** After compression of the chain, the nanotube suffers compression on its radial direction.

To summarize, Raman scattering on FePc@NT21 shows that host carbon nanotubes are barely affected by pressure above 1,5GPa (RBM). Above that pressure, the nanotube deformation induces a stronger confinement of the molecule. 3 compression regimes are observed for some vibrational modes. However, simulations are required to interpret the modification experienced by the guest 1D FePc structure in term of intermolecular distance, angular tilt and order parameter.

5.5 Conclusion

This chapter was dedicated to the study of the FePc@NT hybrid system, and particularly the confinement effect on the structural organization of these square-planar shaped molecules inside the host carbon nanotube. Some work from literature predict a 1D chain of aligned MPc molecules oriented with a tilt angle as compared to the nanotube axis. In order to better understand how this internal packing of the guest molecules is influenced by the diameter of the host nanotube and also the temperature conditions X-ray and neutron diffraction experiments have been coupled to simulations. This led us to give a new interpretation of the diffraction pattern of these hybrid systems. Firstly the peak appearing on the diffraction pattern at ~ 0.5 Å^{-1} called 1D peak, arises from the bundle lattice. Secondly, the broad

band appearing at high angles is related to the encapsulated structure, and characterized by distances around $\sim$ 3.4 Å similar to intermolecular distance in the crystal stacking. Therefore, it appears clearly that further temperature and pressure neutron diffraction investigations have to be planned in the future in an extended Q range covering this intermolecular distance. Preliminary Raman scattering pressure experiments have also been performed to give an overview of the pressure effect on the encapsulated FePc on a very wide range of pressure and have shown different compression regimes in correlation with the behaviour of the host nanotube. However, as all these experimental results were obtained very recently, the relevant analysis of the data still has to be achieved with the support of simulations.

Conclusion

The work done in this thesis was devoted to the confinement effect on dyes inside the hollow core of SWCNT as a function of the size of the nanocontainers.

The part I of this manuscript aimed at studying the interactions between encapsulated oligothiophene ($4TCH_3$) and SWCNT. We first (chapter 3) investigated of the vibrational dynamics of the encapsulated $4TCH_3$ molecules by means of inelastic neutron scattering taking advantage of the huge scattering cross section of hydrogen atom. We accessed here to energy transfer from 0 to 450 meV, thus probing both lattice and intramolecular dynamics. Experimental vDOS were compared to DFT calculations in order to assign the vibrational modes. The results indicate that the low frequency dynamics related to methyl libration is deeply affected by the confinement. As a matter of fact, a large degree of orientational disorder has been shown shown for methyl libration in this system, associated to a low symmetry of their local environment. Temperature dependence of INS results suggests the onset of long range ordering of the molecules inside the nanotube. These results are consistent with our models for which the methyl end termination are oriented along the tube axis, *i.e.* with minimal interaction with the nanotube wall, whatever its diameter. The thienylene out-of-plane bending modes frequencies upshifts when the tube diameter increases, thus showing sensitivity not only for encapsulation but also confinement. Based on our simulations, we suggest that the molecules's cycles align parallel to the inner nanotube surface. In larger tube (diameter around 14 Å), this configuration minimizes of the C-H_{methyl}-π_{NT} interactions and a maximizes C-$H_{thienylene}$-π_{NT} and $\pi_{thienylene}$-$\pi_{(NT)}$ interactions. For small tubes, below the critical diameter of 1.1 nm, our results suggest that $\pi_{thienylene}$-π_{NT} are not anymore the dominant key factor of the interactions.

In chapter 4, the potential interactions between both subsystems in terms of energy transfers and charge transfers were studied using an experimental approach combining photoluminescence and Resonant Raman scattering. Through our investigation, no energy transfer between oligomer and nanotube is exhibited. However, electron transfer from the confined dies to the nanotubes is shown for tube diameter below around 11 Å. This charge transfer leads to an important enhancement of the photoluminescence intensity by a factor

of nearly five depending on the tube diameter. Moreover, charge transfer between both subsystems is deeply affected when increasing the diameter. Our results suggest that, for tube diameters below around 11 Å, the transfer is significant as only one $4TCH_3$ is encapsulated inside the hollow core of the tube. In addition, close to the molecule resonance, through the analysis of G band intensity and shift, a photo-induced electron transfer is suggested for these small tubes. In $4TCH_3$@SWNT where nanotube are defective, we showed that metallic nanotubes recover electron phonon coupling after endohedral functionalization. Therefore, it suggests that the confined species enable a change of position for the Fermi level of defective nanotubes, thus allowing to monitor their opto-electronic properties. For larger nanotube diameter neither negative electronic charge transfer is foreseen from DFT calculations and nor negative charge transfer can be proven from Raman results due competition between the non adiabatic effect and lattice contraction. The results suggest that the nature of the charge transfer between the nanotubes and the $4TCH_3$ molecules in these hybrid nanotubes could be modulated by confinement effects changing the diameter of the nanotube.

In the part II of the thesis, we present different hybrid systems where FePc macrocycles are encapsulated within single wall carbon nanotube. For this exploratory work, the confinement effects on the structural properties of the encapsulated macrocycles have been studied through neutron diffraction. We first show that for confinement matrices of diameter 14 Å and 21 Å, a signature of the structural order appears for the encapsulated species. In a second time, a modulation of the confinement as a function of pressure has been investigated through neutron diffraction up to 1.4 GPa and Raman scattering up to 11 GPa for the FePc encapsulated in nanotubes within the largest container (21 Å). The evolution of the confined species (structure and dynamic) are discussed concomitantly with the modifications of the nanotube under pressure.

Part III

Appendices

Appendix A

Detailed vibrational dynamics of $4TCH_3$ in the gas phase

Contents

A.1 Starting model

The DFT-simulated HPDOS were performed in the framework of the PhD thesis of A. Belhboub [108]. The calculations were performed using the SIESTA code, with the non-conservative pseudo-potential (PSP). The calculations were performed only in the Brillouin zone center, at the Γ point. The models that were used in order to perform the DFT calculations are shown in Figure A.1:

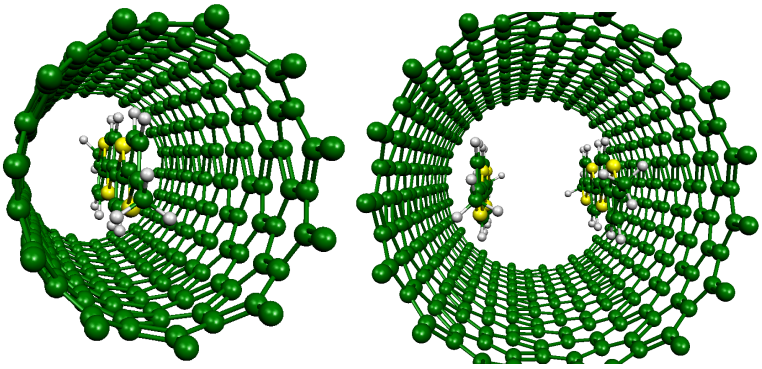

(a) $4TCH_3$@(11,0), with 308 atoms of carbon belonging to the (11,0) nanotube with diameter 8.73 Å.

(b) $4TCH_3$@$(17,0)$, with 476 atoms of carbon belonging to the (17,0) nanotube with diameter 13.49 Å.

Figure A.1 The $4TCH_3$ molecule is shown in Figure A.2 with more details. The number of atoms per encapsulated molecule is: 18 atoms of carbon (green), 14 atoms of hydrogen (white) and 4 atoms of sulphur (yellow).

Before commenting about the vDOS of both encapsulated molecules, it is important to understand the dynamics of the isolated molecule (which is subjected to no confinement). In particular, the energy distribution of the molecular modes which is related to the symmetry of the $4TCH_3$ molecule. For that reason, we remind some results obtained in the framework of the PhD Thesis of P. Hermet [237], on the dynamics of 4T in the crystalline phase.

A.2 Dynamics of the molecule of $4TCH_3$ in the gas phase

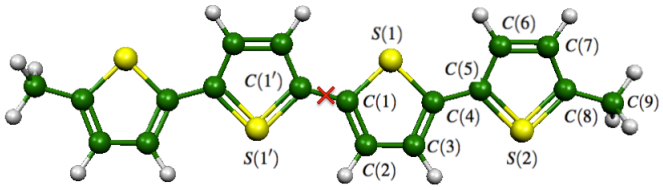

Figure A.2 Atomic structure of the isolated $4TCH_3$. The symmetry center of the molecule is located at the center of it (red x at the center of the molecule). With molecular length assumed to be the C(9)-C(9') distance of (17.203 Å) plus twice the methyl van der Waals radius (Å). The carbon atoms C(2), C(3), C(6), C(7) as well as its symmetric ones are called C_β whereas the carbon atoms C(1), C(4), C(5), C(8) and C(9) and its respective are called C_α.

The molecular point group in the hypothesis of the planar $4TCH_3$ molecule is C_{2h}. The symmetry elements present in this point group are:

- E: identity,
- C_2: proper axis of rotation,
- σ_h: reflexion and mirror plane, perpendicular to the principal rotation axis of symmetry,
- S_2: improper axis of rotation,
- i: inversion center.

The presence of a center of symmetry in these molecules induces the mutual exclusion of the activity of infrared (A_u and B_u) and Raman (A_g and B_g) modes [129]. Where the A (B) is symmetric (antisymmetric) with respect to the principal rotation axis of symmetry and the subscripts g (u) corresponds to symmetric (antisymmetric) to the center of symmetry. INS allows to access all vibrational modes of the molecule. Figure A.2 shows the structure of the isolated (gas phase) $4TCH_3$ molecule used for the DFT simulations with its named atoms. The vibrational modes of the $4TCH_3$ molecule are summarized in the table A.1. All in all, the molecule has 102 vibrational modes. For which, 67 modes are Raman-active and 35 are Infrared-active.

Table A.1 Distribution of the normal modes for the dimethyl-quatherthiophene molecule. Taken from reference [238].

Symmetry	**Optical activity**	**Number of normal modes**
A_g	Raman	34
B_g	Raman	17
A_u	Infrared	18
B_u	Infrared	33

The figure A.3 shows the entire range of simulated vibrational bands for the isolated molecule of $4TCH_3$. There are sharp and peaks in the range of [0-200 meV], followed by a gap (between 200 and 350 meV) and later, some additional peaks in the range [350-400 meV]. The vDOS of the isolated molecule is hereafter divided into three main domains for the sake of simplicity. The small energy transfer domain: [0-60 meV], followed by the medium energy transfer domain, from [60-200 meV]. And at last, the large energy transfer domain: [300-450 meV] is dominated by the stretching of C-H bonds belonging to thienylene rings as well as the aliphatic C-H_3 termination ends.

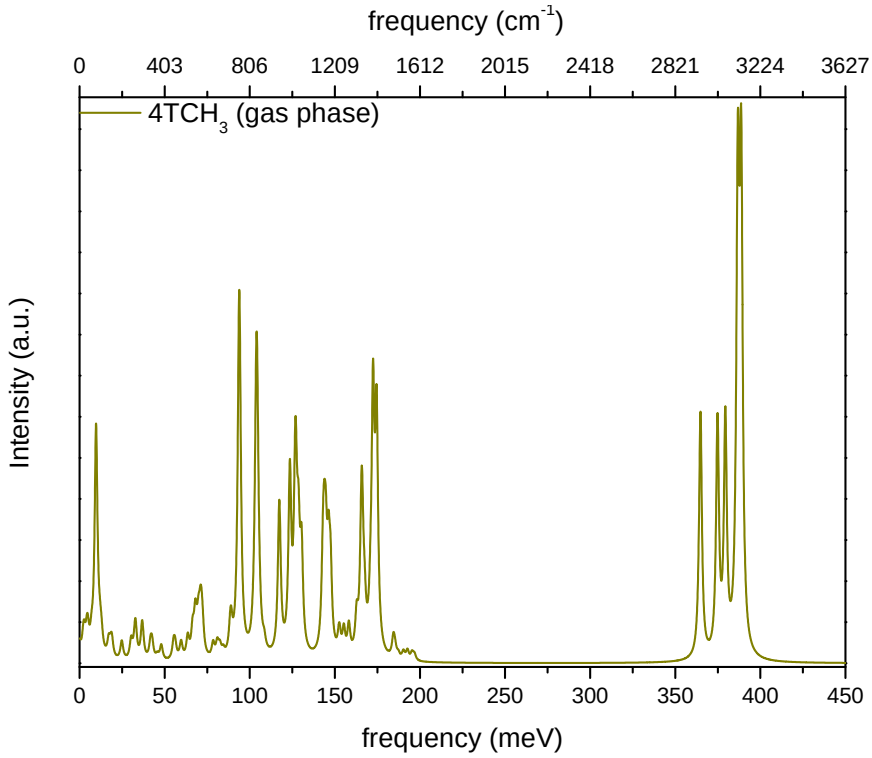

Figure A.3 Calculated HPDOS from [0-450 meV] or [0-483.6 cm^{-1}] of an isolated molecule of $4TCH_3$.

Let us start discussing the modes at the range of small energy transfer vibrational modes of the isolated molecule.

A.2.1 Dynamics of the molecule of $4TCH_3$ in the small energy transfer domain

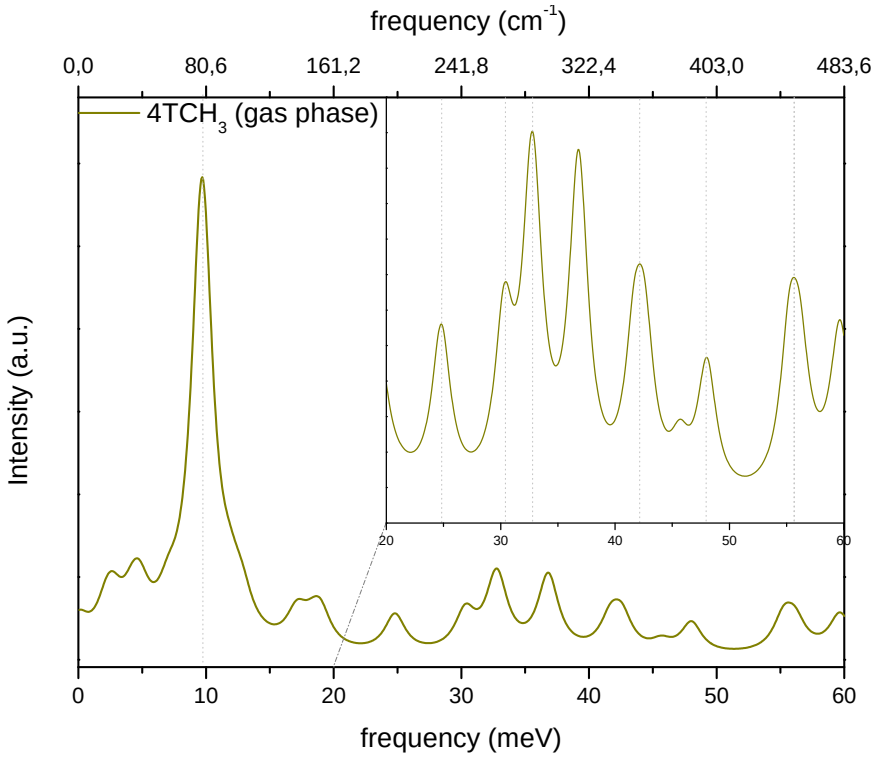

Figure A.4 Calculated HPDOS from [0-60 meV] or [0-483.6 cm^{-1}] of an isolated molecule of $4TCH_3$.

The figure A.4 shows the calculated HPDOS from DFT simulations. The small energy transfer domain comprises the vibrational bands in the range [0-60 meV]. In this energy transfer region, a first and intense vibrational peak, observed at 10meV corresponds to the libration of the aliphatic methyl groups from the $4TCH_3$ (see figures A.5g and A.5h). All the other vibrational features are less intense, as the reader can see in the inset of figure A.4. All vibrational modes comprised in this energy transfer range are described in the table A.2 with respective pictures of Eigenvectors in the figures A.5 and A.6.

Table A.2 Calculated frequencies from [0-60 meV] or [0-483.6 cm^{-1}] of an isolated molecule of $4TCH_3$ with their respective symmetry, activity and description of vibration.

Frequency in meV (cm^{-1})		**Symmetry**	**Optical**	**Approximative**
SIESTA	**DMOL3**		**activity**	**assignment**
2.2 (17.8)	-	-	-	$\rho_w(C_\beta\text{-}C_\beta)$ and $\rho_w(S)$
2.7 (21.9)	1.2 (10.1)	B_g	Raman	ring libration
4.2 (33.9)	1.3 (11.0)	A_u	Infrared	$\rho_w(S)_{\text{inner}}$
4.6 (37.6)	3.6 (28.8)	A_u	Infrared	whole chain libration
4.8 (39.2)	3.9 (31.4)	B_u	Infrared	in-plane rotation
7.0 (56.9)	7.0 (56.7)	B_g	Raman	ring and CH_3 libration
9.6 (77.8)	(80.8)	A_g	Raman	libration of CH_3
9.7 (78.5)	(90.2)	A_u	Infrared	libration of CH_3
11.8 (95.7)	11.6 (93.0)	B_g	Raman	in-plane ring rotation
12.8 (103.3)	12.8 (103.1)	A_u	Infrared	ring rotation
17.1 (138.1)	17.1 (136.8)	B_u	Infrared	inner rings rotation
18.3 (147.8)	18.0 (144.4)	B_g	Raman	translational mode
18.9 (152.9)	18.2 (145.7)	A_g	Infrared	in-plane ring rotation
24.8 (200.0)	25.2 (202.2)	A_u	Infrared	$\delta(CH_3)$
30.3 (244.5)	31.2 (249.7)	B_g	Raman	butterfly mode and $\delta(CH_3)$
32.6 (263.4)	31.9 (263.6)	B_u	Infrared	$\nu(C_\alpha\text{-}S\text{-}C_\alpha)$ and $\delta(CH_3)$
32.9 (265.6)	33.3 (266.9)	A_g	Raman	in-plane ring rotation and $\delta(CH_3)$
36.7 (296.2)	37.4 (299.6)	B_u	Infrared	butterfly mode
36.9 (297.5)	37.5 (300.2)	B_u	Infrared	translational mode inner rings
41.7 (336.3)	42.1 (336.9)	B_g	Infrared	in-plane ring rotation and $\nu(C_\alpha\text{-}S)_{inner}$
42.6 (343.4)	43.7 (349.6)	B_g	Raman	butterfly mode
45.7 (368.3)	46.41 (371.3)	A_g	Raman	ring torsion
48.0 (387.4)	48.9 (391.5)	B_u	Infrared	in-plane ring rotation
55.3 (445.7)	56.7 (454.1)	A_g	Raman	inner ring rotation
56.1 (452.8)	57.7 (462.1)	A_u	Infrared	$\delta(C_\alpha\text{-}S\text{-}C_\alpha)$
59.6 (481.1)	61.7 (494.0)	B_g	Raman	$\rho_t(C_\alpha\text{-}S\text{-}C_\alpha)$

Note: ρ_w: wagging; ν: stretching; δ: deformation; ρ_t: twisting.

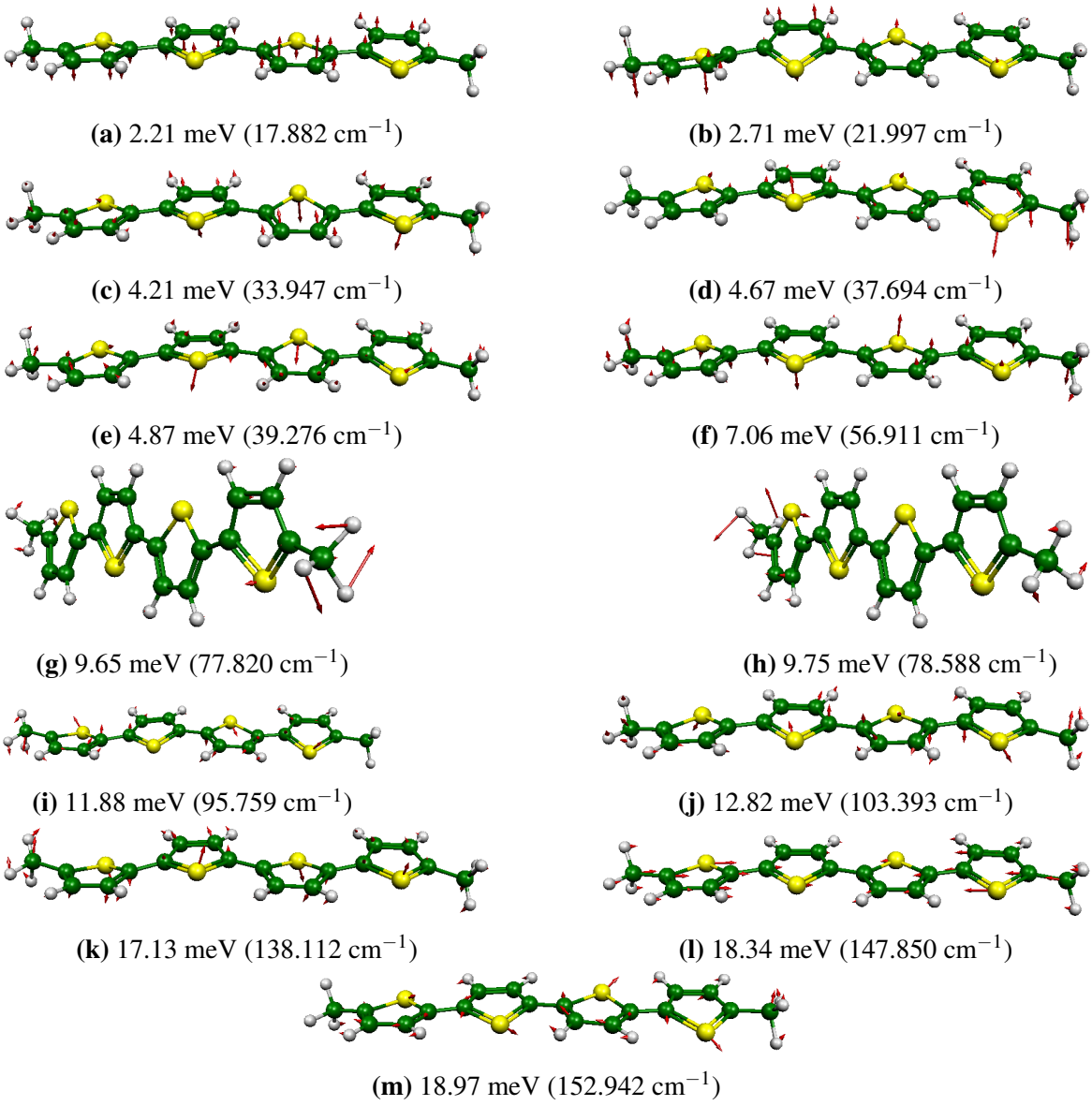

(a) 2.21 meV (17.882 cm^{-1})

(b) 2.71 meV (21.997 cm^{-1})

(c) 4.21 meV (33.947 cm^{-1})

(d) 4.67 meV (37.694 cm^{-1})

(e) 4.87 meV (39.276 cm^{-1})

(f) 7.06 meV (56.911 cm^{-1})

(g) 9.65 meV (77.820 cm^{-1})

(h) 9.75 meV (78.588 cm^{-1})

(i) 11.88 meV (95.759 cm^{-1})

(j) 12.82 meV (103.393 cm^{-1})

(k) 17.13 meV (138.112 cm^{-1})

(l) 18.34 meV (147.850 cm^{-1})

(m) 18.97 meV (152.942 cm^{-1})

Figure A.5 eigenvectors (read arrows) representing normal vibrational modes of the isolated molecule of $4TCH_3$. Vibrational modes from [0-60 meV] or [0-483.93 cm^{-1}], where the frequencies comes from DFT simulations.

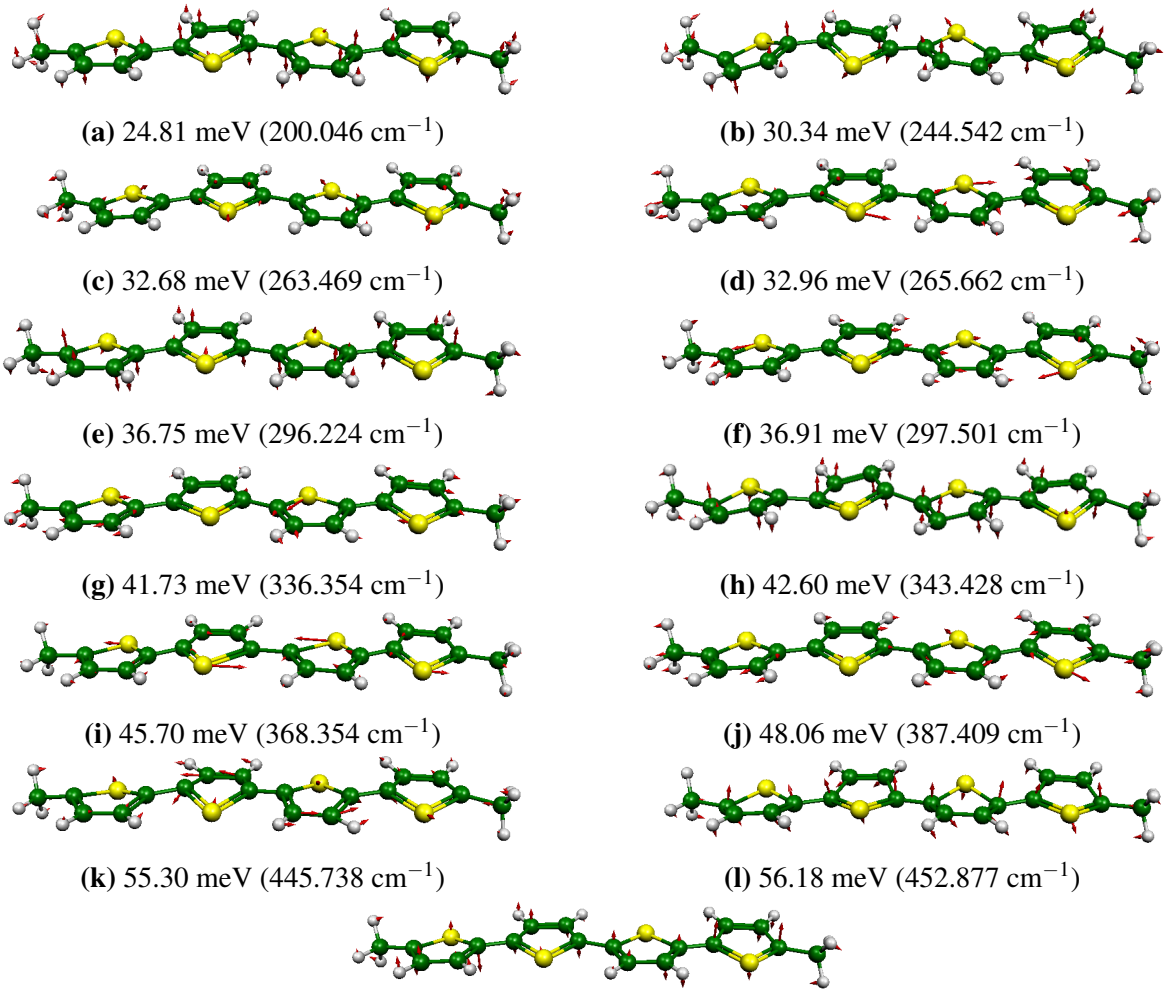

Figure A.6 eigenvectors (read arrows) representing normal vibrational modes of the isolated molecule of $4TCH_3$. Vibrational modes from [0-60 meV] or [0-483.93 cm^{-1}], where frequencies comes from DFT simulations.

A.2.2 Dynamics of the molecule of $4TCH_3$ in the medium energy transfer domain

The figure A.7 shows the calculated HPDOS from DFT simulations at the medium energy transfer domain, which comprises vibrational bands in the range [60-200 meV]. The first feature is located at 71 meV, followed by two intense ones at 93 meV and 103 meV. After that, distinct features are located at 117 meV, 123 meV 126 meV, 143 meV, 165 meV, 172 meV and 174 meV. All vibrational modes comprised in this energy transfer range are described in

the tables A.3 and A.4 with respective pictures of Eigenvectors of the molecule in figures A.8, A.9, A.10 and A.11.

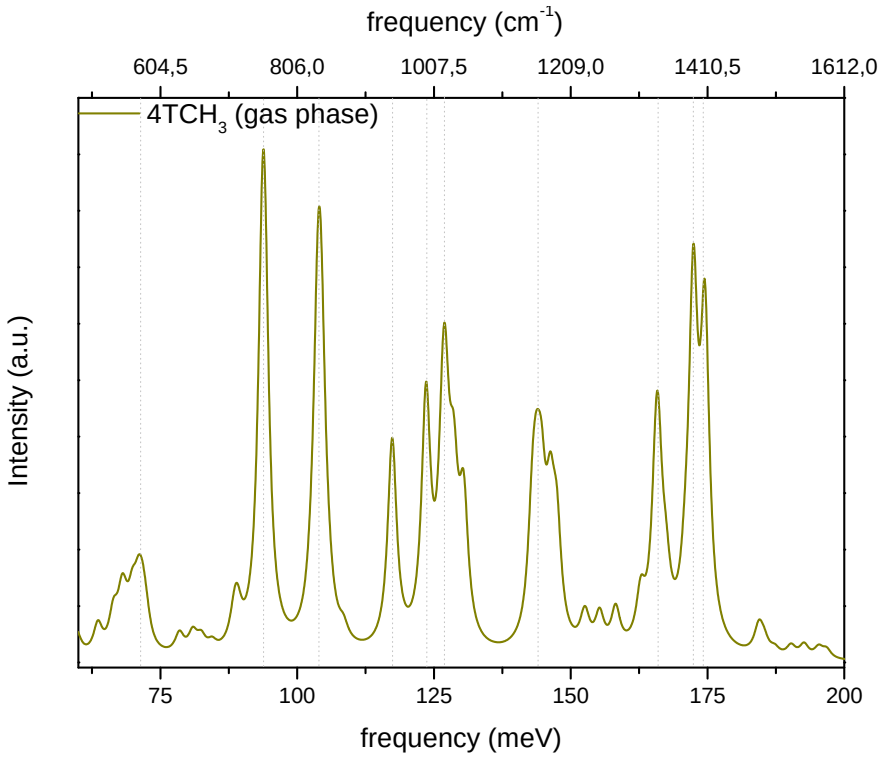

Figure A.7 Calculated HPDOS from [60-200 meV] or [483.6-1612 cm^{-1}] of an isolated molecule of $4TCH_3$.

Table A.3 Calculated frequencies from [60-200 meV] or [483.6-1612 cm^{-1}] of an isolated molecule of $4TCH_3$ with their respective symmetry, optical activity and approximative assignment.

Frequency in meV (cm^{-1})		**Symmetry**	**Optical**	**Approximative**
SIESTA	**DMOL3**		**activity**	**assignment**
63.61 (512.6)	65.9 (527.9)	A_u	Infrared	$\rho_t(C_\alpha\text{-}C_\beta)_\pi$
66.46 (535.7)	68.76 (550.1)	B_g	Raman	$\rho_t(C_\alpha\text{-}C_\beta)_\pi$
68.01 (548.2)	70.8 (566.4)	B_u	Infrared	$\rho_t(C_\alpha\text{-}C_\beta)_\pi$
68.55 (552.5)	70.8 (566.7)	B_u	Infrared	$\nu(C_\alpha\text{-S-}C_\alpha)$
69.91 (563.5)	72.22 (577.8)	B_g	Raman	$\rho_t(C_\alpha\text{-}C_\alpha)$
71.00 (572.3)	74.0 (592.5)	A_u	Infrared	$\rho_t(C_\alpha\text{-}C_\alpha)_{outer}$
71.6 (577.6)	74.5 (596.1)	A_g	Raman	$\rho_t(C_\alpha(\text{-}C_\beta)_{inner}$
72.3 (583.3)	74.6 (597.1)	B_g	Raman	$\nu(C_\alpha\text{-}CH_3)$
78.5 (632.9)	81.4 (651.3)	B_u	Infrared	$\nu(C_\alpha\text{-S-}C_{alpha})$
80.9 (652.6)	84.5 (676.5)	A_g	Raman	$\nu(C_\alpha\text{-S-}C_\alpha)_{outer}$
82.5 (665.0)	86.0 (688.2)	B_u	Infrared	$\nu(C_\alpha\text{-S-}C_\alpha)_{outer}$
84.4 (680.9)	87.8 (702.4)	A_g	Raman	$\nu(C_\alpha\text{-S-}C_\alpha)_{inner}$
88.5 (713.5)	92.1 (737.4)	A_g	Raman	$\nu(C_\alpha\text{-S-}C_\alpha)_{inner}$
88.7 (715.3)	92.4 (739.5)	B_u	Infrared	$\nu(C_\alpha\text{-S-}C_\alpha)_{inner}$
89.1 (718.4)	92.6 (741.5)	B_u	Infrared	$\nu(C_\alpha\text{-S-}C_\alpha)_{outer}$
89.2 (718.9)	92.7 (741.6)	A_g	Raman	$\nu(C_\alpha\text{-S-}C_\alpha)_{outer}$
93.5 (754.8)	95.4 (763.8)	A_u	Infrared	$\rho_w(C_\beta\text{-H})_{inner}$
93.7 (755.4)	95.5 (764.4)	B_g	Raman	$\rho_w(C_\beta\text{-H})_{inner}$
94.1 (758.5)	96.0 (768.2)	A_u	Infrared	$\rho_w(C_\beta\text{-H})_{outer}$
94.1 (758.6)	96.11 (768.9)	B_g	Raman	$\rho_w(C_\beta\text{-H})_{outer}$
102.7 (828.4)	106 (848.0)	A_u	Infrared	$\nu(C_\alpha\text{-S-}C_\alpha)_{inner}$
103.7 (836.2)	106.2 (850.1)	B_g	Raman	ρ_t(C-H)
103.9 (837.7)	106.8 (854.9)	A_u	Infrared	$\rho_t(\text{C-H})_{outer}$
104.2 (840.5)	107.0 (856.3)	B_u	Infrared	ρ_t(C-H)
104.6 (843.1)	107.1 (857.5)	B_g	Raman	$\rho_t(\text{C-H})_{inner}$
105.7 (852.4)	109.7 (877.7)	A_g	Raman	$\nu(\text{S-}C_\alpha\text{-}C_\alpha)$
108.5 (874.9)	112.3 (899.0)	A_g	Raman	$\rho_s(\text{C-C})_{inner}$
117.4 (946.3)	119.1 (953.5)	A_g	Raman	$\delta(CH_3)$
117.4 (947.0)	119.1 (953.7)	B_u	Infrared	$\delta(CH_3)$
123.6 (996.4)	125.9 (1007.5)	A_u	Infrared	$\delta(CH_3)_{both}$
123.6 (996.7)	125.9 (1007.5)	B_g	Raman	$\delta(CH_3)_{both}$

Note: ν: streching; δ: deformation; ρ_w: wagging; ρ_t: twisting. The subscripts correspond to π: out-of-plane; as (s): antisymmetric (symmetric) and outer (inner): the two outer (inner) thienylene rings.

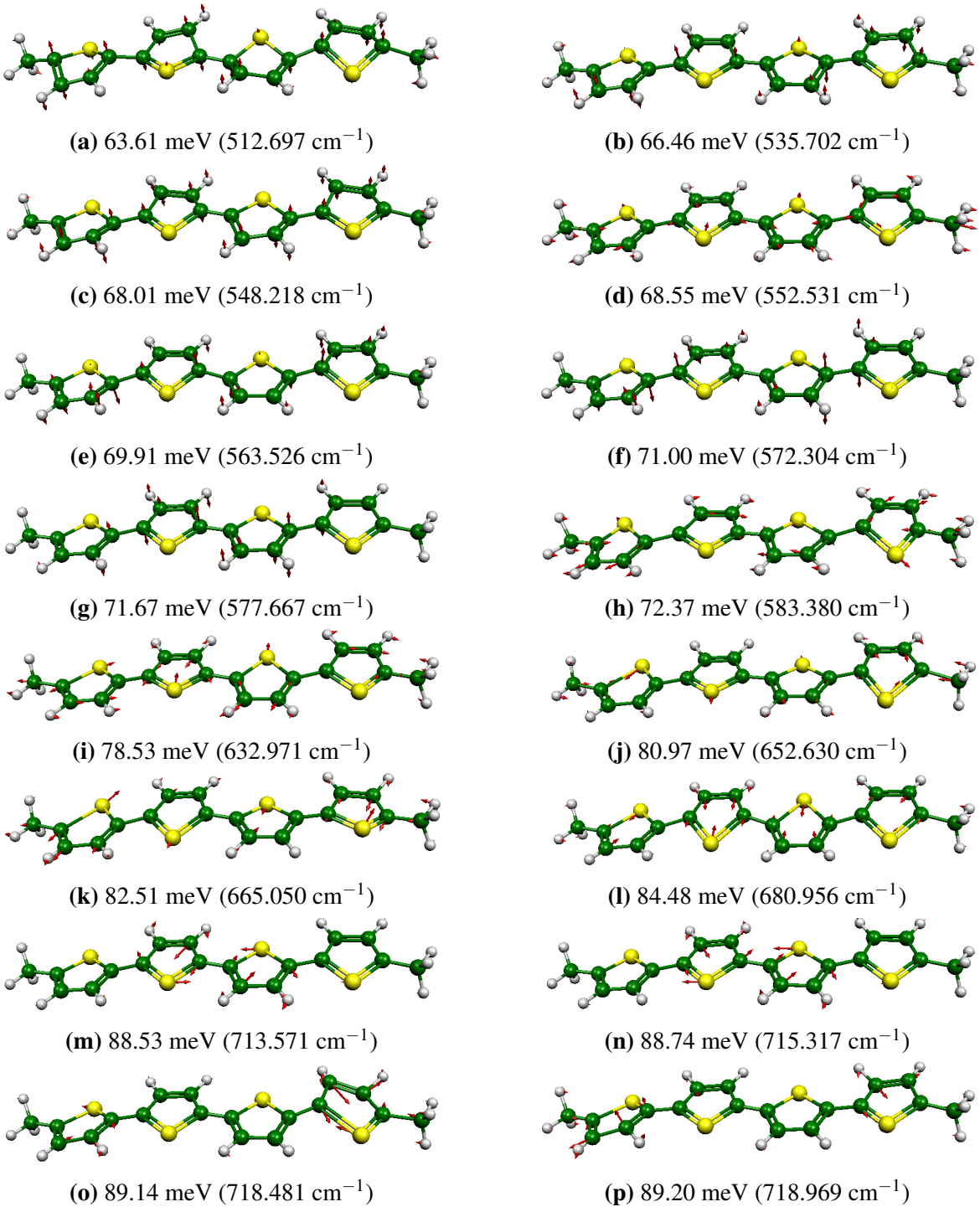

(a) 63.61 meV (512.697 cm^{-1})

(b) 66.46 meV (535.702 cm^{-1})

(c) 68.01 meV (548.218 cm^{-1})

(d) 68.55 meV (552.531 cm^{-1})

(e) 69.91 meV (563.526 cm^{-1})

(f) 71.00 meV (572.304 cm^{-1})

(g) 71.67 meV (577.667 cm^{-1})

(h) 72.37 meV (583.380 cm^{-1})

(i) 78.53 meV (632.971 cm^{-1})

(j) 80.97 meV (652.630 cm^{-1})

(k) 82.51 meV (665.050 cm^{-1})

(l) 84.48 meV (680.956 cm^{-1})

(m) 88.53 meV (713.571 cm^{-1})

(n) 88.74 meV (715.317 cm^{-1})

(o) 89.14 meV (718.481 cm^{-1})

(p) 89.20 meV (718.969 cm^{-1})

Figure A.8 eigenvectors (read arrows) representing normal vibrational modes of the isolated molecule of $4TCH_3$. Vibrational modes in the range [60-200 meV] or [483.6-1612 cm^{-1}], where frequencies comes from DFT simulations.

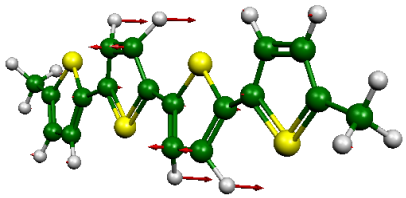

(a) 93.59 meV (754.841 cm^{-1})

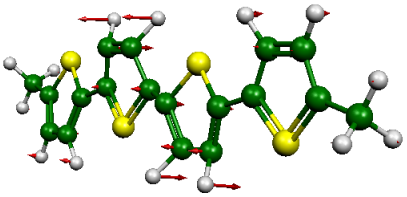

(b) 93.72 meV (755.409 cm^{-1})

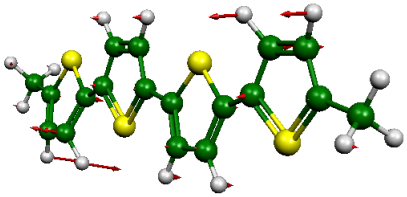

(c) 94.11 meV (758.562 cm^{-1})

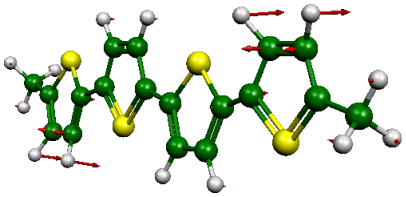

(d) 94.12 meV (758.636 cm^{-1})

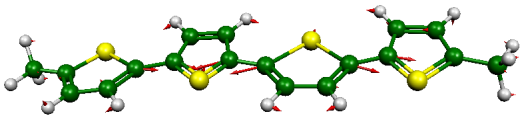

(e) 102.78 meV (828.411 cm^{-1})

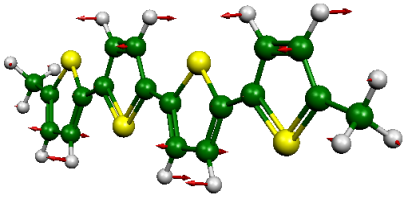

(f) 103.74 meV (836.219 cm^{-1})

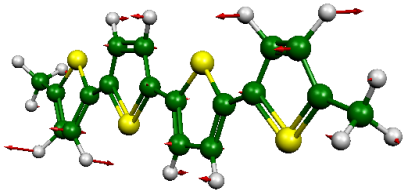

(g) 103.93 meV (837.701 cm^{-1})

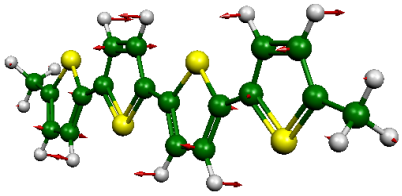

(h) 104.29 meV (840.584 cm^{-1})

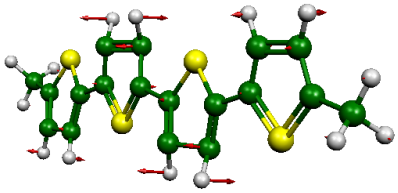

(i) 104.60 meV (843.140 cm^{-1})

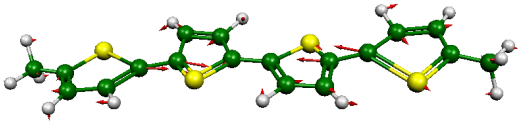

(j) 105.76 meV (852.497 cm^{-1})

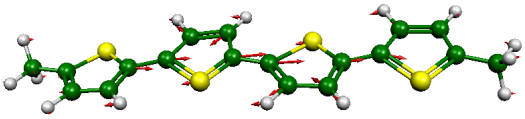

(k) 108.55 meV (874.928 cm^{-1})

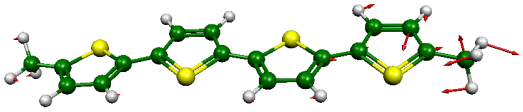

(l) 117.40 meV (946.302 cm^{-1})

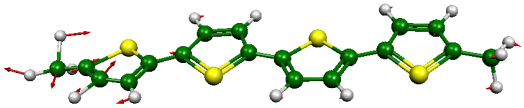

(m) 117.49 meV (947.017 cm^{-1})

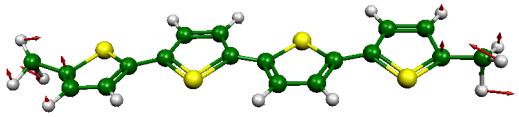

(n) 123.62 meV (996.428 cm^{-1})

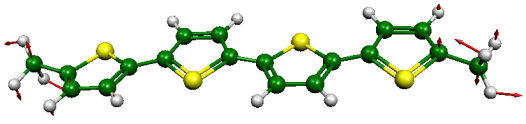

(o) 123.66 meV (996.744 cm^{-1})

Figure A.9 eigenvectors (read arrows) representing normal vibrational modes of the isolated molecule of $4TCH_3$. Vibrational modes from [60-200 meV] or [483.6-1612 cm^{-1}], where frequencies comes from DFT simulations.

Table A.4 Calculated frequencies from [60-200 meV] or [483.6-1612 cm^{-1}] of an isolated molecule of $4TCH_3$ with their respective symmetry, activity and description of vibration.

Frequency in meV (cm^{-1})		**Symmetry**	**Optical**	**Approximative**
SIESTA	**DMOL3**		**activity**	**assignment**
126.7 (1021.5)	128.75 (1030.2)	A_g	Raman	ρ_s(C$_\beta$-H)
127.1 (1025.1)	129.3 (1034.6)	B_u	Infrared	ρ_s(C$_\beta$-H)$_{outer}$
128.6 (1037.3)	130.7 (1045.9)	A_g	Raman	ρ_s(C$_\beta$-H) and ν(C$_\beta$-C$_\beta$)
130.5 (1052.0)	132.6 (1061.3)	B_u	Infrared	ρ_s(C$_\beta$-H) and ν(C$_\beta$-C$_\beta$)
143.0 (1152.9)	145.2 (1162.2)	B_u	Infrared	ρ_r(C-H)$_{inner}$ and ν(C-CH$_3$)
143.3 (1155.5)	146.9 (1175.7)	A_g	Raman	ν(C-CH$_3$)
143.8 (1159.8)	147.8 (1182.7)	B_u	Infrared	ρ_r(C-H) and ν(C-CH$_3$)
144.7 (1166.6)	147.9 (1183.4)	A_g	Raman	ρ_r(C-H) and ν(C-CH$_3$)
146.3 (1179.8)	148.8 (1190.9)	B_u	Infrared	ρ_r(C-H)
147.5 (1189.4)	150.4 (1203.5)	A_g	Raman	ρ_r(C-H)
162.5 (1229.3)	156.5 (1252.5)	A_g	Raman	ν(C-S)$_{inner}$ and ν(C(1)-C(1'))
152.7 (1231.7)	156.5 (1252.7)	B_u	Infrared	ν(C(4)-C(5))
155.3 (1252.3)	159.7 (1277.7)	A_g	Raman	ν(C-C) between rings
158.3 (1276.1)	161.4 (1291.7)	B_u	Infrared	ν(C$_\beta$-C$_\beta$) and ρ_s(C$_\alpha$-S-C$_\alpha$)
162.9 (1313.1)	165.9 (1327.4)	A_g	Raman	ν(C$_\beta$-C$_\beta$)
165.7 (1335.6)	168.0 (1344.7)	B_u	Infrared	δ_s(CH$_3$)
166.1 (1339.0)	168.6 (1349.3)	A_g	Raman	δ_s(CH$_3$)
157.5 (1350.3)	170.7 (1365.9)	B_u	Infrared	ν_{as}(C$_\beta$(-C$_\beta$)
171.0 (1379.0)	174.1 (1393.5)	A_g	Raman	ν_s(C$_\beta$(-C$_\beta$)
172.5 (1390.6)	175.1 (1401.3)	B_g	Raman	ν_{as}(CH$_3$)
172.5 (1390.6)	175.1 (1401.3)	A_u	Infrared	ν_{as}(CH$_3$)
174.6 (1407.4)	177.5 (1420.1)	B_u	Infrared	ν_{as}(CH$_3$)
174.6 (1408.0)	177.6 (1420.9)	A_g	Raman	ν(C$_\beta$-C$_\beta$) and δ(CH$_3$)
184.4 (1486.3)	186.8 (1494.4)	A_g	Raman	ν(C$_\beta$-C$_\beta$)$_{inner}$ and ρ_s(C$_\alpha$-S-C$_\alpha$)
184.6 (1488.1)	187.0 (1496.5)	B_u	Infrared	ν(C$_\alpha$-C$_\beta$-C$_\alpha$)$_{inner}$
185.4 (1495.0)	187.4 (1499.4)	B_u	Infrared	ν(C$_\beta$-C$_\alpha$)
187.4 (1510.7)	190.8 (1526.8)	A_g	Raman	ν(C$_\beta$-C$_\beta$) and ρ_s(C$_\alpha$-S-C$_\alpha$)
190.4 (1534.8)	193.2 (1545.6)	B_u	Infrared	ν(C$_\alpha$-C$_\beta$)
192.7 (1553.9)	195.6 (1564.8)	A_g	Raman	ν(C$_\alpha$-C$_\beta$)
195.4 (1575.5)	198.4 (1587.3)	B_u	Infrared	ν(C$_\alpha$-C$_\beta$)
196.9 (1587.1)	198.6 (1601.2)	A_g	Raman	ν(C$_\alpha$-C$_\beta$)

Note: ν: streching; δ: deformation; ρ_w: wagging; ρ_t: twisting. The subscripts correspond to as (s): antisymmetric (symmetric) and outer (inner): the two outer (inner) thienylene rings. ν_s(CH$_3$) (ν_{as}(CH$_3$): symmetric (antisymmetric) stretching modes of aliphatic CH$_3$; $\nu_s(C-H)$ (ν_{as}(C-H)): symmetric (antisymmetric) stretching modes of C-H from thienylene rings. The subscripts correspond to outer (inner): the two outer (inner) thienylene rings.

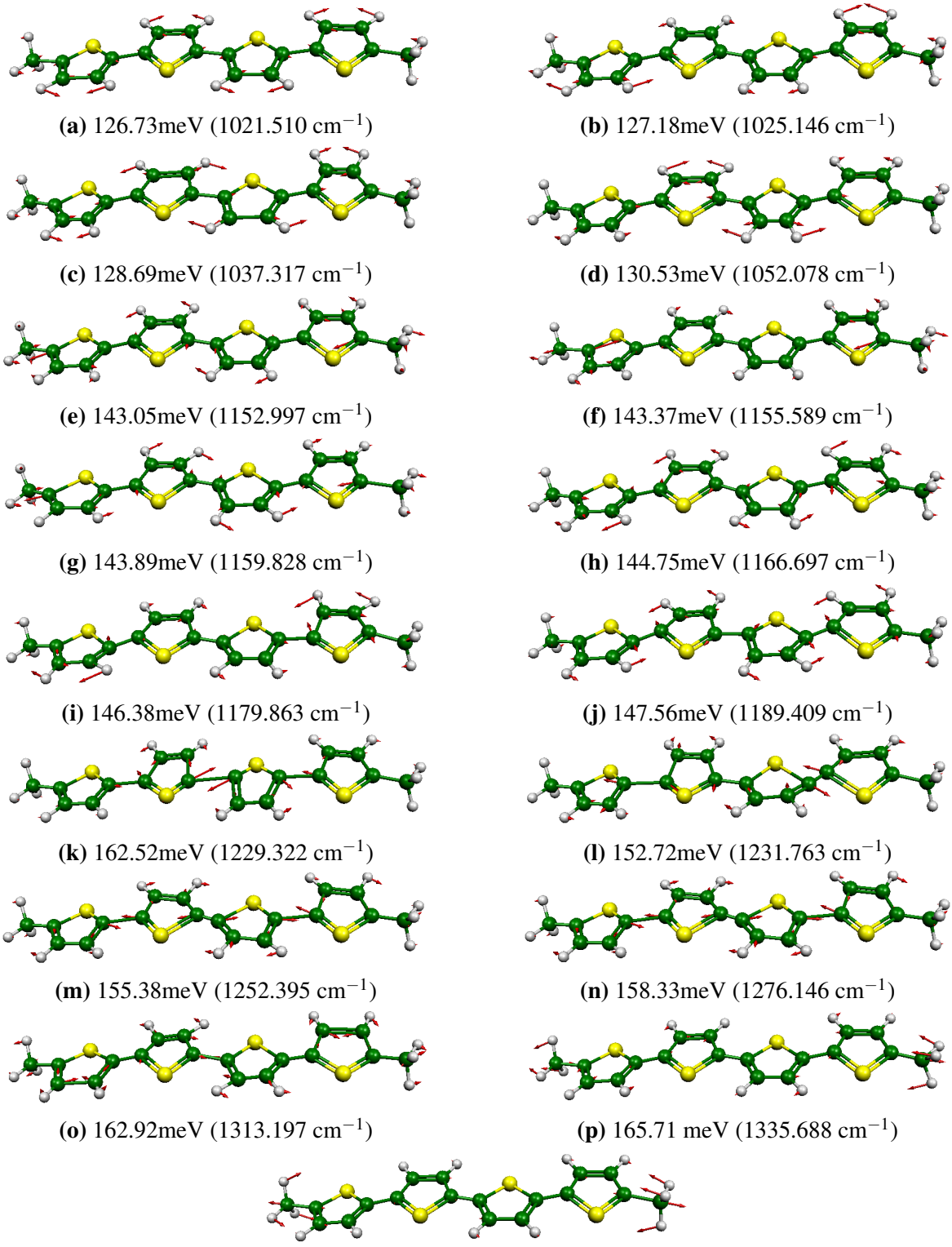

(a) 126.73meV (1021.510 cm^{-1})

(b) 127.18meV (1025.146 cm^{-1})

(c) 128.69meV (1037.317 cm^{-1})

(d) 130.53meV (1052.078 cm^{-1})

(e) 143.05meV (1152.997 cm^{-1})

(f) 143.37meV (1155.589 cm^{-1})

(g) 143.89meV (1159.828 cm^{-1})

(h) 144.75meV (1166.697 cm^{-1})

(i) 146.38meV (1179.863 cm^{-1})

(j) 147.56meV (1189.409 cm^{-1})

(k) 162.52meV (1229.322 cm^{-1})

(l) 152.72meV (1231.763 cm^{-1})

(m) 155.38meV (1252.395 cm^{-1})

(n) 158.33meV (1276.146 cm^{-1})

(o) 162.92meV (1313.197 cm^{-1})

(p) 165.71 meV (1335.688 cm^{-1})

(q) 166.13 meV (1339.029 cm^{-1})

Figure A.10 eigenvectors (read arrows) representing normal vibrational modes of the isolated molecule of $4TCH_3$. Vibrational modes in the range of [60-200 meV] or [483.6-1612 cm^{-1}], where frequencies comes from DFT simulations.

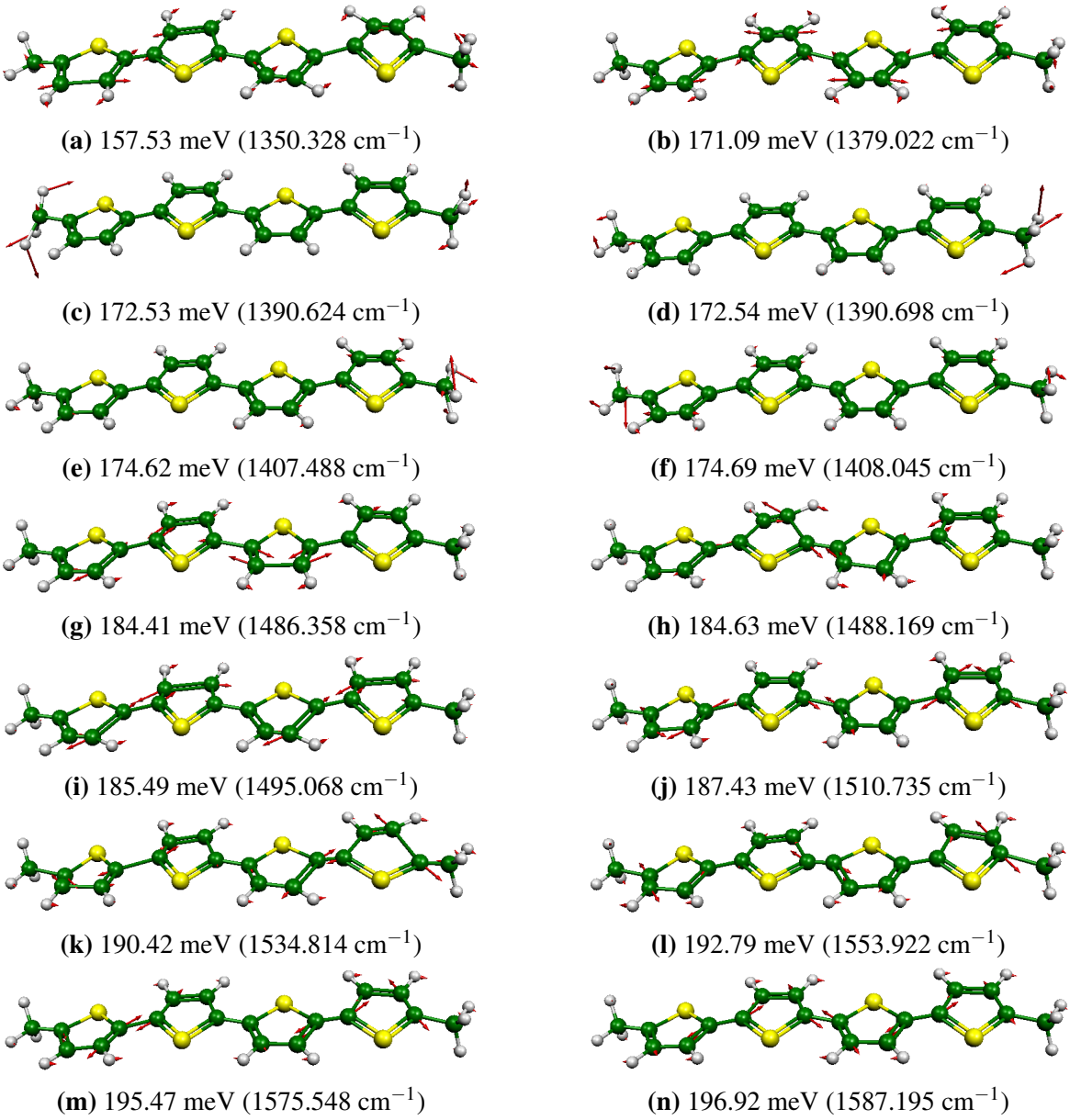

(a) 157.53 meV (1350.328 cm^{-1})

(b) 171.09 meV (1379.022 cm^{-1})

(c) 172.53 meV (1390.624 cm^{-1})

(d) 172.54 meV (1390.698 cm^{-1})

(e) 174.62 meV (1407.488 cm^{-1})

(f) 174.69 meV (1408.045 cm^{-1})

(g) 184.41 meV (1486.358 cm^{-1})

(h) 184.63 meV (1488.169 cm^{-1})

(i) 185.49 meV (1495.068 cm^{-1})

(j) 187.43 meV (1510.735 cm^{-1})

(k) 190.42 meV (1534.814 cm^{-1})

(l) 192.79 meV (1553.922 cm^{-1})

(m) 195.47 meV (1575.548 cm^{-1})

(n) 196.92 meV (1587.195 cm^{-1})

Figure A.11 eigenvectors (read arrows) representing normal vibrational modes of the isolated molecule of $4TCH_3$. Vibrational modes in the range of [60-200 meV] or [483.6-1612 cm^{-1}], where frequencies comes from DFT simulations.

A.2.3 Dynamics of the molecule of $4TCH_3$ in the large energy transfer domain

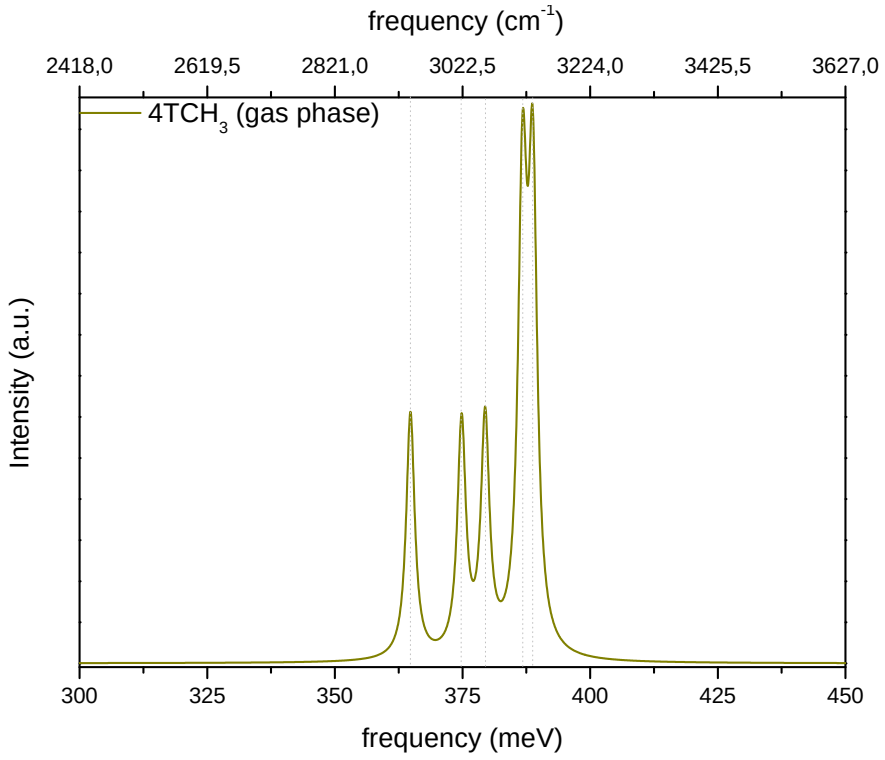

Figure A.12 Calculated HPDOS in the range of [300-450 meV] or [2418-3627 cm^{-1}] of an isolated molecule of $4TCH_3$.

Figure A.12 shows the region in which C-H stretching vibrations occur. It has 4 distinct peaks for which the last one shows a splitting. The first three peaks correspond to either the symmetric or anti-symmetric stretching of the aliphatic methyl groups located at the two extremities of the molecule. Conversely, the last peak, which has the splitting, corresponds to the symmetric and asymmetric stretching of the C-H bonds located at either the two inner or the two outer thienylene rings. Table A.5 summarises all calculated vibrational bands at this energy domain.

Table A.5 Calculated frequencies from [300-450 meV] or [2418-3627 cm^{-1}] of an isolated molecule of $4TCH_3$ with their respective symmetry, optical activity and approximative assignment.

Frequency in meV (cm^{-1})		**Symmetry**	**Optical**	**Approximative**
SIESTA	**DMOL3**		**activity**	**assignment**
365.0 (2942.0)	367.2 (2960.4)	B_u	Infrared	$\nu_s(CH_3)$
365.1 (2943.0)	367.3 (2960.6)	A_g	Raman	$\nu_s(CH_3)$
375.0 (3023.2)	375.5 (3027.1)	B_g	Raman	$\nu_{as}(CH_3)$
375.1 (3023.4)	375.5 (3027.1)	A_u	Infrared	$\nu_{as}(CH_3)$
379.7 (3060.3)	379.8 (3061.3)	B_u	Infrared	$\nu_{as}(CH_3)$
379.7 (3060.6)	379.8 (3061.3)	A_g	Raman	$\nu_{as}(CH_3)$
386.8 (3118.0)	386.6 (3116.7)	B_u	Infrared	$\nu_{as}(C\text{-}H)_{outer}$
386.8 (3118.3)	386.6 (3116.7)	A_g	Raman	$\nu_{as}(C\text{-}H)_{outer}$
387.1 (3120.4)	386.7 (3117.1)	A_g	Raman	$\nu_{as}(C\text{-}H)_{inner}$
387.3 (3121.9)	386.7 (3117.1)	B_u	Raman	$\nu_{as}(C\text{-}H)_{inner}$
388.8 (3134.3)	388.3 (3130.2)	B_u	Infrared	$\nu_s(C\text{-}H)_{outer}$
388.9 (3135.2)	388.3 (3130.3)	A_g	Raman	$\nu_s(C\text{-}H)_{outer}$
389.0 (3136.0)	388.4 (3131.0)	B_u	Infrared	$\nu_s(C\text{-}H)_{inner}$
389.2 (3137.3)	388.4 (3131.0)	A_g	Raman	$\nu_s(C\text{-}H)_{inner}$

Note: $\nu_s(CH_3)$ ($\nu_{as}(CH_3)$): symmetric (antisymmetric) stretching modes of aliphatic CH_3; $\nu_s(C-H)$ ($\nu_{as}(C-H)$): symmetric (antisymmetric) stretching modes of C-H from thienylene rings. The subscripts correspond to outer (inner): the two outer (inner) thienylene rings.

The figures A.13 and A.14 show the eigenvectors of the vibrational modes of the aliphatic methyl groups and the C-H bonds from the rings, respectively.

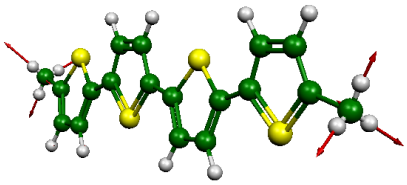

(a) 365 meV (2942.00 cm^{-1})

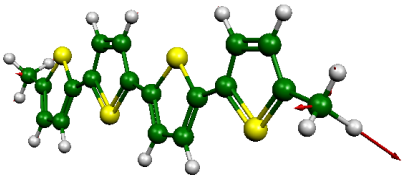

(b) 375 meV (3023.46 cm^{-1})

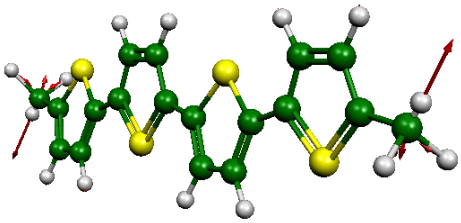

(c) 379 meV (3060.39 cm^{-1})

Figure A.13 eigenvectors (read arrows) representing normal vibrational modes of the aliphatic CH_3. Vibrational modes from [300-450 meV] or [2418-3627 cm^{-1}], where frequencies comes from DFT simulations.

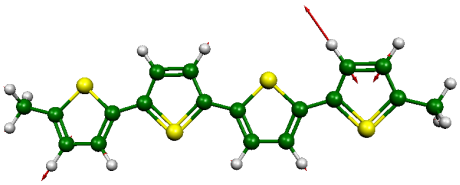

(a) 386 meV (3118.39 cm^{-1})

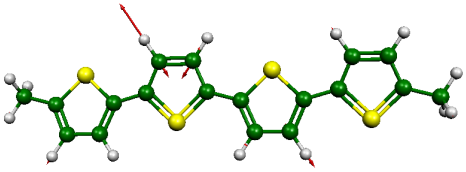

(b) 387 meV (3120.43 cm^{-1})

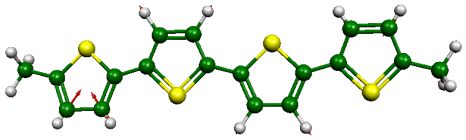

(c) 388 meV (3134.38 cm^{-1})

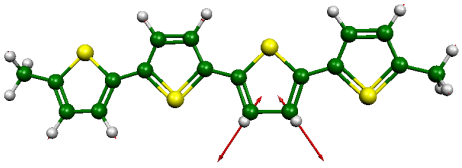

(d) 389 meV (3137.31 cm^{-1})

Figure A.14 eigenvectors (read arrows) representing normal vibrational modes of the C-H located at the thienylene rings. Vibrational modes from [300-450 meV] or [2418-3627 cm^{-1}], where frequencies comes from DFT simulations.

Appendix B

Neutron scattering

Contents

B.1 Introduction

This Appendix discusses the principal aspects of the neutron scattering experimental techniques that have been used in the framework this thesis for characterizing our hybrid carbon nanotubes samples, see Table B.1:

Table B.1 List of neutron scattering experiments performed in the framework of this PhD thesis. Adapted from reference [239].

Name	Energy change	Basic process	Instrument	Information
SANS	Elastic	Coherent	D16 PAXY	structural ordering
Spectroscopy	Inelastic	Incoherent	IN4C IN1-LAGRANGE	vDOS

B.2 Why using neutron scattering?

Neutrons are particles which are very abundant in nature, which are only found stable when confined inside the nucleus part of the atoms. Together with the protons, they participate to the stability of matter linked together by strong nuclear interactions. This is why the production of neutrons either necessitates or releases a large amount of energy. They are produced at large scale facilities, either using steady state reactor or pulsed sources. The principle of production differs from one type of source to another: the steady state reactor use the fission of an ^{235}U enriched core to produce high energy neutrons, while the pulsed sources send compressed pulses of an intense beam onto a heavy target, subsequently producing intense pulses of high energy neutrons. The latter (of several hundreds of MeV) are thermalized, *i.e.* slowed down to the meV energy range to be usable in common scattering experiments on the different instruments.

The as-produced thermal neutrons have characteristic wavelength of $\sim$ 1Å which corresponds to typical energies of $\sim$ 10 meV, which is comparable to the elementary excitations found in solids and liquids (phonons, molecular vibrations...). These peculiar properties make neutron scattering a very natural and powerful probe for studying both the structure and the fluctuations of the atomic positions in condensed matter. By comparisons, the energy of $\sim$ 1 Å X-ray photons are typically of the keV range, rendering the detection of meV large energy transfers very difficult (but feasible in recent synchrotron beamlines). In the other direction, the typical wavelength for lasers is several hundreds of nanometers, which restricts Raman scattering investigation to the center of the Brillouin zone, *i.e.* making difficult (when feasible) the measurement of dispersion curves. However, neutron scattering is a low flux techniques, which is one of the most important limiting factor. As a consequence, the resolution of a beamline in terms of energy or momentum transfer is in general much less than what can be done in equivalent instruments using X-rays or optical spectroscopies.

Also, the sample quantity required for neutron investigations is much larger than the other spectroscopic techniques, making the experiments on individual carbon nanotubes in solution or in a substrate for example, totally impossible at the moment. As usually stated, it is the complementarity of the different techniques, *e.g.* IR, neutron, X-ray and Raman which allowed deriving a coherent picture of the samples we studied.

B.3 Basics of neutron scattering

In this section, there is no question of developing the whole theory of neutron scattering, but simply to provide the reader with the basics to understanding the rest of the manuscript. All the concepts treated in the following sections are developed extensively in the general textbooks of condensed matter physics and neutron scattering [240–242].

The neutron observable when doing a neutron scattering measurement is called the scattering cross section $\frac{\partial^2\sigma}{\partial\Omega\partial\Omega}$. It represents the flux of neutrons with incident wavevector (energy) $\vec{k}_i$ (E_i) which have been scattered with wavevector $\vec{k}_f$ (E_f) in the solid angle $\Omega \pm \partial\Omega$, *i.e.* with energy transfer $\hbar\Omega = E_i - E_f$ and momentum transfer $\hbar\vec{Q} = \vec{k}_i - \vec{k}_f$ to the sample. This quantity can be separated into a *coherent* and an *incoherent* part as a consequence of the peculiar neutron-nuclei interactions so that it can be written in the following form:

$$\frac{\partial^2\sigma}{\partial\Omega\partial\omega} = \left(\frac{\partial^2\sigma}{\partial\Omega\partial\omega}\right)_{coh} + \left(\frac{\partial^2\sigma}{\partial\Omega\partial\omega}\right)_{inc} = \frac{k_f}{k_i}S(\vec{Q},\omega) \tag{B.1}$$

with

$$S(\vec{Q},\omega) = S_{coh}(\vec{Q},\omega) + S_{inc}(\vec{Q},\omega) \tag{B.2}$$

$$\frac{\partial^2\sigma}{\partial\Omega\partial E} = \frac{k_f}{k_i}S(Q,\Omega) \tag{B.3}$$

$S(\vec{Q},\omega)$ is called the total dynamical structure factor of the system, and contains the complete information of the sample state. Alike the cross section, it can be separated into a coherent $S_{coh}(\vec{Q},\omega)$ and an incoherent $S_{inc}(\vec{Q},\omega)$ parts. As we will see, each of these latter quantities can be divided into an elastic and an inelastic part. In particular, the understanding of the *coherent part of the elastic scattering* will allow deriving information on the structure of the sample. By contrast, the *inelastic part of the incoherent scattering* will be analysed to derive the spectroscopic signatures of the encapsulated molecules which contain hydrogen atoms, *i.e.* to derive information about their local environment. We will discuss briefly these notions in the following paragraphs.

B.3.1 Coherent and incoherent scattering cross sections

The notions of coherence and incoherence are the building blocks of neutron scattering. The different materials we have studied during this thesis are mostly composed of carbon, a purely coherent scatterer, and hydrogen which is mostly incoherent. It is therefore useful to precise the meaning of these notions.

When a neutron interacts with a nucleus, it can be either absorbed or scattered, in the latter case its energy and/or trajectory can be affected. The relatively weak energy of the thermal neutrons used in a neutron scattering experiment (in the order of few meV) prevents the excitations of the internal nuclei levels and core electronic states, but is responsible for the sensitivity of the neutrons to the global dynamics of the nuclei, *i.e.* to the instantaneous structure of the material under study. The neutron-nucleus interaction is characterized by a *scattering length* b, which can be a complex quantity for an absorbing material and which quantifies the capacity of an isotope to interact with the neutron beam. This interaction depends on the total spin state $\mathbf{J} = \mathbf{I} + \mathbf{S}$ of the neutron-nucleus system (with $\mathbf{I}$ the nucleus spin and $\mathbf{S}$ that of the neutron). The scattering length therefore varies from one chemical species to another, but also from one isotope to another within the same species: for a given isotope i the statistic average of the scattering length over all the spin states $b_i^{coh} = \overline{b_i}$ is called the *coherent* scattering length. The coherent part of the scattering therefore approximates the ensemble of isotopes i to be all in the same average spin state.

The deviation of the real state of the system from this ideal situation is characterized by the *incoherent* scattering length, $b_i^{inc} = \sqrt{\overline{b_i^2} - \overline{b_i}^2}$, defined as the mean squared of the scattering lengths b_i. The coherent and incoherent cross sections are defined by $\sigma_i^{coh} = 4\pi(b_i^{coh})^2$ and $\sigma_i^{inc} = 4\pi(b_i^{inc})^2$ respectively. For a pure isotope, we will refer to the *spin* origin of the incoherent scattering. Spin incoherence vanishes for isotopes which have the peculiarity that $\overline{b_i^2} = \overline{b_i}^2$. This happens when the atomic numbers Z and A have even values, which is the case for ^{4}H, ^{12}C, ^{16}O, ^{20}Ne… their nucleus having a nuclear spin equal to 0. This is why the scattering for an isotopically pure material made of ^{12}C has no incoherent scattering.

Another source of incoherent scattering originates from the natural distribution of the isotopes of one atomic species. In that case, the scattering lengths have to be calculated in order to account for this distribution, and this is why a natural material made of carbon, *i.e.* containing 1.1% of ^{13}C with $b^{inc}_{^{13}C}$ = -0.52.10^{-15} m has a small but finite incoherent cross section of 0.001 barns. In the rest of this manuscript, we will consider that pure carbon nanostructures scatter neutron purely coherently, with a coherent cross section σ_C^{coh} = 5.551 barns. The situation is entirely reversed for a hydrogen containing material. The neutron cross section of H (82.02 barns) is the largest among the periodic table of the elements. In

particular, its incoherent cross section amounts $\sigma_{\mathrm{H}}^{\mathrm{inc}} = 80.26$ barns which makes this elements mostly incoherent scatterer.

B.3.2 Elastic and inelastic scattering – The van Hove correlation functions

In the introduction part of this chapter we have indicated that the scattering (either coherent or incoherent) can also be qualified as a function of the energy transfer between the neutron probe and the sample:

$$S_{coh}(\vec{Q},\Omega) = S_{coh}^{el}(\vec{Q}) + S_{coh}^{inel}(\vec{Q},\Omega) \tag{B.4}$$

$$S_{inc}(\vec{Q},\Omega) = S_{inc}^{el}(\vec{Q}) + S_{inc}^{inel}(\vec{Q},\Omega) \tag{B.5}$$

Following van Hove [243] the dynamical structure factors are linked to the space and time correlation function via the following double Fourier transforms:

$$S_{coh}(\vec{Q},\Omega) = \frac{1}{2\pi\hbar}\int dt e^{-i\Omega t}\int d^3\vec{r}\,K(\vec{r},t)e^{i\vec{Q}\cdot\vec{r}} \tag{B.6}$$

$$S_{inc}(\vec{Q},\Omega) = \frac{1}{2\pi\hbar}\int dt e^{-i\Omega t}\int d^3\vec{r}\,K_s(\vec{r},t)e^{i\vec{Q}\cdot\vec{r}} \tag{B.7}$$

where $K(\vec{r},t)$ and $K_s(\vec{r},t)$ are the pair and self time–and–space correlation functions respectively. They give the probability of finding an atom located at $\vec{r}$ at time t if this atom strictly (for the self) or any atom (for the pair) is located at the origin at time $t = 0$.

Elastic scattering

In case of no energy transfer (the neutron is scattered without any change of its initial speed/wavelength) the scattering is elastic and the pertinent variable to consider is the momentum transfer $\vec{Q}$ between the neutron wave and the sample. $S_{coh}^{el}(\vec{Q})$ provides information on the atomic structure of the sample at *long* time. Here the adjective *long* refers to the maximum correlation time provided by the instrument, *i.e.* it depends on the energy resolution of the neutron spectrometer used in the experiment: the sharper the instrumental resolution, the longer the correlation time. For a diffractometer, the energy resolution is extremely broad by construction (there is no energy analyser for a diffractometer), so that the scattered intensity is integrated *over the complete energy transfer range*, and we qualify the scattering as *total scattering* with the (total) structure factor:

$$S_{coh}(\vec{Q}) = \int_{-\infty}^{+\infty} d\Omega S_{coh}(\vec{Q},\Omega) \tag{B.8}$$

According to the equation B.6 one can easily show that

$$S_{coh}(\vec{Q}) = \int d^3\vec{r}\, K(\vec{r},0) e^{i\vec{Q}\cdot\vec{r}} \tag{B.9}$$

with $K(\vec{r},0) = \delta(\vec{r}) + \rho_0 g(\vec{r})$

$$S_{coh}(\vec{Q}) = 1 + \rho_0 \int g(\vec{r})\, exp(i\vec{Q}\cdot\vec{r}) d^3r \tag{B.10}$$

If one wants to make visible the forward scattering at $Q = 0$, $\rho_0\, \delta\,(\vec{Q})$, then one can write:

$$S_{coh}(\vec{Q}) = 1 + \rho_0 \int g(\vec{r}) exp(i\vec{Q}\cdot\vec{r}) d^3r + \rho_0 \delta(\vec{Q}) - \rho_0 \delta(\vec{Q}) \tag{B.11}$$

$$S_{coh}(\vec{Q}) = 1 + \rho_0 \int [g(\vec{r}) - 1] exp(i\vec{Q}\cdot\vec{r}) d^3r + \rho_0 \delta(\vec{Q}) \tag{B.12}$$

In an experiment, the forward scattering at $Q = 0$ is not measured, so that the experimental quantity accessible is:

$$S_{coh}(\vec{Q}) = 1 + \rho_0 \int (g(\vec{r}) - 1) exp(i\vec{Q}\cdot\vec{r}) d^3r \tag{B.13}$$

For isotropic samples, one has $g(\vec{r}) = g(r)$, and the previous equation can be further reduced to:

$$S_{coh}(Q) - 1 = \int G(r) \frac{sin(Qr)}{Q} dr \tag{B.14}$$

with the reduced atomic pair distribution function $G(r) = 4\pi r \rho_0 (g(r) - 1)$. By using the properties of the inverse Fourier transform, one can show that the reduced PDF $G(r)$ can be expressed by:

$$G(r) = \frac{2}{\pi} \int Q[S(Q) - 1] sin(Qr) dQ \tag{B.15}$$

The total scattering therefore provides an instantaneous picture of the atomic correlations in the sample, *i.e.* its instantaneous structure. The reduced PDF function $G(r)$ provides an excellent way of characterizing the atomic structure of materials containing a considerable amount of disorder or reduced coherent length.

The elastic incoherent scattering appears as a background in the diffraction measurements. It can be expressed as:

$$S^{el}_{inc}(\vec{Q}) = \sum_{j \in H} exp(-2W_j(\vec{Q})) \tag{B.16}$$

with $W_j(\vec{Q})$ the Debye-Waller term of the hydrogen atom j in the sample.

Eq. B.17 is valid for an oriented (crystalline) sample. The powders we have studied are isotropic, so that the latter expressions have to be averaged over all the directions of the $\vec{Q}$ vector. The structure factor then depends only on the amplitude of $\vec{Q}$ so that we will write:

$$S_{inc}^{el}(Q) = \overline{\sum_{j \in H} exp(-2W_j(\vec{Q}))} \tag{B.17}$$

with $\overline{X}$ denoting the orientation average of the quantity X.
It is usual for an isotropic sample to approximate the Debye-Waller term $W_j(\vec{Q})$ by its isotropic expression $W_j(Q) = \frac{1}{6}Q^2U_j^2$, with U_j being the mean squared displacement of the hydrogen atoms j. If U_j are not too different from one type of hydrogen to another, U_j can be replaced by an atomic averaged mean square displacement U, so that B.17 can be written as:

$$S_{inc}^{el}(Q) = N_H exp\left(-\frac{1}{3}Q^2U^2\right) \tag{B.18}$$

The latter expression shows that the intensity of the elastic line is proportional to the quantity of H atoms in the sample and has a very smooth dependence with the momentum transfer Q. It provides a very useful mean for deriving the number of hydrogen atoms present in the sample, as well as an estimation of their averaged mean square displacement.

Inelastic scattering

By contrast to elastic scattering, a subsequent part of the kinetic energy of the neutrons is transferred to the sample for inelastic scattering. The analysis of the resulting *inelastic spectrum* $S(\vec{Q}, \Omega)$ provides information on the energy levels of the sample under study. These levels can be magnetic (crystal field, spin waves), and/or nuclear. In the latter case they reflect the fluctuations of the atomic positions in the system, which vary with the thermodynamics conditions (P, T ...) of the sample. The time (and space) periodic variations of the atomic positions will reflect the interactions at stake in the sample. They will be revealed by their corresponding (eigen) frequency Ω_λ, either characteristic of stiff molecular vibrations, or soft lattice (phonon) modes. The energy distribution of these modes will be the main subject of this thesis.

In this part, we give the expressions of the coherent and incoherent structure factors for inelastic scattering. As developed in the textbooks [240, 241], we consider here that the movement of the atoms is limited to short range fluctuations, *i.e.* vibrations around

their equilibrium positions. In particular, we do not consider here any long range diffusion of the atoms nor anharmonic terms in the interatomic potential. We restrict therefore the development of the inelastic structure factor in power of the displacement of the atoms to the first order, *i.e.* to *one phonon events*. We will consider that the coherent part of the scattering originates essentially from carbon contributions and will develop the incoherent term as if originating uniquely from hydrogen atoms belonging to the encapsulated dyes. If this approach is valid for pure hydrogenated carbon nano-structures, one has to bear in mind that hydrogen atoms have a non negligible coherent scattering cross section. Also, in the powdered samples of carbon nanotubes, the contribution of the metallic nanoparticles used as catalysers should not be neglected. In particular, Ni, Li and Na atoms have coherent and incoherent cross sections which should be taken into account in the interpretation of their spectra. However, the extrapolation of the proposed formalism to the real cases is straightforward, and therefore we will restrict our discussion here to a pure carbon nanotube containing hydrogen-rich dyes as guests.

The development of the expressions of the dynamical structure factors is based on the knowledge of the atomic positions $\vec{r_n}$ in the sample and of the normal modes $|\lambda\rangle$ and normal frequency Ω_λ. The latter are respectively the eigenvector and the eigenvalues of the 3N $\times$ 3N dynamical matrix (or Hessian matrix, N being the total number of atoms in the structure) which is constituted of the force constant elements of the system calculated from the derivatives of the harmonic interatomic potential of the system around its equilibrium state [242, 244].

In case of coherent scattering, simplifications arise if one can describe the structure of the carbon structure as the periodical arrangement of unit cells. The latter can be derived from the simple graphene cell (*i.e.* composed of only two inequivalent C atoms) or constructed from the symmetry inequivalent parts of a more complex structure if one consider the case of the fulleride crystals for example. For such crystals, the atoms are indexed according to the cell l they belong to, and are given a type d, so that N_d denotes the number of inequivalent atoms in the carbon unit cell and N_l the number of cells in the sample. Thanks to the translational symmetry of the structure, the 3N $\times$ 3N problem is reduced to the evolution of the eigenvalues $\Omega_j(\vec{q})$ and eigenvectors $|j\vec{q}\rangle$ of a $3N_d \times 3N_d$ matrix as a function of wavevectors $\vec{q}$ belonging to the first Brillouin zone of the crystal. The quantum number λ of the total hamiltonian is therefore replaced by the couple $(j, \vec{q})$.

In phonon creation (Stokes), the coherent dynamical structure factor in the one phonon process approximation [240, 241] $S_{coh}(\vec{Q},\Omega)$ can be written:

$$S_{coh}(\vec{Q},\Omega) = N_l \frac{n(\Omega,T)+1}{2\Omega} \sum_j F_j(\vec{Q})\delta(\Omega - \Omega_j(\vec{Q})) \tag{B.19}$$

with the one phonon form factor:

$$F_j(\vec{Q}) = \| \sum_{d=1}^{N_d} \frac{b_d^{coh} e^{-W_d(\vec{Q})}}{\sqrt{(M_d)}} \vec{Q}\cdot\vec{e}_j(\vec{Q} \mid d)\|^2 \tag{B.20}$$

and the Bose thermal population factor $n(\Omega,T) = (exp(\hbar\Omega/k_\beta T)-1)^{-1}$. Index d refers to the dth atom among the N_d atoms in the unit cell, with mass M_d and coherent scattering length b_d^{coh}. $W_d(\vec{Q})$ is the Debye-Waller factor of atom d, and $\vec{e}_j(\vec{Q} \mid d)$ is the displacement of atom d in the normal mode $|j\vec{Q}\rangle$.

For a powder the isotropic averaging of the expression $S_{coh}(\vec{Q},\Omega)$ is given by

$$S_{coh}(Q,\Omega) = \frac{1}{4\pi}\int d^2\Omega S(\vec{Q},\Omega) \tag{B.21}$$

The one phonon incoherent cross section writes:

$$S_{inc}(\vec{Q},\Omega) = \frac{n(\Omega,T)+1}{2\Omega}\frac{b_H^{inc}}{M_H}\sum_{d\in H} e^{-2W_d(Q)} \sum_{j,\vec{Q}} \|\vec{Q}\cdot\vec{e}_j(\vec{q} \mid d)\|^2 \delta(\Omega - \Omega_j(\vec{q})) \tag{B.22}$$

which in the case of a powder can be approximated to:

$$S_{inc}(Q,\Omega) = \frac{n(\Omega,T)+1}{2\Omega}\frac{3NQ^2}{2}\frac{b_H^{inc}}{M_H}\sum_{d\in H} e^{-2W_d(Q)} g_d(\Omega) \tag{B.23}$$

with $g_d(\Omega)$ being the partial phonon density of state of atom d:

$$g_d(\Omega) = \frac{1}{3N}\sum_\lambda \|\vec{e_\lambda}(d)\|^2 \delta(\Omega - \Omega_\lambda) \tag{B.24}$$

In case that only one type of hydrogen atoms exists in the sample (or if we make the assumption that their dynamics is not significantly different), one can further simplifies the previous expression as:

$$S_{inc}(Q,\Omega) = \frac{n(\Omega,T)+1}{2\Omega}\frac{3NQ^2}{2}\frac{b_H^{inc}}{M_H}e^{-2W_H(Q)}g_H(\Omega) \tag{B.25}$$

with $g_H(\Omega)$ being the hydrogen partial phonon density of states, and resulting from the statistical averaging of the different atomic hydrogen types in the sample:

$$g_H(\Omega) = \sum_{d\in H} g_d(\Omega) \tag{B.26}$$

From the expressions B.19 and B.22 one clearly sees that coherent scattering has a condition that ensures - in addition to the conservation of energy - the conservation of the total momentum of the neutron-sample system. This appear as an additional condition over the $\vec{Q}$ vector in the expression B.19. This condition has made the success of neutron scattering in condensed matter science, providing an experimental mean of the measurement of the dispersion curves, *e.g.* sound waves or spin waves. In the data, this conditions and *i.e.* the strong Q dependence of the coherent form factor $F_j(\vec{Q})$ of expression B.19 makes possible the distinction between a coherent and an incoherent signal: while the former possesses a rather complex dependence with Q, the latter is rather monotonous in Q, resulting from the competition between an increasing Q^2 term and an exponentially decreasing Debye-Waller (see figure B.1).

Inelastic neutron scattering data handling and representations

When the energy dependence is essentially discussed, we use the generalized density of state $G(\bar{\theta},\Omega)$ representation. It is defined as:

$$G(\bar{\theta},\Omega) = \frac{S(\bar{\theta},\Omega)}{Q(\bar{\theta},\Omega)^2}\frac{\Omega}{n_B^{\pm}(\Omega,T)} \tag{B.27}$$

where $S(\bar{\theta},\Omega)$ represents the dynamical structure factor $S(\theta,\Omega)$ at a fixed angle θ averaged over a certain angular width[1]. The scattering is further considered as originating from an averaged set of mean angles $\bar{\theta}$, *i.e.* implying effective momentum transfers $Q(\bar{\theta},\Omega)$ expressed as:

$$Q(\bar{\theta},\Omega) = k_i^2 + k_f^2 - 2k_i k_f cos(\bar{\theta}) \tag{B.28}$$

In the expression B.27, the term $n_B^{\pm}(\Omega,T)$ is the population factor (also called Bose factor) with $n_B^+ = \frac{1}{e^{\beta\hbar\Omega}-1}+1$ for positive $\hbar\Omega$ (Stokes) and $n_B^- = \frac{1}{e^{\beta|\hbar\Omega|}-1}$ for negative $\hbar\Omega$ (anti-Stokes).

[1] If statistics is required, one can even sum up the scattered intensity at fixed energy transfer over the total range of angles allowed by the spectrometer geometry.

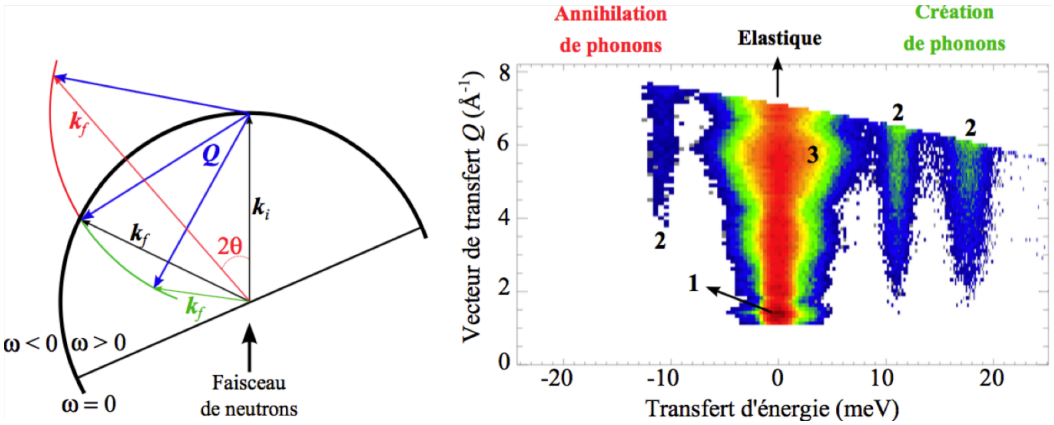

Figure B.1 *Left:* Characteristic set up of an inelastic neutron scattering experiment. *Right:* Dynamical structure factor $S(\vec{Q},\omega)$ of a powder composed of fullerene-cubane $C_{60}\cdot C_8H_8$ measured on the IN4C spectrometer at the ILL. The incoming neutron beam with wavevector $\vec{k}_i$ is scattered with wavevector $\vec{k}_f$. If $k_i = k_f$, the scattering is elastic ($\Omega = 0$) giving rise to the intense vertical band in the $S(\vec{Q},\omega)$ map, showing intense Bragg spots at specific Q. In case $k_f > k_i$, neutrons are accelerated through the annihilations of some phonons (anti-Stokes scattering). At the contrary, the energy released by the neutrons to the sample when $k_f < k_i$, permits the creation of phonons (Stokes scattering). The region of $S(\vec{Q},\omega)$ indicated by **2** localizes inelastic features whose monotonous Q dependence (and strong intensity) suggests they arise from phonons implying vibrations of a strong incoherent scatterer *i.e.* from the H atoms attached to the cubane molecules in this case. The region marked by **3** is called "quasielastic" scattering and represents low frequency modes, *i.e.* Debye modes or relaxations (free rotations...). Here, the strong Q modulation of the latter scattering indicates a coherent nature of the signal: it characterizes the free rotations of the C_{60} molecules in the structure [245].

In the hight temperature approximation one can consider that $\Omega^{-1}\chi''(\Omega) \propto \Omega^{-2}G(\Omega)$ [246]. As a consequence, the susceptibility of the system does not depend on temperature for harmonic crystals. Any departure from this constant behaviour would reflect the onset of anharmonicity in the material under investigation.

When a quantitative comparison between the data and the simulations is required, we further corrected the as-obtained generalized density of states $G(\theta,\Omega)$ in Eq. B.27 from the Debye-Waller decrease at high Q. The method employed is called the "interpolation at low Q" an is valid only for incoherent scattering, *i.e.* was used only for hydrogenated samples. This is based on the fact that $G(\bar{\theta},\Omega)$ contains the term $exp(-2W_H)$ as part of the structure factor $S_{inc}(\bar{\theta},\Omega)$ (see B.25), with $W_H = \frac{Q(\bar{\theta},\Omega)^2 u_H^2}{3}$. The method consist of a linear fit of the quantity $ln(G(\bar{\theta},\Omega))$ plotted as a function of $Q(\bar{\theta},\Omega)^2$ for each value of the energy transfer Ω: $ln(G(\bar{\theta},\Omega)) = A(\Omega) * Q(\bar{\theta},\Omega)^2 + K(\Omega)$. $K(\Omega)$ therefore stands for the the generalized

density of states interpolated to $Q = 0$, *i.e.* should be free from any Q dependence in the case of an incoherent scatterer[2].

B.4 Neutron scattering – Small Angle Neutron Scattering (SANS)

B.4.1 The small-angle scattering spectrometer PAXY

PAXY is a small-angle spectrometer, which uses large-wavelength neutrons from the cold neutron source. It measures diffraction patterns over a 2θ-range from -3 to 60° of scattering angle (for a distance sample/detector < 3.5m), equivalent to momentum transfer range of $[3 \times 10^{-3}, 1\ \text{Å}^{-1}]$.

Principle: The principle of the Small Angle Neutron Scattering is to measure the constructive interference of elastically scattered neutrons close to the axis of the neutron beam. An incident monochromatic wavelength is provided by a focussing crystal monochromator from the white cold neutron beam. The scattered neutrons are recorded into the 2D high-resolution large area detector which moves on the 2θ detector platform, accessing the diffracted small angle range of interest.

Instrument description: PAXY is built on the G2 cold neutron guide at the LLB. Three types of monochromatization are used. A mechanical selector, the neutron guide which and the time-of-flight method

The total area of the XY monochromator is $64 \times 64\text{cm}^2$. The boron trifluoride BF_3 detector can move within a vacuum chamber of 7m of length.

[2]This is a valid assumption as far as multiphonon scattering is negligible. In case of high temperatures and/or scattering processes involving large Q transfers, it is often better to let the data uncorrected from the Debye–Waller contribution as the latter and that from the multiphonon scattering often compensates each other to a large extend.

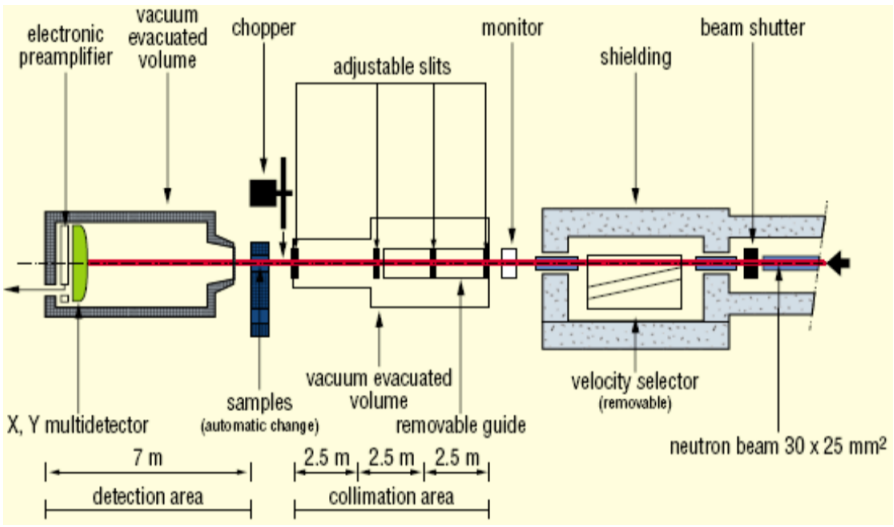

Figure B.2 Layout of the small-angle scattering spectrometer PAXY [247].

B.4.2 The diffractometer D16

For the SANS measurements that were performed on the D16 diffractometer, the sample constituted of 50g of powder, for the room pressure measurements and 30g of powder in the liquid transmitting of deuterated 4:1 methanol/ethanol.

D16 is a two-axis diffractometer, which uses large-wavelength neutrons from the cold neutron source. It measures diffraction patterns over a large 2θ-range from -5 to +120 °, being an instrument with measurement angles in between SANS and diffraction techniques. D16 has suited configuration for having high neutron flux and resolution [248, 249], crucial few tens of *mg* of carbon nanotubes.

Principle: The principle of the Small Angle Neutron Scattering is to measure the constructive interference of elastically scattered neutrons close to the axis of the neutron beam. An incident monochromatic wavelength is provided by a focussing crystal monochromator from the white cold neutron beam. The scattered neutrons are recorded into the $2D$ high-resolution large area detector which moves on the 2θ detector platform, accessing the diffracted small angle range of interest.

Instrument description: D16 is built on the H521 cold neutron guide at the ILL. The available monochromators are two vertically bending mosaic crystals of either Highly Oriented Pyrolitic Graphite (HOPG) or a Rubidium Graphite-Intercalated crystal (Rb-GIC). With two different take-off angles, such combination provides a choice over four wavelengths,

see Table B.2. The total area of the monochromator is $122\times60\text{mm}^2$. The high neutron flux and resolution at the sample position are tuned by vertical and horizontal collimation slits. Attenuator is used for measuring the empty beam with 15% of attenuation. Beryllium filters are used for $\lambda/2$ harmonic contamination.

Table B.2 Wavelengths available on D16

Take-off	HOPG	Rb-GIC
85°	4.5Å	7.5Å
115°	5.7Å	9.5Å

Note: Table taken from reference [249].

Vertical and horizontal slits are located after the pre-sample flight path and before the sample to allow better regulation of the incoming neutron beam so that the sample is illuminated the maximum and avoiding border effects.

The sample is mounted either inside an Vanadium cylindrical cell or a *TiZr* clamp cell in the sample table, see figure B.5.

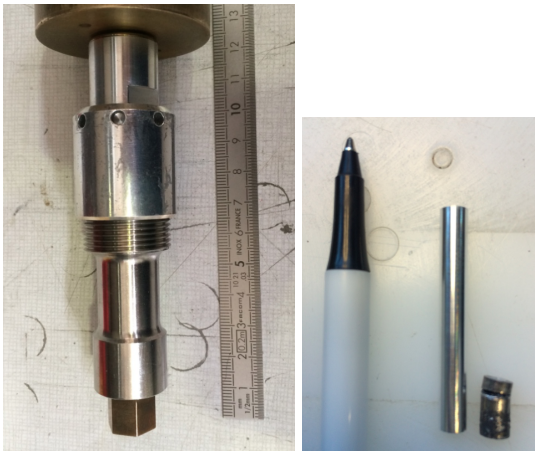

(a) **(b)**

Figure B.4 (a) TiZr clamp cell [250] mounted on the cryostat sample holder. **(b)** Cylindrical Al 4mm of diameter which is inserted inside the clamp cell to be charged with the powdered sample and liquid transmitting medium. On the right side, the Al cell completely compressed after an experiment.

The detector is made of high-pressure ^{3}He detectors forms an array of wired cathodes and anodes with 1mm of spacing, allowing a pixel resolution of $1\times1\text{mm}^2$.

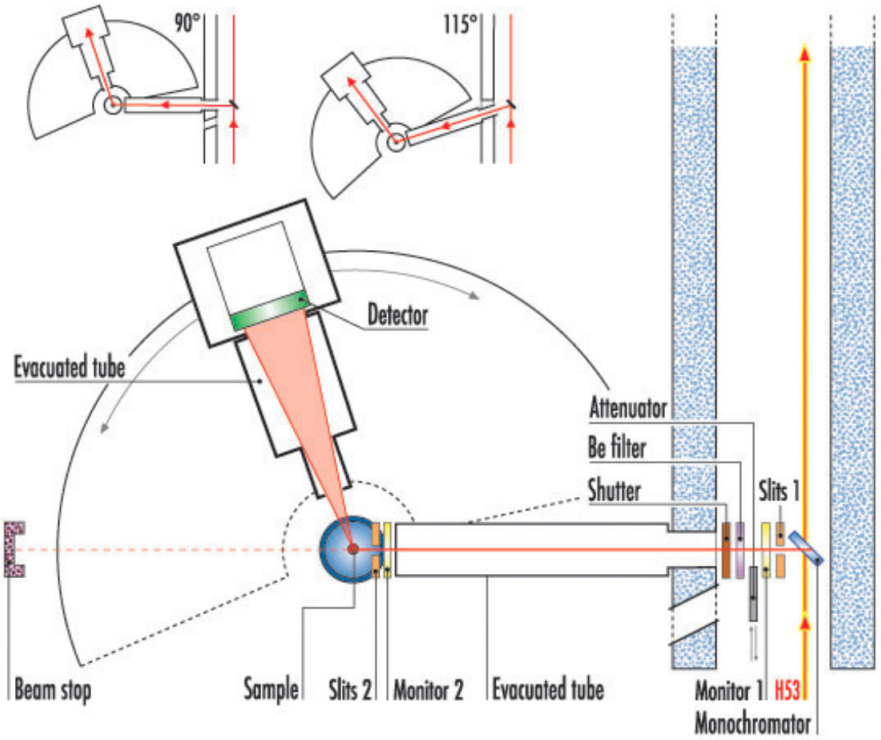

Figure B.3 Layout of the small momentum transfer diffractometer with variable vertical focusing D16 [248]. The focusing monochromators are composed of nine vertically bending mosaic crystals which are motorized which can be changed continuously. Both evacuated tubes located before (after) the detector has the function of minimising the pre (post) sample flight path neutron through air in order to avoid scattering from nitrogen.

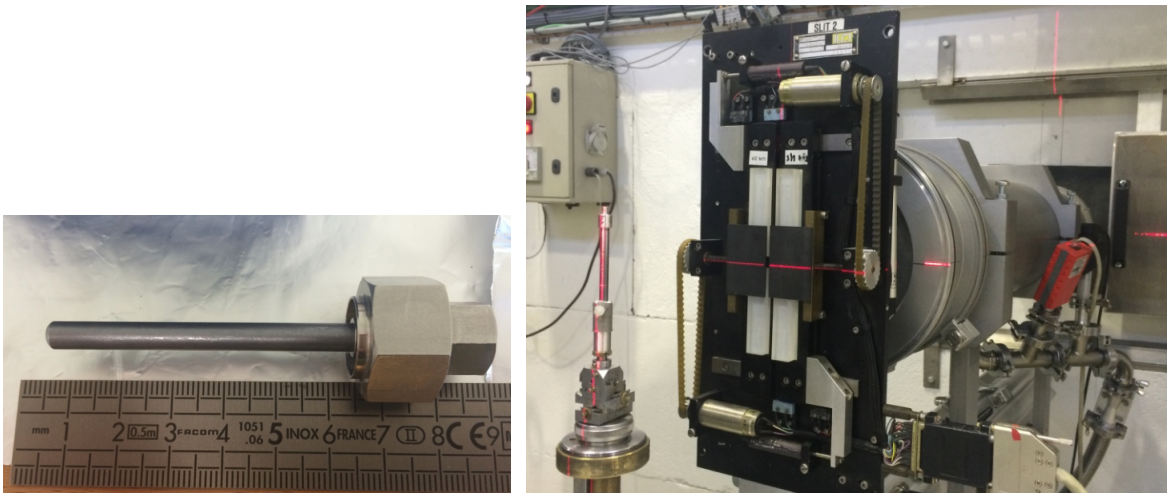

Figure B.5 Left-hand side: Image of a Vanadium cylindrical sample holder of 4mm of diameter used for powdered samples at room pressure experiments. **Right-hand side:** The pre-sample flight path and the two slits along with cadmium compact cylinder of 4mm of diameter fixed on the sample table of D16. Laser is used in order to check both vertical and horizontal alignments. *Reproduction not authorized.*

Data treatment: The data reduction consisted of the following operations and were performed using both a SANS treatment procedure in LAMP and a .prox file procedure developed by the Computing for Science group at ILL.

1. Calculates the beam center for the empty beam with 15% of attenuation measurement.
2. Calculates the transmission of all measurements.
3. Reads the 3D data for $N_{acquisitions}$, where the later means the number of gamma positions measured, and normalizes to the calibration data (*i.e.* correction of the variation of efficiency of the detectors for standards with known cross sections, *e.g.* water and vanadium [251]). If a calibration file has been previously loaded, each run is divided by the calibration file.
4. Combines the scans to the same gamma position and sorts them by gamma value.
5. Integrates over pixel having the same scattering angle (2θ-integration).
6. Subtraction of background given by equation B.29. The sample intensity
7. Normalize the sample by the normalization (vanadium) run.

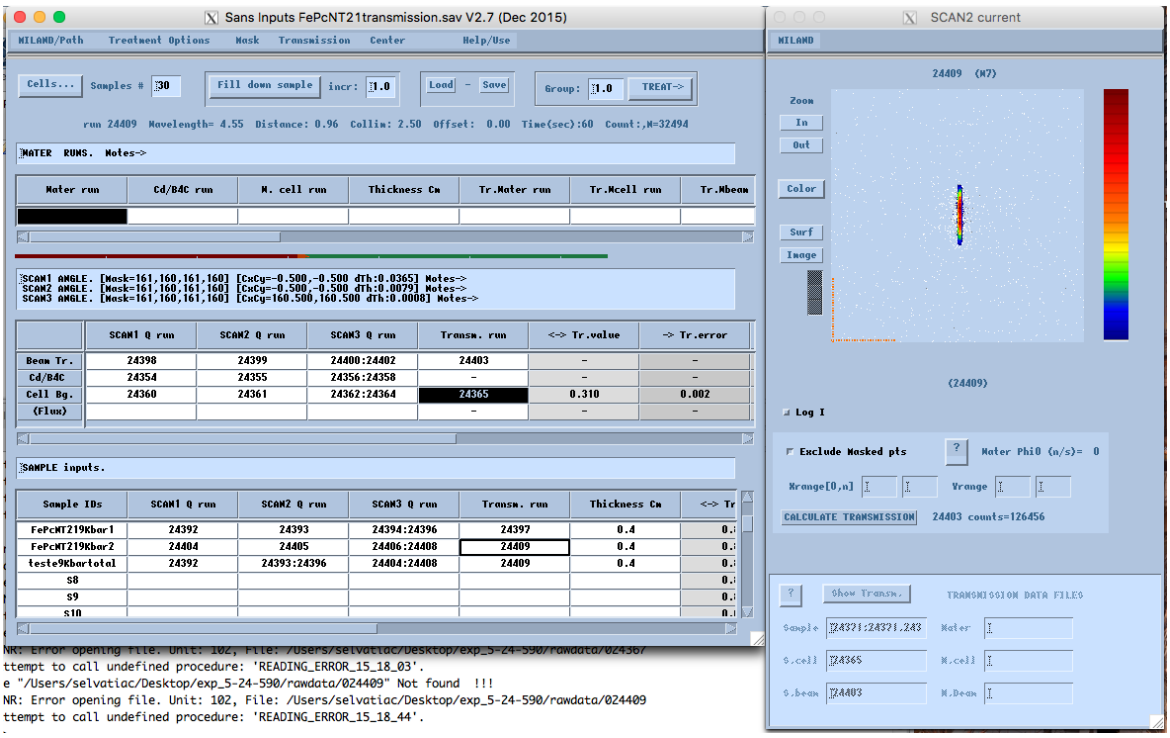

Figure B.6 LAMP graphical interface.

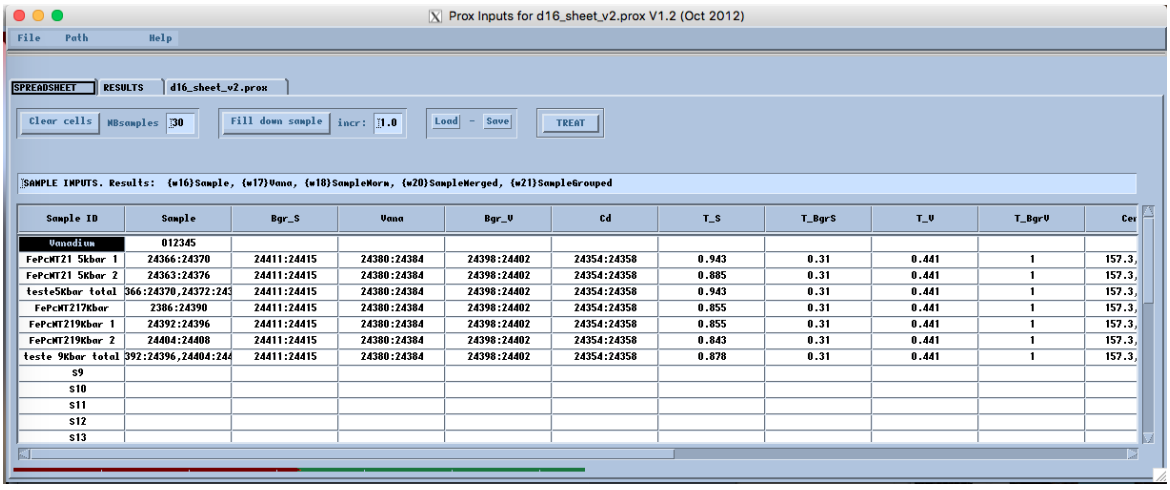

Figure B.7 D16 sheet layout.

8. Join and sort the $N_{acquisitions}$ composing a scan (*i.e.* all gamma positions are combined, normalized intensity versus 2θ).

9. Reduce the number of points and improve statistics by averaging N point together, where N

$$I_S = \frac{I_{S,EC} - I_{Cd}}{t_{S,EC}\, t_{EC}} - \frac{I_{EC} - I_{Cd}}{t_{EC}} \tag{B.29}$$

Where $I_{S,EC}$ the intensity measured from the sample inside the empty cell, t denotes the transmission with the subscripts S, sample, EC empty cell, Cd cadmium.

B.5 Neutron spectroscopy – Inelastic neutron scattering

In this section, we describe the principle of the two neutron spectrometers that were used during this thesis: the thermal time-of-flight spectrometer IN4C and the hot filter-analyser spectrometer IN1-LAGRANGE.

The first cited instrument belongs to the direct, crystal monochromator, category of the time-of-fight instruments (*i.e.* hybrid TOF). This means that the incident neutrons have their wavelength (energy E_i) chosen by a crystal monochromator and that the final energy E_f of the scattered neutrons is analysed by measuring their time of flight. IN4C is built on the thermal beam H12 at the ILL, therefore allowing the investigation of energy and momentum transfer range from [0-100 meV] and [0.5-10 $Å^{-1}$] respectively. This instrument is very well suited to the measurement of lattice excitations (phonons, rotations, librations...) and molecular vibrations up to 100 meV. Its large sensitivity to molecular rotations (either free quantum rotors levels or hindered rotations) makes it very useful to probe the quantity hydrogenated molecular units (C-H or -CH_3) in the sample, *e.g.* dimethyl-quaterthiophene or iron-phthalocyanine.

The inverse analyser spectrometer IN1-LAGRANGE has a different principle. It uses also a crystal monochromator to vary the incident neutron energy E_i, while the scattered energy E_f is fixed by the (002) Bragg reflexion of a monocrystal block of HOPG in the case of LAGRANGE. IN1 is an instrument built on the hot source at the ILL. It delivers neutrons from several tens of meV to several eV, *i.e.* covering a very large range of energy transfer. It is very useful for measuring the molecular vibrations. These modes can be separated into the so-called bending and stretching components, which have intense signatures in the [75-200 meV] and [350-400 meV] range respectively. These modes give the spectral signature of the C-H and CH_3 local environment.

B.5.1 Time of Flight principle and the spectrometer IN4C

For the inelastic neutron scattering measurements that were performed on the time of flight spectrometer IN4C, the sample were constituted of powders (about 100 mg) filled in air tight aluminium cells (transparent to neutrons), of dimensions ($4 \times 3 \times 0.02$ cm^3), see figure B.8a. The sides of the cell were covered during acquisition by cadmium, absorbing neutrons in order to reduce the background noise. As we will show in this paragraph, the measurements of vibrational excitations in powders using time of flight spectrometry proved suitable. We explain below the principles of this technique.

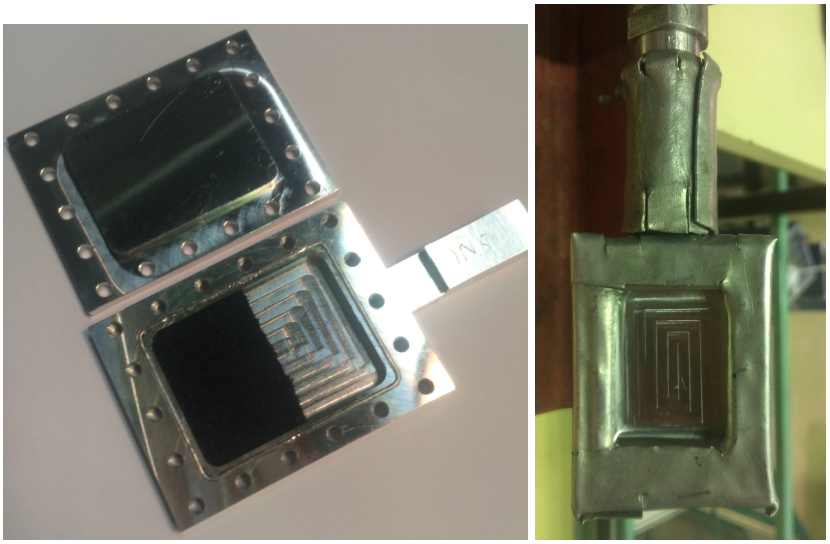

(a) **(b)**

Figure B.8 (a) Image of a flat Aluminium sample holder half filled with powdered hybrid nanotubes used during the experiment on IN4C. Note the indium wire used in order to seal the enclosure of the sample. **(b)** Flat Aluminium sample holder covered by cadmium mask.

Principle: The principle of the time of flight method is to measure the number of neutrons scattered in a certain solid angle as a function of time. The kinetic energy of each scattered neutron is evaluated by its time of flight t, *i.e.* the time it takes for the neutrons to cover the sample to detector distance, which can be traced back to its speed. Knowing its initial energy - chosen by the crystal monochromator - one can access to the energy transfer $\hbar\Omega$ between the neutron and the sample. Figure B.9 shows the layout of the IN4C time of flight spectrometer (ILL, Grenoble) used for our investigations.

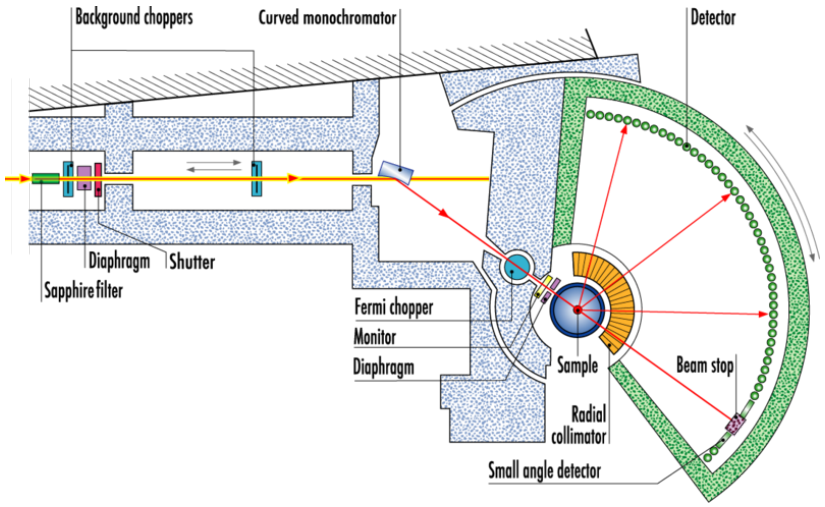

Figure B.9 Layout of the IN4C spectrometer (ILL, Grenoble). Background choppers are neutron opaque discs and drilled of holes, through which only selected neutrons can pass. They are placed perpendicularly to the incident beam and rotate with a typical speed of about 1000 rpm. The curved monochromator consists of an assembly of 55 graphite or copper single crystals, forming an angle with the incident neutron beam determined by the choice of the incident wavelength. The Fermi chopper is formed by an aluminium cassette containing an assembly consisting of a succession of layers of aluminium blades glued together using a ^{10}B enriched epoxy resin. This optical element ensures a sharp chopping of the incident beam into short time pulses and defines the origin of time t = 0. It also provides a way to tune the resolution of the instrument using the time focusing principle [252].

Instrument description: A "white" beam of neutrons comes from the neutron beam tube H12, whose aperture is located in the core neighborhood at the position of the maximum thermal neutron density. These neutrons are produced by the enriched uranium core and further thermalized by the heavy water moderator at ambient temperature.
A set of two "wheels" type steel choppers, with their horizontal axis of rotation and made of eight windows each, provides a long pulse and a rough selection of the wavelength. It also prevents higher or lower orders of the incident wavelength contaminating the measurements. They role mostly is to ensure protection against fast epithermal neutrons of the direct beam which can add a significant contribution to the background, in addition to the action of a sapphire filter positioned far upstream of the instrument. This beam is then made monochromatic by a double-curved monochromator, see figure B.10c (*i.e.* having a variable horizontal and vertical curvature). It consists of a set of 55, 2 × 4 cm single crystals mounted on a mechanism that allows to obtain a nearly spherical surface, geometrically focussing much of the divergent incident beam on a small sample volume. Bragg's law is used to select the wavelength of the incident neutrons:

$$2\frac{d_{mono}}{p}sin(\Theta_B) = \lambda_i \tag{B.30}$$

where d_{mono} is the inter-reticular distance of the selected monochromator Θ_B the angle between the lattice planes and the incident neutron beam, p an integer indicating the order of reflection and λ_i the desired wavelength.

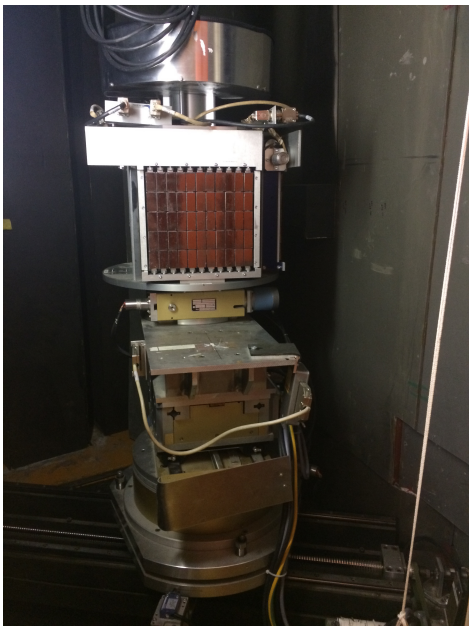

(a)

(b)

(c)

Figure B.10 (a) Photo of the IN4C monochromator. **(b)** Photo of the IN4C Time-Of-Flight path (a view from the inside). **(c)** Double-curved Cu(220) monochromator. *Reproduction not authorized.*

The resulting monochromatic beam is finally "chopped" by a Fermi chopper. This latter consists of a horizontal rotor whose function is to run an assembly of aluminium slats glued together by epoxy glue[3] enriched in ^{10}B atoms[4] at high speed (up to 40 000 rpm). In this way, the monochromatic beam can only pass through the slats when the latter ones are positioned parallel to the beam. Their fast rotation therefore transforms the long pulses into sharp monochromatic flashes of neutrons. The Fermi chopper is connected to an electronic counting device that will trip with some delay compared to the top of the Fermi. This moment, denoted t_0 is the time reference for measuring the travel time of the neutron from the Fermi

[3]This optical component is called *slit pack*

[4]This component is highly absorbent to thermal neutrons

chopper down to the ^{3}He detectors through the sample: it is the *time of flight* of the neutrons (see figure B.10b).

Neutrons scattered by the sample are therefore recorded as a function of their time of arrival (and therefore energy transfer) at the detector located at an angle 2θ. Neutrons having gained energy from the sample will arrive first at the detectors (anti-Stokes region), followed by those elastically scattered arriving in the *elastic channel*. Finally neutrons that have transferred their energy to the sample reach the detectors the last (Stokes region).

The energy resolution $\frac{\Delta E}{E}$ of the IN4C spectrometer varies between 4 and 6% (at elastic scattering). Its best performances are found for incident wavelengths between 0.7 and 4 Å. The multidetector is composed of 396 ^{3}He gas tubes covering scattering angles ranging from 3 ° to 135 °. This large detector coverage allows one to measure a large domain in (Q, $\bar{\Omega}$) for a single setup, see figure B.11.

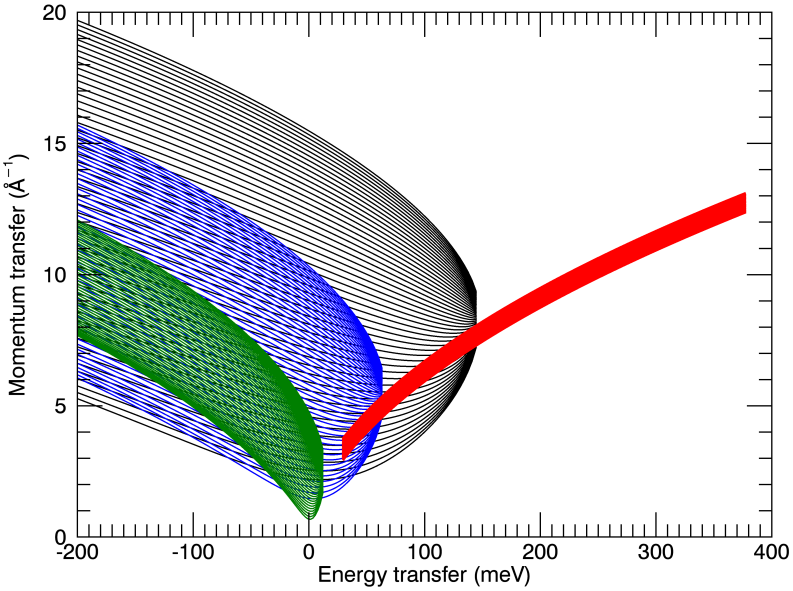

Figure B.11 (Q, $\hbar\Omega$) regions covered during the INS experiments: on IN4C using the incident wavelength 0.74 Å (black), 1.11 Å (blue) and 2.41 Å (green) - on IN1-LAGRANGE (red line).

Data treatment: There are multiple ways of doing the data treatment. This mainly depends on the physical quantity one wants to highlight. Several softwares are available at the ILL to perform the different data reductions. We have used the suite of TOF routines available in

the LAMP platform, developed by the CS group at the ILL. Its native language is IDL (see figure B.12).

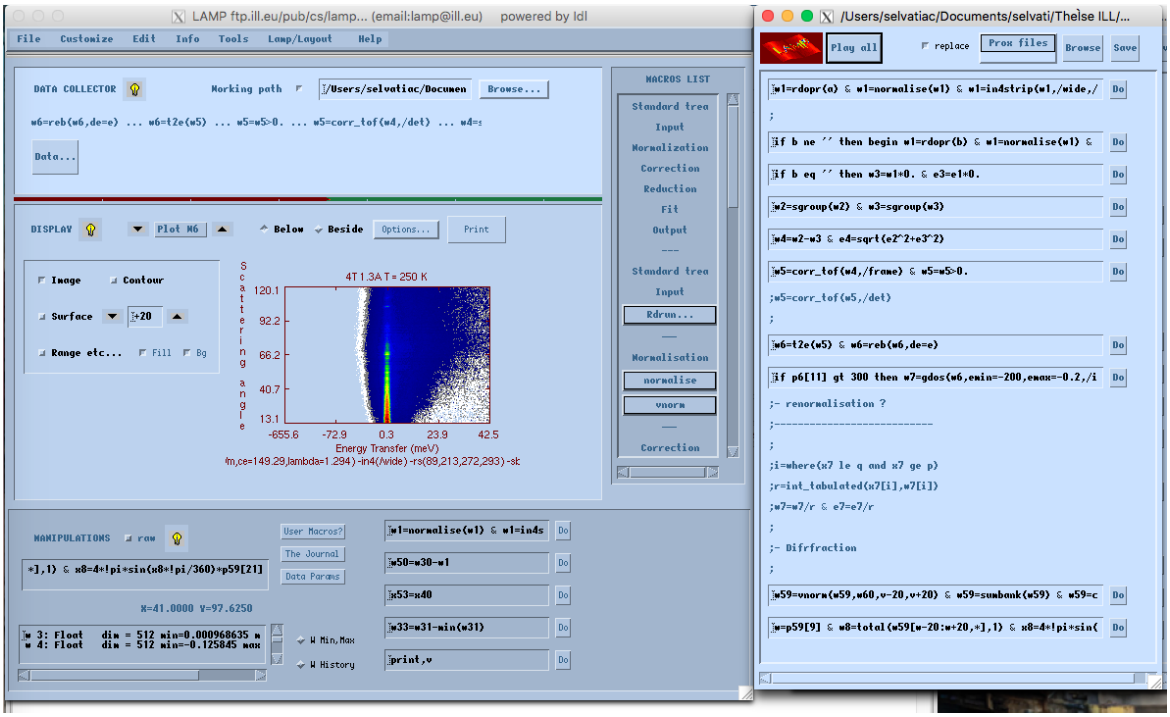

Figure B.12 LAMP graphical interface.

A classical basic treatment consists of:

1. Normalization of the data to the monitor counts (*i.e.* to the number of incident neutron).
2. Subtraction of the contribution of the sample holder - particular care should be taken for sample transmission.
3. Normalization of the data to a Vanadium standard. Vanadium being an almost purely incoherent scatterer, the elastic intensity (*i.e.* integration of the signal over the elastic channels) of its spectrum should be independent of the scattering angle. Hence, it provides a correct account for the sole Debye-Waller decrease at high Q.
4. Correction of the data from the neutron speed dependent efficiency of the detector.
5. Detector grouping of the data: this allows to improve the statistics of the signal (the new "average list of scattering angle are denoted $\bar{\theta}$).
6. Time of flight to energy conversion. At this stage, the $S(\bar{\theta}, \Omega)$ spectrum is obtained.

7. $S(\bar{\theta},\Omega)$ spectrum can be further treated in order to provide the Generalised Density Of States $G(\bar{\theta},\Omega)$ given by the relation B.27.

8. At a final stage, a triangulation and interpolation scheme is used to convert the $S(\bar{\theta},\Omega)$ maps into the more physical $S(Q,\Omega)$.

B.5.2 The inverse graphite analyser spectrometers IN1-LAGRANGE

The IN1-LAGRANGE (former IN1BeF) instrument, simply called "LAGRANGE" in the rest of this manuscript, was chosen to investigate high-frequency vibrations in a wide energy range [50, 450 meV], where the internal modes of C-H bonds in oligothiophene and iron-phthalocyanine are expected. Due to its analyzing set-up, it provides a relatively higher energy resolution (approximately 2% in the energy range probed, from 50 to 450 meV). This, together with a high flux, allows for short acquisition times at various temperatures, making it particularly suitable to inspect fine features in the spectra and follow their evolution with temperature in great details. The samples (about 100 mg) were held at 5K within a cylindrical aluminium sachet (see figure B.13) using a standard Orange cryostat.

LAGRANGE is the unique option for studying the high frequency excitations in materials at the ILL. It is installed on the hot beam H8 and constitutes the secondary spectrometer of the IN1. This instrument shares the primary spectrometer, constituted of a monochromator, with the IN1-TAS triple axis spectrometer option. LAGRANGE has been recently commissioned [161, 253]. It replaces the IN1-Be filter option. During this thesis, we have used both, but we will focus the description of the instrument on the LAGRANGE option.

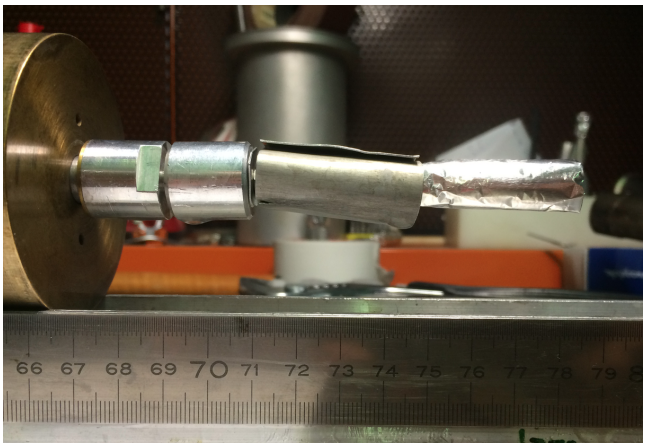

Figure B.13 Image of a cylindrical aluminium sachet (*papillote*, in french) containing the powdered sample connected to the Orange cryostat cane. Note that the upper part is covered with cylindrical Cadmium mask in order to reduce scattering from other than the sample.

Principle: By contrast to IN4C, where the incident wavelength of the neutron is prepared and the scattered energy is analysed by TOF, the principle on LAGRANGE resides on scanning the incident energy E_i for a fixed scattered energy E_f set by the crystal analysers. This is a continuous "point by point" instrument, *i.e.* the instrument changes its configuration at each energy step (at each E_i), alike what is generally done on triple axis spectrometers.

Owing to the relatively large scattered angles defined by the LAGRANGE geometry, the spectrometer probes a relatively thick region in (Q,ω), as described in figure B.11. However, the Q domain available to the instrument at each energy transfer is integrated at the detector, so that no Q dependence on the scattering can be analysed, but the integration results in a very intense signal.

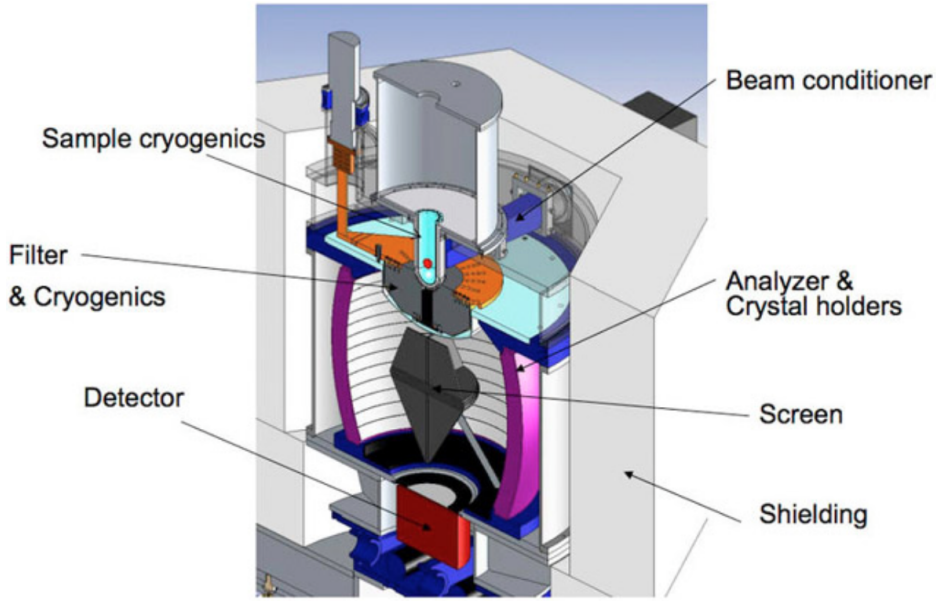

Figure B.14 Vertical cut of the LAGRANGE insert (or secondary spectrometer): the scattered neutrons with final energy of 4.5 meV are focussed to the ^3He detector by the arrangement of HOPG analyser mounted on an ellipsoidal surface, with the sample located at one of its locus. The spectra are obtained by varying the incident neutron energy. This is achieved by scanning the Bragg take-off angle of several crystal monochromators. A cooled block of polycrystalline Be is used as a large band low pass filter, reducing the background. The direct view of the secondary source (the sample) is avoided by placing a container filled with B_4C powder between the sample and the detector, *i.e.* significantly reducing the background [161].

Instrument description: IN1-LAGRANGE is installed on the hot beam H8, having a direct view of the ILL hot source, made of a graphite block heated at high temperature. A large double-focussing multi-face crystal monochromator supplies the secondary spectrometer LAGRANGE with a monochromatic beam in the intermediate and high neutron energy

ranges (mosaic Cu(220) and Cu(331) crystal faces) as well as in the lower energy range (elastically bent Si(111) and Si(311) reflections). The incident energy E_i is fixed by the Bragg angle between the monochromator face and the sample.

The IN1-Lagrange uses the combination of a cooled Be-filter and a large area, space focussing crystal analyzer, to collect the 4.5 meV energy scattered neutrons over a large solid angle of 2.5 steradian. The focussed scattered neutron are all recorded with a relatively small single counter (a He^3 gas detector). This permits, contrary to typical TOF instruments, to decouple large solid angle detections from counting volume which results in a substantial lowering of the corresponding background.

The focussing reflecting surface of $\sim$1 m^2 is built around the vertical sample-detector axis from 612 pyrolytic graphite (PG) crystals set to reflect neutrons with a fixed average energy of 4.5 meV. The appropriately shaped beryllium filter, cooled at a temperature of 20 K, is installed immediately after the sample in order to remove higher-order harmonics in the analyser reflections.
The carefully designed screen of boron-containing absorber is installed on the sample-detector axis in order to suppress the intense elastic scattering from the sample. Further reduction of the instrument background, contaminated by the high neutron energy components, is achieved through massive polyethylene shielding built around the whole analyser. The whole instrument can be considered as a variant of a classical three-axis spectrometer with a very large barrel-like fixed-energy analyser. There are no mutually moving parts within the secondary spectrometer which is positioned as a whole around the monochromator in order to record the inelastic scattering spectra changing step-by-step the incident energy similarly to a typical experiment on a three-axis spectrometer. The energy transfer, which corresponds to excitation energy in the sample, is obtained by a subtraction of the analyser energy of 4.5 meV from the energy of incident monochromatic neutrons.

Data treatment: The following data treatment was performed:

1. Subtraction of the contribution of the sample holder and instrument global contributions to the measured signal.

2. Calibration of the intensity to that of a liquid water standard.

3. Subtraction of a sample and energy dependent background, originating from *e.g.* multiphonon contributions at large energy transfer.

4. Normalization of the integrated signal to unity.

Note that the measurements were performed at a constant monitor value for each incident energy. This prevents the monitor normalization and detector efficiency steps of the TOF reductions to be performed.

Summary of Neutron scattering techniques and spectrometers/diffractometers

INS The inelastic scattering of neutrons is a powerful tool in order to probe the H atoms motions present in the encapsulated molecules only. Since its incoherent scattering cross-section is huge, if compared to the other atoms of the sample, the probed physical quantity is the Hydrogen Partial Density of States

IN4C The thermal neutrons spectrometer have access to the energy transfer range [0, 60 meV] which probes inter and intra-molecular vibrations. Orange cryostat 1.5 K

IN1-LAGRANGE the hot neutrons allow the access of the [60, 500 meV], region which the intra-molecular vibrations and C-H stretching domain of the . Orange cryostat 5 K

SANS Since the neutron wavelength is comparable with the inter-tube distance in the bundles of nanotubes as well as the one dimensional chain of FePc are probed interfere constructively

PAXY This SANS instrument allows access to a large range of momentum transfer $[3\times10^{-3}, 1\ ^{-1}]$.

D16 This diffractometer for small angles allows the high-resolution measurement of the scattered intensity in the momentum transfer range [0, 2.5 $\mathring{A}^{-1}$]. It fits perfectly

Appendix C

Carbon nanotubes and peapods under high-pressure

Carbon nanotubes have been widely studied at high pressure through Diffraction, Raman scattering and Optical Absorption [205–210, 213, 219, 221, 223, 225]. Neutrons diffraction studies performed without transmitting media, on single wall nanotubes with mean diameter 13.2 Å organized into bundles report strong variations of the (10) peak up to 5 GPa. An upshift is observed assigned to a contraction of the lattice, see figure C.1. A decrease in intensity is also observed indicating a deterioration of the bundle trigonal structure.

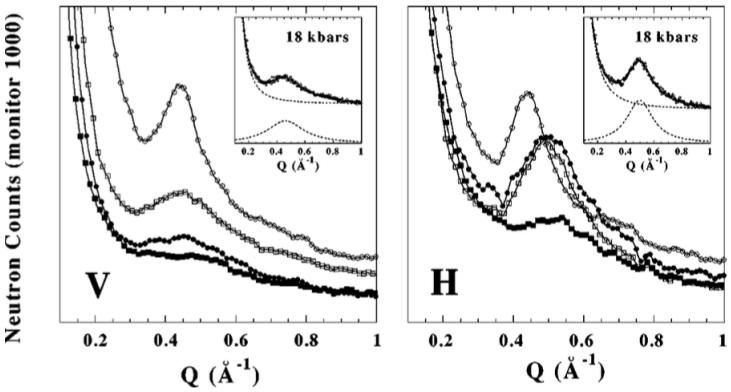

Figure C.1 Experimental SANS data recorded in two configurations: **Left-hand side:** . Taken from reference [211].

Several works have been reported on Raman spectroscopy of carbon nanotubes under high pressure. For instance, upshifting, broadening and disappearance of RBM are reported [254]. For the G band an upshift and a strong broadening are observed. However, not all studies agree on the pressure dependance of G band: some authors report a continuous

evolution [206], others, a change of slope [205], and sometime a plateau [254], see figure C.2. The discrepancies between these different studies have been explained by different factors such as nanotube diameter, bundling and transmitting media. Indeed, several works have shown a strong influence of transmitting media that was suspected, depending on its nature, to penetrate in the hollow core of nanotubes or eventually in the interstitial site between bundles (Ar for example) [209, 255].

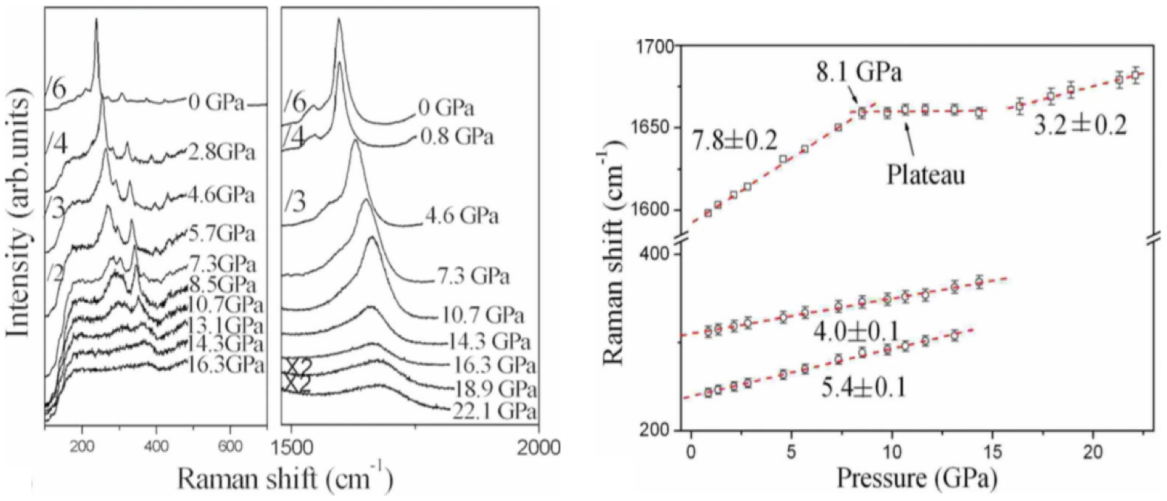

Figure C.2 Left-hand side: Raman spectra in the RBM and G-band regions for SWNTs, measured with 830 nm laser excitation using liquid argon as pressure transmitting medium. **Right-hand side:** The frequencies of two RBMs circles and the most intense G-band peak squares near 1594 cm^{-1} as a function of pressure. Taken from reference [254].

High pressure measurements of light absorption are also reported in references [219, 256] for single and double wall carbon nanotubes. Absorption band are shown to redshift under high pressure, with two anomalies associated to two critical pressures, see figure C.3.

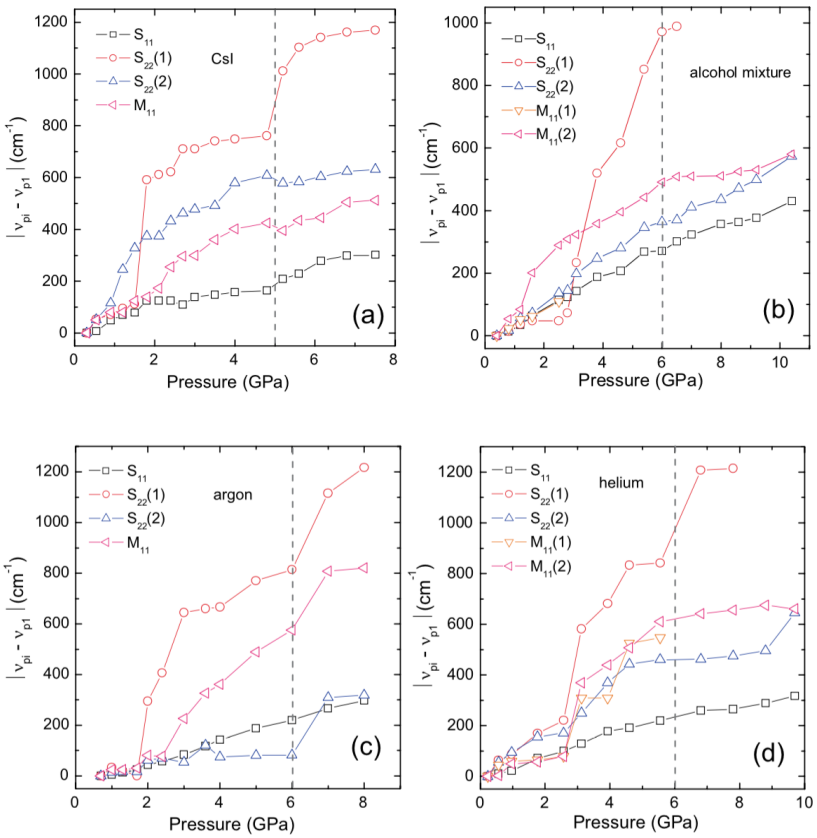

Figure C.3 Pressure-induced energy shifts of the optical transitions with respect to the lowest pressure for the as pressure transmitting medium: **(a)** CsI; **(b)** alcohol mixture; **(c)** argon; **(d)** helium. Taken from reference [219].

The different phenomena such as (10) peak shift and quenching, RBM disappearance, G band frequency dependance and anomalies in the optical absorption, all observed when the applied pressure increases have been explained by a deformation of the nanotubes cross section. A polygonization (from circular to hexagonal) of the nanotube has been proposed to explain the modifications observed for (10) peak [211]. Polygonalization has been proposed to explain the disappearance of RBM [212] as well as a deformation from circular to oval section (ovalization) [205]. The first anomaly in absorption dependence [219] has also been assigned to ovalization of the cross section of the nanotubes whereas the collapse of the nanotube would explain the second accounted anomaly. Therefore, carbon nanotubes would experience different change of shape when pressure increases, as shown on figure C.4.

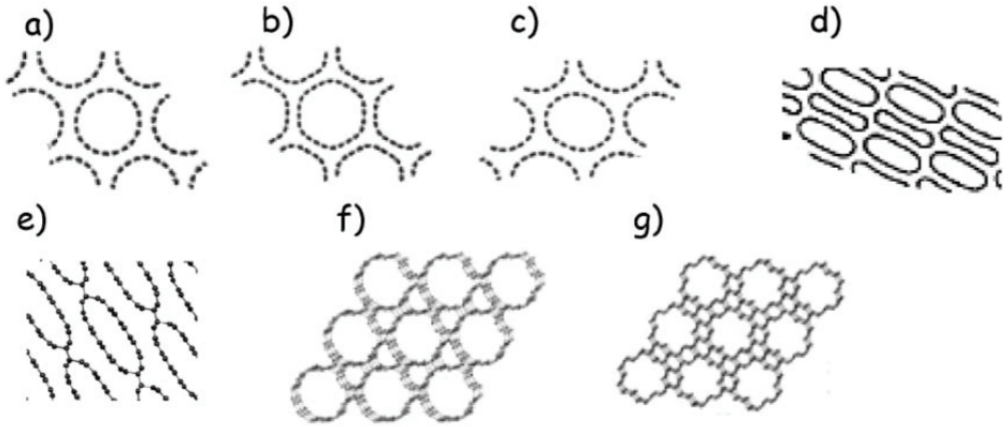

Figure C.4 a) Trigonal lattice of bundle of nanotubes at room pressure; **b)** Hexagonal poligonization; **c)** Ovalized cross-section of the nanotubes; **d)** racetrack-type and peanut-like; **e)** 1D poligonization of ovalized nanotubes; **f)** One variety of 2-D polymerization of non-deformed nanotubes; **g)** Other variety of 2-D polymerization of non-deformed nanotubes. Taken from reference [207].

The pressure at which the collapse of nanotube into peanuts or racetrack would appears has been discussed, and with support of simulation, it has been shown that this critical pressure strongly depends on the nanotube diameter [225]. It was recently shown through density functional tight binding that the collapse pressure fits a d-3 law with collapse pressure larger than that estimated on classical potentials [213]. They explore the different possible collapse channels, showing that some chiral archairs with chiral vector (3n+3,3n+3) and zigzag tubes with chiral vector (3n+3,0) would adopt a polygonal section before collapse, large tubes are also expected to go through polygonization whereas small ones would prefer a path through ovalization before collapse. It is also reported that pressure range for polygonization is shorter than for ovalization. Simulations have also explored the evolution of the structure of bundles when the tube section undergoes strong deformations [221] see figure C.5. Cerqueira shows that an arrangement with parallel nanotubes (b,d) is more energetically more favorable for tubes with larger diameters, maximizing van der Waals interactions between nanotube walls.

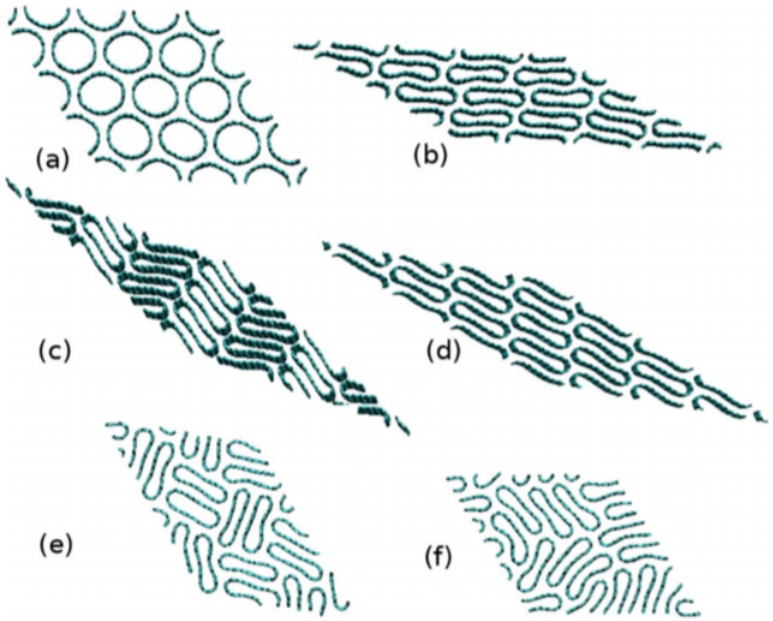

Figure C.5 (a) Bundle of (10,10) arm-chair nanotubes of diameter 13.59 Å. Snapshots of the collapsed phases at 3 GPa: **(b)** linear-o. **(c)** herringbone. **(d)** linear-n. **(e)** Basket-weave. **(f)** disordered structures. Taken from reference [221].

It has been shown also that, when nanotubes are filled the collapsing pressure is delayed to higher pressures.The molecule within the nanotube would modify the dynamic of the nanotube and the collapsing process. Such effect was firstly demonstrated on peapods [220]. Moreover, some coupled effect between the guest fullerene and the nanotube were observed after the first transition (1 GPa above) and for the second transition (downshift of G band and concomitant disappearance of the signal from C_{70}), see figure C.6. Some interaction tube/guest are also reported for C_{60} [224].

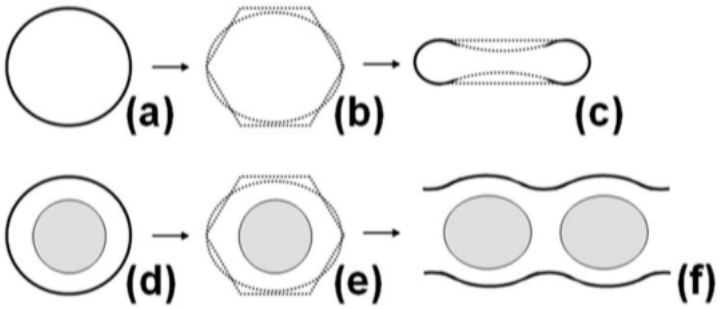

Figure C.6 Proposed nanotube cross section evolution upon pressure from **(a)** to **(c)** for pristine nanotubes and from **(d)** to **(f)** for peapods. Taken from reference [220].

A theoretical work by Shavanas [221] on carbon nanotubes filled with argon shown that at ambient pressure, a partial ordering and shell formation takes place. Depending on the filling rate the distance between Argon molecules and the nanotube wall would fall on the attractive part of the potential (few molecules), then collapse would be favoured. In the case of short distance (high filling), van de Waals force is repulsive and would create an internal resisting pressure, that would prevent the tube from an early collapse. The structures adopted at 10 GPa, strongly depend on the filling rate (see figure C.5). At high density a favored nanotube polygonization is reported. The reduction of intertubular spaces (polygonization/filling interstices with gas) would reduce the fluctuations leading to collapse that would thus be delayed. The simulated diffraction pattern predicts a strong decrease of (10) Bragg peak when the filled tube collapse independently of the bundle ordering (linear or herringbone).

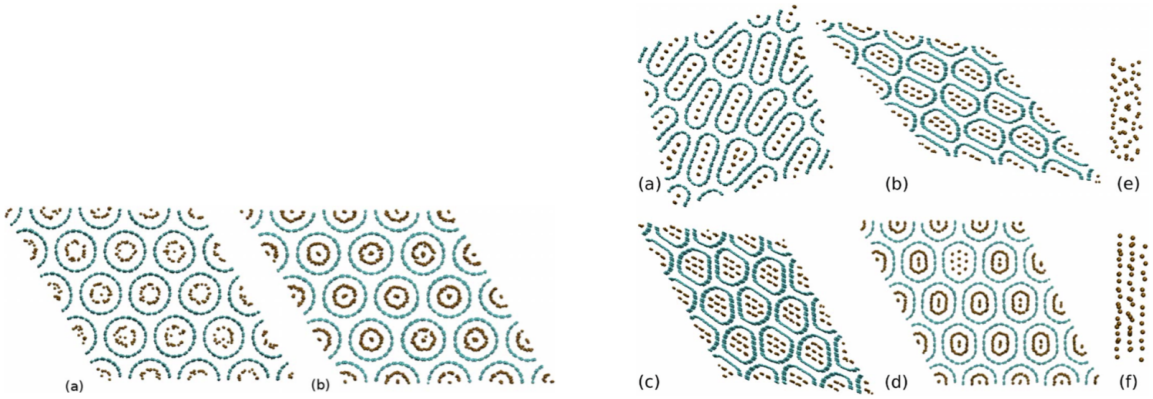

(a) Left-hand side **(b)** Right-hand side

Figure C.7 Left-hand side: Simulation cell containing **(a)** 40 and **(b)** 60 argon atoms per nanotube at 0 GPa and 300 K. **Right-hand side:** High-pressure phases of nanotubes at 10 GPa: **(a)** 40, **(b)** 50, **(c)** 60, **(d)** 70 argon atoms per nanotube. Side view argon atoms at **(e)** 0 GPa and **(f)** 10 GPa. Taken from reference [221]

Some recent experimental works also have also been reported on water encapsulated within carbon nanotubes of selected diameters [222]. The collapse pressure is also found to be much higher for filled nanotubes than for the corresponding empty tubes. Moreover, thanks to simulations it was possible to demonstrate that, under pressure, some structural ordering of water into 1D molecular chains or 2D nanoribbons could be predicted depending on the number of water molecules within the nanotube section, see figure C.8.

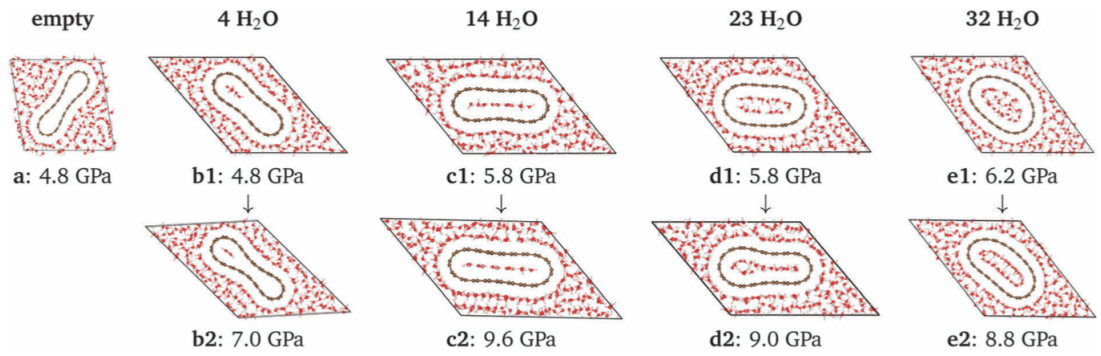

Figure C.8 Snapshots of cross-section of collapsed SWCNTs filled with various quantities of CO_2. Taken from reference [223].

Therefore, from bibliographic results we could expect an early deformation in the case of NT21, as regard of their size, (about 1 GPa according to reference [225]), and confinement effects on encapsulated FePc should also appear at rather small pressure.

Appendix D

Calculation of the diffracted intensity for a powder of peapods

This appendix describes the theory behind the model used to calculate the diffraction diagrams of a powder of an object that we call "peapods", the term "peapods" being used here in the general sense *i.e.* it refers to a 1D chain of identical objects confined in the center of a bundle of single-walled carbon nanotubes. In the case of the carbon peapods (C_{60}@SWNT), the object is a sphere.

Modelization

Our model is based on the following hypothesis: a bundle is constituted of parallel single-walled carbon nanotubes, represented as hollow cylinders with a homogeneous surface density, positioned on a finite size hexagonal lattice. These nanotubes contains a 1D lattice of an homogeneous object $_{obj}$. Each nanotube is therefore constructed as a 1D lattice of a section of tube containing one object. The length of this 1D cell is the separation between two adjacent objects. In our model, the 1D chains are not correlated in position from one tube to another, *i.e.* there is no 3D ordering of the objects. The variables of our model are shown schematically in the Figure D.1

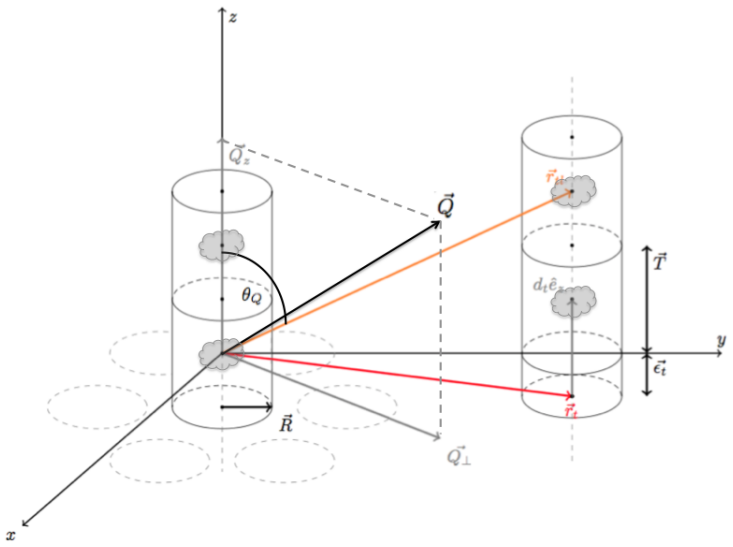

Figure D.1 Schematic description of the model used in the calculation.

Each cell can be localised by the knowledge of the index t and l, the former referring to the tube t in the bundle and the latter to the cell l along this tube. Let $\vec{r}_{lt}$ be the position of the center of the cell l in the tube t (*i.e.* the cell (lt)) with regards to a referential defined by the origin O and axis (Ox), $(0y)$ and (Oz) along the unit vectors $\vec{e}_x$, $\vec{e}_y$ and $\vec{e}_z$. One can take the origin of the referential at the center of the cell of the central tube in the bundle, as shown on Fig. D.1. We have:

$$\vec{r_{lt}} = \vec{r}_t + lT\vec{e}_z + \varepsilon_t\vec{e}_z\,, \tag{D.1}$$

where the parameter ε_t is a random value comprised between 0 and T associated to each tube. It assures an uncorrelated shift of the chain from one tube to another. The total scattering density $\rho(\vec{r})$ of the model can be written:

$$\rho(\vec{r}) = \sum_{t=1}^{N_l}\sum_{1}^{N_t}\rho_m(\vec{r}-\vec{r_{lt}}) \tag{D.2}$$

with N_t the number of tubes in the bundle, N_l the number of 1D cells per tube and $\rho_m(\vec{r}-\vec{r_{lt}})$ the density of one cell.

The scattered amplitude $A(\vec{Q})$ of a diffracted beam is proportional to the Fourier transform of the scatterer $\rho_m(\vec{r}-\vec{r_{lt}})$:

$$A(\vec{Q}) \propto \sum_l\sum_t\int d^3\vec{r}_{lt}\ \exp\Big\{i(\vec{Q}\cdot\vec{r}_{lt})\Big\}\rho_m(\vec{r}-\vec{r_{lt}}) \tag{D.3}$$

with

$$\rho_m(\vec{r}) = \rho_{NT}(\vec{r}) + \rho_{obj}(\vec{r}) \tag{D.4}$$

Let us introduce the vector $\vec{R}$:

$$\vec{R} = \vec{r}_{lt} + \vec{r} \rightarrow \vec{R} = \vec{R}_l + nT\hat{e}_z + d_t\hat{e}_z + \vec{r} \tag{D.5}$$

Where the scattered amplitude from equation **??** is proportional to four terms:

$$A(\vec{Q}) \propto \sum_l \exp\Big\{i(\vec{Q}_\perp \cdot \vec{R}_l)\Big\} \sum_t \exp\{i(Q_z nT + d_t)\} \int d^3\vec{r} \exp\Big\{i(\vec{Q}\cdot\vec{r})\Big\} \rho_m(\vec{r} - \vec{r}_{lt}), \tag{D.6}$$

and each of the three term is either a structure factors $S(\vec{Q})$ or a form factors $F(\vec{Q})$:

$$A(\vec{Q}) \propto S_l(\vec{Q})\, S_t(\vec{Q})\, F(\vec{Q}) \tag{D.7}$$

The second term in equation (D.7) is equal to:

$$S_t(\vec{Q}) = \sum_{t=-N/2}^{N/2} \exp\{i(Q_z(nT))\} = \frac{\sin\left(Q_z N_t P/2\right)}{\sin\left(Q_z P/2\right)} \tag{D.8}$$

The last term in equation (D.7) is the form factor of the peapods:

$$F(\vec{Q}) = F_{obj@NT}(\vec{Q}) = \int \exp\Big\{i(\vec{Q}\cdot\vec{r})\Big\} \rho_{obj@NT}(\vec{r}) d^3\vec{r} \tag{D.9}$$

$$F_{obj@NT}(\vec{Q}) = \int \exp\Big\{i(\vec{Q}\cdot\vec{r})\Big\} (\rho_{NT}(\vec{r}) + \rho_{obj}(\vec{r})) d^3\vec{r} \tag{D.10}$$

The form factor of the hybrid FePc@NTs can be written as:

$$F_{obj@NT}(\vec{Q}) = F_{NT}(\vec{Q}) + F_{obj}(\vec{Q}) \tag{D.11}$$

Therefore, the scattered amplitude of a bundle of peapods is given by:

$$\boxed{A_{obj@NT}(\vec{Q}) \propto \sum_t \exp\Big\{i(\vec{Q}_\perp \cdot \vec{R}_t)\Big\} \left[\frac{\sin\left(Q_z N_h P/2\right)}{\sin\left(Q_z P/2\right)}\right] \sum_t \exp\{i(Q_z d_t)\}[F_{NT}(\vec{Q}) + F_{obj}(\vec{Q})]} \tag{D.12}$$

D.0.1 Form factor of a carbon nanotube

The cylinder that in our model represents the carbon nanotube has its axis aligned along z axis, its length is equal to L and radius r_{NT}. The cylinder is easily described by the cylindrical coordinates. The form factor of the cylinder is given by equation (D.13):

$$F_{NT}(\vec{Q}) = 2\pi\,\sigma_{NT}\,r_{NT}\,T\,J_0(Q_\perp r_{NT})\left[\frac{\sin(Q_z L/2)}{(Q_z L/2)}\right] \tag{D.13}$$

D.0.2 Form factor of a solid cylinder of FePc

If one considers that the encapsulated object is approximated by a full cylinder of uniform density σ_c, of radius R_c and thickness ε then the form factor of the object writes:

$$F_{obj}(\vec{Q}) = 2\sigma_c\left[\frac{\sin(Q_z \varepsilon/2)}{(Q_z \varepsilon/2)}\right]\frac{J_1(Q_\perp r_d)}{Q_\perp r_d} \tag{D.14}$$

with J_1 the cylindrical Bessel function of first order.

Different cases are consider in this thesis:

First case: ε = T

This represents the case of a uniform filling of the nanotube by a rod. In that case, there is no variation of the scattering density along the direction (Oz).

$$F_{obj}(\vec{Q}) = 2\sigma_c\left[\frac{\sin(Q_z T/2)}{(Q_z T/2)}\right]\frac{J_1(Q_\perp R_c)}{Q_\perp R_c} \tag{D.15}$$

Second case: ε = 0

This represents the case of a 1D packing of uniform disks along the nanotube axis.

$$F_{obj}(\vec{Q}) = 2\sigma_c\frac{J_1(Q_\perp R_c)}{Q_\perp R_c} \tag{D.16}$$

For a specific value of momentum transfer $\vec{Q}$, the scattered intensity $I(\vec{Q})$ is proportional to the square of the scattering amplitude:

$$I(\vec{Q}) = || A(\vec{Q}) ||^2 = [S_t(\vec{Q})]^2 \; || S_h(\vec{Q}) ||^2 \; [F_{NT}(\vec{Q}) + F_{obj}(\vec{Q})]^2 \tag{D.17}$$

Bibliography

[1] S Iijima and T Ichihashi. Single-shell carbon nanotubes of 1-nm diameter. 1993.

[2] Matthew Y Sfeir, Feng Wang, Limin Huang, Chia-Chin Chuang, J Hone, Stephen P O'Brien, Tony F Heinz, and Louis E Brus. Probing electronic transitions in individual carbon nanotubes by Rayleigh scattering. *Science*, 306(5701):1540–1543, 2004.

[3] JY Huang, S Chen, ZQ Wang, K Kempa, YM Wang, SH Jo, G Chen, MS Dresselhaus, and ZF Ren. Superplastic carbon nanotubes. *Nature*, 439(7074):281–281, 2006.

[4] SC Tsang, YK Chen, PJ Harris, ML Green, et al. A simple chemical method of opening and filling carbon nanotubes. *Nature*, 372(6502):159–162, 1994.

[5] Brian W Smith, Marc Monthioux, and David E Luzzi. Encapsulated C_{60} in carbon nanotubes. *Nature*, 396:323–324, 1998.

[6] Andrei N Khlobystov, David A Britz, and G Andrew D Briggs. Molecules in carbon nanotubes. *Accounts of chemical research*, 38(12):901–909, 2005.

[7] Ryo Kitaura and Hisanori Shinohara. Carbon-Nanotube-Based Hybrid Materials: Nanopeapods. *Chemistry–An Asian Journal*, 1(5):646–655, 2006.

[8] Andrey Chuvilin, Andrei N Khlobystov, Dirk Obergfell, Miroslav Haluska, Shihe Yang, Siegmar Roth, and Ute Kaiser. Observations of Chemical Reactions at the Atomic Scale: Dynamics of Metal-Mediated Fullerene Coalescence and Nanotube Rupture. *Angewandte Chemie International Edition*, 49(1):193–196, 2010.

[9] Lain-Jong Li, AN Khlobystov, JG Wiltshire, GAD Briggs, and RJ Nicholas. Diameter-selective encapsulation of metallocenes in single-walled carbon nanotubes. *Nature Materials*, 4(6):481–485, 2005.

[10] Yupeng Ren and Giorgia Pastorin. Incorporation of hexamethylmelamine inside capped carbon nanotubes. *Advanced Materials*, 20(11):2031–2036, 2008.

[11] Yoko Iizumi, Toshiya Okazaki, Zheng Liu, Kazu Suenaga, Takeshi Nakanishi, Sumio Iijima, Georgios Rotas, and Nikos Tagmatarchis. Host–guest interactions in aza-fullerene ($C_{59}N$)-single-wall carbon nanotube (SWCNT) peapod hybrid structures. *Chemical Communications*, 46(8):1293–1295, 2010.

[12] Jeremy Sloan, Angus I Kirkland, John L Hutchison, and Malcolm LH Green. Structural characterization of atomically regulated nanocrystals formed within single-walled carbon nanotubes using electron microscopy. *Accounts of chemical research*, 35(12):1054–1062, 2002.

[13] Jing Lu, Shigeru Nagase, Dapeng Yu, Hengqiang Ye, Rushan Han, Zhengxiang Gao, Shuang Zhang, and Lianmao Peng. Amphoteric and controllable doping of carbon nanotubes by encapsulation of organic and organometallic molecules. *Physical review letters*, 93(11):116804, 2004.

[14] Pedro MFJ Costa, Dmitri Golberg, Masanori Mitome, Silke Hampel, Albrecht Leonhardt, Bernd Buchner, and Yoshio Bando. Stepwise current-driven release of attogram quantities of copper iodide encapsulated in carbon nanotubes. *Nano letters*, 8(10):3120–3125, 2008.

[15] Jian-guo Wang, Yong-an Lv, Xiao-nian Li, and Mingdong Dong. Point-defect mediated bonding of Pt clusters on (5,5) carbon nanotubes. *The Journal of Physical Chemistry C*, 113(3):890–893, 2008.

[16] Jean-Philippe Tessonnier, Ovidiu Ersen, Gisela Weinberg, Cuong Pham-Huu, Dang Sheng Su, and Robert Schlogl. Selective deposition of metal nanoparticles inside or outside multiwalled carbon nanotubes. *Acs Nano*, 3(8):2081–2089, 2009.

[17] Won Young Choi, Jeong Won Kang, and Ho Jung Hwang. Structures of ultrathin copper nanowires encapsulated in carbon nanotubes. *Physical Review B*, 68(19):193405, 2003.

[18] Elliott H Lieb and Daniel C Mattis. *Mathematical physics in one dimension: exactly soluble models of interacting particles*. Academic Press, 2013.

[19] Jamie H Warner, Yasuhiro Ito, Mujtaba Zaka, Ling Ge, Takao Akachi, Haruya Okimoto, Kyriakos Porfyrakis, Andrew AR Watt, Hisanori Shinohara, and G Andrew D Briggs. Rotating fullerene chains in carbon nanopeapods. *Nano letters*, 8(8):2328–2335, 2008.

[20] Karla S Troche, Vitor R Coluci, Scheila F Braga, David D Chinellato, Fernando Sato, Sergio B Legoas, Riccardo Rurali, and Douglas S Galvão. Prediction of ordered phases of encapsulated C_{60}, C_{70}, and C_{78} inside carbon nanotubes. *Nano letters*, 5(2):349–355, 2005.

[21] Colin Bousige, Stéphane Rols, Erwan Paineau, Stéphan Rouzière, Cristian Mocuta, Bart Verberck, Jonathan P Wright, Hiromichi Kataura, and Pascale Launois. Progressive melting in confined one-dimensional C_{60} chains. *Physical Review B*, 86(4):045446, 2012.

[22] Lunhui Guan, Kazu Suenaga, Zujin Shi, Zhennan Gu, and Sumio Iijima. Polymorphic structures of iodine and their phase transition in confined nanospace. *Nano letters*, 7(6):1532–1535, 2007.

[23] JA Misewich, R Martel, Ph Avouris, JC Tsang, S Heinze, and J Tersoff. Electrically induced optical emission from a carbon nanotube FET. *Science*, 300(5620):783–786, 2003.

[24] Jia Chen, Vasili Perebeinos, Marcus Freitag, James Tsang, Qiang Fu, Jie Liu, and Phaedon Avouris. Bright infrared emission from electrically induced excitons in carbon nanotubes. *Science*, 310(5751):1171–1174, 2005.

[25] Phaedon Avouris, Marcus Freitag, and Vasili Perebeinos. Carbon-nanotube photonics and optoelectronics. *Nature photonics*, 2(6):341–350, 2008.

[26] V Derycke, R Martel, J Appenzeller, and Ph Avouris. Controlling doping and carrier injection in carbon nanotube transistors. *Applied Physics Letters*, 80(15):2773–2775, 2002.

[27] R Martel, V Derycke, C Lavoie, J Appenzeller, KK Chan, J Tersoff, and Ph Avouris. Ambipolar electrical transport in semiconducting single-wall carbon nanotubes. *Physical Review Letters*, 87(25):256805, 2001.

[28] Masashi Shiraishi, Taishi Takenobu, Atsuo Yamada, Masafumi Ata, and Hiromichi Kataura. Hydrogen storage in single-walled carbon nanotube bundles and peapods. *Chemical Physics Letters*, 358(3):213–218, 2002.

[29] E Jouguelet, C Mathis, and P Petit. Controlling the electronic properties of single-wall carbon nanotubes by chemical doping. *Chemical Physics Letters*, 318(6):561–564, 2000.

[30] Moonsub Shim, Ali Javey, Nadine Wong Shi Kam, and Hongjie Dai. Polymer functionalization for air-stable n-type carbon nanotube field-effect transistors. *Journal of the American Chemical Society*, 123(46):11512–11513, 2001.

[31] H Kataura, Y Maniwa, M Abe, A Fujiwara, T Kodama, K Kikuchi, H Imahori, Y Misaki, S Suzuki, and Y Achiba. Optical properties of fullerene and non-fullerene peapods. *Applied Physics A*, 74(3):349–354, 2002.

[32] Franco Dinelli, Raffaella Capelli, Maria A Loi, Mauro Murgia, Michele Muccini, Antonio Facchetti, and Tobin J Marks. High-Mobility Ambipolar Transport in Organic Light-Emitting Transistors. *Advanced Materials*, 18(11):1416–1420, 2006.

[33] Amanda R Murphy and Jean MJ Frechet. Organic semiconducting oligomers for use in thin film transistors. *Chemical reviews*, 107(4):1066–1096, 2007.

[34] Myung-Han Yoon, Sara A DiBenedetto, Matthew T Russell, Antonio Facchetti, and Tobin J Marks. High-performance n-channel carbonyl-functionalized quaterthiophene semiconductors: thin-film transistor response and majority carrier type inversion via simple chemical protection/deprotection. *Chemistry of Materials*, 19(20):4864–4881, 2007.

[35] Markus KR Fischer, Sophie Wenger, Mingkui Wang, Amaresh Mishra, Shaik M Zakeeruddin, Michael Grätzel, and Peter Bäuerle. D-π-A sensitizers for dye-sensitized solar cells: linear vs branched oligothiophenes. *Chemistry of Materials*, 22(5):1836–1845, 2010.

[36] Maria Antonietta Loi, Jia Gao, Fabrizio Cordella, Pascal Blondeau, Enzo Menna, Barbora Bártová, Cécile Hébert, Sorin Lazar, Gianluigi A Botton, Matus Milko, et al. Encapsulation of Conjugated Oligomers in Single-Walled Carbon Nanotubes: Towards Nanohybrids for Photonic Devices. *Advanced Materials*, 22(14):1635–1639, 2010.

[37] Laurent Alvarez, Yann Almadori, Raul Arenal, R Babaa, Thierry Michel, Rozenn Le Parc, Jean-Louis Bantignies, Bruno Jousselme, Serge Palacin, Patrick Hermet, et al. Charge transfer evidence between carbon nanotubes and encapsulated conjugated oligomers. *The Journal of Physical Chemistry C*, 115(24):11898–11905, 2011.

[38] Kazuhiro Yanagi, Konstantin Iakoubovskii, Hiroyuki Matsui, Hiroyuki Matsuzaki, Hiroshi Okamoto, Yasumitsu Miyata, Yutaka Maniwa, Said Kazaoui, Nobutsugu Minami, and Hiromichi Kataura. Photosensitive function of encapsulated dye in carbon nanotubes. *Journal of the American Chemical Society*, 129(16):4992–4997, 2007.

[39] Jia Gao, Pascal Blondeau, Patrizio Salice, Enzo Menna, Barbora Bártová, Cécile Hébert, Jens Leschner, Ute Kaiser, Matus Milko, Claudia Ambrosch-Draxl, et al. Electronic interactions between "pea" and "pod": the case of oligothiophenes encapsulated in carbon nanotubes. *Small*, 7(13):1807–1815, 2011.

[40] Chao Zhou, Sihao Chen, Jianzhong Lou, Jihu Wang, Qiujie Yang, Chuanrong Liu, Dapeng Huang, and Tonghe Zhu. Graphene's cousin: the present and future of graphane. *Nanoscale research letters*, 9(1):1–9, 2014.

[41] Stefano Piscanec, Michele Lazzeri, John Robertson, Andrea C Ferrari, and Francesco Mauri. Optical phonons in carbon nanotubes: Kohn anomalies, Peierls distortions, and dynamic effects. *Physical Review B*, 75(3):035427, 2007.

[42] Riichiro Saito, Gene Dresselhaus, Mildred S Dresselhaus, et al. *Physical properties of carbon nanotubes*, volume 35. World Scientific, 1998.

[43] Stephanie Reich, Christian Thomsen, and Janina Maultzsch. *Carbon nanotubes: basic concepts and physical properties*. John Wiley & Sons, 2008.

[44] Mildred S Dresselhaus, G Dresselhaus, R Saito, and A Jorio. Raman spectroscopy of carbon nanotubes. *Physics reports*, 409(2):47–99, 2005.

[45] Philip Richard Wallace. The band theory of graphite. *Physical Review*, 71(9):622, 1947.

[46] Phaedon Avouris. Graphene: electronic and photonic properties and devices. *Nano letters*, 10(11):4285–4294, 2010.

[47] Ge G Samsonidze, A R Saito, D A Jorio, E Pimenta, Filho Souza, F A Grüneis, D G Dresselhaus, MS Dresselhausa, et al. The concept of cutting lines in carbon nanotube science. *Journal of nanoscience and nanotechnology*, 3(6):431–458, 2003.

[48] Noriaki Hamada, Shin-ichi Sawada, and Atsushi Oshiyama. New one-dimensional conductors: graphitic microtubules. *Physical Review Letters*, 68(10):1579, 1992.

[49] Riichiro Saito, Mitsutaka Fujita, Gene Dresselhaus, and Mildred S Dresselhaus. Electronic structure of graphene tubules based on C_{60}. *Physical Review B*, 46(3):1804, 1992.

[50] Valentin N Popov. Carbon nanotubes: properties and application. *Materials Science and Engineering: R: Reports*, 43(3):61–102, 2004.

[51] CT White and JW Mintmire. Density of states reflects diameter in nanotubes. *Nature*, 394(6688):29–30, 1998.

[52] H Kataura, Y Kumazawa, Y Maniwa, I Umezu, S Suzuki, Yo Ohtsuka, and Y Achiba. Optical properties of single-wall carbon nanotubes. *Synthetic metals*, 103(1):2555–2558, 1999.

[53] Stephanie Reich, Janina Maultzsch, Christian Thomsen, and Pablo Ordejon. Tight-binding description of graphene. *Physical Review B*, 66(3):035412, 2002.

[54] A Jorio, MA Pimenta, AG Souza Filho, R Saito, G Dresselhaus, and MS Dresselhaus. Characterizing carbon nanotube samples with resonance Raman scattering. *New Journal of Physics*, 5(1):139, 2003.

[55] Sergei M Bachilo, Michael S Strano, Carter Kittrell, Robert H Hauge, Richard E Smalley, and R Bruce Weisman. Structure-assigned optical spectra of single-walled carbon nanotubes. *Science*, 298(5602):2361–2366, 2002.

[56] Jean-Sébastien Lauret, Christophe Voisin, Guillaume Cassabois, Claude Delalande, Ph Roussignol, Oliver Jost, and L Capes. Ultrafast carrier dynamics in single-wall carbon nanotubes. *Physical review letters*, 90(5):057404, 2003.

[57] Jassduke Gao and MA Loi. Photophysics of polymer-wrapped single-walled carbon nanotubes. *The European Physical Journal B*, 75(2):121–126, 2010.

[58] J Gao, M Kwak, J Wildeman, A Herrmann, and MA Loi. Effectiveness of sorting single-walled carbon nanotubes by diameter using polyfluorene derivatives. *Carbon*, 49(1):333–338, 2011.

[59] Karimulla Mulla, Shuai Liang, Haseena Shaik, Eyad A Younes, Alex Adronov, and Yuming Zhao. Dithiafulvenyl-grafted phenylene ethynylene polymers as selective and reversible dispersants for single-walled carbon nanotubes. *Chemical Communications*, 51(1):149–152, 2015.

[60] J Maultzsch, S Reich, C Thomsen, H Requardt, and P Ordejón. Phonon dispersion in graphite. *Physical review letters*, 92(7):075501, 2004.

[61] Eduardo B Barros, Ado Jorio, Georgii G Samsonidze, Rodrigo B Capaz, Antônio G Souza Filho, Josué Mendes Filho, Gene Dresselhaus, and Mildred S Dresselhaus. Review on the symmetry-related properties of carbon nanotubes. *Physics Reports*, 431(6):261–302, 2006.

[62] MS Dresselhaus, G Dresselhaus, A Jorio, AG Souza Filho, and R Saito. Raman spectroscopy on isolated single wall carbon nanotubes. *Carbon*, 40(12):2043–2061, 2002.

[63] MS Dresselhaus, G Dresselhaus, A Jorio, AG Souza Filho, and R Saito. Raman spectroscopy on isolated single wall carbon nanotubes. *Carbon*, 40(12):2043–2061, 2002.

[64] MS Dresselhaus and PC Eklund. Phonons in carbon nanotubes. *Advances in Physics*, 49(6):705–814, 2000.

[65] Inc Carbon-Solutions. P2-SWCNT, 2016.

[66] R Saito, T Takeya, T Kimura, G Dresselhaus, and MS Dresselhaus. Raman intensity of single-wall carbon nanotubes. *Physical Review B*, 57(7):4145, 1998.

[67] P Giura, N Bonini, G Creff, JB Brubach, P Roy, and M Lazzeri. Temperature evolution of infrared-and Raman-active phonons in graphite. *Physical Review B*, 86(12):121404, 2012.

[68] J Maultzsch, H Telg, S Reich, and C Thomsen. Radial breathing mode of single-walled carbon nanotubes: Optical transition energies and chiral-index assignment. *Physical Review B*, 72(20):205438, 2005.

[69] R.A. Jishi, L. Venkataraman, M.S. Dresselhaus, and G. Dresselhaus. Phonon modes in carbon nanotubules. *Chemical Physics Letters*, 209(1):77 – 82, 1993.

[70] A Jorio, R Saito, JH Hafner, CM Lieber, M Hunter, T McClure, G Dresselhaus, and MS Dresselhaus. Structural (n,m) determination of isolated single-wall carbon nanotubes by resonant Raman scattering. *Physical Review Letters*, 86(6):1118, 2001.

[71] M Milnera, J Kürti, Martin Hulman, and Hans Kuzmany. Periodic resonance excitation and intertube interaction from quasicontinuous distributed helicities in single-wall carbon nanotubes. *Physical Review Letters*, 84(6):1324, 2000.

[72] Michael S Strano, Stephen K Doorn, Erik H Haroz, Carter Kittrell, Robert H Hauge, and Richard E Smalley. Assignment of (n,m) Raman and optical features of metallic single-walled carbon nanotubes. *Nano Letters*, 3(8):1091–1096, 2003.

[73] H Telg, J Maultzsch, S Reich, F Hennrich, and C Thomsen. Chirality distribution and transition energies of carbon nanotubes. *Physical review letters*, 93(17):177401, 2004.

[74] Ado Jorio, C Fantini, MA Pimenta, RB Capaz, Ge G Samsonidze, G Dresselhaus, MS Dresselhaus, J Jiang, N Kobayashi, A Grüneis, et al. Resonance Raman spectroscopy (n,m)-dependent effects in small-diameter single-wall carbon nanotubes. *Physical Review B*, 71(7):075401, 2005.

[75] Paulo T Araujo, Stephen K Doorn, Svetlana Kilina, Sergei Tretiak, Erik Einarsson, Shigeo Maruyama, Helio Chacham, Marcos A Pimenta, and Ado Jorio. Third and fourth optical transitions in semiconducting carbon nanotubes. *Physical Review Letters*, 98(6):067401, 2007.

[76] F Tuinstra and J L_ Koenig. Raman spectrum of graphite. *The Journal of Chemical Physics*, 53(3):1126–1130, 1970.

[77] A Jorio, AG Souza Filho, G Dresselhaus, MS Dresselhaus, AK Swan, MS Ünlü, BB Goldberg, MA Pimenta, JH Hafner, CM Lieber, et al. G-band resonant Raman study of 62 isolated single-wall carbon nanotubes. *Physical Review B*, 65(15):155412, 2002.

[78] Orest Dubay and Georg Kresse. Accurate density functional calculations for the phonon dispersion relations of graphite layer and carbon nanotubes. *Physical Review B*, 67(3):035401, 2003.

[79] SDM Brown, A Jorio, P Corio, MS Dresselhaus, G Dresselhaus, R Saito, and K Kneipp. Origin of the Breit-Wigner-Fano lineshape of the tangential G-band feature of metallic carbon nanotubes. *Physical Review B*, 63(15):155414, 2001.

[80] M. Cardona and M. V. Klein. Light scattering in solids I. In *Light Scattering in Solids I*, pages 169–172. Springer, 1983.

[81] O Dubay, G Kresse, and H Kuzmany. Phonon softening in metallic nanotubes by a Peierls-like mechanism. *Physical review letters*, 88(23):235506, 2002.

[82] S Piscanec, M Lazzeri, Francesco Mauri, AC Ferrari, and J Robertson. Kohn anomalies and electron-phonon interactions in graphite. *Physical review letters*, 93(18):185503, 2004.

[83] W Kohn. Image of the Fermi Surface in the Vibration Spectrum of a Metal. *Physical Review Letters*, 2(9):393, 1959.

[84] Benjamin Hatting, Sebastian Heeg, Kenichi Ataka, Joachim Heberle, Frank Hennrich, Manfred M Kappes, Ralph Krupke, and Stephanie Reich. Fermi energy shift in deposited metallic nanotubes: A Raman scattering study. *Physical Review B*, 87(16):165442, 2013.

[85] Yang Wu, Janina Maultzsch, Ernst Knoesel, Bhupesh Chandra, Mingyuan Huang, Matthew Y Sfeir, Louis E Brus, J Hone, and Tony F Heinz. Variable electron-phonon coupling in isolated metallic carbon nanotubes observed by Raman scattering. *Physical review letters*, 99(2):027402, 2007.

[86] SM Bose, S Gayen, and SN Behera. Theory of the tangential G-band feature in the Raman spectra of metallic carbon nanotubes. *Physical Review B*, 72(15):153402, 2005.

[87] S Iijima et al. Helical microtubules of graphitic carbon. *nature*, 354(6348):56–58, 1991.

[88] M. S. Dresselhaus. Down the straight and narrow. *Nature*, 358:195–196, 1992.

[89] B. I. Dunlap J. W. Mintmire and C. T. White. Are fullerene tubules metallic? *Phys. Rev. Lett.*, 68:631–634, Feb 1992.

[90] G. Dresselhaus R. Saito, M. Fujita and M. S. Dresselhaus. Electronic structure and growth mechanism of carbon tubules. *Materials Science and Engineering: B*, 19(1):185–191, 1993.

[91] Beatrice Burteaux, Agnès Claye, Brian W Smith, Marc Monthioux, David E Luzzi, and John E Fischer. Abundance of encapsulated C_{60} in single-wall carbon nanotubes. *Chemical Physics Letters*, 310(1):21–24, 1999.

[92] P. M. Ajayan et al. Capillarity-induced filling of carbon nanotubes. *Nature*, 361(6410):333–334, 1993.

[93] Taishi Takenobu, Takumi Takano, Masashi Shiraishi, Yousuke Murakami, Masafumi Ata, Hiromichi Kataura, Yohji Achiba, and Yoshihiro Iwasa. Stable and controlled amphoteric doping by encapsulation of organic molecules inside carbon nanotubes. *Nature materials*, 2(10):683–688, 2003.

[94] K Yanagi, Y Miyata, and H Kataura. Highly Stabilized β-Carotene in Carbon Nanotubes. *Advanced Materials*, 18(4):437–441, 2006.

[95] K. Porfyrakis A. Ardavan G. A. D. Briggs D. A. Britz, A. N. Khlobystov. Chemical reactions inside single-walled carbon nano test-tubes. *Chemical communications*, (1):37–39, 2005.

[96] G Bongiovanni, C Botta, G Di Silvestro, MA Loi, A Mura, and R Tubino. Energy transfer in nanostructured oligothiophene inclusion compounds. *Chemical physics letters*, 345(5):386–394, 2001.

[97] M Zavelani-Rossi, G Lanzani, M Anni, G Gigli, R Cingolani, G Barbarella, and L Favaretto. Organic laser based on thiophene derivatives. *Synthetic Metals*, 139(3):901–903, 2003.

[98] Ping Liu, Xiaobo Wang, Yamin Zhang, Xiaoping Zhou, and Wenji Deng. Synthesis and photovoltaic properties of oligothiophene derivatives. *Synthetic metals*, 155(3):565–568, 2005.

[99] W. Orellana and S. O. Vásquez. Endohedral terthiophene in zigzag carbon nanotubes: Density functional calculations. *Phys. Rev. B*, 74:125419, Sep 2006.

[100] Matus Milko, Peter Puschnig, and Claudia Draxl. Predicting the electronic structure of weakly interacting hybrid systems: The example of nanosized peapod structures. *Physical Review B*, 86(15):155416, 2012.

[101] Martin Kalbáč, Ladislav Kavan, Sandeep Gorantla, Thomas Gemming, and Lothar Dunsch. Sexithiophene Encapsulated in a Single-Walled Carbon Nanotube: An In Situ Raman Spectroelectrochemical Study of a Peapod Structure. *Chemistry–A European Journal*, 16(38):11753–11759, 2010.

[102] Soon-Kil Joung, Toshiya Okazaki, Naoki Kishi, Susumu Okada, Shunji Bandow, and Sumio Iijima. Effect of Fullerene Encapsulation on Radial Vibrational Breathing-Mode Frequencies of Single-Wall Carbon Nanotubes. *Physical review letters*, 103(2):027403, 2009.

[103] AL Maniero, A Barbon, M Bortolus, and M Brustolon. Dyes included in channels: effects of the confinement on the photoexcited triplets: A TR-EPR study. *Synthetic metals*, 147(1):127–131, 2004.

[104] Norman Troullier and José Luís Martins. Efficient pseudopotentials for plane-wave calculations. *Physical review B*, 43(3):1993, 1991.

[105] Y Almadori, L Alvarez, R Le Parc, R Aznar, F Fossard, A Loiseau, B Jousselme, S Campidelli, P Hermet, A Belhboub, et al. Chromophore ordering by confinement into carbon nanotubes. *The Journal of Physical Chemistry C*, 118(33):19462–19468, 2014.

[106] E Gaufrès, NY-Wa Tang, F Lapointe, J Cabana, M-A Nadon, N Cottenye, F Raymond, T Szkopek, and R Martel. Giant Raman scattering from J-aggregated dyes inside carbon nanotubes for multispectral imaging. *Nature Photonics*, 8(1):72–78, 2014.

[107] M Kalbac, H Farhat, L Kavan, J Kong, and MS Dresselhaus. Competition between the spring force constant and the phonon energy renormalization in electrochemically doped semiconducting single-walled carbon nanotubes. *Nano letters*, 8(10):3532–3537, 2008.

[108] A. Belhboub. *Confinement d'oligomères π-conjugués dans les nanotubes de carbone: Modélisation de la dynamique vibrationnelle infrarouge*. PhD thesis, Université de Montpellier, 2015.

[109] Enhancing the Infrared Activity From Oligo-quaterthiophenes Interaction. 2016.

[110] Nanotube Research at the University of Oklahoma. CoMoCAT process, 2016.

[111] J. H. Harwell D. E. Resasco B. Kitiyanan, W. E. Alvarez. Controlled production of single-wall carbon nanotubes by catalytic decomposition of CO on bimetallic Co/Mo catalysts. *Chemical Physics Letters*, 317(3):497–503, 2000.

[112] Veena Choudhary. Arc discharge set-up, 2016.

[113] C Journet, WK Maser, P Bernier, A Loiseau, M Lamy De La Chapelle, de la S Lefrant, P Deniard, R Lee, and JE Fischer. Large-scale production of single-walled carbon nanotubes by the electric-arc technique. *nature*, 388(6644):756–758, 1997.

[114] Takeshi Saito, Satoshi Ohshima, Wei-Chun Xu, Hiroki Ago, Motoo Yumura, and Sumio Iijima. Size control of metal nanoparticle catalysts for the gas-phase synthesis of single-walled carbon nanotubes. *The Journal of Physical Chemistry B*, 109(21):10647–10652, 2005.

[115] Takeshi Saito, Wei-Chun Xu, Satoshi Ohshima, Hiroki Ago, Motoo Yumura, and Sumio Iijima. Supramolecular catalysts for the gas-phase synthesis of single-walled carbon nanotubes. *The Journal of Physical Chemistry B*, 110(12):5849–5853, 2006.

[116] Takeshi Saito, Satoshi Ohshima, Toshiya Okazaki, Shigekazu Ohmori, Motoo Yumura, and Sumio Iijima. Selective diameter control of single-walled carbon nanotubes in the gas-phase synthesis. *Journal of nanoscience and nanotechnology*, 8(11):6153–6157, 2008.

[117] Takeshi Saito. MEIJO eDIPS, 2016.

[118] Sigma-Aldrich. (7,6) Carbon nanotube, single-walled, 2016.

[119] Takeshi Saito. DIPS-CNT TEAM, 2016.

[120] S. Niyogi S. M. Rickard M. A. Hamon H. Hu B. Zhao M. E. Itkis, D. E. Perea and R. C. Haddon. Purity evaluation of as-prepared single-walled carbon nanotube soot by use of solution-phase near-IR spectroscopy. *Nano Letters*, 3(3):309–314, 2003.

[121] Sigma-Aldrich. Characterisation and Properties of CoMoCAT Carbon Nanotubes, 2016.

[122] M. L. H. Green S. C. Tsang, P. J. F. Harris et al. Thinning and opening of carbon nanotubes by oxidation using carbon dioxide. *Nature*, 362:520–520, 1993.

[123] Y. Mortazavi O. Sahraei F. Pourfayaz S. Sedghi M. V. Naseh, A. A. Khodadadi and S. Mosadegh. Functionalization of carbon nanotubes using nitric acid oxidation and DBD plasma. *World Academy of Science, Engineering and Technology*, 49:177–179, 2009.

[124] Y. Almadori. *Fonctionnalisation non-covalente de nanotubes de carbone monofeuillets: étude du confinement de molécules photo-actives et intercalation de rubidium*. PhD thesis, Université de Montpellier II, 2013.

[125] Sigma-Aldrich. 2,2':5',2":5",2"'-Quaterthiophene, 2016.

[126] Erwan Paineau, Pierre-Antoine Albouy, Stephan Rouziere, Andrea Orecchini, Stephane Rols, and Pascale Launois. X-ray scattering determination of the structure of water during carbon nanotube filling. *Nano letters*, 13(4):1751–1756, 2013.

[127] M. Kharlamova N. Kiselev A. Eliseev, L. Yashina. *One-dimensional crystals inside single-walled carbon nanotubes: growth, structure and electronic properties*. INTECH Open Access Publisher, 2011.

[128] T. Morisato R. Kuwahara, Y. Kudo and K. Ohno. Encapsulation of Carbon Chain Molecules in Single-Walled Carbon Nanotubes. *The Journal of Physical Chemistry A*, 115(20):5147–5156, 2011. PMID: 21542616.

[129] S. Lefrant G. Louarn, J. P. Buisson and D. Fichou. Vibrational Studies of a Series of. alpha.-Oligothiophenes as Model Systems of Polythiophene. *The Journal of Physical Chemistry*, 99(29):11399–11404, 1995.

[130] Y. Kanemitsu J. T. Navarrete V. Hernández, J. Casado. Vibrational study of a well–barrier–well thiophene–based oligomer in relation to the effective π-conjugation length. *The Journal of chemical physics*, 110(14):6907–6915, 1999.

[131] National institute of advanced industrial science and technology. Nanomaterials Research Institute, 2016.

[132] P. Nikolaev H. Dai A. Thess, R. Lee. Crystalline ropes of metallic carbon nanotubes. *Science*, 273(5274):483, 1996.

[133] Julien Cambedouzou, Vincent Pichot, Stéphane Rols, Pascale Launois, Pierre Petit, Robert Klement, Hiromichi Kataura, and Robert Almairac. On the diffraction pattern of C_{60} peapods. *The European Physical Journal B-Condensed Matter and Complex Systems*, 42(1):31–45, 2004.

[134] J. Cambedouzou. *Etude structurale et vibrationelle de composés à base de nanotubes de carbone: nanotubes bifeuillets peapods et composés ternaires*. PhD thesis, Université de Montpellier II, 2005.

[135] Inc Carbon-Solutions. AP-SWCNT, 2016.

[136] Inc Carbon-Solutions. P3-SWCNT, 2016.

[137] Elettra Sincrotrone Trieste. BEAR (Bending Magnet for Emission Absorption and Reflectivity), 2016.

[138] Tirandai Hemraj-Benny, Sarbajit Banerjee, Sharadha Sambasivan, Mahalingam Balasubramanian, Daniel A Fischer, Gyula Eres, Alexander A Puretzky, David B Geohegan, Douglas H Lowndes, Weiqiang Han, et al. Near-Edge X-ray Absorption Fine Structure Spectroscopy as a Tool for Investigating Nanomaterials. *Small*, 2(1):26–35, 2006.

[139] Brigitte Vigolo, Claire Hérold, Jean-François Marêché, Jaafar Ghanbaja, Michal Gulas, François Le Normand, Robert Almairac, Laurent Alvarez, and Jean-Louis Bantignies. A comprehensive scenario for commonly used purification procedures of arc-discharge as-produced single-walled carbon nanotubes. *Carbon*, 48(4):949–963, 2010.

[140] Anya Kuznetsova, Irene Popova, John T Yates, Michael J Bronikowski, Chad B Huffman, Jie Liu, Richard E Smalley, Henry H Hwu, and Jingguang G Chen. Oxygen-containing functional groups on single-wall carbon nanotubes: NEXAFS and vibrational spectroscopic studies. *Journal of the American Chemical Society*, 123(43):10699–10704, 2001.

[141] Xiaoming Wang, Nan Li, Jeffrey A Webb, Lisa D Pfefferle, and Gary L Haller. Effect of surface oxygen containing groups on the catalytic activity of multi-walled carbon nanotube supported Pt catalyst. *Applied Catalysis B: Environmental*, 101(1):21–30, 2010.

[142] M Abbas, ZY Wu, J Zhong, K Ibrahim, A Fiori, S Orlanducci, V Sessa, ML Terranova, and Ivan Davoli. X-ray absorption and photoelectron spectroscopy studies on graphite and single-walled carbon nanotubes: oxygen effect. *Applied Physics Letters*, 87(5):051923, 2005.

[143] WH Eugen Schwarz. Continuous change from valence to Rydberg type states. An example of XUV spectroscopy. *Chemical Physics*, 9(1-2):157–164, 1975.

[144] M Han, Y Luo, JE Moryl, RM Osgood, and JG Chen. A near-edge X-ray absorption fine structure study of atomic layer epitaxy: the chemistry of the growth of CdS layers on ZnSe(100). *Surface science*, 415(3):251–263, 1998.

[145] J Stöhr, JL Gland, EB Kollin, RJ Koestner, Allen L Johnson, EL Muetterties, and F Sette. Desulfurization and structural transformation of thiophene on the Pt (111) surface. *Physical Review Letters*, 53(22):2161, 1984.

[146] Liang Zhang, Liwen Ji, Per-Anders Glans, Yuegang Zhang, Junfa Zhu, and Jinghua Guo. Electronic structure and chemical bonding of a graphene oxide–sulfur nanocomposite for use in superior performance lithium–sulfur cells. *Physical Chemistry Chemical Physics*, 14(39):13670–13675, 2012.

[147] Colin Bousige, Stéphane Rols, Jacques Ollivier, Helmut Schober, Peter Fouquet, Giovanna G Simeoni, Viatcheslav Agafonov, Valery Davydov, Yoshiko Niimi, Kazutomo Suenaga, et al. From a one-dimensional crystal to a one-dimensional liquid: A comprehensive dynamical study of C_{60} peapods. *Physical Review B*, 87(19):195438, 2013.

[148] Alexander I Kolesnikov, Jean-Marc Zanotti, Chun-Keung Loong, Pappannan Thiyagarajan, Alexander P Moravsky, Raouf O Loutfy, and Christian J Burnham. Anomalously soft dynamics of water in a nanotube: a revelation of nanoscale confinement. *Physical review letters*, 93(3):035503, 2004.

[149] Confirming a Predicted Selection Rule in Inelastic Neutron Scattering Spectroscopy: The Quantum Translator-Rotator H_2 Entrapped Inside C_{60}, author=Xu, Minzhong and Jiménez-Ruiz, Mónica and Johnson, Mark R and Rols, Stéphane and Ye, Shufeng and Carravetta, Marina and Denning, Mark S and Lei, Xuegong and Bačić, Zlatko and Horsewill, Anthony J, journal=Physical review letters, volume=113, number=12, pages=123001, year=2014, publisher=APS.

[150] Julien Cambedouzou, Stéphane Rols, Robert Almairac, J-L Sauvajol, Hiromichi Kataura, and Helmut Schober. Low-frequency excitations of C_{60} chains inserted inside single-walled carbon nanotubes. *Physical Review B*, 71(4):041403, 2005.

[151] S Rols, Z Benes, E Anglaret, JL Sauvajol, P Papanek, JE Fischer, G Coddens, H Schober, and AJ Dianoux. Phonon density of states of single-wall carbon nanotubes. *Physical review letters*, 85(24):5222, 2000.

[152] S. Rols. *Structure et dynamique des nanotubes de carbone. Une étude par diffusion élastique et inélastique des neutrons*. PhD thesis, Université de Montpellier II, 2000.

[153] Stéphane Rols, Jean Cambedouzou, M Chorro, H Schober, V Agafonov, P Launois, V Davydov, AV Rakhmanina, H Kataura, and J-L Sauvajol. How confinement affects the dynamics of C_{60} in carbon nanopeapods. *Physical review letters*, 101(6):065507, 2008.

[154] C. Bousige. *Structure et dynamique de systémes unidimensionnels modèles: les nano-peapods de carbone*. PhD thesis, Université de Paris XI, 2012.

[155] S Rols, C Bousige, J Cambedouzou, P Launois, J-L Sauvajol, H Schober, VN Agafonov, VA Davydov, and J Ollivier. Unravelling low lying phonons and vibrations of carbon nanostructures: The contribution of inelastic and quasi-elastic neutron scattering. *The European Physical Journal Special Topics*, 213(1):77–102, 2012.

[156] A. Rahmani J.-L. Sauvajol P. Hermet, J.-L. Bantignies and M. R. Johnson. Polymorphism of crystalline α-quaterthiophene and α-sexithiophene: ab initio analysis and comparison with inelastic neutron scattering response. *The Journal of Physical Chemistry A*, 109(18):4202–4207, 2005.

[157] Jing Kong and Hongjie Dai. Full and modulated chemical gating of individual carbon nanotubes by organic amine compounds. *The Journal of Physical Chemistry B*, 105(15):2890–2893, 2001.

[158] Xueshen Wang, Qunqing Li, Jing Xie, Zhong Jin, Jinyong Wang, Yan Li, Kaili Jiang, and Shoushan Fan. Fabrication of ultralong and electrically uniform single-walled carbon nanotubes on clean substrates. *Nano letters*, 9(9):3137–3141, 2009.

[159] Sofie Cambré, Jochen Campo, Charlie Beirnaert, Christof Verlackt, Pegie Cool, and Wim Wenseleers. Asymmetric dyes align inside carbon nanotubes to yield a large nonlinear optical response. *Nature nanotechnology*, 10(3):248–252, 2015.

[160] Kazuhiro Yanagi and Hiromichi Kataura. Carbon nanotubes: Breaking Kasha's rule. *Nature Photonics*, 4(4):200–201, 2010.

[161] Institut Laue-Langevin. IN1 LAGRANGE (Large Area GRaphite ANalyser for Genuine Excitations), 2016.

[162] Institut Laue-Langevin. IN4C High-flux time-of-flight spectrometer, 2016.

[163] UD Wdowik, K Parlinski, Tapan Chatterji, S Rols, and H Schober. Lattice dynamics of rhenium trioxide from the quasiharmonic approximation. *Physical Review B*, 82(10):104301, 2010.

[164] T. Yumura and H. Yamashita. The role of weak bonding in determining the structure of thiophene oligomers inside carbon nanotubes. *The Journal of Physical Chemistry C*, 116(17):9681–9690, 2012.

[165] Daniel Sánchez-Portal, Pablo Ordejon, Emilio Artacho, and Jose M Soler. Density-functional method for very large systems with LCAO basis sets. *International Journal of Quantum Chemistry*, 65(5):453–461, 1997.

[166] John P Perdew, Kieron Burke, and Matthias Ernzerhof. Generalized gradient approximation made simple. *Physical review letters*, 77(18):3865, 1996.

[167] Stefan Grimme. Semiempirical GGA-type density functional constructed with a long-range dispersion correction. *Journal of computational chemistry*, 27(15):1787–1799, 2006.

[168] Michele Lazzeri, Stefano Piscanec, Francesco Mauri, AC Ferrari, and J Robertson. Phonon linewidths and electron-phonon coupling in graphite and nanotubes. *Physical review B*, 73(15):155426, 2006.

[169] Valentin N Popov and Philippe Lambin. Radius and chirality dependence of the radial breathing mode and the G-band phonon modes of single-walled carbon nanotubes. *Physical Review B*, 73(8):085407, 2006.

[170] M. L. Usrey P. W. Barone M. J. Allen H. Shan C. Kittrell R. H. Hauge J. M. Tour R. E. Smalley M. S. Strano, C. A. Dyke. Electronic structure control of single-walled carbon nanotube functionalization. *Science*, 301(5639):1519–1522, 2003.

[171] V. Perebeinos J. Liu J. C. Tsang, M. Freitag and P. Avouris. Doping and phonon renormalization in carbon nanotubes. *Nature nanotechnology*, 2(11):725–730, 2007.

[172] Mildred S Dresselhaus and G Dresselhaus. Intercalation compounds of graphite. *Advances in physics*, 51(1):1–186, 2002.

[173] R Arenal, F De la Pena, O Stephan, M Walls, M Tence, A Loiseau, and C Colliex. Extending the analysis of EELS spectrum-imaging data, from elemental to bond mapping in complex nanostructures. *Ultramicroscopy*, 109(1):32–38, 2008.

[174] C Jeanguillaume and Ch Colliex. Spectrum-image: the next step in EELS digital acquisition and processing. *Ultramicroscopy*, 28(1):252–257, 1989.

[175] Hong Lin, Raul Arenal, Shaïma Enouz-Vedrenne, Odile Stephan, and Annick Loiseau. Nitrogen configuration in individual CN x-SWNTs synthesized by laser vaporization technique. *The Journal of Physical Chemistry C*, 113(22):9509–9511, 2009.

[176] R Arenal, O Stephan, P Bruno, and DM Gruen. Spatially resolved electron energy loss spectroscopy on n-type ultrananocrystalline diamond films. *Applied Physics Letters*, 94(11):1905, 2009.

[177] Paola Ayala, R Arenal, M Rümmeli, Angel Rubio, and T Pichler. The doping of carbon nanotubes with nitrogen and their potential applications. *Carbon*, 48(3):575–586, 2010.

[178] Samuel D Stranks, Johannes K Sprafke, Harry L Anderson, and Robin J Nicholas. Electronic and mechanical modification of single-walled carbon nanotubes by binding to porphyrin oligomers. *ACS nano*, 5(3):2307–2315, 2011.

[179] Anton V Naumov, Sergei M Bachilo, Dmitri A Tsyboulski, and R Bruce Weisman. Electric field quenching of carbon nanotube photoluminescence. *Nano letters*, 8(5):1527–1531, 2008.

[180] Xianjie Liu, Hans Kuzmany, Paola Ayala, Matteo Calvaresi, Francesco Zerbetto, and Thomas Pichler. Selective Enhancement of Photoluminescence in Filled Single-Walled Carbon Nanotubes. *Advanced Functional Materials*, 22(15):3202–3208, 2012.

[181] A Rakitin, C Papadopoulos, and JM Xu. Carbon nanotube self-doping: Calculation of the hole carrier concentration. *Physical Review B*, 67(3):033411, 2003.

[182] Christian G Claessens, Uwe Hahn, and Tomas Torres. Phthalocyanines: from outstanding electronic properties to emerging applications. *The Chemical Record*, 8(2):75–97, 2008.

[183] Hiroshi Imahori, Tomokazu Umeyama, and Seigo Ito. Large π-aromatic molecules as potential sensitizers for highly efficient dye-sensitized solar cells. *Accounts of Chemical Research*, 42(11):1809–1818, 2009.

[184] Alexander W Hains, Ziqi Liang, Michael A Woodhouse, and Brian A Gregg. Molecular semiconductors in organic photovoltaic cells. *Chemical reviews*, 110(11):6689–6735, 2010.

[185] Giovanni Bottari, Gema de la Torre, Dirk M Guldi, and Tomás Torres. Covalent and noncovalent phthalocyanine- carbon nanostructure systems: synthesis, photoinduced electron transfer, and application to molecular photovoltaics. *Chemical reviews*, 110(11):6768–6816, 2010.

[186] Sandrine Heutz, Chiranjib Mitra, Wei Wu, Andrew J Fisher, Andrew Kerridge, Marshall Stoneham, AH Harker, Julie Gardener, H-H Tseng, Tim S Jones, et al. Molecular thin films: a new type of magnetic switch. *Advanced Materials*, 19(21):3618–3622, 2007.

[187] John Mack and Martin J Stillman. Assignment of the optical spectra of metal phthalocyanines through spectral band deconvolution analysis and ZINDO calculations. *Coordination Chemistry Reviews*, 219:993–1032, 2001.

[188] Yongzhong Bian, Lei Li, Jianmin Dou, Diana YY Cheng, Renjie Li, Changqin Ma, Dennis KP Ng, Nagao Kobayashi, and Jianzhuang Jiang. Synthesis, structure, spectroscopic properties, and electrochemistry of (1, 8, 15, 22-tetrasubstituted phthalocyaninato) lead complexes. *Inorganic chemistry*, 43(23):7539–7544, 2004.

[189] Jakub D Baran and J Andreas Larsson. Inversion of the shuttlecock shaped metal phthalocyanines MPc (M= Ge, Sn, Pb), a density functional study. *Physical Chemistry Chemical Physics*, 12(23):6179–6186, 2010.

[190] Jianzhuang Jiang. *Functional phthalocyanine molecular materials*, volume 135. Springer, 2010.

[191] Adriyan S Milev, Nguyen Tran, GS Kamali Kannangara, Michael A Wilson, and Isak Avramov. Polymorphic transformation of iron-phthalocyanine and the effect on carbon nanotube synthesis. *The Journal of Physical Chemistry C*, 112(14):5339–5347, 2008.

[192] SE S. E. Harrison and K. H. Ludewig. Conductivity and crystal phase change in phthalocyanines. *The Journal of Chemical Physics*, 45(1):343–348, 1966.

[193] Yannick Rio, M Salome Rodriguez-Morgade, and Tomas Torres. Modulating the electronic properties of porphyrinoids: a voyage from the violet to the infrared regions of the electromagnetic spectrum. *Organic & biomolecular chemistry*, 6(11):1877–1894, 2008.

[194] Karina Schulte, Janine C Swarbrick, Nicholas A Smith, Federica Bondino, Elena Magnano, and Andrei N Khlobystov. Assembly of cobalt phthalocyanine stacks inside carbon nanotubes. *Advanced Materials*, 19(20):3312–3316, 2007.

[195] K Schulte, C Yan, M Ahola-Tuomi, A Stróżecka, PJ Moriarty, and AN Khlobystov. Encapsulation of cobalt phthalocyanine molecules in carbon nanotubes. In *Journal of Physics: Conference Series*, volume 100, page 012017. IOP Publishing, 2008.

[196] Janine C Swarbrick, Tsu-Chien Weng, Karina Schulte, Andrei N Khlobystov, and Pieter Glatzel. Electronic structure changes in cobalt phthalocyanine due to nanotube encapsulation probed using resonant inelastic X-ray scattering. *Physical Chemistry Chemical Physics*, 12(33):9693–9699, 2010.

[197] Laurent Alvarez, Fallou Fall, Anouar Belhboub, Rozenn Le Parc, Yann Almadori, Raul Arenal, Raymond Aznar, Philippe Dieudonné-George, Patrick Hermet, Abdelali Rahmani, et al. One-dimensional molecular crystal of phthalocyanine confined into single-walled carbon nanotubes. *The Journal of Physical Chemistry C*, 119(9):5203–5210, 2015.

[198] Toshiya Okazaki, Yoko Iizumi, Shingo Okubo, Hiromichi Kataura, Zheng Liu, Kazu Suenaga, Yoshio Tahara, Masako Yudasaka, Susumu Okada, and Sumio Iijima. Coaxially Stacked Coronene Columns inside Single-Walled Carbon Nanotubes. *Angewandte Chemie International Edition*, 50(21):4853–4857, 2011.

[199] Ilya V Anoshkin, Alexandr V Talyzin, Albert G Nasibulin, Arkady V Krasheninnikov, Hua Jiang, Risto M Nieminen, and Esko I Kauppinen. Coronene Encapsulation in Single-Walled Carbon Nanotubes: Stacked Columns, Peapods, and Nanoribbons. *ChemPhysChem*, 15(8):1660–1665, 2014.

[200] S Rols, R Almairac, L Henrard, E Anglaret, and J-L Sauvajol. Diffraction by finite-size crystalline bundles of single wall nanotubes. *The European Physical Journal B-Condensed Matter and Complex Systems*, 10(2):263–270, 1999.

[201] J-L Sauvajol, E Anglaret, S Rols, and L Alvarez. Phonons in single wall carbon nanotube bundles. *Carbon*, 40(10):1697–1714, 2002.

[202] S. Rols E. Anglaret and J.-L. Sauvajol. Comment on "Effect of the Growth Temperature on the Diameter Distribution and Chirality of Single-Wall Carbon Nanotubes". *Physical review letters*, 81(21):4780, 1998.

[203] M Chorro, Stéphane Rols, Jean Cambedouzou, Laurent Alvarez, Robert Almairac, J-L Sauvajol, J-L Hodeau, L Marques, M Mezouar, and H Kataura. Structural properties of carbon peapods under extreme conditions studied using in situ X-ray diffraction. *Physical Review B*, 74(20):205425, 2006.

[204] Julien Cambedouzou, Stéphane Rols, Robert Almairac, J-L Sauvajol, Hiromichi Kataura, and Helmut Schober. Low-frequency excitations of C_{60} chains inserted inside single-walled carbon nanotubes. *Physical Review B*, 71(4):041403, 2005.

[205] MJ Peters, Laurie E Mcneil, Jian Ping Lu, and Daniel Kahn. Structural phase transition in carbon nanotube bundles under pressure. *Physical review B*, 61(9):5939, 2000.

[206] N Bendiab, R Almairac, J-L Sauvajol, S Rols, and E Elkaim. Orientation of single-walled carbon nanotubes by uniaxial pressure. *Journal of applied physics*, 93(3):1769–1773, 2003.

[207] Alfonso San-Miguel. Nanomaterials under high-pressure. *Chemical Society Reviews*, 35(10):876–889, 2006.

[208] JE Proctor, MP Halsall, A Ghandour, and DJ Dunstan. Raman spectroscopy of single-walled carbon nanotubes at high pressure: Effect of interactions between the nanotubes and pressure transmitting media. *physica status solidi (b)*, 244(1):147–150, 2007.

[209] Kun Gao, RC Dai, Z Zhao, ZM Zhang, and ZJ Ding. Effects of pressure transmitting media on Raman features of single-walled carbon nanotubes. *Solid State Communications*, 147(1):65–68, 2008.

[210] Mingguang Yao, Shuangchen Lu, Junping Xiao, Zhen Yao, Linhai Jiang, Tian Cui, and Bingbing Liu. Probing factors affecting the Raman modes and structural collapse of single-walled carbon nanotubes under pressure. *physica status solidi (b)*, 250(7):1370–1375, 2013.

[211] S Rols, IN Goncharenko, R Almairac, JL Sauvajol, and I Mirebeau. Polygonization of single-wall carbon nanotube bundles under high pressure. *Physical Review B*, 64(15):153401, 2001.

[212] UD Venkateswaran, EA Brandsen, U Schlecht, Apparao M Rao, E Richter, I Loa, K Syassen, and PC Eklund. High Pressure Studies of the Raman-Active Phonons in Carbon Nanotubes. *physica status solidi (b)*, 223(1):225–236, 2001.

[213] Tiago FT Cerqueira, Silvana Botti, Alfonso San-Miguel, and Miguel AL Marques. Density-functional tight-binding study of the collapse of carbon nanotubes under hydrostatic pressure. *Carbon*, 69:355–360, 2014.

[214] A Abouelsayed, K Thirunavukkuarasu, F Hennrich, and CA Kuntscher. Role of the pressure transmitting medium for the pressure effects in single-walled carbon nanotubes. *The Journal of Physical Chemistry C*, 114(10):4424–4428, 2010.

[215] Pallavi V Teredesai, AK Sood, DVS Muthu, Rahul Sen, A Govindaraj, and CNR Rao. Pressure-induced reversible transformation in single-wall carbon nanotube bundles studied by Raman spectroscopy. *Chemical Physics Letters*, 319(3):296–302, 2000.

[216] Pallavi V Teredesai, AK Sood, Surinder M Sharma, S Karmakar, SK Sikka, A Govindaraj, and CNR Rao. Pressure effects on single wall carbon nanotube bundles. *physica status solidi: B*, 223:479–487, 2001.

[217] Alexandre Merlen, Nedjma Bendiab, Pierre Toulemonde, Anna Aouizerat, Alfonso San Miguel, Jean-Louis Sauvajol, Gilles Montagnac, Hervé Cardon, and Pierre Petit. Resonant Raman spectroscopy of single-wall carbon nanotubes under pressure. *Physical Review B*, 72(3):035409, 2005.

[218] Alexandre Merlen, Pierre Toulemonde, Nedjma Bendiab, Anna Aouizerat, Jean-Louis Sauvajol, Gilles Montagnac, Hervé Cardon, Pierre Petit, and Alfonso San Miguel. Raman spectroscopy of open-ended Single Wall Carbon Nanotubes under pressure: effect of the pressure transmitting medium. *physica status solidi (b)*, 243(3):690–699, 2006.

[219] CA Kuntscher, A Abouelsayed, K Thirunavukkuarasu, and F Hennrich. Pressure-induced phenomena in single-walled carbon nanotubes: Structural phase transitions and the role of pressure transmitting medium. *physica status solidi (b)*, 247(11-12):2789–2792, 2010.

[220] Ch Caillier, D Machon, A San-Miguel, R Arenal, G Montagnac, H Cardon, M Kalbac, M Zukalova, and L Kavan. Probing high-pressure properties of single-wall carbon nanotubes through fullerene encapsulation. *Physical Review B*, 77(12):125418, 2008.

[221] KV Shanavas and Surinder M Sharma. Molecular dynamics simulations of phase transitions in argon-filled single-walled carbon nanotube bundles under high pressure. *Physical Review B*, 79(15):155425, 2009.

[222] Abraao Cefas Torres Dias. *Effects of high pressure on empty and water-filled single-wall carbon nanotubes studied by Raman spectroscopy*. PhD thesis, Lyon 1, 2014.

[223] Wenwen Cui, Tiago FT Cerqueira, Silvana Botti, Miguel AL Marques, and Alfonso San-Miguel. Nanostructured water and carbon dioxide inside collapsing carbon nanotubes at high pressure. *Physical Chemistry Chemical Physics*, 18(29):19926–19932, 2016.

[224] Yonggang Zou, Bingbing Liu, Mingguang Yao, Yuanyuan Hou, Lin Wang, Shidan Yu, Peng Wang, Bing Li, Bo Zou, Tian Cui, et al. Raman spectroscopy study of carbon nanotube peapods excited by near-IR laser under high pressure. *Physical Review B*, 76(19):195417, 2007.

[225] James A Elliott, Jan KW Sandler, Alan H Windle, Robert J Young, and Milo SP Shaffer. Collapse of single-wall carbon nanotubes is diameter dependent. *Physical Review Letters*, 92(9):095501, 2004.

[226] JW Otto, JK Vassiliou, and G Frommeyer. Nonhydrostatic compression of elastically anisotropic polycrystals. I. Hydrostatic limits of 4:1 methanol-ethanol and paraffin oil. *Physical Review B*, 57(6):3253, 1998.

[227] S Klotz, L Paumier, G Le March, and P Munsch. The effect of temperature on the hydrostatic limit of 4:1 methanol–ethanol under pressure. *High Pressure Research*, 29(4):649–652, 2009.

[228] UD Venkateswaran, Apparao M Rao, E Richter, M Menon, A Rinzler, RE Smalley, and PC Eklund. Probing the single-wall carbon nanotube bundle: Raman scattering under high pressure. *Physical Review B*, 59(16):10928, 1999.

[229] I Loa. Raman spectroscopy on carbon nanotubes at high pressure. *Journal of Raman Spectroscopy*, 34(7-8):611–627, 2003.

[230] AK Sood, Pallavi V Teresdesai, DVS Muthu, Rahul Sen, A Govindaraj, and CNR Rao. Pressure behaviour of single wall carbon nanotube bundles and fullerenes: A Raman study. *physica status solidi: B*, 215:393–401, 1999.

[231] Bernard Delley. An all-electron numerical method for solving the local density functional for polyatomic molecules. *The Journal of chemical physics*, 92(1):508–517, 1990.

[232] Bernard Delley. From molecules to solids with the DMol^3 approach. *The Journal of chemical physics*, 113(18):7756–7764, 2000.

[233] Inc Accelerys. BIOVIA Materials Studio, 2016.

[234] Y. Zhang Z. Liu, X. Zhang and J. Jiang. Theoretical investigation of the molecular, electronic structures and vibrational spectra of a series of first transition metal phthalocyanines. *Spectrochimica Acta Part A: Molecular and Biomolecular Spectroscopy*, 67(5):1232–1246, 2007.

[235] GSS Saini, Sukhwinder Singh, Sarvpreet Kaur, Ranjan Kumar, Vasant Sathe, and SK Tripathi. Zinc phthalocyanine thin film and chemical analyte interaction studies by density functional theory and vibrational techniques. *Journal of Physics: Condensed Matter*, 21(22):225006, 2009.

[236] Daniel R Tackley, Geoffrey Dent, and W Ewen Smith. IR and Raman assignments for zinc phthalocyanine from DFT calculations. *Physical Chemistry Chemical Physics*, 2(18):3949–3955, 2000.

[237] P. Hermet. *Modélisation de la dynamique vibrationnelle des oligothiophènes*. PhD thesis, Université de Montpellier II, 2004.

[238] F. J. Ramirez G. Zotti S. Hotta V. Hernandez, J. Casado and J. T. Navarrete. Efficient π electrons delocalization in α, α-dimethyl end-capped oligothiophenes: A vibrational spectroscopic study. *The Journal of chemical physics*, 104(23):9271–9282, 1996.

[239] B. S. Hudson. Vibrational spectroscopy using inelastic neutron scattering: Overview and outlook. *Vibrational spectroscopy*, 42(1):25–32, 2006.

[240] Gordon Leslie Squires. *Introduction to the theory of thermal neutron scattering*. Cambridge university press, 2012.

[241] Stephen W Lovesey. *Theory of neutron scattering from condensed matter*. 1984.

[242] ND Mermin Ashcroft, Neil W. *Solid State Physics*. Saunders College, Philadelphia, 1976.

[243] Léon Van Hove. The occurrence of singularities in the elastic frequency distribution of a crystal. *Physical Review*, 89(6):1189, 1953.

[244] Alexei A Maradudin. *Theory of lattice dynamics in the harmonic approximation*. Number 3. Academic Pr, 1971.

[245] Colin Bousige, Stéphane Rols, Julien Cambedouzou, Bart Verberck, Sándor Pekker, Éva Kováts, Gábor Durkó, István Jalsovsky, Éric Pellegrini, and Pascale Launois. Lattice dynamics of a rotor-stator molecular crystal: Fullerene-cubane $C_{60}{\cdot}C_8H_8$. *Physical Review B*, 82(19):195413, 2010.

[246] H Schober, A Tölle, B Renker, R Heid, and F Gompf. Microscopic dynamics of A C_{60} compounds in the plastic, polymer, and dimer phases investigated by inelastic neutron scattering. *Physical Review B*, 56(10):5937, 1997.

[247] Laboratoire Léon Brillouin. Small Angle Neutron Scattering Facility PAXY, 2016.

[248] Institut Laue-Langevin. D16 Small momentum transfer diffractometer with variable vertical focusing, 2016.

[249] Viviana Cristiglio, Benjamin Giroud, Luc Didier, and Bruno Demé. D16 is back to business: more neutrons, more space, more fun. *Neutron News*, 26(3):22–24, 2015.

[250] Institut Laue-Langevin Sample Environment. TiZr Null Matrix Alloy, 2016.

[251] Peter Lindner. Water calibration at DLL verified with polymer samples. *Journal of applied crystallography*, 33(3):807–811, 2000.

[252] H Mutka. Coupled time and space focusing for time-of-flight inelastic scattering. *Nuclear Instruments and Methods in Physics Research Section A: Accelerators, Spectrometers, Detectors and Associated Equipment*, 338(1):144–150, 1994.

[253] Alexandre Ivanov, Mónica Jimenéz-Ruiz, and Jiri Kulda. IN1-LAGRANGE–the new ILL instrument to explore vibration dynamics of complex materials. In *Journal of Physics: Conference Series*, volume 554, page 012001. IOP Publishing, 2014.

[254] Mingguang Yao, Zhigang Wang, Bingbing Liu, Yonggang Zou, Shidan Yu, Wang Lin, Yuanyuan Hou, Shoufu Pan, Mingxing Jin, Bo Zou, et al. Raman signature to identify the structural transition of single-wall carbon nanotubes under high pressure. *Physical Review B*, 78(20):205411, 2008.

[255] John E Proctor, Matthew P Halsall, Ahmad Ghandour, and David J Dunstan. Effect of chemical environment on high-pressure Raman response of single-walled carbon nanotubes. *High Pressure Research*, 26(4):335–339, 2006.

[256] Jesús Marquina, Enmanuel Flahaut, and Jesús González. High-pressure optical absorption studies of double-walled carbon nanotubes. *physica status solidi (RRL)-Rapid Research Letters*, 6(9-10):382–384, 2012.

Confinement d'oligomères π-conjugués dans des nanotubes de carbone mono-feuillets : interactions, dynamique et structure

Résumé : Ce travail est dédié à l'étude de l'encapsulation de molécules organiques photoactives dans des nanotubes de carbone mono-feuillets. L'effet de confinement sur les propriétés vibrationnelles, structurales, et les interactions entre les sous-systèmes est étudié en fonction de la taille des nanotubes.

La première partie du manuscrit est consacrée à l'étude du confinement de diméthyl- quaterthiophènes dans les tubes. La dynamique vibrationnelle des molécules confinées est étudiée par diffusion inélastique des neutrons et par des simulations DFT. L'étude des interactions entre les deux sous-systèmes, en termes de transfert d'énergie et de transfert de charge, est réalisée en combinant des études de photoluminescence et de Raman. La nature des transferts de charge dépend de la taille du nanotube. Pour des tubes de petits diamètres (<1.1nm), un transfert de charge photo-induit est obtenu lorsque la longueur d'excitation correspond à l'absorption de la molécule.

La deuxième partie est dédiée à l'étude de l'organisation structurale de molécules de phtalocyanine encapsulées à l'intérieur des nanotubes. Ce travail combine des études expérimentales par diffraction neutronique et spectroscopie Raman à pression ambiante et sous hautes pressions. Les études structurales sont confrontées à des simulations par dynamique moléculaire.

Mots clés : Nanotubes de carbone mono-feuillets, Oligothiophène, Phthalocyanine, Diffusion Neutronique élastique et inélastique, Spectroscopie Raman, Pression, Simulations

Confinement of π-conjugated oligomers inside single-walled carbon nanotubes : interaction, dynamics and structure

Abstract : This work is dedicated to the study of the encapsulation of photoactive molecules within single wall carbon nanotubes. The confinement effect on vibrational, structural and interactions between host and guest is studied as a function of nanotube size.

The first part of the manuscript is dedicated to the confinement of dimethyl-quaterthiophene within carbon nanotubes. Vibrational dynamics for the encapsulated molecules is studied coupling neutron scattering and DFT simulations. Interactions molecule/nanotube, in terms of energy transfer and charge transfer are studied combining photoluminescence and Raman spectroscopies. The nature of charge transfers depends on the size of the nanotube. For small diameters (<1.1nm) a photo-induced charge transfer is obtained when the excitation wavelength matches the absorption of the molecule.

The second part of the manuscript focuses on the structural organization of encapsulated phthalocyanine molecules. This work combines neutron diffraction and Raman spectroscopy experimental studies at room and high pressures. Structural studies are discussed together with molecular dynamics simulations.

Key words : Single-walled carbon nanotubes, Oligothiophene, Phthalocyanine, Encapsulation, Inelastic and Elastic Neutron Scattering, Raman Spectroscopy, Pressure, Simulations

Discipline : Physique

Laboratoire de rattachement :

Laboratoire Charles Coulomb, UMR 5221
CNRS, Université de Montpellier
Montpellier, France